

STRUCTURE-PROPERTY RELATIONS IN Sr, Nb, Ba DOPED LEAD ZIRCONATE TITANATE



I am very grateful to my supervisor, Dr I.M. Reaney and my University of Sheffield for their contribution to funding my research via a Doctoral Training and Starting Researcher Grant (DTSRG) over the period of my PhD studies.

By
Hong Zheng

Thesis submitted in partial fulfilment of the requirements for the degree of
Doctor of Philosophy in the Department of Engineering Materials,
University of Sheffield

Thesis Supervisors: Dr. I.M. Reaney and Prof. W.E. Lee

November 1998 - November 2001

ACKNOWLEDGEMENTS

This thesis was accomplished during the period from November 1998 to November 2001, in co-operation between piezoelectric ceramics research group, Morgan Electroceramics, Ruabon, and the Department of Engineering Materials, University of Sheffield.

I wish to express my deepest gratitude to my supervisors Dr. Ian M. Reaney and Professor William E. Lee for giving me the opportunity to work on this project. Without their supervision, advice and encouragement throughout the duration of this project and the preparation of this thesis, I would never have finished it this quickly.

I am very grateful to Morgan Electroceramics and the University of Sheffield for their contribution to funding my research via the Overseas Research Scholarship (ORS) over the period of my PhD study.

There are many people, too many to mention in these few paragraphs, who helped me to get to this point. I would like to take this opportunity to thank some of them who contributed most.

Dr. Howard Thomas, Mr. Nik Jones and other fellows from the piezoelectric ceramic research group, Morgan Electroceramics for assisting me with piezoelectric measurements.

Dr. Dave Hall from Manchester Materials Science Centre, University of Manchester and UMIST for helping me with hysteresis loop measurements.

Mr. Heath Bagshaw for helping me with dielectric property and TG/DTA measurements.

Dr. Peter Kogal, Miss Dawn Bussey, Mrs. Jane Ladson from the Sorby Centre for training and practical help on SEM and TEM microscopy.

Many past and present members of Dr. I. M. Reaney and Prof. W. E. Lee's research groups have lent their knowledge, experience and statistical discussion, and given me many suggestions.

I also wish to thank all the academic, technical and secretarial staff in the Department of Engineering Materials for their practical and intellectual help.

In particular, I would like to thank Prof. Toft Sorensen from the Materials Research Department, Risoe National Laboratory, Denmark, who encouraged me to come to Sheffield for Ph.D study and his spiritual support throughout my PhD period.

On a personal note, my sincerest thanks go to my close friend Mr. Xiaoxu Ren, who has helped in preparing this thesis and supported me over the past three years, and all my Chinese friends for a good and memorable time in Sheffield.

Finally, this thesis is dedicated to my parents in China for their perpetual support, encouragement and enthusiasm. From the beginning, they always encouraged me to excel and achieve the goals that I set for myself. Without their encouragement and support, I would never have made it this far. I wish they could share this with me!

SUMMARY

Lead zirconate titanate (PZT) ceramics have been utilised for several decades to fabricate electromechanical sensors and actuators. Compositional modifications have led to the development of 'hard' and 'soft' PZT's. Soft PZT's are used in applications such as receiving transducers requiring high sensitivity, pulsed transmitting transducers with high acoustic outputs, high sensitivity receivers and actuators with large displacements.

In this investigation a systematic study was performed on a range of soft PZT materials. Their structures, microstructures and domain structures were characterised using X-ray diffraction, scanning and transmission electron microscopy. This data was then used to interpret dielectric, ferroelectric and piezoelectric properties.

The relative importance of three known softening methods in PZT was assessed: i) donor doping using Nb^{5+} on the B-site, ii) proximity to a morphotropic phase boundary (MPB), and iii) lowering the paraelectric-ferroelectric phase transition temperature (T_C) by substitution of Sr^{2+} or Ba^{2+} on the A-site.

Nb^{5+} substitution onto the B-site reduced the grain size although the domain structure ($\sim 100 \text{ nm}$ wide) remained the same except finer-scale domains ($\sim 20 \text{ nm}$ wide) and higher dislocations were present in ceramics with 7.2 mol% Nb^{5+} . T_C was lowered and the piezoelectric coefficient (d_{33}) increased. Nb-doped PZT could be stabilised either in rhombohedral or tetragonal forms or as mixture of the two (MPB), depending on Zr:Ti ratio. Zr:Ti ratio strongly affected d_{33} , which was maximised in the tetragonal phase close to, but not at, the MPB.

Sr^{2+} substitution on the A-site promoted tetragonality in PZT, greatly reducing T_C , and broadening the dielectric maximum. As the Sr^{2+} content was increased, Zr:Ti ratio was adjusted to maximise d_{33} and the optimised d_{33} values increased from 410 $p\text{C/N}$ ($\text{Sr}^{2+} = 0$) to 640 $p\text{C/N}$ ($\text{Sr}^{2+} = 0.12$), commensurate with a decrease in the T_C . However, for ceramics where $\text{Sr}^{2+} > 0.12$, optimised d_{33} decreased with respect to the values for ceramics where $\text{Sr}^{2+} = 0.12$ even though T_C was lowered. Electron diffraction patterns revealed superlattice reflections occurring at $1/2\{\text{hkl}\}$ positions associated with rotations of oxygen octahedra in anti-phase. It was suggested that Sr^{2+} substitution on the A-site decreased the tolerance factor t , resulting in the onset of oxygen octahedral tilting.

Co-doping PZT with Sr^{2+} and Ba^{2+} on the A-site resulted in the disappearance of the $1/2\{\text{hkl}\}$ superlattice reflections. However, the d_{33} was not improved. Evidence of relaxor behaviour revealed by TEM in Sr, Ba co-doped PZT was thought to be responsible for the deterioration in piezoelectric properties.

Effect of sintering temperature on the decomposition of perovskite phase was also examined. PbO loss was detected in Sr-doped PZT (PSZT) at the sample surface $\geq 1170^\circ\text{C}$, which was accompanied by the formation of a second phase. The second phase was identified as monoclinic ZrO_2 . An increase in degree of tetragonality was also observed in the perovskite matrix.

CONTENTS

ACKNOWLEDGEMENTS

SUMMARY

1. INTRODUCTION	1
2. LITERATURE REVIEW	4
2.1. Basic principles and definitions.....	4
2.1.1. Piezoelectricity.....	4
2.1.2. Basis of piezoelectricity in solids.....	5
2.1.3. Ferroelectricity.....	7
2.1.4. Hysteresis loop.....	7
2.1.5. Curie Weiss law.....	8
2.1.6. Domains and domain walls.....	9
2.1.7. Basic piezoelectric equations and constants.....	10
2.2. Crystal chemistry.....	13
2.2.1. Crystal structure of perovskites.....	13

2.2.2. Tolerance factor (t) in perovskites.....	14
2.2.3. Octahedral tilt transitions in perovskites.....	15
2.2.4. Origin of ferroelectricity in perovskites.....	16
2.2.5. Phase equilibria and structures of PZT.....	18
2.3. Materials.....	21
2.3.1. Chronological history of ferroelectric materials.....	21
2.3.2. Piezoelectric effects in ferroelectric ceramics.....	22
2.4. “Soft” PZT’s and softening mechanisms.....	24
2.4.1. “Soft” PZTs.....	24
2.4.2. Proximity to the MPB.....	25
2.4.3. Nb ⁵⁺ doping on the B-site.....	27
2.4.4. Decreasing T_C	29
2.5. New materials.....	29
2.5.1. Relaxors.....	29
2.5.2. PNN-PZT.....	31
2.5.3. PZN-PT single crystals.....	32
2.5.4. PZT composites.....	33
2.6. Processing and fabrication of PZT ceramics.....	36
2.6.1. Powder preparation.....	37
2.6.2. PbO loss upon sintering.....	38
2.6.3. Densification.....	40
2.6.4. Sintering aids.....	40
2.6.5. Multi-layer techniques.....	41
2.7. Applications of piezoelectric and ferroelectric ceramics.....	42

2.7.1. Piezoelectric transducers, generators, motors.....	42
2.7.2. Piezoelectric transformers.....	42
2.7.3. Filters, resonators.....	43
2.8. Novel piezoelectric devices.....	43
2.8.1. Moonies.....	44
2.8.2. RAINBOW devices.....	45
3. EXPERIMENTAL PROCEDURES	46
3.1. Raw materials.....	46
3.2. Ceramic processing.....	47
3.3. Two-step calcination route.....	49
3.4. Compositions.....	50
3.4.1. Nb-doped PZT compositions.....	50
3.4.2. Sr-doped PZT compositions.....	51
3.4.3. Sr, and Ba co-doped PZT compositions.....	53
3.5. Characterisation techniques.....	54
3.5.1. Combined TG and DTA studies.....	54
3.5.2. Particle size analysis.....	55
3.5.3. Estimation of crystallographic density.....	56
3.5.4. Archimedes' density measurements.....	56
3.5.5. X-ray diffraction (XRD).....	57
3.5.6. Scanning electron microscopy (SEM).....	59
3.5.7. Transmission electron microscopy (TEM).....	60

3.5.8. Dielectric properties.....	61
3.5.9. d_{33} measurements.....	61
3.5.10. K_p coupling factor measurements.....	62
3.5.11. Hysteresis loop measurements.....	62
3.6. Measurement error analysis.....	63
3.6.1. Errors of measurement.....	63
3.6.2. Determinate and indeterminate errors.....	63
3.6.3. Evaluation of measurement errors.....	64
3.6.4. Importance of repeated measurements.....	64
4. CHARACTERISATION OF PROCESSING ROUTE	66
4.1. Starting raw powders.....	66
4.1.1. Combined TG/DTA studies.....	66
4.1.2. Particle shape and size analyses.....	68
4.1.3. XRD analysis.....	76
4.2. Calcined powders.....	80
4.2.1. A comparison between ball-milling and attrition-milling.....	80
4.2.2. Perovskite phase formation.....	83
4.3. Dense ceramics.....	84
4.3.1. Effect of sintering temperature on phase formation.....	84
4.3.2. Effect of grinding and polishing.....	86
4.4. Conclusions.....	87
5. EFFECT OF B-SITE Nb⁵⁺ DOPING ON PZT	89

5.1. Effect of Nb⁵⁺ content.....	89
5.1.1. XRD.....	89
5.1.2. Grain structure.....	91
5.1.3. Domain structure.....	93
5.1.4. Dielectric properties.....	98
5.1.5. d_{33} piezoelectric coefficients.....	100
5.2. Effect of Zr:Ti ratio in 2.4 mol% Nb-doped PZT.....	102
5.2.1. XRD.....	102
5.2.2. Grain structure.....	103
5.2.3. Domain structure.....	105
5.2.4. Dielectric properties.....	106
5.2.5. d_{33} piezoelectric coefficients.....	107
5.2.6. Hysteresis loops.....	109
5.3. Conclusions.....	110
6. EFFECT OF A-SITE Sr²⁺ SUBSTITUTION ON PZT	112
6.1. Effect of Sr²⁺ content.....	112
6.1.1. Structure and microstructure.....	112
6.1.2. Electrical characterisation.....	117
6.2. Effect of Zr:Ti ratio in 8 mol% Sr-doped PZT.....	120
6.2.1. Structure.....	120
6.2.2. Electrical characterisation.....	121
6.3. Effect of Zr:Ti ratio in 16 mol% Sr-doped PZT.....	125
6.3.1. Structure.....	125

6.3.2. Electrical characterisation.....	126
6.4. Conclusions.....	130
7. OXYGEN OCTAHEDRAL TILTING IN Sr-DOPED PZT	131
7.1. Phase structure.....	132
7.2. Selected area electron diffraction.....	133
7.3. Anti-phase oxygen octahedral tilting.....	137
7.4. Electrical characterisation.....	139
7.5. Conclusions.....	144
8. EFFECT OF A-SITE Sr, Ba CO-DOPING ON PZT	145
8.1. Sr, Ba co-doped PZT with a fixed Zr:Ti ratio.....	146
8.1.1. Structure.....	146
8.1.2. Electrical characterisation.....	147
8.2. 6mol% Sr and Ba co-doped PZT with varying Zr:Ti ratio.....	148
8.2.1. Structure and microstructure.....	149
8.2.2. Electrical characterisation.....	153
8.3. Conclusions.....	156
9. SURFACE DECOMPOSITION OF Sr-DOPED PZT	157
9.1. Effect of sintering temperature on perovskite phase stability.....	157
9.2. Microstructure.....	160
9.3. Mechanism of decomposition.....	165

9.4. Dielectric properties.....	167
9.5. Conclusions.....	169
10. TWO-STEP CALCINATION PROCESSING ROUTE	170
10.1. Two-step calcination route.....	171
10.2. Effect of calcination temperature on ZrTiO ₄ phase formation.....	171
10.3. Phase structure of PSZT prepared by two-step calcination route.....	173
10.4. Electrical characterisation.....	175
10.5. Conclusions.....	177
11. GENERAL DISCUSSION	178
12. CONCLUSIONS	187
12.1. Nb-doped PZT Ceramics.....	187
12.2. Sr, Nb-doped PZT Ceramics.....	188
12.3. Ba, Sr, Nb-doped PZT Ceramics.....	189
12.4. Surface decomposition in soft PZT ceramics.....	190
12.5. One-step and two-step calcination routes.....	190
13. FUTURE WORK	191
PUBLICATIONS AND CONFERENCE PRESENTATIONS	193

REFERENCES

195

1. INTRODUCTION

Perovskite-structured (general formula, ABO_3) lead zirconate titanate (PZT) piezoelectric ceramics have been utilised for several decades to fabricate electromechanical sensors and actuators. Many compositional modifications to PZT have been developed, which may be broadly categorised as either having higher-valency (donor) or lower-valency (acceptor) substitutions onto either the A or B site^[1]. Donor doping such as La^{3+} on the A-site or Nb^{5+} on the B-site often leads to an enhanced ease of polarisation switching under the ac field and these ceramics are referred to as “soft” PZT’s^[1], while lower valent substituent such as K^+ on the A-site or Fe^{3+} on the B-site results in an enhanced difficulty of polarisation switching and a reduced domain mobility and these ceramics are termed “hard” PZT’s^[1-2].

With respect to undoped and “hard” PZT, “soft” PZT materials have high relative permittivities, low coercive electric fields and high remnant polarisation. Therefore, they may be used in applications such as receiving transducers requiring high sensitivity, pulsed transmitting transducers with high acoustic outputs, high sensitivity receivers and actuators with large displacements. The high relative permittivity also offers the advantage of an increased capacitance with small components.

Soft PZT materials have typical piezoelectric coefficients (d_{33}) above 400 pC/N compared to 200 pC/N for undoped PZT ceramics. Recently, compositions based on PZT with lead nickel niobate (PNN) additions have been fabricated with the d_{33} values in excess of 1000 pC/N ^[3].

In bulk PZT ceramics, the room temperature dielectric and piezoelectric properties result from a combination of intrinsic behaviour of the material, which can be characterised by averaging the response expected from a single domain single crystal and extrinsic or domain wall contributions^[4-6]. Ferroelectric (180°) and ferroelectric-ferroelastic ($\text{non-}180^\circ$, typically 90°) domain wall motions both enhance the measured permittivity but only the motion of ferroelectric-ferroelastic domains ($\text{non-}180^\circ$) enhances the d_{33} . The magnitude of extrinsic contributions to the piezoelectric properties of PZT is responsible for the difference between hard and soft PZT's.

Through measurements of the temperature dependence of d_{33} , Zhang *et al.*^[4] demonstrated that in soft PZT, approximately one half of the room temperature piezoelectric properties are extrinsic in origin. On the basis of hydrostatic piezoelectric measurements, Zhang *et al.*^[5] calculated that, in soft PZT ceramics, approximately 60% of the room temperature d_{33} is attributable to domain wall motion. Similarly, through application of the Rayleigh law, Damjanovic *et al.*^[6] assigned $\sim 19\%$ of the room temperature d_{33} of PZT near the morphotropic phase boundary to irreversible domain wall motion with the remaining extrinsic response presumably due to reversible motion. However, to date few systematic studies on soft PZT correlating composition, domain and microstructure with piezoelectric properties have been carried out.

The objectives of this investigation were thus to perform a systematic study on a range of soft PZT materials; characterise their electrical properties as a function of composition and relate their electrical behaviour to their phase assemblage and microstructure. Particular attention was paid to the observation of the ferroelectric domain structure by transmission electron microscopy (TEM).

The main aim of the project was to assess the relative importance of three known softening methods in PZT:

- i) donor doping,
- ii) proximity to a morphotropic phase boundary (MPB) and

- iii) lowering the paraelectric-ferroelectric phase transition temperature (T_C)

The final goal was to optimise soft PZT compositions towards specific actuator applications, based on the understanding achieved.

2. LITERATURE REVIEW

2.1 Basic Principles and Definitions

2.1.1 Piezoelectricity

Piezoelectricity is a property, possessed by some materials, of becoming electrically charged when subjected to a mechanical stress. Such materials also exhibit the converse effect, i.e., the occurrence of mechanical deformation on application of an electrical field. This phenomenon was first discovered by Pierre and Jacques Curie in crystals such as quartz, zinc blende, tourmaline and Rochelle salt in 1880^[7]. The term “piezoelectricity” (pressure electricity) was first suggested by W. Hankel in 1881^[8]. Cady^[9] later defines piezoelectricity as “electric polarisation produced by mechanical strain in crystals belonging to certain classes, the polarisation being proportional to the strain and changing sign when the direction of the strain is reversed”.

However, piezoelectricity must be distinguished from electrostriction. Cady^[9] clearly defines the differences between piezoelectricity and electrostriction. In electrostriction, the sign of the deformation, which occurs with an applied electric field is independent of the polarity of the field, and proportional to the field (E^2). It is a phenomenon, which is present weakly in all materials, whether amorphous or crystalline, centrosymmetric or polar. With the piezoelectric effect, in contrast, the deformation is linear with respect to applied field, and changes sign when the electric field is reversed. In materials of high dielectric constant, and especially in ferroelectric

materials just above their Curie point, electrostriction can be of sufficient magnitude to be of interest.

2.1.2 Basis of Piezoelectricity in Solids

Our knowledge of piezoelectricity in solids is based on an understanding of the structure and microstructure of a material. A single crystallite is made up of ions that are constrained to occupy positions in a specific repeating relationship to each other, thus building up the lattice of the crystal. The smallest repeating unit of the lattice is called the unit cell, and the specific symmetry possessed by the unit cell determines whether it is possible for piezoelectricity to exist in the crystal.

The elements that are utilised to define symmetry about a point in space, e.g., the centre point of a unit cell, are: (1) a centre of symmetry, (2) axes of rotation, (3) mirror planes and (4) combinations of these. All crystals can be thus divided into 32 different point groups. These 32 point groups are subdivisions of seven basic crystal systems that are, in order of ascending symmetry, triclinic, monoclinic, orthorhombic, tetragonal, rhombohedral, hexagonal, and cubic. Of these 32 point groups, 21 are non-centrosymmetric i.e. not possessing a centre of symmetry and 20 of these are piezoelectric. One class, although lacking a centre of symmetry, is not piezoelectric because of other combined symmetry elements. Therefore, only non-centrosymmetric materials are piezoelectric.

Ferroelectrics belong to a subgroup of piezoelectric ceramics. Figure 2.1 shows the interrelationship of piezoelectrics and their subgroups such as ferroelectric or pyroelectric on the basis of symmetry.

In general, there are four groups of ferroelectric ceramics based on unit cell structure, (1) the tungsten-bronze group, (2) the oxygen octahedral group, (3) the pyrochlore group and (4) the bismuth layer-structure group. Of these, the second group (ABO_3 perovskite type) is by far the most important category, economically. In this

family, compositions BaTiO_3 (BT), PZT, La-doped PZT (PLZT), PbTiO_3 (PT) and $\text{Pb}(\text{Mg}_{1/3}\text{Nb}_{2/3})\text{O}_3$ (PMN) represent the bulk of the ferroelectric ceramics manufactured in the world today.

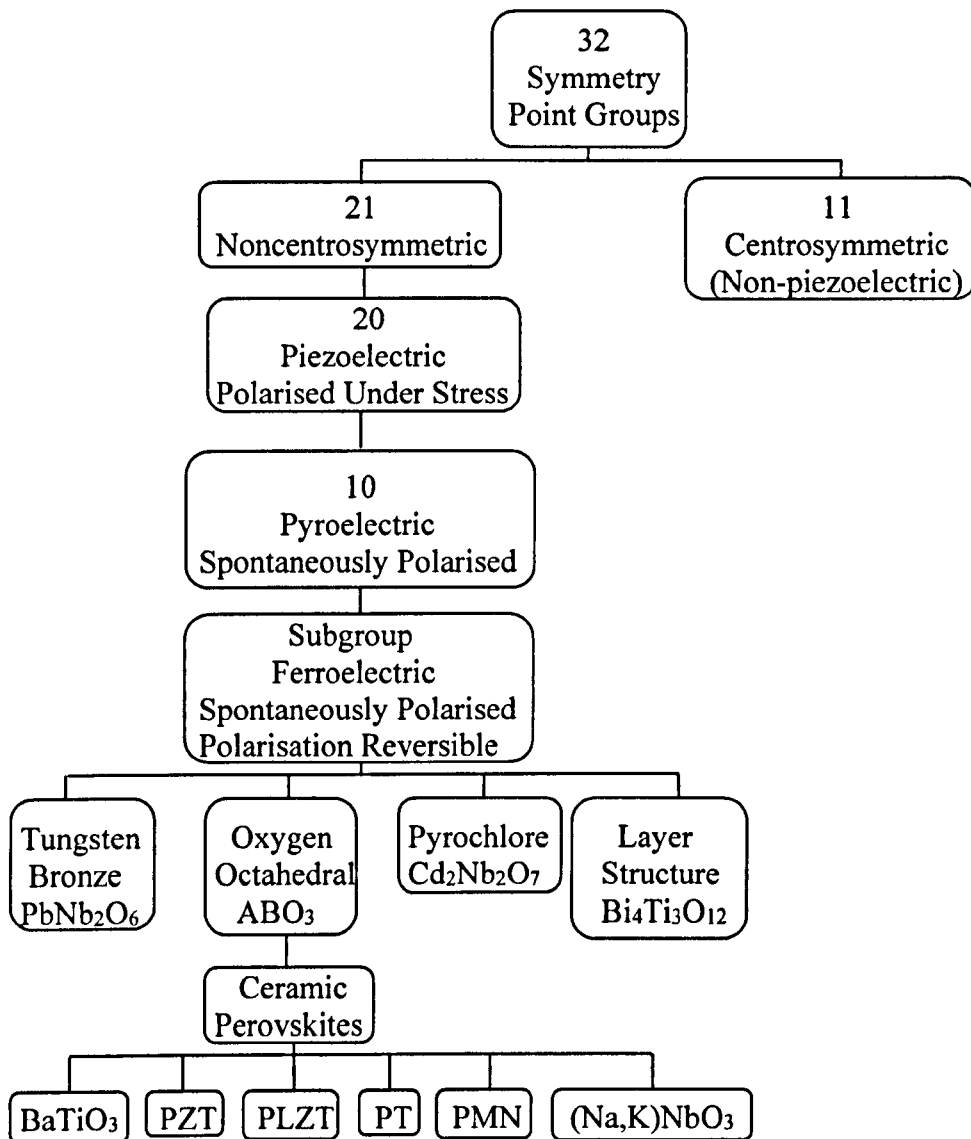


Figure 2.1 Interrelationship between piezoelectric and subgroups based on symmetry^[10]

2.1.3 Ferroelectricity

Piezoelectricity may be induced in certain compounds by the application of a strong electric field (polarisation). These materials are termed ferroelectric, all of which are therefore piezoelectric.

Ferroelectricity was first discovered by Joseph Valasek^[11] in Rochelle Salt in 1921. Two conditions are necessary to classify a material as ferroelectric (FE):

- i) the existence of spontaneous polarisation and
- ii) the direction of this polarisation can be reversed by the application of a sufficiently high electric field^[12].

2.1.4 Hysteresis Loop

Reversibility of polarisation in ferroelectrics is due to their polar structure, which arises as a result of a phase transition from a non-polar, paraelectric (PE) to the ferroelectric (FE) phase.

On plotting the values of macroscopic polarisation (P) against the external electric field (E), a hysteresis loop is obtained (Figure 2.2).

It can be seen from Figure 2.2 that, after the removal of the electric field, there is a remnant polarisation P_r in the material. The saturation polarisation, P_s , can be read on the ordinate axis by drawing a tangent to the loop at its tip. The value of coercive field strength, E_C , i.e., the field strength required to remove the remnant polarisation can also be obtained from the hysteresis curve.

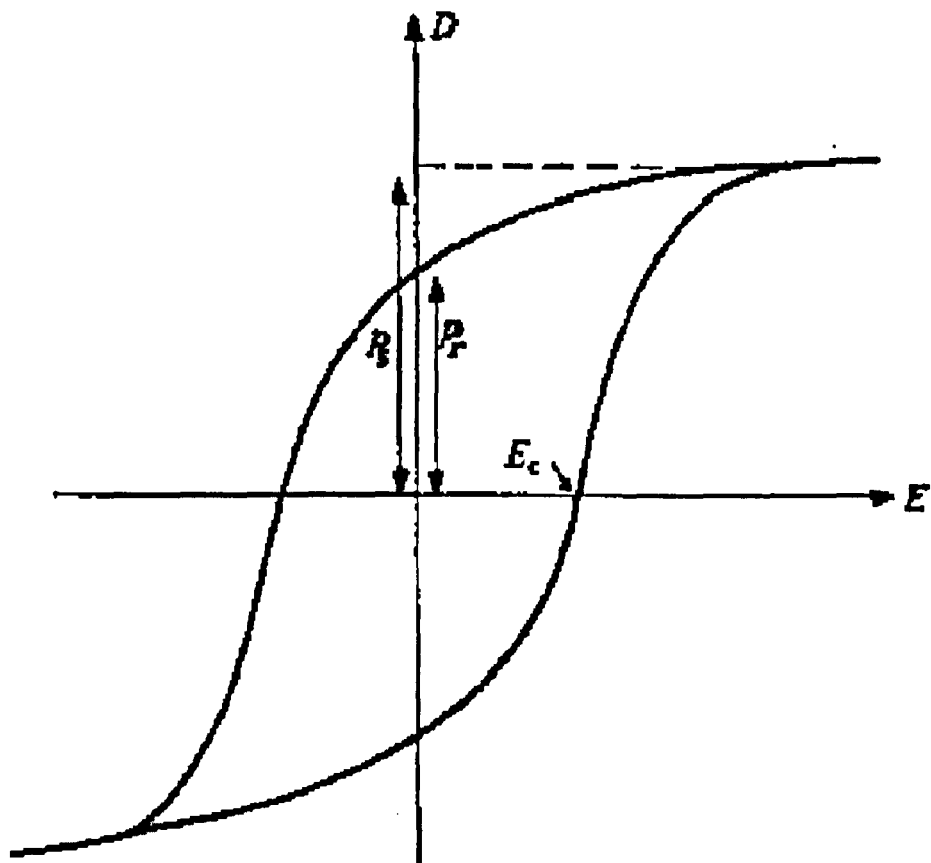


Figure 2.2 Hysteresis loop of a ferroelectric ceramic

2.1.5 Curie Weiss Law

Ferroelectricity only exists in a defined temperature range below a certain value^[13]. The temperature at which the material becomes FE on cooling is known as the Curie point (T_C). The dielectric constant, when plotted against temperature, shows a maximum at or close to T_C . In the PE state, the change in dielectric constant as a function of temperature may be described by the Curie-Weiss law^[14]:

$$\epsilon = \epsilon_\infty + A/(T - \Theta) \quad (2.1)$$

where ε_∞ is the value of dielectric constant at temperature $T \gg \Theta$, Θ is a constant characteristic of the substance, the Curie point, C is a constant of the substance and T is the temperature. According to the Curie Weiss law, the dielectric constant will be infinite at T_C .

2.1.6 Domains and Domain Walls

A domain^[15] is a region in a crystal where the dipoles are aligned in the same direction giving a net polarisation across its width. A domain wall separates two neighbouring regions in which the direction of polarisation differs. The driving force for the formation of ferroelectric domain walls is known as the depolarising field, which effectively minimises the macroscopic polarisation across the body of the ferroelectric. Formation of domains results in an electrically neutral body, thereby decreasing free energy in the system. The domain walls however, have a small positive interfacial energy^[16].

Some materials such as PZT and BaTiO₃ undergo a spontaneous strain as well as polarisation at T_C . This manifests itself, on cooling, as a distortion (in the same crystallographic direction as the polarisation) to a lower symmetry crystal class (e.g. cubic to tetragonal). The net result is that domains are present not only to minimise macroscopic polarisation but also to relieve stress associated with the spontaneous distortion. In these materials, ferroelastic (strain) domains (typically 90°) may exist across which there is also a net polarisation. Application of a strong electric field aligns electric dipoles that are coupled directly to deformation or strain on a unit cell level. This is the origin of the strong piezoelectric response in ferroelectrics.

2.1.7 Basic Piezoelectric Equations and Constants

The direct piezoelectric effect (designated as a generator) occurs when electric charge (polarisation) is generated by a mechanical stress, whereas the converse effect (designated as a motor) is associated with mechanical movement (strain) generated by the application of an electric field. The basic equations that describe these two effects are:

$$D = dT + \epsilon^T E \text{ (generator)} \quad (2.2)$$

$$S = s^E T + dE \text{ (motor)} \quad (2.3)$$

where D is the dielectric displacement (consider it equal to polarisation), T , the stress, E , the electric field, S , the strain, d , piezoelectric coefficient, s , the material compliance (inverse of modulus of elasticity) and ϵ , the dielectric constant or relative permittivity. The superscripts indicate a quantity held constant, in the case of ϵ^T , the stress is held constant, which means that the piezoelectric element is mechanically unconstrained, and in the case of s^E , the electric field is held constant, which means the electrodes on the element are shorted together.

These properties are directional quantities, and, hence, they are usually specified with subscripts to identify the conditions under which they are determined. The convention is to define the poling direction as the 3 axis, as illustrated in Figure 2.3. For example, d_{31} indicates that this piezoelectric coefficient relates to the generation of polarisation in electrodes perpendicular to the 3 or vertical direction and to the stress mechanically applied in the 1 or lateral direction.

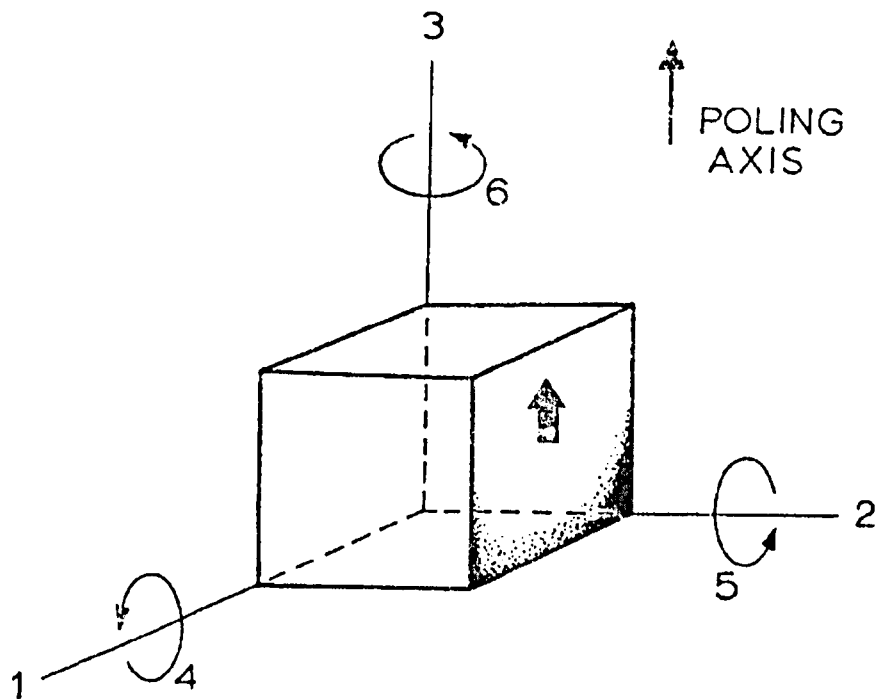


Figure 2.3 Notation of axes for poled ceramic element

d_{33} indicates the polarisation generated in the 3 direction when the stress is also applied in the 3 direction. Typical relationships for this coefficient are:

$$D_3 = d_{33} T_3 \text{ (direct effect)} \quad (2.4)$$

$$S_3 = d_{33} E_3 \text{ (converse effect)} \quad (2.5)$$

where the d coefficients are numerically equal in both equations. The d coefficients are usually expressed as pC/N for the direct effect and pm/V for the converse effect. Shear planes are indicated by the subscripts 4, 5, and 6 and are perpendicular to directions 1, 2, and 3 respectively.

There are also piezoelectric coefficients corresponding to hydrostatic stress, $d_h = d_{33} + 2d_{31}$. High d coefficients are desirable for those materials that are utilised in motional or vibrational devices, such as sonar and sounders.

In addition to the d coefficients, open-circuit g coefficients are also used to evaluate piezoelectric ceramics for their ability to generate large amounts of voltage per unit of input stress. The g constant is related to the d constant via the relationship:

$$g = d/\epsilon\epsilon_0 \quad (2.6)$$

where ϵ is the relative permittivity and ϵ_0 , the permittivity of free space ($8.854 \times 10^{-12} F/m$). Thus, a high g constant is possible for a given d coefficient if the material has a low ϵ . High- g -constant ceramics are usually ferroelectrically hard materials that do not switch their polarisation readily and possess low ϵ values. They are used in devices such as portable gas ignitors and patio lighters.

The piezoelectric coupling factor (e.g., k_{33} , k_{31} , and k_p) is a convenient and direct measurement of the overall strength of the electromechanical effect, i.e., the ability of the ceramic transducer to convert one form of energy to another. It is defined as either:

- i) the square root of the ratio of energy output in electrical form to the total mechanical energy input (direct effect) or,
- ii) the square root of the ratio of the energy available in mechanical form to the total electrical energy input (converse effect).

Because the conversion of electrical to mechanical energy (or vice versa) is always incomplete, k is less than unity. Commonly used as a figure-of-merit for piezoelectrics, higher k values are most desirable and constantly sought after in new materials. For ceramics, k_p is a typical measurement used in comparing materials-values ranging from 0.35 for BaTiO₃ to as high as 0.72 for PLZT.

2.2 Crystal Chemistry

2.2.1 Crystal Structure of Perovskites

The perovskite structure is a term, which is used to describe an arrangement of anions and cations similar to CaTiO_3 but where the symmetry of each phase can be quite different. The ideal perovskite crystal structure usually refers to the structure of the highest-temperature phase, the aristotype in Megaw's terminology^[17-18]. When the cations are displaced or the octahedra are tilted, different types of structures are produced, hettotypes, which are always of lower symmetry than the aristotype.

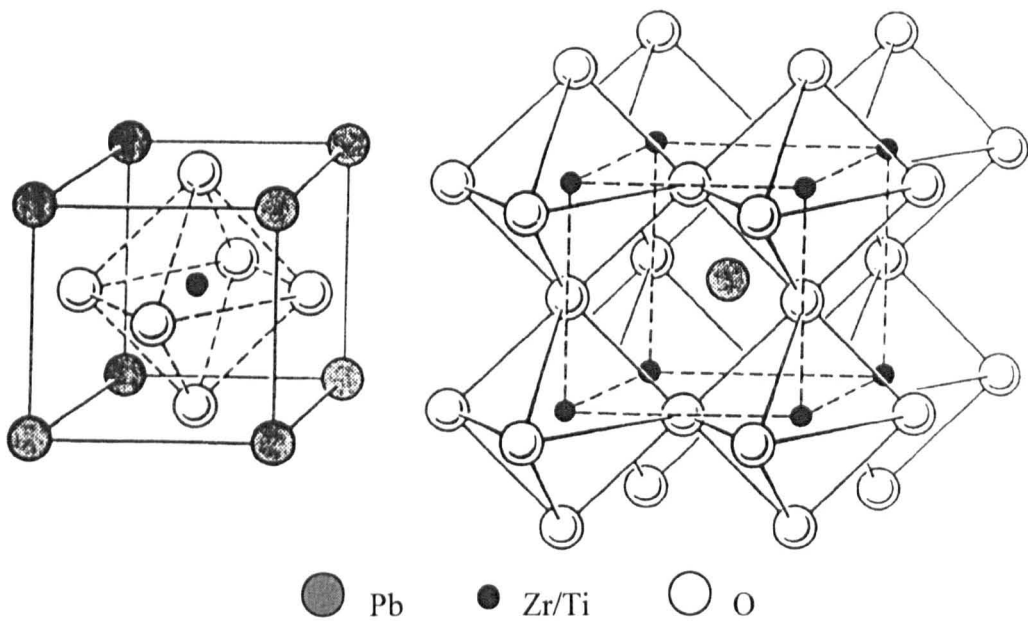


Figure 2.4 Crystal structure of PZT ceramics

Figure 2.4 shows the ideal crystal structure of PZT perovskite, which consists of a corner-linked network of oxygen octahedra with Zr^{4+} and Ti^{4+} ions occupying the B sites within the octahedral cage and the Pb^{2+} ions situated in the interstices (A sites) created by the linked octahedra.

2.2.2 Tolerance Factor (t) in Perovskites

To determine the stability of the perovskite phase for a given set of anions and cations, the tolerance factor (t) was first suggested by Megaw^[17], which is given by eq. (2.7):

$$t = (R_A + R_O) / (\sqrt{2}(R_B + R_O)) \quad (2.7)$$

where R_A , R_B and R_O are the radii of the A and B site ions and the oxygen ion, respectively.

In general, when the value of t is close to 1, the perovskite structure will be formed. This is typified by $SrTiO_3$ where $t = 1.0$. If t is very far from 1, then the perovskite structure will not form, such as $MgTiO_3$ ($t = 0.81$), which adopts only the ilmenite structure^[18].

The tolerance factor, however, is not only able to predict whether compounds will adopt the perovskite structure, it also is able to distinguish whether compounds are likely to distort from ideal cubic on cooling. For example, both strontium and barium zirconates exhibit the perovskite structure. At room temperature, however, $BaZrO_3$ is cubic with $t = 1.01$ and $SrZrO_3$ is orthorhombic with $t = 0.94$. The symmetry is lower for the material with the lower tolerance factor.

It has been suggested by Megaw^[18] and Glazer^[19-20] that lowering of the symmetry in perovskites often results from tilting of octahedra. Tilting arises because

the ionic radii of the A-site species are too small to fully occupy the available volume (i.e., at a critical value of the tolerance factor).

2.2.3 Octahedral Tilt Transitions in Perovskites

Many materials with the perovskite structure, e.g. CaTiO_3 , are polymorphic undergoing several phase transitions involving rotations of the octahedra on cooling, each one lowering the overall symmetry.

Tilting causes the B cation-anion bond in one octahedron to rotate in an opposite direction to that in a neighbouring octahedron, thus giving rise to a doubling of the repeat distances perpendicular to the tilt axis. All tilts can be described as combinations of component rotations about the three tetrad axes of the BO_6 octahedra, *a*, *b* and *c*. There are basically two types: in-phase where the octahedra along an axis rotate in the same direction denoted by the superscript, '+', and in anti-phase where the octahedra rotate along a given axis in the opposite direction, denoted by the superscript, '-'. The simplest way to investigate the structural modifications caused by the octahedral tilt transitions is to observe the types of superlattice reflections appearing in diffraction patterns, which appear as a result of cell doubling. In-phase tilting gives rise to reflections of the type odd-odd-even, while anti-phase tilts produce odd-odd-odd reflections when considering a unit cell doubled in all 3 principle directions^[19-20].

Reaney *et al.*^[21] examined the dielectric properties as a function of tolerance factor *t* in Sr and Ba based complex perovskites, and concluded that, when $0.99 < t < 1.04$, the lattice is untilted, whereas when $t \leq 0.985$ a series of phase transitions occurs initially involving tilting of the octahedra in antiphase and followed by in-phase rotations as *t* drops to ~ 0.96 .

2.2.4 Origin of Ferroelectricity in Perovskites

BaTiO_3 , the first ceramic material in which ferroelectric behaviour was observed, is the ideal model for a discussion of ferroelectricity phenomenon from the point of view of crystal structure and microstructure.

BaTiO_3 is cubic above its Curie point, but below, it is slightly distorted to the tetragonal form with a dipole moment along the c direction. X-ray studies have established that in the tetragonal form, taking the four central (B) oxygen ions in the cubic phase as origin, the other ions are slightly shifted as shown in Figure 2.5.

It is evident that, if the central Ti^{4+} ion is closer to one of the O^{2-} ions (marked A), it will be energetically favourable for the Ti^{4+} ion on the opposite side of A to be located more distantly from that O^{2-} ion, thus engendering a similar displacement of all the Ti^{4+} ions in a particular column in the same direction. Coupling between neighbouring columns occurs in BaTiO_3 so that all the Ti^{4+} ions are displaced in the same direction.

Neutron diffraction studies show that the atoms in the unit cell of BaTiO_3 are in the following positions^[22]:

Ba atom at $0\ 0\ 0$

Ti atom at $0.5,\ 0.5,\ 0.512$

One oxygen atom at $0.5,\ 0.5,\ 0.023$

and two oxygen atoms at $0.5,\ 0,\ 0.486;\ 0,\ 0.5,\ 0.486$.

The displacements are greater in PbTiO_3 than BaTiO_3 and the room temperature tetragonal form of PbTiO_3 has its atoms in these following positions in its unit cell:

Pb atom at $0\ 0\ 0$

Ti atom at $0.5, 0.5, 0.541$

One oxygen atom at $0.5, 0.5, 0.112$

and two oxygen atoms at $0.5, 0, 0.612$; $0, 0.5, 0.612$

In contrast, in the orthorhombic perovskite PbZrO_3 the Zr^{4+} ions in neighbouring columns are displaced in opposite senses so that the overall dipole moment is zero. Such a structure is termed antiferroelectric if the material shows a Curie point.

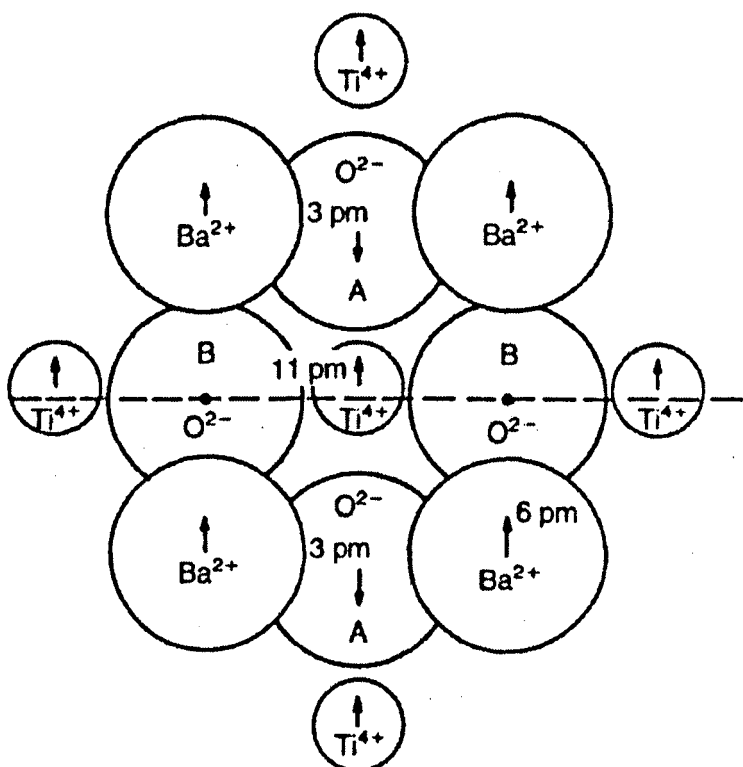


Figure 2.5 Ion displacements in the cubic-tetragonal distortion in BaTiO_3 ^[23]

In tetragonal BaTiO_3 the energy of the Ti^{4+} ion, in terms of its position along the c axis takes the form of two wells. An applied field in the opposite direction to the polarisation may enable a Ti^{4+} ion to pass over the energy barrier between the two states and so reverse the direction of the polarity at that point. When this happens the energy barriers for neighbouring ions are reduced and the entire region affected by the field will eventually switch into the new direction. A similar mechanism is available for changes

of polarity through 90° but in this case there is an accompanying dimensional change because the polar c axis is longer than the non-polar a axis. Switching through 90° can be induced through the ferroelastic effect by applying a compressive stress along the polar axis without an electric field. Switching through 180° is unaffected by mechanical stress.

An immediate consequence of the onset of spontaneous polarisation in a body is the appearance of a surface charge density and an accompanying depolarising field E_D . The energy associated with the polarisation in the depolarising field is minimised by twinning, a process in which the crystal is divided into many oppositely polarised domains.

2.2.5 Phase Equilibria and Structures of PZT

In 1950's the solid solution system, PZT, was first investigated by Shirane *et al.*^[24] in Japan and the first commercial PZT composition was developed by Jaffe *et al.*^[25] in the United States. PZT compositions are now by far the most widely exploited of all piezoelectric ceramics.

The PZT phase diagram is shown in Figure 2.6 (Jaffe *et al.*^[26]). All compositions are cubic above T_C with the ideal perovskite structure. Below T_C , pure PZ transforms to an antiferroelectric (AFE) orthorhombic structure which persists at room temperature with up to $\sim 5\%$ Ti^{4+} substituted for Zr^{4+} .

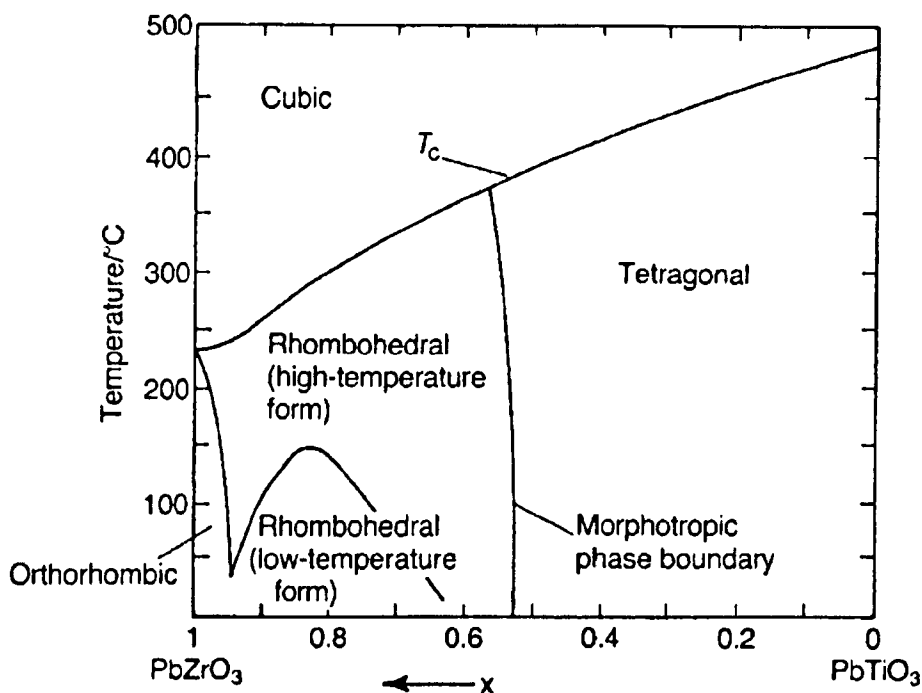


Figure 2.6 Phase stabilities in the system $\text{Pb}(\text{Ti}_{1-x}\text{Zr}_x)\text{O}_3$

Figure 2.7 is a structure diagram of the AFE orthorhombic phase PbZrO_3 . The lattice parameters, a , b and c are approximately equal to $\sqrt{2}a, 2\sqrt{2}a, 2a$, where a is the ideal perovskite lattice parameter. The supercell is due to antiparallel alignment of dipoles arising from the off centre displacement of Pb^{2+} along $<110>$ pseudocubic directions. The AFE transition is coupled to rotations of the antiphase octahedra around the c -axis.

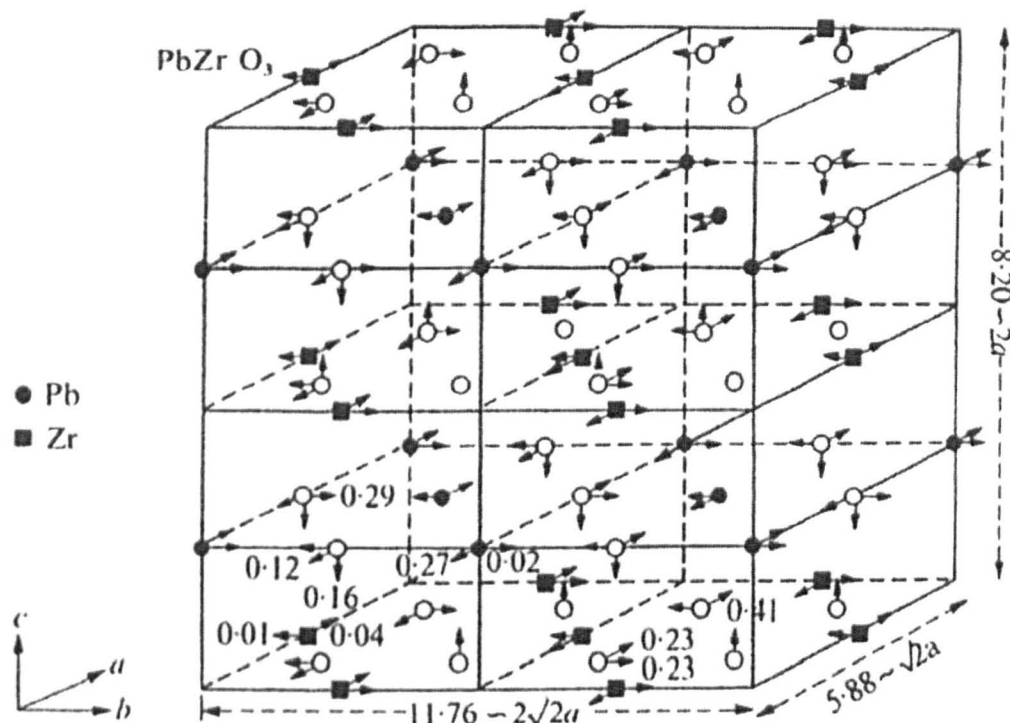


Figure 2.7 Crystal structure of PbZrO_3 ^[27]

Compositions between 5-47% Ti^{4+} on the B-site are FE rhombohedral below T_C whereas compositions with > 47% Ti^{4+} are FE tetragonal. The boundary between the tetragonal and rhombohedral phases is nearly independent of temperature and is known as the morphotropic phase boundary (MPB).

In the rhombohedral ferroelectric region of PZT, a transformation between high and low temperature states ($\text{FE}_{\text{R(HT)}}-\text{FE}_{\text{R(LT)}}$) has been previously been reported. The $\text{FE}_{\text{R(HT)}}$ structure is distinguished from the $\text{FE}_{\text{R(LT)}}$ structure by an antiphase rotation of the successive oxygen layers along the $\langle 111 \rangle$ directions^[28].

2.3 Materials

2.3.1 Chronological History of Ferroelectric Materials

A chronological listing of many notable events in the history of ferroelectric materials is given in Table 2.1. The piezoelectric and ferroelectric effect did not become commercially significant until the discovery of BaTiO₃ in the 1944. Although kept secret for a number of years, it was this event that resulted in the field of piezoelectric and ferroelectric ceramics.

Table 2.1 Chronological history of FE materials (after Haertling^[10])

Time line	Event
1880	Piezoelectricity discovered in Rochelle salt, quartz
1921	Ferroelectricity discovered in Rochelle salt
1935	Ferroelectricity discovered in KH ₂ PO ₄
1944	Ferroelectricity discovered in ABO ₃ -type perovskite BaTiO ₃
1945	BaTiO ₃ reported as useful piezo transducers, US Pat. No. 2486560
1949	Phenomenological theory of BaTiO ₃ introduced
1949	LiNbO ₃ and LiTaO ₃ reported as FE
1951	Concept of antiferroelectricity introduced
1952	PZT reported as FE solid-solution system, phase diagram established
1953	PbNb ₂ O ₆ reported as FE
1954	PZT reported as useful piezo transducer, US Pat. No. 2708244
1959	PZT 5A and 5H piezoelectric compositions, US Pat. No. 2911370
1961	Lattice dynamics theory for FE materials, soft modes introduced
1961	Relaxation phenomena in Pb(Mg _{1/3} Nb _{2/3})O ₃ (PMN) reported

1964	Oxygen/atmosphere sintering for FEs developed
1970	La doped PZT (PLZT) compositional phase diagram established, US Pat. No. 3666666
1971	Useful electrooptic properties reported for PLZT, US Pat. No. 3737211
1977	FE thin films developed
1978	Engineered (connectivity designed) FE composites developed
1980	Electrostrictive relaxor PMN devices developed, US Pat. No. 5345139
1983	Photostrictive effects reported in PZT and PLZT
1991	Piezoelectric flexextensional (Moonie) devices developed, US Pat. No. 4999819
1992	Piezoelectric bending actuators (RAINBOW) developed, US Pat. No. 5471721
1993	Integration of FE films to silicon technology, US Pat. No. 5038323
1997	Single-crystal materials for piezoelectric transducers

2.3.2 Piezoelectric Effects in Ferroelectric Ceramics

Grey^[29] first discovered that an external electric field could permanently orient the domains within the grains of a ferroelectric, thus producing a ceramic material that acted in a similar way to a single crystal, possessing both ferroelectric and piezoelectric properties. This electrical aligning, or “poling” process was the key to turning an inert ceramic into an electromechanically active material with a multitude of commercial uses.

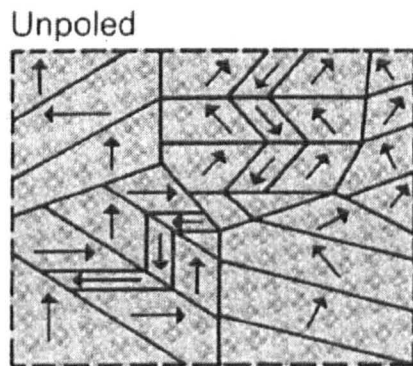


Figure 2.8 Ceramic in unpoled state

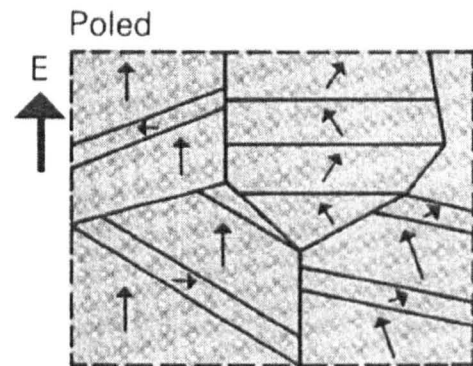


Figure 2.9 Ceramic in the poled state

Figure 2.8 represents randomly-oriented dipoles within an isotropic ceramic material before polarisation. The poling process involves the application of an electric field across the ceramic, usually at an elevated temperature, causing switching or realignment of the dipoles in the direction of the field (Figure 2.9). The resulting ceramic is now anisotropic and can be returned to its unpolarised isotropic condition by either raising its temperature above the Curie temperature or by mechanically overstressing.

During the poling process, there is a small expansion of the material along the poling axis and a slight contraction in both directions perpendicular to it. The strength of the poling field, often in combination with elevated temperature, is an important factor in determining the extent of alignment and, hence, the resulting properties. Alignment is never complete but ranges from 83% to 86% for the tetragonal and rhombohedral phases, respectively, and up to 91% for the orthorhombic phase, when compared with single-domain, single-crystal values.

2.4 “Soft” PZT’s and Softening Methods

2.4.1 “Soft” PZT’s

PZT’s have high piezoelectric and electromechanical coupling coefficients (typically, $d_{33} \approx 200 \text{ pC/N}$ and $k_{33} \approx 0.4$). Their properties can be controlled by a suitable choice of Zr:Ti ratio (usually close to the MPB) and dopant ions (e.g. Nb^{5+}), giving rise to the classifications; “soft”^[30] and “hard”^[31].

Soft PZT is usually distinguished by high values of piezoelectric coefficient ($d_{33} > 400 \text{ pC/N}$), low coercive fields ($E_c < 2 \text{ kV/mm}$) and high remnant polarisation ($P_r > 0.3 \mu\text{C/mm}^2$). Hard PZT’s have lower ($\sim 200 \text{ pC/N}$) but more consistent values of d_{33} as a function of the number of cycles of the applied field and therefore exhibit less aging^[32].

Soft behaviour of PZT’s is believed to arise from the easier domain wall motion under the action of electric field or mechanical stress. In PZT, several methods are thought to promote domain wall motion^[1-6, 26]:

- i) proximity to the MPB;
- ii) donor doping such as Nb^{5+} on the B site; and
- iii) reducing phase transition temperature by substitutions of e.g. Sr^{2+} for Pb^{2+} on the A-site

2.4.2 Proximity to the MPB

The PZT compositions for piezoelectric applications are usually confined to the vicinity of the MPB as close to this boundary ceramics exhibit the highest piezoelectric coupling coefficients as well as maximum relative permittivities. The mechanism resulting in these enhanced properties is believed to arise from the coexistence of tetragonal and rhombohedral phases, which gives a total of fourteen possible pseudocubic polarisation directions, six $<100>$ in the tetragonal and eight $<111>$ in the rhombohedral phase^[33]. The large number of polarisation directions enables optimised crystallographic orientations to be established from grain to grain upon poling.

However, recent high-resolution synchrotron X-ray diffraction measurements by Noheda *et al.*^[34-36] have suggested that an intermediate monoclinic phase exists between the rhombohedral and tetragonal phases in PZT. The phase transition from tetragonal to monoclinic is reported to be due to the condensation of local Pb displacements in the tetragonal phase along one of the $<110>$ directions. The monoclinic unit cell is doubled with respect to the tetragonal one and has b as the unique axis. a_m and b_m are directed along the pseudocubic $[\bar{1} \bar{1} 0]$ and $[1 \bar{1} 0]$ directions, respectively, while c_m is close to the tetragonal c axis, along the $[0 0 1]$, but tilted away from it such that angle β between the a_m and b_m is slightly larger than 90° . This monoclinic phase has unique characteristics in comparison to all other ferroelectric perovskite phases. The polar axis is not determined by the symmetry and can be directed anywhere within the monoclinic ac plane; that is, the polar axis is allowed to rotate within this plane. In the case of PZT, the pseudocubic $[1 1 1]$ and $[0 0 1]$ directions are contained within the monoclinic plane and the monoclinic polar axis is tilted away from the polar axis of the tetragonal phase $[0 0 1]$ towards that of the rhombohedral phase $[1 1 1]$. Noheda *et al.*^[34-36] also proposed that the presence of this monoclinic distortion is the origin of the unusually high piezoelectric response in the vicinity of the MPB in PZT. The observation of this monoclinic phase has allowed a preliminary modification of the PZT phase diagram (Figure 2.6), as shown in Figure 2.10.

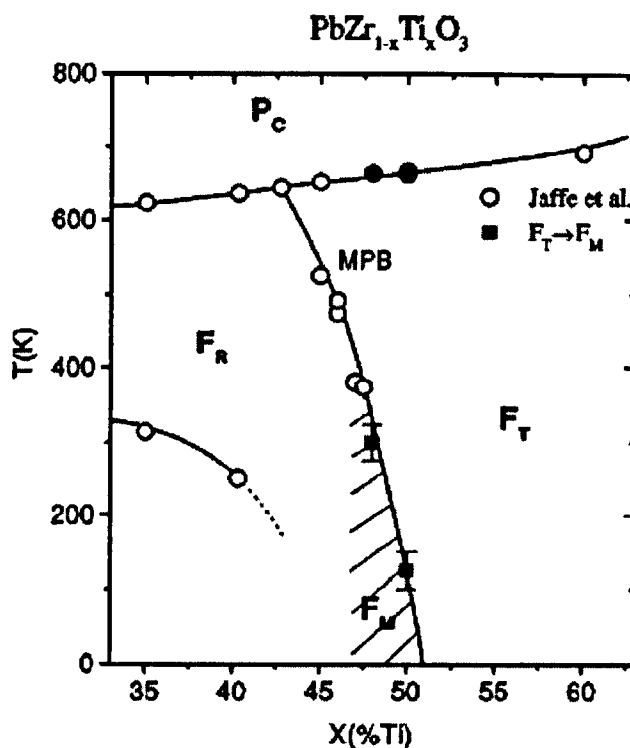


Figure 2.10 Preliminary modification of the PZT phase diagram. The data of Jaffe *et al.*^[26] are plotted as open circles. The $F_T - F_M$ and $P_C - F_T$ transition temperatures for $x = 0.48$ and $x = 0.50$ are plotted as solid symbols^[34] where F_T , F_R and F_M represent ferroelectric tetragonal, rhombohedral and monoclinic phases respectively, and P_C is the para-ferroelectric cubic phase.

Figure 2.11 illustrates the tetragonal (a), monoclinic (b), and rhombohedral (c) distortions of the perovskite unit cell projected on the pseudocubic (110) plane.

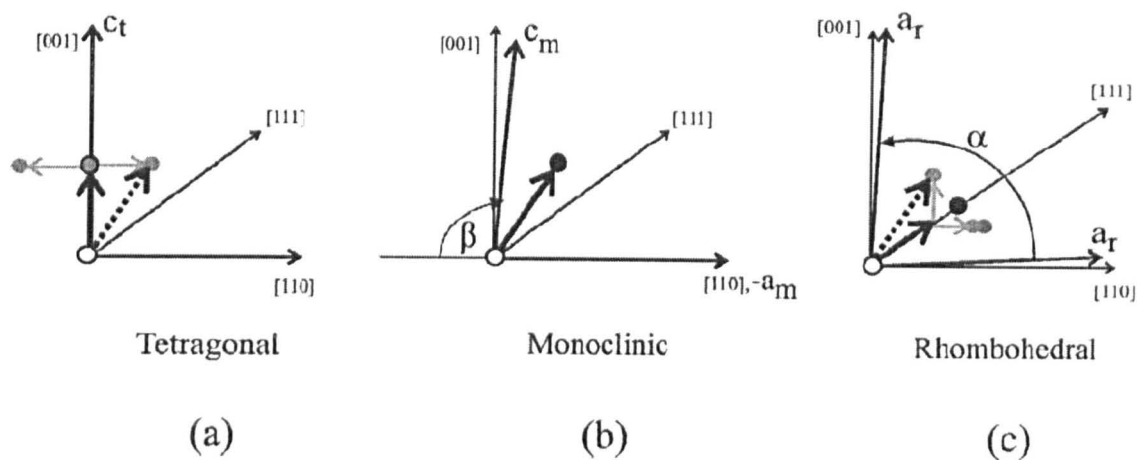


Figure 2.11 Schematic illustration of (a) tetragonal, (b) monoclinic, and (c) rhombohedral distortions of the perovskite unit cell projected on the pseudocubic (110) plane. The solid circles represent the observed shifts with respect to the ideal cubic structure. The light grey circles represent the four locally disordered $<100>$ shifts in the tetragonal structure (a) and the three locally disordered shifts in the rhombohedral structure (c). The heavy dashed arrows represent the freezing-out of one of these shifts to give the monoclinic structure^[34].

2.4.3 Nb⁵⁺ Doping on the B-site

Further improvements in the properties of PZT are made through compositional modifications. Common dopants in perovskite-type ceramics are listed in Table 2.2^[37].

Table 2.2 Common aliovalent substituents in PZT

A-site donors	La ³⁺ , Bi ³⁺ , Nd ³⁺
B-site donors	Nb ⁵⁺ , Ta ⁵⁺ , Sb ⁵⁺
A-site acceptors	K ⁺ , Rb ⁺
B-site acceptors	Co ³⁺ , Fe ³⁺ , Sc ³⁺ , Ga ³⁺ , Cr ³⁺ , Mn ³⁺ , Mn ²⁺ , Mg ²⁺ , Cu ²⁺

Donor dopants, those of higher charge than that of the ions they replace, are compensated by cation vacancies or a reduction of numbers of oxygen vacancies. Acceptors, dopants of lower charge than that of the replaced ions, are compensated by the creation of oxygen vacancies. The significant difference between oxygen vacancies and cation vacancies in perovskite-type ceramics is the higher mobility of the former. Cations and cation vacancies tend to be separated by oxygen ions so that there is a considerable energy barrier to be overcome before the ion and its vacancy can be interchanged. Oxygen ions, however, form a continuous lattice structure so that oxygen vacancies have oxygen ion neighbours with which they can easily exchange.

In acceptor doped or hard PZT, dipoles are formed between negatively-charged defects and positively-charged oxygen vacancies. These defect dipoles align along the polar direction by a combination of diffusion of oxygen vacancies and the action of the local field associated with remnant polarisation^[23]. The dipoles then provide an internal field stabilising the domain configuration, preventing easy switching.

In soft PZT, substitutions such as La³⁺ for Pb²⁺ on the A-site or Nb⁵⁺ for Zr⁴⁺ or Ti⁴⁺ on the B-site, maintain electrical neutrality is by creating cation vacancies or reducing oxygen vacancy concentration. The marked changes in properties of La-, and Nb-doped PZT, such as the low aging and high electrical and mechanical loss, are related to a considerable increase in domain-wall mobility. This increase may be due to the presence of Pb vacancies in the crystal lattice caused by the substitution^[38]. On the other hand, the substitution of donor-doping leads to a reduction in the concentration of oxygen vacancies; that are domain-stabilising defect pairs or dipoles^[39]. A reduction in domain-stabilising defect dipoles enhances the domain wall mobility, which results in an increase in permittivity, dielectric loss, elastic compliance and piezoelectric and coupling coefficients along with a commensurate reduction in coercive electric field.

Small quantities of Nb⁵⁺, Bi³⁺, and La³⁺ were shown to stabilise ceramic PbTiO₃ against cracking and to permit successful poling to produce a piezoelectric effect^[26]. With 4 atom % Nb⁵⁺, a d_{33} of $40 \times 10^{-12} \text{ C/N}$ was obtained by poling at 60 kV/cm at

200°C^[26]. The c/a ratio was reduced from 1.063 to 1.046 by the admixture^[26]. With La³⁺ admixture, which has a more extensive field of solid solubility (greater than 15 atom%), even better results were obtained^[26]. A planar coupling factor of 0.25 was obtained for a composition with 6 atom% La³⁺. The La³⁺ admixture decreases both the cell volume and the c/a ratio. With up to 15 atom% La³⁺, the c/a ratio decreases to 1.023^[26].

2.4.4 Decreasing T_C

The soft behaviour of PZT may also be enhanced by isovalent substitutions. Doping PZT with Sr, Ca or Ba cations on the A-site has the effect of lowering the Curie temperature (Sr²⁺ lowers the T_C about 9.5° for every atom % added^[26]). The T_C is shifted to lower temperatures resulting in an increased room-temperature permittivity. Since the coupling factor is not greatly altered, this has the effect of raising the d_{33} . For instance, Pb_{0.94}Sr_{0.06}Zr_{0.53}Ti_{0.47}O₃ has a relative permittivity of 1300 and a Curie point of 328°C compared with values of 730, and 386°C for equivalent undoped compositions^[23]. The activation energy to induce domain wall motion in a ceramic decreases as the phase transition is approached. Reducing T_C brings ambient closer to the phase transition, thereby inducing soft behaviour.

2.5 New Materials

2.5.1 Relaxors

Relaxors belong to a particular class of ferroelectrics, which are mainly characterised by^[40]:

- i) a very broad dispersive dielectric peak. This does not necessarily reflect a ferroelectric phase transition but rather a thermal slowing down of a relaxational process,
- ii) hysteresis loops above the temperature of the dielectric maximum and a frequency dependence of this maximum, and
- iii) no evidence for any symmetry transformations.

Relaxor behaviour is believed to arise from compositional or structural heterogeneity, which acts to break the translational invariance of the polarisation^[41-42]. This compositional or structural heterogeneity leads to a distribution of microvolumes within the samples, which have widely different Curie temperatures. Thus on cooling from high temperature, there is a Curie range rather than a distinct Curie point, and within this Curie range the material exhibits an intimate mixture of paraelectric and ferroelectric regions^[43].

Viehland *et al.*^[44] have recently attributed the breaking of the translational symmetry in the mixed B-site cation relaxor family to the formation of a locally-charged phase. As a consequence polar nanodomains form which are inhibited from undergoing a normal long-range ordered ferroelectric transformation. At lower temperatures, these polar nanodomains have been shown to undergo a Vogel-Fucher-like slowing down of the polarisation fluctuations^[45-46]. These glass-like characteristics were attributed to correlations between polar nanodomains. Fluctuating mottled contrast, observed by Reaney *et al.*^[47], Randall *et al.*^[48] and Viehland *et al.*^[44] using transmission electron microscopy, has been attributed to polar nano-regions ($5-10\text{ nm}$) in many mixed B-site cation relaxors such as $\text{Pb}(\text{Sc}_{1/2}\text{Ta}_{1/2})\text{O}_3$ (PST)^[48] and $\text{Pb}(\text{Mg}_{1/3}\text{Nb}_{2/3})\text{O}_3$ (PMN)^[41,49,50].

Similar sized polar nanodomains have also been found in La-modified PZT (PLZT)^[42]. Coarsening of polar nanodomains with reducing temperature has also been observed in PLZT^[42], in which the number and size of stable polar nanodomains increased at the expense of the paraelectric matrix. Decreasing temperature may result in enhanced tendencies towards long-range ordering (LRO), however the system did not

transform the mixture of polar nanodomains and the paraelectric matrix into a completely LRO ferroelectric state. The application of an electric field is known to align the polar nanodomains transforming the relaxor to a LRO state. This transition is often referred to in the literature as the field induced micro- to macro- domain transition.

Relaxor materials have large electrostrictive coefficients, which lead to many potential applications. Relaxor (electrostrictive) materials can be operated either in the electrostrictive mode or in the field-biased piezoelectric mode. In the latter case, a dc electric field bias is applied to the material to induce a ferroelectric polarisation. The material then will act as a normal piezoelectric as long as the field is applied.

Some advantages of electrostrictive materials over conventional piezoelectrics are (1) hysteresis in the strain-field dependence is minimal or negligible in a selected temperature range, (2) realised deformation is more stable and comparable to the best piezoelectric ceramics, and (3) no poling is required. These advantages, however, are balanced by the disadvantages of (1) a limited usable temperature range due to the strong temperature-dependence of the electrostrictive effect and (2) especially small deformation at low fields, as electrostriction is very nearly a quadratic function at low electric fields, which usually necessitates higher operating voltages to achieve moderate deflection.

2.5.2 PNN-PZT

Since the 1970's, there has been a growing interest for mixed compositions of relaxors and normal ferroelectrics because they exhibit very high dielectric permittivities, high coupling coefficients and high piezoelectric coefficients. Among the various compositions studied, one of the most interesting materials is $\text{Pb}(\text{Ni}_{1/3}\text{Nb}_{2/3})\text{O}_3 - \text{Pb}(\text{Zr},\text{Ti})\text{O}_3$ (PNN-PZT).

Lead nickel niobate (PNN) is a well-known relaxor material. Solid solutions of PNN with PZT exhibit excellent piezoelectric properties. PNN-PZT piezoelectric

ceramics with various compositions have been studied and the morphotropic boundary compositions for the PNN-PZT system reported^[51-52]. Luff *et al.*^[52] investigated the change in the piezoelectric properties with composition and reported that the composition with the highest performance ($d_{33} = 1100 \text{ pC/N}$) appeared at 0.65PNN-0.35PZT.

In PNN-PZT solid solutions, the ferroelectric phase may be stabilised either in a tetragonal or rhombohedral structure by changing the Zr:Ti ratio. In keeping with conventional PZT's, commercial compositions always lie close to the MPB.

Zhu *et al.*^[53] investigated the dependence of dielectric and piezoelectric properties of the ternary system PNN-PZT modified with bismuth and zinc, and found that the Curie temperature was decreased towards room temperature with increasing PNN content. When the PNN content was constant, the Curie temperature varied almost linearly with the Zr:Ti ratio and a similar phenomenon occurred for the Curie temperature versus PNN content when Zr:Ti ratio was constant. By suitably controlling PNN content and Zr:Ti ratio, the MPB compositions can be achieved and the Curie temperature can be adjusted. Zhu *et al.*^[53] found that the highest planar coupling factor K_p was 0.70 and d_{31} was $-274 \times 10^{-12} \text{ C/N}$.

2.5.3 PZN-PT Single Crystals

The extremely large coupling factor of $k_{33} = 92\%$ in 0.91 Pb(Zn_{1/3}Nb_{2/3})O₃-0.09PbTiO₃ (PZNT91/9) single crystals was first reported by Kuwata *et al.*^[54] in 1982. Recent developments have shown that Pb(Zn_{1/3}Nb_{2/3})O₃-PbTiO₃ exhibits high piezoelectric properties such as $k_{33} \sim 94\%$ and $d_{33} > 2500 \text{ pC/N}$ at room temperature^[55]. This effect is thought to result from an engineered domain state not achievable with conventional PZT, and also an induced phase switching with strong electric fields^[56].

Pb(Zn_{1/3}Nb_{2/3})O₃ is a relaxor ferroelectric. It has a disordered perovskite structure, in which the Zn²⁺ and Nb⁵⁺ ions exhibit short-range ordering on the B site,

resulting in regional composition variations on the nanometre scale^[57]. Like PZT, in the PZN-PT solid solution, the ferroelectric phases are divided by a morphotropic phase boundary, separating the rhombohedral and tetragonal phases. However, there is still uncertainty about the true symmetry of the high PZN composition, so the pseudorhombohedral structure is referred to here. The engineered domain state (rhombohedral phase) shows high stability and very high piezoelectric activity at room temperature. Optimum crystallographic orientation was found to be pseudocubic <001> for rhombohedral crystals. Single crystal PZNT 91/9, which has low acoustic impedance ($Z_{33} = 22 \times 10^6 \text{ kg/m}^2\text{s}$) in addition to a large coupling factor, is the most promising candidate for realising array probes, which have greater sensitivity and broader bandwidth^[58].

2.5.4 PZT Composites

In an electromechanical transducer, it is necessary to maximise the piezoelectric sensitivity, minimise the density to obtain good acoustic matching with water, and make the transducer mechanically flexible to conform to a curved surface. Neither piezo ceramic or polymer satisfies these requirements. Piezoelectric ceramic polymer composites however, combine the desired piezoelectric sensitivity and dielectric constant of ceramics with the low density and flexibility of polymers.

Piezoelectric composites consist of an active ceramic phase embedded in a passive polymer. The properties of the composite depend on the connectivity of the phases, volume percent of ceramic, and the spatial distribution of the active phase in the composite. The concept of connectivity developed by Newnham *et al.*^[59], and later amended by Pilgrim *et al.*^[60], describes the arrangement of the component phases within a composite. It is critical in determining the electromechanical properties of the composite. Figure 2.12 shows the 16 different types of connectivity possible in a diphasic composite. It is shown in the form A-B where “A” refers to the number of directions in which the active phase is self connected or continuous and “B” is the number of continuity directions of the passive phase.

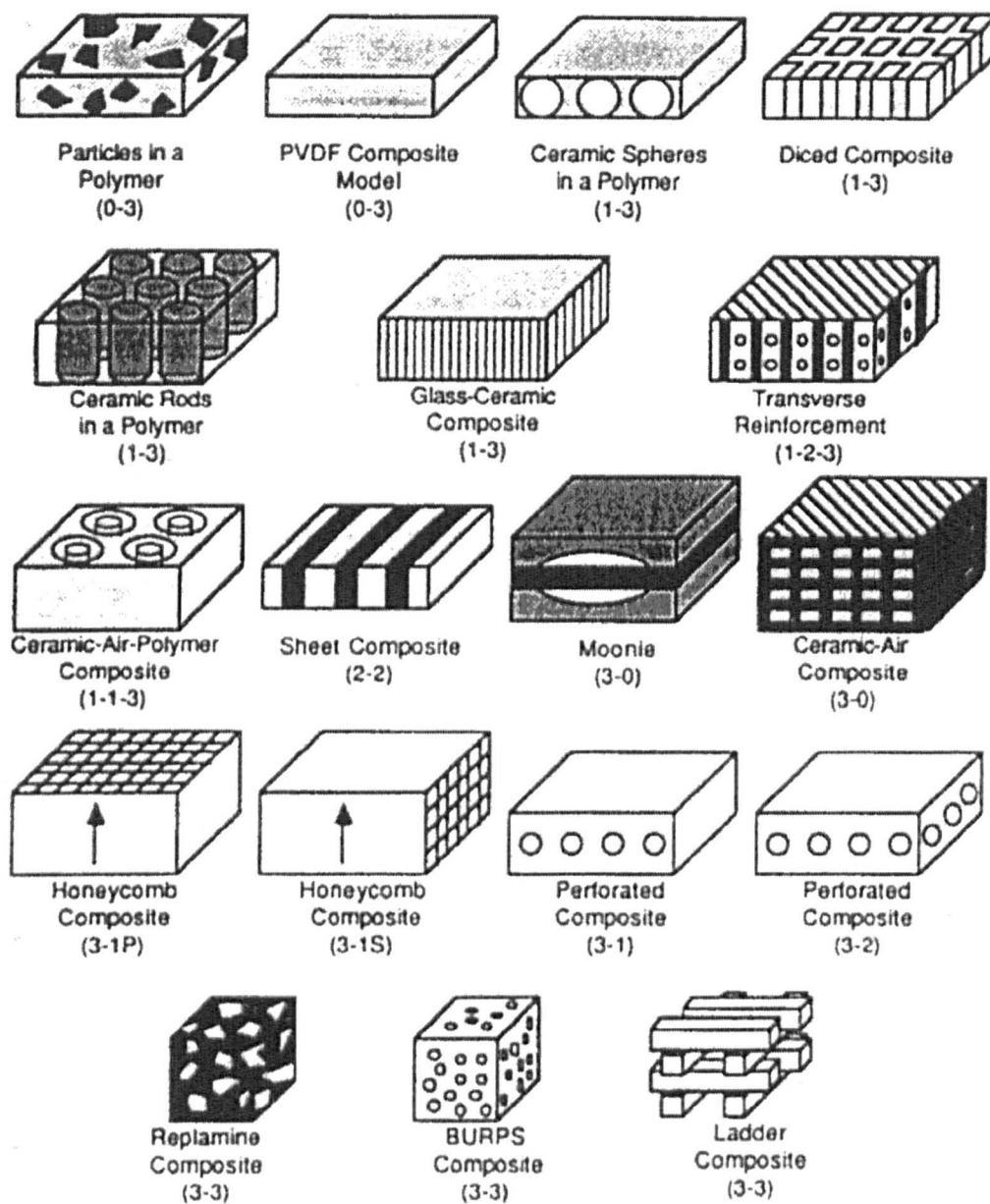


Figure 2.12 Schematic diagrams of various piezoelectric ceramic/polymer composites (after Gururaja *et al.*^[61])

Numerous processing techniques have been developed for forming composites of different connectivities. Most of the work has been limited to the connectivity patterns, which are easier to form, namely the 0-3, 1-3, 2-2, 3-0, 3-1, 3-2, and 3-3 connectivities.

There are several excellent reviews^[61-62] on the processing and properties of piezoelectric/polymer composites. These papers discuss the formation of composites for both passive applications such as hydrophones, and active, or pulse-echo applications, such as medical imaging. All of these composites showed improved piezoelectric properties compared to single-phase piezoceramics. The hydrostatic strain/voltage coefficients (Figure of Merit $d_{h,g}$) for these composites are compared in Figure 2.13.

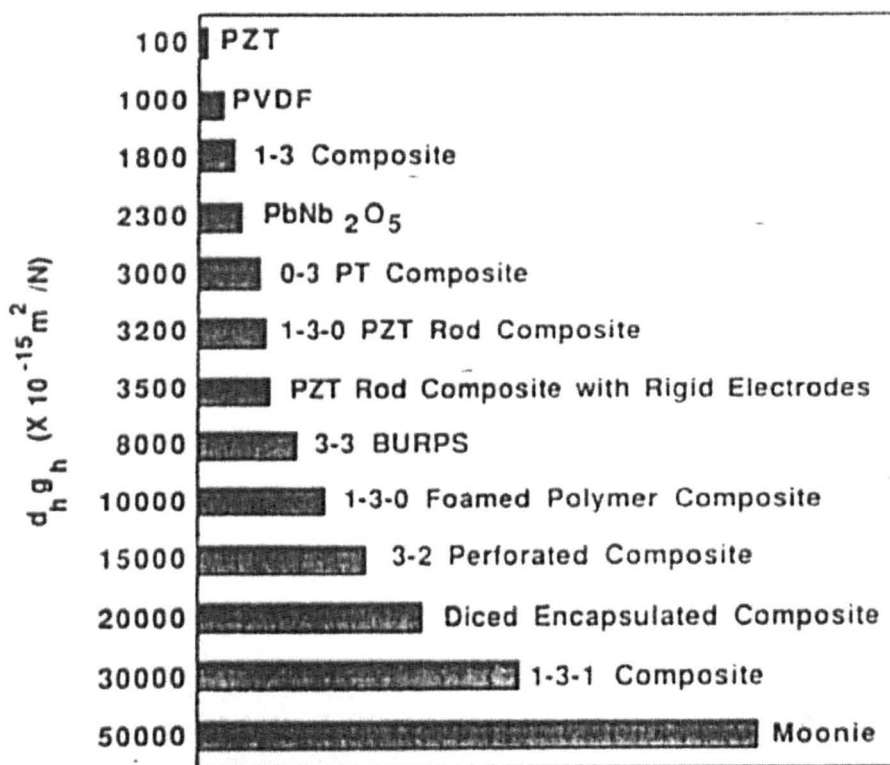


Figure 2.13 Comparison of hydrostatic Figure of Merit for various piezoelectric ceramic/polymer composites (after Safari *et al.*^[62])

The density, acoustic impedance, dielectric constant and piezoelectric and electromechanical coupling coefficient change with the volume fraction of ceramic. Optimum material and piezoelectric parameters for medical ultrasound applications are obtained for ~20-25 vol.% PZT ceramic in a composite.

2.6 Processing and Fabrication of PZT Ceramics

The final properties of ferroelectric ceramics depend greatly on the processing conditions. Each step of processing has to be carefully controlled and monitored to get the best product. A flow chart for a typical ferroelectric oxide ceramic manufacturing process is shown in Figure 2.14.

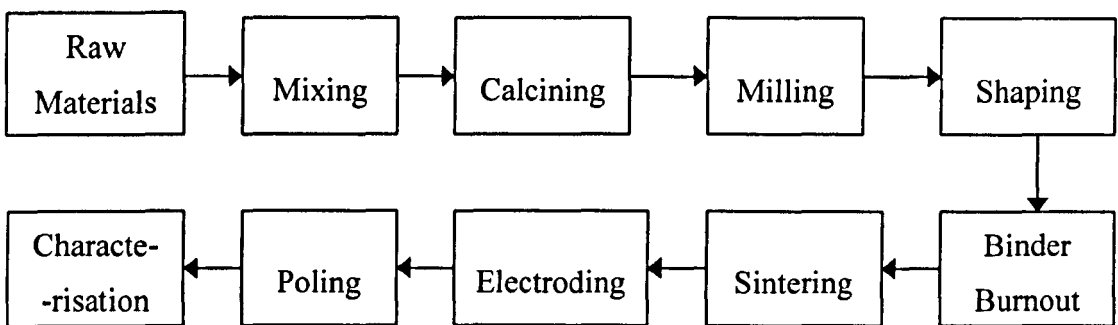


Figure 2.14 Flowchart of ferroelectric ceramic manufacturing process

The raw materials (metal oxides or metal carbonates) are first weighed according to the stoichiometric formula of the ferroelectric ceramic desired. The raw materials should be of high purity and the particle size of the powders is better in the submicron range for the solid phase reactions to occur by atomic diffusion.

The powders are then mixed either mechanically or chemically. Mechanical mixing is usually done by either ball-milling or attrition-milling. Chemical mixing on the other hand is more homogeneous involving the precipitation of the relevant precursors.

During the calcination step the solid phase reaction takes place between the constituents giving the ferroelectric phase. The calcination temperature is important as it influences the density and the properties of the final product. In general, higher homogeneity and density of the final ceramic product can be achieved when the calcination temperature is higher. However, calcining Pb-based ceramics at $T > 800^{\circ}\text{C}$ could lead to lead loss, resulting in a detrimental effect on the electric properties^[63]. Careful choice of right calcination temperature is necessary to obtain the best electric properties.

After calcining, the resulting hard agglomerates are ground by milling. The shaped green bodies should have a certain minimum density before they can be sintered and need to be heated to between $500\text{-}600^{\circ}\text{C}$ to remove any binder present. After the binder burnout is over, the samples are taken to a higher temperature for sintering. The sintering temperature and time should be optimised for proper densification and the sintering can be carried out either in an oxidising atmosphere or in air.

2.6.1 Powder Preparation

Particle size, surface area, composition, crystalline structure and morphology of powders are crucially important to the quality of the final products. A primary objective of the powder preparation techniques thus is to increase powder reactivity, thereby achieving full density and maximum chemical homogeneity, potentially at lower temperatures.

PZT ceramics are traditionally made from powders formulated from individual oxides obtained and refined from minerals. Nowadays, piezoelectric ceramics are prepared from the most economical, mixed-oxide (MO) process whereas optical ceramics utilise powders produced by chemical processes (CP) such as chemical coprecipitation^[64-65] or hydrothermal^[66] techniques since electrooptic applications

require defect-free, high-purity ceramics, which can only be obtained by using more homogeneous highly reactive powders.

Recently, PZT powders have been synthesised by sol-gel methods^[67], which provides considerable advantages over conventional techniques. As well as high purity, good homogeneity and ease of compositional control, sol-gel methods allow synthesis and sintering of the ceramic at lower temperatures.

The essential differences between MO and these chemical process methods occur in the powder forming and densification stages. The MO method consists of wet milling individual oxides or other compounds, such as carbonates that decompose to the oxides during calcination. On the other hand, chemical processes involve liquid inorganic or organometallic precursors. The starting materials are usually solutions that are mutually soluble in each other, thus producing an atomically homogeneous precursor solution from which the solid is precipitated while blending. Because the particle sizes of CP powders are much finer than the MO powders, ($0.03\text{-}0.1\mu\text{m}$ vs. $1\mu\text{m}$), the CP powders are more reactive and can be calcined at a lower temperature, typically~ 500°C .

However, despite the advantages offered by chemical process methods, their high cost and relatively small-scale production mean that they are still not widely applied in industrial production of PZT powders.

2.6.2 PbO Loss Upon Sintering

Irrespective of the source of raw material, the volatility of the PbO component of PZT ceramics during sintering has historically been a stumbling block to the reproducible production of high-quality PZT ferroelectric ceramics^[68]. PbO volatilisation and the resultant variation in composition affect both the density and the intrinsic electrical properties.

Using excess PbO, with respect to stoichiometric to compensate for volatilisation is critical for achieving high densities and good electrical properties^[69]. However, the excess PbO level is an important factor. During the sintering of PZT based ceramics with excess PbO, a liquid phase is formed because of the low melting point of PbO (888°C ^[70]). A small amount of excess PbO favours for the formation of the perovskite structure and densification of the materials. But if there is too much excess PbO, the PbO will stay in the grain boundary and form a grain boundary layer^[71]. Since PbO has a low dielectric constant of about 20, the overall dielectric constant will be decreased due to its presence.

In addition, Atkin and Fulrath^[72], and Kingon and Clark^[73] have suggested the use of atmosphere powders such as PbZrO₃ and ZrO₂ in the sintering enclosures. This creates a partial vapour pressure of PbO above the sample reducing the effective volatilisation from the ceramic.

Atkin and Fulrath^[72] proposed that, to establish and maintain the desired stoichiometry, PZT must be heat-treated in an atmosphere, which contains the correct O₂ and PbO partial pressure. Equilibrium of the vapour-phase reaction:



is assumed, so that any two vapour pressures fix the Pb and O activities. Clearly the concentration of lattice vacancies changes with the activity of PbO. With the O₂ pressure fixed, the crystal will saturate with A-site vacancies when the Pb activity is sufficient low. Subsequent loss of PbO will result in the formation of a second phase, but the PbO activity of the system will remain constant^[72]. According to vapour pressure measurements of mixtures of PZT with ZrO₂ and TiO₂^[74], PbO pressure is greater for PbZrO₃ than for Pb(Zr_{0.5}Ti_{0.5})O₃. Thus, when a specimen of Pb(Zr_{0.5}Ti_{0.5})O₃ is buried in a mixture of PbZrO₃ and ZrO₂ and heat-treated at a high temperature, vapour transport of PbO will allow the specimen to equilibrate with the packing powder. Transport of TiO₂ and ZrO₂ is negligible at 1200°C , so that the Zr:Ti ratio of the specimen will be unchanged^[72].

2.6.3 Densification

Addition of excess PbO and powder-packed sintering both help the densification of PZT ceramics. Another method of improving densification is the use of an oxygen atmosphere for sintering lead-containing ceramics. With air atmosphere only, densities of ~96% of theoretical can be achieved, but with an oxygen atmosphere, this value can approach 99%.

In recent years, other densification methods have been adopted successfully. These include, hot isostatic pressing (HIP)^[75], and a two-step process of sintering and then hot isostatic pressing. The two-step technique was developed to eliminate the need for a cladding enclosure in the final gas isostatic hot pressing step. HIP is an effective process for production of fully dense powder compacts via simultaneous application of heat and high gas pressure. Haertling *et al.*^[76] first reported the electro-optic application of PLZT ceramics by using hot-pressing method to achieve optical transparency. Ewsuk and Messing^[77] used HIP and successfully fabricated fully dense PZT ceramics with enhanced dielectric properties, particularly dielectric breakdown strength.

2.6.4 Sintering Aids

The sintering temperature of ceramics can be reduced by utilising low-melting-point additives. However, some results indicate that electrical properties of sintered ceramics using sintering aids are degraded^[78]. Therefore it is important to select a suitable sintering aid. Lead germanium oxide ($Pb_5Ge_3O_{11}$: PGO) powder, which is a ferroelectric material with a low melting point of 738°C, was effective for low-temperature sintering of BaTiO₃ and PZT ceramics^[78]. Hayashi *et al.*^[79] demonstrated that PZT powder coated with PGO, prepared from a precursor solution of Ge(OiPr)₄ and Pb(NO₃)₂ by the sol-gel method, could be densified at lower temperatures and 2 wt% PGO-added PZT bodies sintered at 850°C exhibited an electromechanical coupling

factor of about 65%. Lithium bismuth oxide (LiBiO_2 : LBiO) is also expected to be effective as a sintering aid as it has a lower melting point of 700°C , although it is not a ferroelectric material. Hayashi *et al.*^[78] concluded that the best piezoelectric properties were obtained for LBiO-added PZT based ceramics fabricated at 1000°C .

2.6.5 Multi-Layer Techniques

Multi-layer ceramics (MLC's) constitute a significant portion of the multibillion dollar electronic ceramics business. The technology for their production was developed in the 1970's and was refined in the early 1980's to include base metal electrodes for ceramic capacitor production. More recently, the same technology has been applied to piezoelectric ceramics to prepare multilayer actuators.

Advances in tape casting technology have made it possible to make dielectric or piezoelectric layers $< 20\mu\text{m}$ thick. A slurry with a suitable binder/solvent system is first made from the dielectric ceramic powder. Thin green sheets of the ceramic are then made by tape casting. An ink, consisting of an electrode and organic, is screen printed on the dielectric sheets and then hundreds of sheets are stacked one on top of the other. A low pressure at a temperature between ~ 50 and 70°C is applied to laminate the sheets. These laminates are then diced to form a monolithic green multilayer. The binder removal is accomplished by heating the green body very slowly at a temperature of ~ 300 - 400°C . The multilayer is then sintered at a high temperature depending on the type of ceramic. A critical step in the fabrication of the multilayers is the formation of thin uniform green sheets from the ceramic slurry. Any non-uniformity in the thickness could lead to dielectric breakdown during device operation. The ceramic tapes and metal electrodes should be compatible and should not react with each other on co-firing. To date base metal technology has not been applied to multilayer actuators.

2.7 Applications of Piezoelectric and Ferroelectric Ceramics

Applications of ferroelectric and piezoelectric ceramics range from piezoelectric transducers, radio and communication filters, pyroelectric surveillance devices, positive temperature coefficient devices, and electrooptic light valves. More recent developments in the field of ferroelectric ceramics include medical ultrasonic composites, high-displacement piezoelectric actuators, photostrictors, and thin and thick films for ferroelectric memory applications and piezoelectric sensors.

2.7.1 *Piezoelectric Transducers, Generators, Motors*

Large piezoelectric and coupling coefficients in ferroelectrics make them attractive for transducer applications^[80]. A transducer converts changes in electric field into mechanical motion, as in ultrasonic motors, loudspeakers, tweeters, camera shutters, buzzers, micropositioners, ink jet printers, or pulse generators for use with sonic delay lines. A transducer may also convert small motions into electric charge, an effect useful in ultrasonic detectors, strain-gauges, phonograph cartridges, microphones, hydrophones, microphones, phonograph cartridges, gas ignitors, accelerometers, pickups, sensors and devices to measure the extent of vibrations.

2.7.2 *Piezoelectric Transformers*

This category of applications use combined motor and generator functions in a single device such as sonar, ranging transducers, non-destructive testing (ultrasound) and medical ultrasound and piezo transformers.

2.7.3 Filters, Resonators

Piezoelectrics are also commonly used to control oscillator frequencies, or to provide the significant element in narrow-band wave filters. These uses arise because a piezoelectric has a natural resonant frequency, determined by the geometry of the specimen. A piezoelectric behaves at frequencies near to resonance like a series LCR (inductance-capacitance-resistance) circuit together with a parallel capacitor. Applications include ultrasonic cleaners, ultrasonic welders, surface acoustic wave (SAW) filters, transformers and delay lines.

2.8 Novel Piezoelectric Devices

Piezoelectric ceramics are widely used as micro- and macro-piezoelectric actuators. The micro-devices utilise the basic piezoelectric strain of the ceramic (usually measured in micrometres), whereas the macro-devices (usually measured in millimetres) use a displacement amplifying mechanism to enhance the fundamental strain. A variety of direct extensional configurations, composite flexextensional structures, and bending-mode devices have been developed to achieve an optimum mechanical output. For example, maximum stress generation (40 MPa) or loading capacity is noted for all the direct extensional devices, their strain (displacement) is only limited to $\sim 0.5\%$ or less. However, displacement of several tens of percent can be achieved by amplification using designs such as the so-called Moonie and RAINBOW structures.

2.8.1 Moonies

The Moonie devices, which first appeared in the early 1990's, were so named because of their crescent-shaped, shallow cavities on the interior surfaces of the end caps, which are bonded to a conventionally-electroded piezoelectric ceramic disk (Figure 2.15).

When the ceramic is activated electrically, the shallow cavities permit the end caps to flex, thus converting and amplifying the radial displacement of the ceramic into a large axial motion at the centre of the end caps.

Advantages of the Moonie include: (1) a factor of 10 enhancement of the longitudinal displacement, (2) an unusually large d_{33} exceeding 2500pC/N and (3) enhanced hydrostatic response^[81- 82]. Recent improvements in the basic Moonie design have resulted in an element called a Cymbal, a device that possesses more flexible end caps and higher displacement^[83].

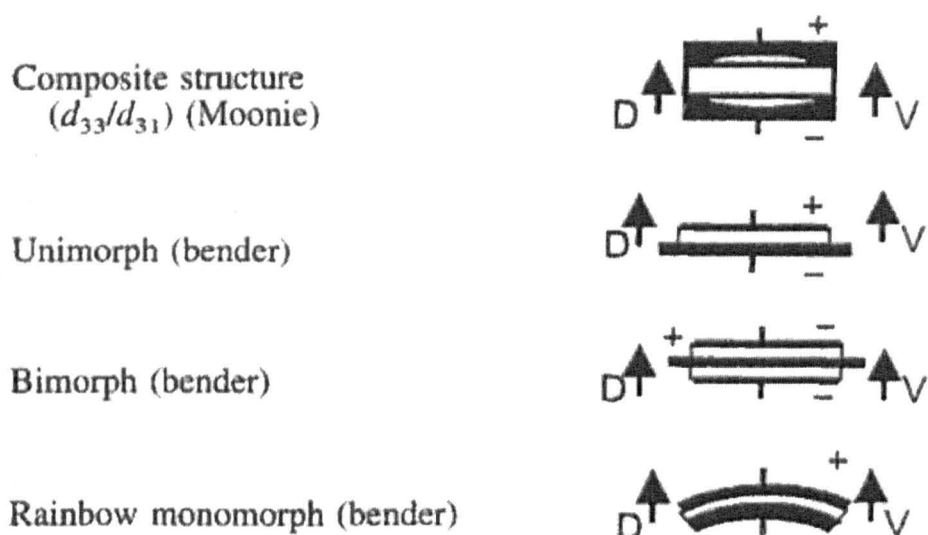


Figure 2.15 Configurations of Moonie and RAINBOW devices (after Haertling^[10])
where V is voltage and D is actuator displacement

2.8.2 RAINBOW devices

Another device, recently developed to increase the force-displacement performance of a piezoelectric actuator, is the RAINBOW. RAINBOW is an acronym for reduced and internally biased oxide wafer. This technology involves the local reduction of one surface of a ceramic wafer, thereby achieving an anisotropic, stress-biased dome or saddle-shaped configuration with significant internal tensile and compressive stresses that act to amplify the axial motion of the wafer and also increase the overall strength of the material. After reduction, the flat wafer changes its shape to one that resembles a contact lens (Figure 2.15). This is believed to be due to the reduction in volume of the reduced layer (largely metallic lead), compared to the unreduced material, the differential thermal contraction between the reduced and unreduced layers on cooling to room temperature, and the volume change in going from the paraelectric to ferroelectric state at its T_C .

Typical steps for the RAINBOW process involves placing a flat wafer on a graphite block, inserting the block and wafer into a furnace preheated to 975°C for 1h and then removing it for cooling to room temperature in ~45 min. This results in a monolithic structure consisting of an unreduced piezoelectric layer that is highly stressed, primarily in compression, and an electrically-conducting reduced layer that produces the stress. These internal stresses have been shown to be instrumental in achieving unusually high axial bending displacement as well as enhanced load-bearing capability.

3. EXPERIMENTAL PROCEDURES

3.1 Raw Materials

The raw ceramic powders used in this study are listed in Table 3.1.

Table 3.1 Information on raw materials

Compound	Manufacturer	Purity
PbO	Fisher Scientific, Loughborough, UK	99+ %
TiO ₂	Aldrich-Chemicals, Milwaukee, USA	99.9+%
ZrO ₂	Carpenter, Z-Tech, Bow, NH, USA	99+ %
Nb ₂ O ₅	Meldform Metals, Royston, Herts, UK	99.8%
SrCO ₃	Solvay, Hemel Hempstead, UK	99.4+ %
BaCO ₃	Aldrich-Chemie, GmbH, Steinheim, Germany	99+ %
Sb ₂ O ₃	Berkshire Ores & Chemicals, Hollycombe, UK	99.9+%

The manufacturers' data sheets (Table 3.2) give some information on impurities and particle size of these raw materials.

Table 3.2 Manufacturers' assay of raw materials

Compounds	Impurities (wt.)	Particle size
PbO	Pb < 0.01%, $(CO_3)^{2-}$ < 0.1%, Fe < 0.001%	< 0.03% above 63 μm
ZrO ₂	SiO ₂ < 0.2%, TiO ₂ < 0.14%, Fe ₂ O ₃ < 0.05%	50% < 2 μm
TiO ₂	ZrO ₂ < 0.02%	50% < 2 μm
Nb ₂ O ₅	Si < 0.006%, W < 0.006%	50% < 2 μm
SrCO ₃	Fe < 0.002%, Cl < 0.02%	50% < 1.8 μm
BaCO ₃	Ca < 0.005%, Cl < 0.002%	50% < 3 μm
Sb ₂ O ₃	PbO < 0.1%	50% < 3 μm

Due to the limited information provided by the manufacturers, all the raw powders used in this study were fully characterised in terms of particle size distribution, shape and phase purity by XRD and the results will be given in Chapter 4.

3.2 Ceramic Processing

Polycrystalline ceramic materials were obtained from appropriate amounts of reagent-grade raw materials: lead oxide (PbO), zirconium dioxide (ZrO₂), titanium dioxide (TiO₂), niobium pentoxide (Nb₂O₅), strontium carbonate (SrCO₃), barium carbonate (BaCO₃) and antimony oxide (Sb₂O₃).

The starting reagents weighed in appropriate ratios with addition of 2 wt.% excess PbO were mixed in distilled water and attrition-milled (Szegvari Attritor System, Union Process, Ohio, USA) for 2h, using 3 mm dia. ZrO₂ media. The slurry was then dried 48h at 70°C. The powder obtained was crushed in a mortar with a pestle, and sieved through a 180 µm nylon sieve. The powder was calcined 4h at 925°C, at a heating rate of 75°C/h and a cooling rate of 300°C/h. For some of the PZT compositions, two-step calcination route was adopted and details will be given in Section 3.3.

The calcined powder was attrition-milled again for 2h with addition of 2 wt.% Carbowax PEG 10K (Whyte Chemicals, London) as a binder. Dried and sieved powders were pressed uniaxially at 180MN/m² into 10 mm dia. pellets. The binder was burned off at 600°C for 3h. The sintering process was conducted in a lead-rich environment. Pellets were embedded in 90 wt.% PbZrO₃ + 10 wt.% ZrO₂ powder and fired in closed alumina crucibles to minimise lead oxide volatilisation. Pellets were sintered 4h in an electric tube furnace (int. dia. 50 mm and ext. dia. 60 mm, Lenton Furnaces, Unit C₂, Leicestershire, UK) in the temperature range from 1100°C to 1240°C, depending on composition. The heating and cooling rates are 180°C/h, and 360°C/h respectively. Pellets were weighed before and after sintering to estimate weight loss during sintering. The processing flow chart used to prepare samples is illustrated in Figure 3.1.

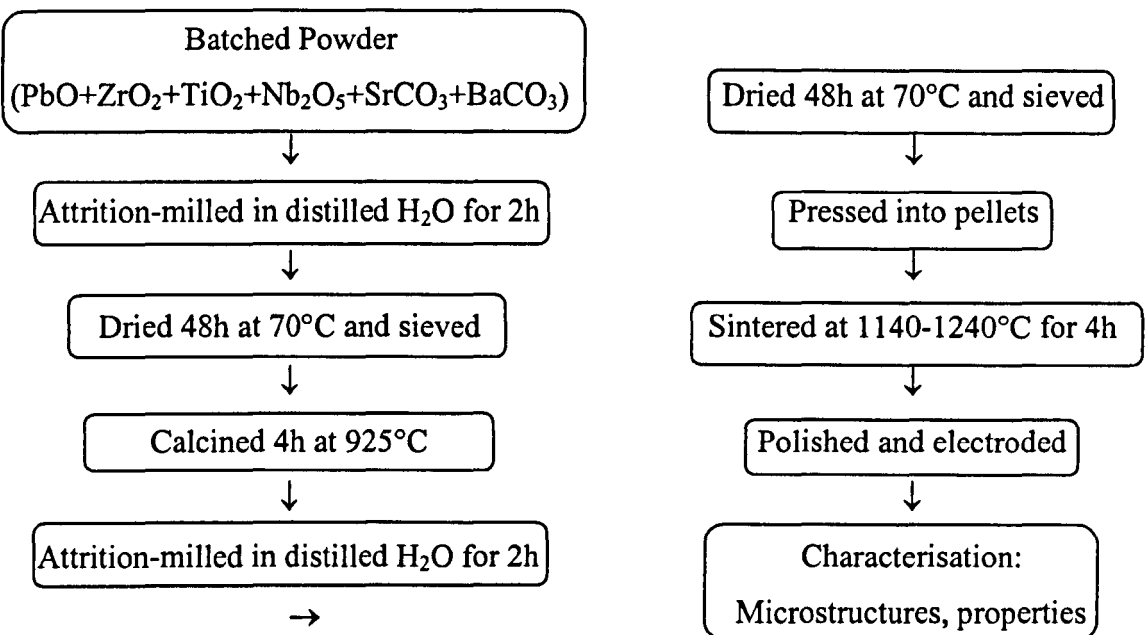
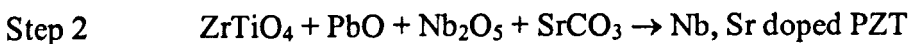
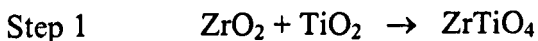


Figure 3.1 Processing flow chart of PZT Ceramics

3.3 Two-step calcination route

The synthesis of doped PZT powder was carried out by a B-site precursor method. The following reactions take place during a two-step calcination process:



The desired ratios of ZrO_2 and TiO_2 raw materials were mixed and attrition-milled in distilled water for 2h. The milled powder, after drying and sieving, was heat treated 4h at various temperatures ranging from 1100°C to 1300°C. Heat treated

powders were analysed by XRD to identify the lowest temperature at which complete reaction to ZrTiO_4 occurs (calcination temperature). The ZrTiO_4 precursor was then mixed with PbO , Nb_2O_5 and SrCO_3 etc., depending on composition. Mixed powder was attrition-milled in distilled water for 2h, dried, sieved and then calcined 4h at 925°C in a covered crucible. The powders obtained as a result of the above preparation processes were milled, mixed with binder and then pressed into discs 10 mm in diameter. The pellets were sintered at temperatures between 1140 to 1240°C in closed crucibles, identical to the process described in Section 3.2.

3.4 Compositions

Compositions studied in this work are chosen based on the three softening methods mentioned in Section 2.4. They are classified by the dopants used, i.e., Nb-doped, Sr-doped and Ba, Sr, co-doped PZT, which are shown in the following tables.

3.4.1 Nb-doped PZT Compositions

The substitution of B-site $\text{Zr}^{4+}/\text{Ti}^{4+}$ ions by Nb^{5+} , was made according to the formula $\text{Pb}(\text{Zr}_{1-x}\text{Ti}_x)_{1-y}\text{Nb}_y\text{O}_3$ and the abbreviation is PNZT $100y/100x$, where N represents Nb^{5+} , y is the Nb^{5+} content and x is the Ti^{4+} content.

Table 3.3 Nb-doped PZT compositions with a fixed Zr:Ti ratio of 1.128 (53/47)

Designation	Composition	Nb ⁵⁺	Zr:Ti ratio
PNZT0/47	Pb(Zr _{0.53} Ti _{0.47})O ₃	0.0	1.128
PNZT2.4/46	Pb((Zr _{0.53} Ti _{0.47}) _{0.976} Nb _{0.024})O ₃	0.024	1.128
PNZT4.8/46	Pb((Zr _{0.53} Ti _{0.47}) _{0.952} Nb _{0.048})O ₃	0.048	1.128
PNZT7.2/46	Pb((Zr _{0.53} Ti _{0.47}) _{0.928} Nb _{0.072})O ₃	0.072	1.128

Table 3.4 Nb-doped PZT compositions with a fixed Nb⁵⁺ content of 2.4 mol%

Designation	Composition	Nb ⁵⁺	Zr:Ti ratio
PNZT2.4/34	Pb(Zr _{0.64} Ti _{0.336} Nb _{0.024})O ₃	0.024	1.905
PNZT2.4/41	Pb(Zr _{0.57} Ti _{0.406} Nb _{0.024})O ₃	0.024	1.404
PNZT2.4/44	Pb(Zr _{0.533} Ti _{0.443} Nb _{0.024})O ₃	0.024	1.203
PNZT2.4/46	Pb(Zr _{0.517} Ti _{0.459} Nb _{0.024})O ₃	0.024	1.128
PNZT2.4/47	Pb(Zr _{0.510} Ti _{0.466} Nb _{0.024})O ₃	0.024	1.094
PNZT2.4/48	Pb(Zr _{0.50} Ti _{0.476} Nb _{0.024})O ₃	0.024	1.050
PNZT2.4/49	Pb(Zr _{0.488} Ti _{0.488} Nb _{0.024})O ₃	0.024	1.000

3.4.2 Sr-doped PZT Compositions

The substitution of A-site ions by Sr²⁺, was made according to the formula Pb_{1-y}Sr_y(Zr_{0.976-x}Ti_xNb_{0.024})O₃, where Nb⁵⁺ content is fixed at 2.4 mol% and the abbreviation

is PSZT $100y/100x$, where S represents Sr^{2+} , y is the Sr^{2+} content and x is the Ti^{4+} content.

Table 3.5 Sr-doped PZT compositions with a fixed Zr:Ti ratio of 1.094

Designation	Composition	Zr:Ti ratio	Sr^{2+} (mol%)	Nb^{5+} (mol%)
PSZT0/47	$\text{Pb}(\text{Zr}_{0.510}\text{Ti}_{0.466}\text{Nb}_{0.024})\text{O}_3$	1.094	0	2.4
PSZT4/47	$(\text{Pb}_{0.96}\text{Sr}_{0.04})(\text{Zr}_{0.510}\text{Ti}_{0.466}\text{Nb}_{0.024})\text{O}_3$	1.094	4	2.4
PSZT8/47	$(\text{Pb}_{0.92}\text{Sr}_{0.08})(\text{Zr}_{0.510}\text{Ti}_{0.466}\text{Nb}_{0.024})\text{O}_3$	1.094	8	2.4
PSZT16/47	$(\text{Pb}_{0.84}\text{Sr}_{0.16})(\text{Zr}_{0.510}\text{Ti}_{0.466}\text{Nb}_{0.024})\text{O}_3$	1.094	16	2.4
PSZT32/47	$(\text{Pb}_{0.68}\text{Sr}_{0.32})(\text{Zr}_{0.510}\text{Ti}_{0.466}\text{Nb}_{0.024})\text{O}_3$	1.094	32	2.4

Table 3.6 8 mol% Sr-doped PZT compositions with various Zr:Ti ratios

Designation	Composition	Zr:Ti ratio	Sr^{2+} (mol%)	Nb^{5+} (mol%)
PSZT8/38	$(\text{Pb}_{0.92}\text{Sr}_{0.08})(\text{Zr}_{0.598}\text{Ti}_{0.378}\text{Nb}_{0.024})\text{O}_3$	1.582	8	2.4
PSZT8/42	$(\text{Pb}_{0.92}\text{Sr}_{0.08})(\text{Zr}_{0.558}\text{Ti}_{0.418}\text{Nb}_{0.024})\text{O}_3$	1.335	8	2.4
PSZT8/44	$(\text{Pb}_{0.92}\text{Sr}_{0.08})(\text{Zr}_{0.533}\text{Ti}_{0.443}\text{Nb}_{0.024})\text{O}_3$	1.203	8	2.4
PSZT8/47	$(\text{Pb}_{0.92}\text{Sr}_{0.08})(\text{Zr}_{0.510}\text{Ti}_{0.466}\text{Nb}_{0.024})\text{O}_3$	1.094	8	2.4

Table 3.7 16 mol% Sr-doped PZT compositions with various Zr:Ti ratios

Designation	Composition	Zr:Ti ratio	Sr ²⁺ (mol%)	Nb ⁵⁺ (mol%)
PSZT16/34	(Pb _{0.84} Sr _{0.16})(Zr _{0.638} Ti _{0.338} Nb _{0.024})O ₃	1.888	16	2.4
PSZT16/38	(Pb _{0.84} Sr _{0.16})(Zr _{0.598} Ti _{0.378} Nb _{0.024})O ₃	1.582	16	2.4
PSZT16/42	(Pb _{0.84} Sr _{0.16})(Zr _{0.558} Ti _{0.418} Nb _{0.024})O ₃	1.335	16	2.4
PSZT16/44	(Pb _{0.84} Sr _{0.16})(Zr _{0.538} Ti _{0.438} Nb _{0.024})O ₃	1.228	16	2.4
PSZT16/47	(Pb _{0.84} Sr _{0.16})(Zr _{0.510} Ti _{0.466} Nb _{0.024})O ₃	1.094	16	2.4

3.4.3 Sr, and Ba co-doped PZT Compositions

The substitution of A-site ions by Sr²⁺ and Ba²⁺, was made according to the formula Pb_{1-y-z}Sr_yBa_z(Zr_{0.976-x}Ti_xSb_{0.024})O₃, where Sb⁵⁺ content is fixed at 2.4 mol% and the abbreviation is PSBZT100y/100z/100x, where S, and B represent Sr²⁺, and Ba²⁺, respectively, y is the Sr²⁺ content, x is the Ba²⁺ content and x is the Ti⁴⁺ content. In these Sr, Ba co-doped PZT compositions, Sb⁵⁺ instead of Nb⁵⁺ was used as the donor doping on the B-site (the doping level was identical), which was designed to keep consistent with the commercial composition of Morgan Electroceramics. The effect of Sb⁵⁺ substitution on the B-site could be regarded identical to that of Nb⁵⁺ substitution, which was justified empirically by Morgan Electroceramics.

Table 3.8 Sr, and Ba co-doped PZT compositions (Sb⁵⁺ content is fixed at 2.4%)

Designation	Composition	Zr:Ti ratio	Sr ²⁺ (mol%)	Ba ²⁺ (mol%)
PSBZT12/0/44	(Pb _{0.88} Sr _{0.12})(Zr _{0.538} Ti _{0.438} Sb _{0.024})O ₃	1.228	12	0
PSBZT9/3/44	(Pb _{0.92} Sr _{0.09} Ba _{0.03})(Zr _{0.538} Ti _{0.438} Sb _{0.024})O ₃	1.228	9	3
PSBZT6/6/44	(Pb _{0.92} Sr _{0.06} Ba _{0.06})(Zr _{0.538} Ti _{0.438} Sb _{0.024})O ₃	1.228	6	6
PSBZT6/6/47	(Pb _{0.92} Sr _{0.06} Ba _{0.06})(Zr _{0.508} Ti _{0.468} Sb _{0.024})O ₃	1.085	6	6
PSBZT6/6/49	(Pb _{0.92} Sr _{0.06} Ba _{0.06})(Zr _{0.488} Ti _{0.488} Sb _{0.024})O ₃	1.000	6	6
PSBZT6/6/52	(Pb _{0.92} Sr _{0.06} Ba _{0.06})(Zr _{0.458} Ti _{0.518} Sb _{0.024})O ₃	0.884	6	6

3.5 Characterisation Techniques

3.5.1 Combined TG and DTA Studies

Pre-calcined powders were attrition-milled and sieved through a 180 µm nylon sieve before DTA/TG experiments. TG/DTA measurements were performed on a Perkin Elmer DTA 7 (Perkin Elmer Instruments LLC., USA), using PYRIS software on Unix operation system. Samples were heated up in an alumina crucible in Ar atmosphere and cooled using compressed air. A heating and cooling rate in air of 5°C/min was used to a maximum temperature of 1200°C. The temperature at which the desired perovskite phase formed was then determined for each composition. Information on the extent of PbO loss during high-temperature treatment was also

obtained. Calcination temperature, and the amount of excess lead oxide, could thus be chosen for each composition.

3.5.2 Particle Size Analysis

Particle size distribution analysis was performed on raw materials, pre-calcined (ball-milled or attrition-milled) and calcined powders, using a Coulter LS130 (Electronics Ltd., Luton Beds, UK). The Coulter LS130 Laser Sizing Unit uses Fraunhofer diffraction pattern analysis to determine the size of particles from 1 to $900 \mu\text{m}$ and a separate unit (PIDS, Polarisation Intensity Differential Scattering) to measure submicron particles down to $0.1 \mu\text{m}$.

Different deflocculants were tried during particle size distribution measurements. It was found that a value of 1 vol\% Calgon deflocculant (Allied Colloids, Bradford, W. Yorks, UK) gave the minimum mean particle size. Therefore 1 vol\% Calgon deflocculant was used for all samples to minimise powder agglomeration.

A dilute powder suspension is placed in a metal container and pumped via plastic tubes to the diffraction and PIDS sample cells. The light from the laser source (wave length = 750 nm) is diffracted by the particles and measured by photodetectors. The computer software uses Fraunhofer diffraction theory to calculate particle size $> 1 \mu\text{m}$ from the intensity and position of the scattered radiation. The intensity of the forward scattered light is proportional to d^2 (the area of the particle) but the diffraction angle varies inversely with particle size i.e. θ is proportional to $1/d$ from Braggs Law. The PIDS unit uses white light and several filter/polarisers to select light at a particular wavelength and polarisation parallel or perpendicular to the scattering plane. The filter carousel is rotated sequentially for the photodetectors to measure scattered light patterns for different combinations of filters and polarisers. Particle size distribution data are presented in differential relative volume percentage graphs.

3.5.3 Estimation of Crystallographic Density

Taking PNZT0/47 ($\text{Pb}(\text{Zr}_{0.53}\text{Ti}_{0.47})\text{O}_3$) as an example, the theoretical density of compositions may be calculated by:

$$\begin{aligned}\rho &= \frac{m}{v} = \frac{(207.2 + 47.86 \times 0.47 + 91.224 \times 0.53 + 15.999 \times 3)}{((4.036 \times 4.036 \times 4.146 \times 10^{-24}) \times 6.022 \times 10^{23})} \\ &= \frac{326.04}{40.7} = 8.01(\text{g/cm}^3)\end{aligned}\tag{3.1}$$

where 207.2, 47.86, 91.224, and 15.999 are the atomic mass of Pb, Ti, Zr, and O respectively, 4.036 and 4.146 are a , and c lattice parameters.

The crystallographic densities of all the compositions made in this study were calculated according to this formula.

3.5.4 Archimedes' Density Measurements

The bulk density of sintered samples was determined by the Archimedes' method using mercury as the liquid. The mass of mercury displaced by the sample is determined using a Doulton Densitometer. The sample is weighed in air (w_1). The sample holder is lowered into a beaker of Hg sitting on a weighing balance and the micrometer needle adjusted to just touch the surface of the Hg at a zero reading. The sample holder is lifted and the sample placed in it and lowered until immersed. The pointer needle is adjusted to just touch the surface of the Hg using the micrometer adjustment. The balance is read and the weight w_2 is the upthrust due to Hg displaced plus the sample weight. Sample total volume $V_t = w_2/\rho_{Hg}$ where ρ_{Hg} is the density of Hg at the experiment temperature. Bulk density is equal to w_1/V_t .

Archimedes density measurements were performed on all the sintered samples of each composition. Relative density was then obtained by comparing to their crystallographic density. All the samples made in this study had relative densities $\geq 95\%$.

3.5.5 X-ray diffraction (XRD)

An X-ray diffractometer (Model PW 1730/10 Philips, Holland) with Cu $K\alpha$ source ($\lambda=1.540562 \text{ \AA}$), operated at 50 kV and 30 mA , was used for the identification of phases and the measurement of lattice parameters. A step size of 0.02° , a scan rate of $2^\circ/\text{min}$, and scan ranges of $10\text{-}80^\circ$ (2θ) were adopted. Raw powders were checked by XRD to indicate the major phases present. Powders calcined at different temperatures were examined by XRD to investigate the reaction mechanism leading to the formation of perovskite phase. Sintered pellets were examined by XRD to identify phase structures and to calculate the lattice parameters.

XRD traces analysis was conducted using a Trace Processing Software (version 4.2, © 1997 Diffraction Technology, Pty. Ltd., Australia) and STOE WinXPOW software (version 1.06, © STOE & Cie GmbH, Darmstadt, Germany). XRD patterns were analysed by comparing the d-spacings obtained to those published for similar compounds in the “X-ray Powder Diffraction Data Files” published by “International Centre for Diffraction Data” (1982). Table 3.9 lists ICDD card numbers used in this study.

Table 3.9 ICDD card number and crystal system information

Compound	Crystal System	ICDD Card
PbO	Orthorhombic	38-1477
TiO ₂	Tetragonal	21-1272
ZrO ₂	Monoclinic	37-1484
Nb ₂ O ₅	Orthorhombic	21-1313
SrCO ₃	Orthorhombic	5-418
BaCO ₃	Orthorhombic	5-378
Sb ₂ O ₃	Cubic	43-1071
Pb(Zr _{0.52} Ti _{0.48})O ₃	Tetragonal	33-784
Pb(Zr _{0.75} Ti _{0.25})O ₃	Rhombohedral	86-1710
ZrTiO ₄	Orthorhombic	74-1504

Unit cell constants of tetragonal structure were calculated using the d-spacings of (200) and (002) peaks according to:

$$\frac{1}{d} = \sqrt{\frac{h^2 + k^2}{a^2} + \frac{l^2}{c^2}} \quad (3.2)$$

where d is the d-spacings and h, k, l is the plane index of each peak.

Polished pellet samples for XRD analysis were first ground systematically with SiC grinding papers. Then the surface was brought to a final polish with $6 \mu\text{m}$ diamond paste for 3 min, $3 \mu\text{m}$ for 3 min and $1 \mu\text{m}$ for 3 min.

3.5.6 Scanning Electron Microscopy (SEM)

A Camscan Series II (Cambridge, England) SEM, fitted with a Link AN 10000 (Cambridge, England) Energy Dispersive Spectroscopy (EDS) facility was used to determine grain size of polished and thermally-etched samples. Sintered pellet samples were first ground systematically with SiC grinding papers. The surface was then brought to a final polish using diamond pastes (6 , 3 and $1\ \mu m$) on synthetic polishing cloths. Thermal etching of polished surfaces was performed using a heating rate of $5^{\circ}C/min$ at a temperature that was $100^{\circ}C$ below the sintering temperature for $0.5h$.

Samples were mounted on aluminium pin stubs using silver paste (Agar Scientific Ltd., Essex, UK), which were then coated with gold (EMSCOPE SC500A sputter coater, Thermo VG Scientific, UK) or carbon (Carbon coating unit, model: 12E6/1598, Edwards High Vacuum Ltd., UK) to reduce the charging effects before secondary electron image (SEI) observations. The working voltage for SEI of pellet samples was $20\ kV$ and the working distance was $20\ mm$. Average grain sizes were determined on polished and thermally-etched ceramic surfaces by the linear intercept technique using ~ 150 grains.

To determine the particle size and morphology of raw, calcined, and attrition-milled powders, samples were mounted on pin stubs using double-sided conducting carbon tape (Agar Scientific Ltd., Essex, UK), and then coated with gold or carbon. The working voltage for SEI of powder samples was $10\ kV$ and the working distance was $20\ mm$. All samples for EDS analysis were coated with carbon and the working distance was $35\ mm$.

3.5.7 Transmission Electron Microscopy (TEM)

Samples for TEM were ground parallel to $\sim 25 \mu\text{m}$ thickness on glass slides using 1200 grit SiC paper. A 3 mm dia. Cu support ring with a 1 mm dia. hole (Agar Scientific Ltd., Essex, England) was glued onto the ground ceramic using epoxy resin. After cleaning with acetone, samples were ion thinned using a Gatan dual ion mill (Model 600, Gatan Inc., Pleasanton, California, USA), operating at an accelerating voltage of 6 kV , a beam current of 0.3 mA per gun, and milling incidence angles of $10\text{--}15^\circ$. Specimens were coated with carbon (Emitech K950 carbon coater, Pfeiffer Vacuum, Germany) before TEM examination. TEM studies were done on Tecnai 20 (Philips, Holland, operating at 200 kV), Philips 420 (Philips, Holland, operating at 120 kV), JEOL 200CX (JEOL, Japan, operating at 200 kV), and JEOL 3010 (JEOL, Japan, operating at 300 kV) TEM's.

TEM specimens were tilted to a two-beam condition using the double-tilt specimen holder. The two-beam condition is an orientation at which only one set of planes is strongly diffracting. Bright-field (BF) imaging was then achieved by using an objective aperture to cover only the transmitted beam.

Electron diffraction patterns were obtained using the selected-area (SA) diffraction technique. To record the SA diffraction pattern, firstly a BF-TEM image in the SA magnification range is required. Then a SA aperture of appropriate diameter is inserted and the objective aperture is removed. By selecting the right camera length, adjusting the intensity of illumination to a suitable level and focusing, the diffraction pattern is obtained.

Energy dispersive (EDS) X-ray detectors and Link ISIS analysis systems, fitted to the TEM's, were used to analyse chemical compositions of features in some samples.

Electron diffraction patterns were solved using simulated patterns generated by either CaRine Crystallography 3-1 (C. Boudias and D. Monceau © 1989-1998) or EMS (Electron Microscopy Image Simulation). EMS is a software package for electron diffraction analysis, developed by Pierre Stadelmann at the Centre Interdepartmental de Microscopie Electronique of the Ecole Polytechnique Fédérale de Lausanne.

3.5.8 Dielectric Properties

The dielectric response was measured using an inductance-capacitance-resistance (LCR) meter (Model 4284A, Hewlett Packard), at a frequency of 1 kHz. The LCR meter was used in conjunction with a computer-controlled temperature chamber (50 mm in diam. and 250 mm in length) to measure capacitance as a function of temperature. The temperature was measured via a platinum resistance thermocouple mounted directly on the ground electrode of the sample fixture. Measurements were taken in the temperature range from 25 to 650°C on heating as well as cooling at a rate of 2°C/min. Capacitance was converted to dielectric permittivity, using the sample geometry and the permittivity of air:

$$\epsilon = \frac{Cd}{\epsilon_0 A} \quad (3.3)$$

where C is the capacitance (F), d is the thickness (m), and A is the area (m^2) of the samples, ϵ_0 is the permittivity of free space: $8.85434 \times 10^{-12} (F/m)$.

3.5.9 d_{33} Measurements

Samples for d_{33} testing were sliced using diamond saw into ~ 0.8 mm thick discs and subsequently polished. Polished samples were electroded using silver paste (Elverson, Pennsylvania 520, USA) and poled in insulation oil at 100°C for 3 minutes at

a field strength of 2 kV/mm. Measurements were then performed, 24 hours after the poling, using a Piezometer System PM 2C (Manchester, UK) at a frequency of 100Hz. d_{33} measurements were carried out at Morgan Electroceramics, Ruabon.

3.5.10 K_p Coupling Factor Measurements

A 4194A impedance/gain-phase analyser (testing frequency range: 100-40MHZ, Hewlett Packard), fitted with a 16047D test fixture (Hewlett Packard) was used to find the strongest well defined minimum and maximum impedance frequencies of the samples (f_m and f_n).

The planar coupling factor K_p was then obtained according to the relationship of K_p versus $(f_p-f_s)/f_s$, which can be found in IEEE standard on piezoelectricity: Determination of elastic, piezoelectric and dielectric constants, 1984^[84]. f_p is the parallel resonance frequency, and f_s is the series resonance frequency. With piezoelectric ceramics of high coupling factor, the differences between (f_p-f_s) and (f_n-f_m) are negligible. Planar coupling factor measurements were carried out at Morgan Electroceramics, Ruabon.

3.5.11 Hysteresis Loop Measurements

Hysteresis loop measurements were conducted at room temperature on the same samples prepared for d_{33} testing, using a computer-controlled function generator (HP 33120A) and a high voltage amplifier (Trek 609D-6). A current amplifier (Stanford Research System, Model SR570, UK) was used to measure the induced current, which was then integrated numerically to yield the charge Q and hence the polarisation P . Applied field and induced current waveforms were downloaded to the PC using a Tektronix TDS 420 DSO. The measurements were carried out using a “burst mode” waveform comprising 2 complete sinusoidal cycles. This procedure was used in

preference to a continuous waveform in order to avoid field-forced deaging effects. Hysteresis loop measurements were carried out at UMIST Materials Research Centre.

3.6 Measurement Error Analysis

3.6.1 Errors of Measurement

No measurement is perfectly accurate or exact. Many instrumental, physical and human limitations cause measurements to deviate from the "true" values of the quantities being measured. These deviations are called "experimental uncertainties or errors"^[85].

The "true value" of a measured quantity is the value after all errors from instruments and procedure have been eliminated. Since it is impossible to eliminate measurement errors entirely, the true values can never be measured. The "error" in a quantity is an estimate of how much that measurement is likely to deviate from the true value of the quantity. This estimate is founded on a physical analysis of the measurement process and a mathematical analysis of the equations, which apply to the instruments and to the physical process being studied^[85].

3.6.2 Determinate and Indeterminate Errors

Experimental errors are of two types: (1) indeterminate and (2) determinate (or systematic) errors.

Indeterminate errors are present in all experimental measurements. The name "indeterminate" indicates that there's no way to determine the size or sign of the error in

any individual measurement. Indeterminate errors cause a measuring process to give different values when that measurement is repeated many times (assuming all other conditions are held constant to the best of the experimenter's ability). Indeterminate errors can have many causes, including operator errors or biases, fluctuating experimental conditions, varying environmental conditions and inherent variability of measuring instruments. Indeterminate errors can be reduced by taking repeated measurements then calculating their average^[85]. The average is a better representation of the "true value" than any single measurement, because errors of positive and negative sign tend to compensate each other in the averaging process. All the measurements performed in this study were therefore repeated three times.

Determinate or systematic error means that the size and sign of the errors are determinable. A common cause of determinate error is instrumental or procedural bias. Another cause is an outright experimental blunder. To minimise the possibility of these errors, careful calibration of the apparatus and use of the best possible measurement techniques are essential. Determinate errors cannot be reduced by averaging repeated measurements^[85].

3.6.3 Evaluation of Measurement Errors

The experimental error can be expressed in error limit in the form $Q \pm q$ where Q is the measured quantity and q is the magnitude of its limit of error. This expresses the experimenter's judgement that the "true" value of Q lies between $Q - q$ and $Q + q$. This entire interval within which the measurement lies is called the range of error.

3.6.4 Importance of Repeated Measurements

A single measurement of a quantity is not sufficient to convey any information about the quality of the measurement. Repeated measurements are needed to determine the indeterminate error. The total measurement error is the sum of indeterminate error

and systematic error i.e., the precision of the instrument and the accuracy of the measurement setup.

As a result all measurements reported in this thesis give a mean value and the standard deviation (the root mean square deviation of the data, measured from the mean) in the form $Q \pm q$ where Q is the measured quantity and q is the magnitude of its limit of error (standard deviation). Error ranges are incorporated into all curves and graphical representations.

4. CHARACTERISATION OF PROCESSING ROUTE

4.1 Starting Raw Powders

4.1.1 Combined TG and DTA Studies

TG analysis of a mixed PNZT0/47 powder before calcination, suggests that the weight loss starts at $\sim 760^{\circ}\text{C}$ and exceeds 18 wt.% by 1060°C after 1 hour, Figure 4.1(a). It is assumed that this weight loss is mainly due to the volatilisation of lead components at high temperatures.

DTA, Figure 4.1(b), of a mixed PNZT0/47 powder before calcination, shows an endothermic trough, which begins at $\sim 815^{\circ}\text{C}$ and which is complete by 925°C . Since there is no decomposition of carbonates during the reaction process, this anomaly is assumed to be the onset temperature for the formation of perovskite phase.

As a result of this investigation, it was concluded that excess PbO was required in the starting batch composition and the calcination was fixed at $\sim 925^{\circ}\text{C}$ (above the onset reaction temperature). By trial and error during ceramic processing a value of 2 wt.% PbO was considered sufficient to compensate for lead loss during powder calcination and pellet sintering.

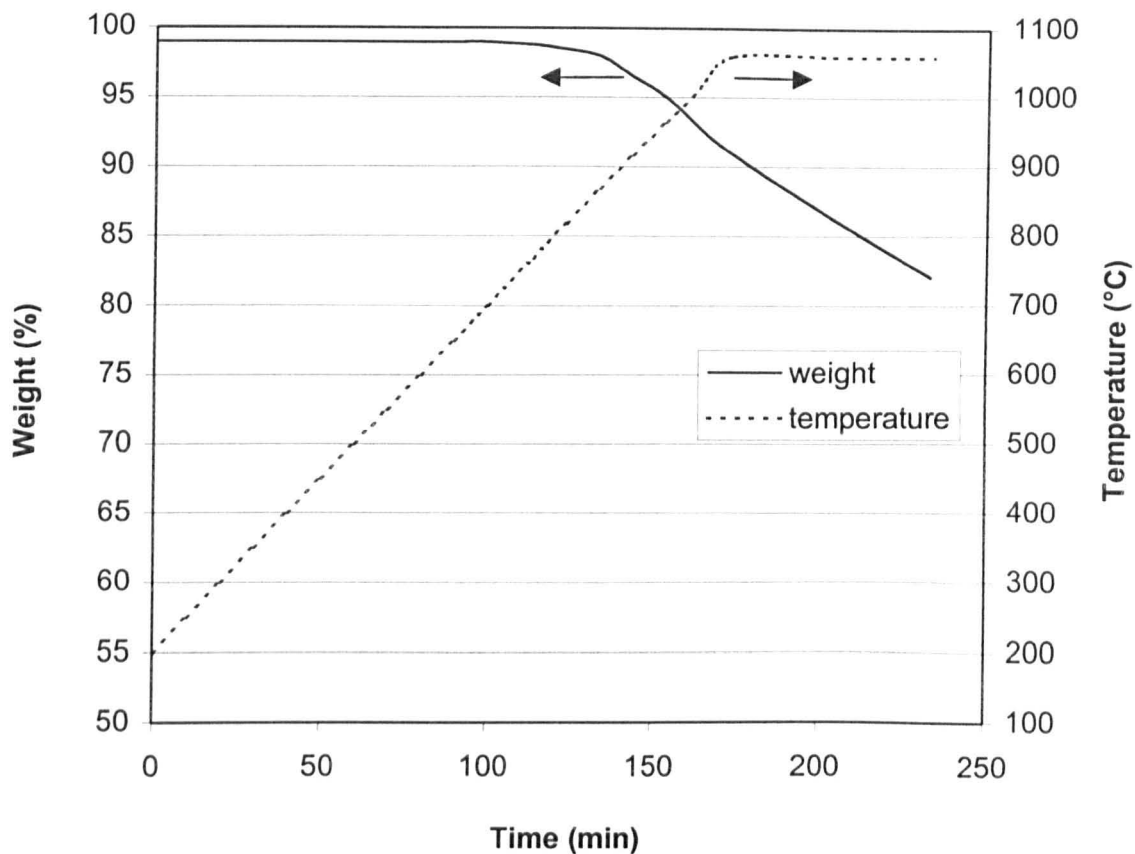


Figure 4.1(a) TG analysis of a mixed PNZT0/47 powder before calcination

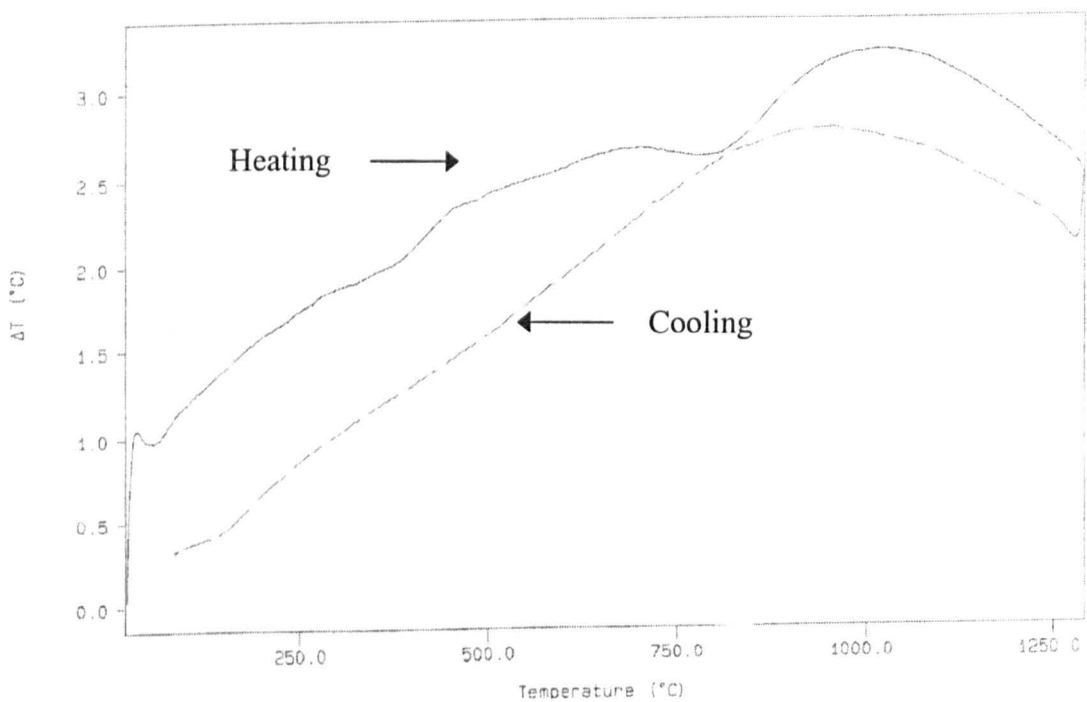


Figure 4.1(b) DTA data of a mixed PNZT0/47 powder before calcination

4.1.2 Particle Shape and Size Analyses

Particle morphologies and particle size distributions of the raw powders are illustrated in Figures 4.2 – 4.8. Particle size distribution data are presented in differential volume percentage graphs where the abscissa is the particle size and the ordinate is the relative volume percentage of particles at this size. The mean particle size values can be also derived from differential volume percentage graphs.

In general, PbO particles have plate-like shapes and they are rather coarse with the majority in the range from 1.8 to $23.6 \mu\text{m}$.

TiO₂ particles are fine with a median size of $1.5 \pm 0.1 \mu\text{m}$ and largely spherical-shaped. ZrO₂ powder has serious agglomeration with the agglomerates consisting of submicron individual particles.

Most of the ZrO₂ particles are less than $1.3 \mu\text{m}$, but a multi-modal size distribution with large particles in the range of $1.3 - 34 \mu\text{m}$ is also present.

Nb₂O₅ particles are very fine with 90% of the particles below $1.5 \mu\text{m}$ and round-shaped.

Both SrCO₃ and BaCO₃ powders have acicular shapes and broad particle size distributions. It is evident that some very large agglomerates exist for these two powders.

Sb₂O₃ particles are irregularly shaped with mean particle size of $2.4 \pm 0.2 \mu\text{m}$.

All these powders have asymmetric size distributions with most of them skewed to the right (i.e. lognormal). The particle sizes obtained from SEM studies are in good agreement with the results from particle size distribution measurements.

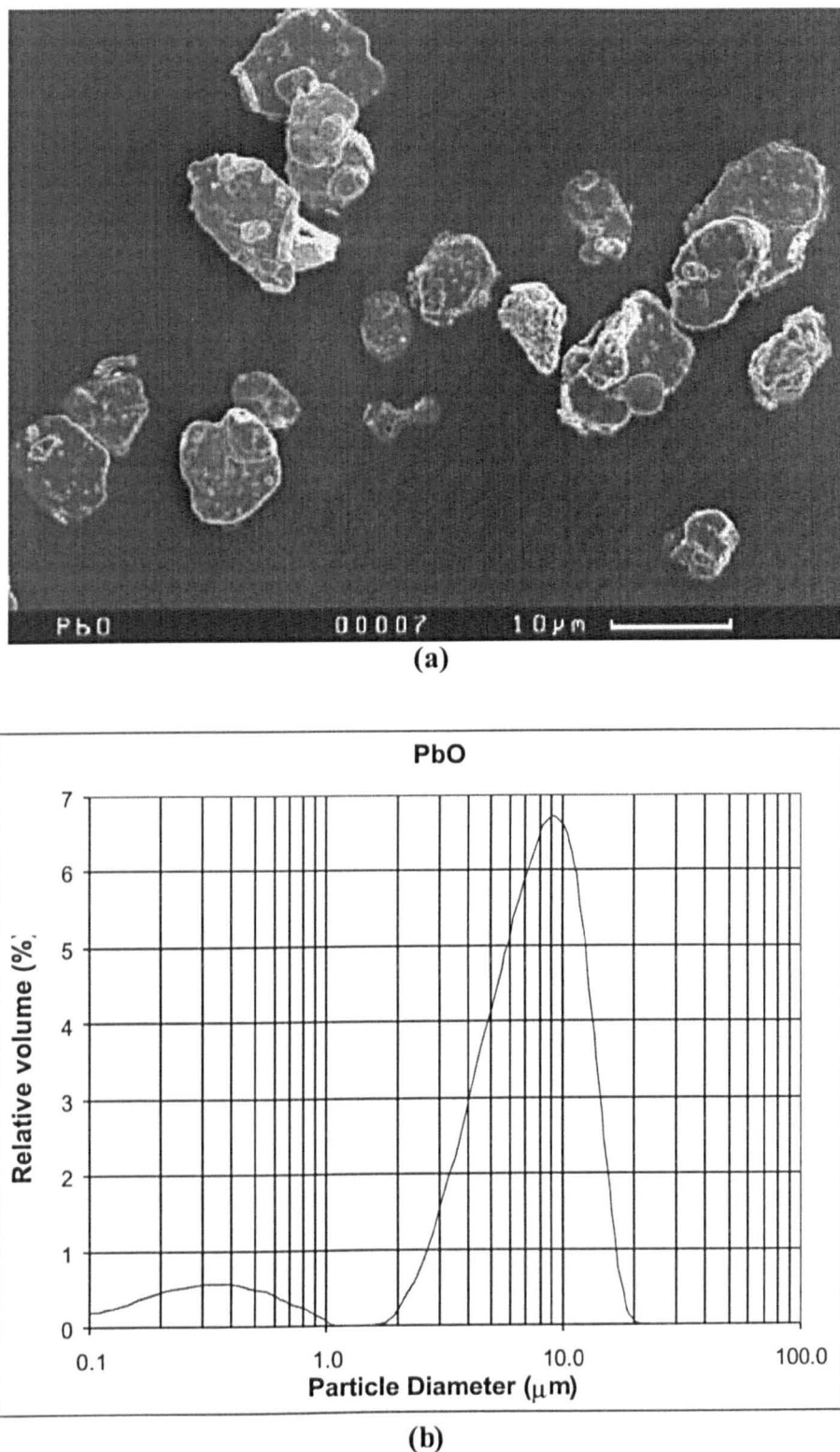


Figure 4.2 Particle morphology (a) and size distribution (b) of raw material PbO

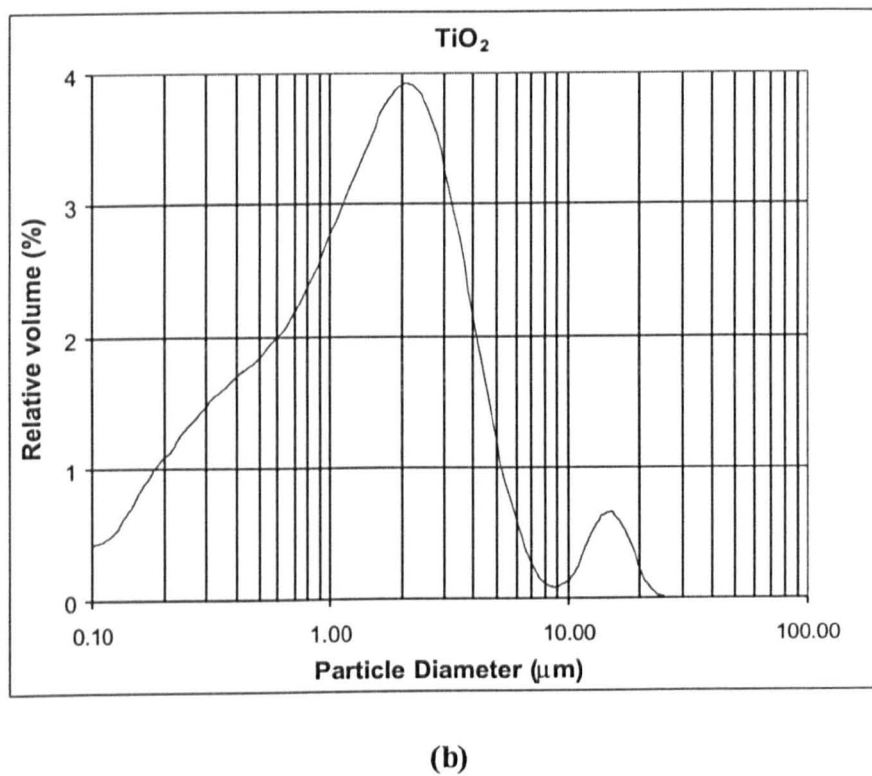
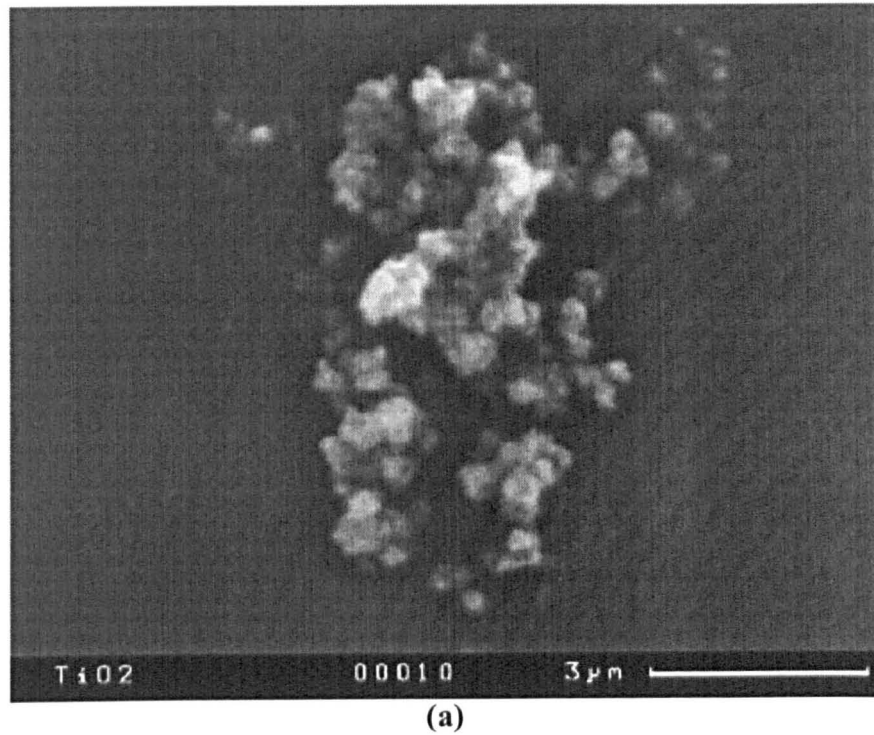


Figure 4.3 Particle morphology (a) and size distribution (b) of raw material TiO_2

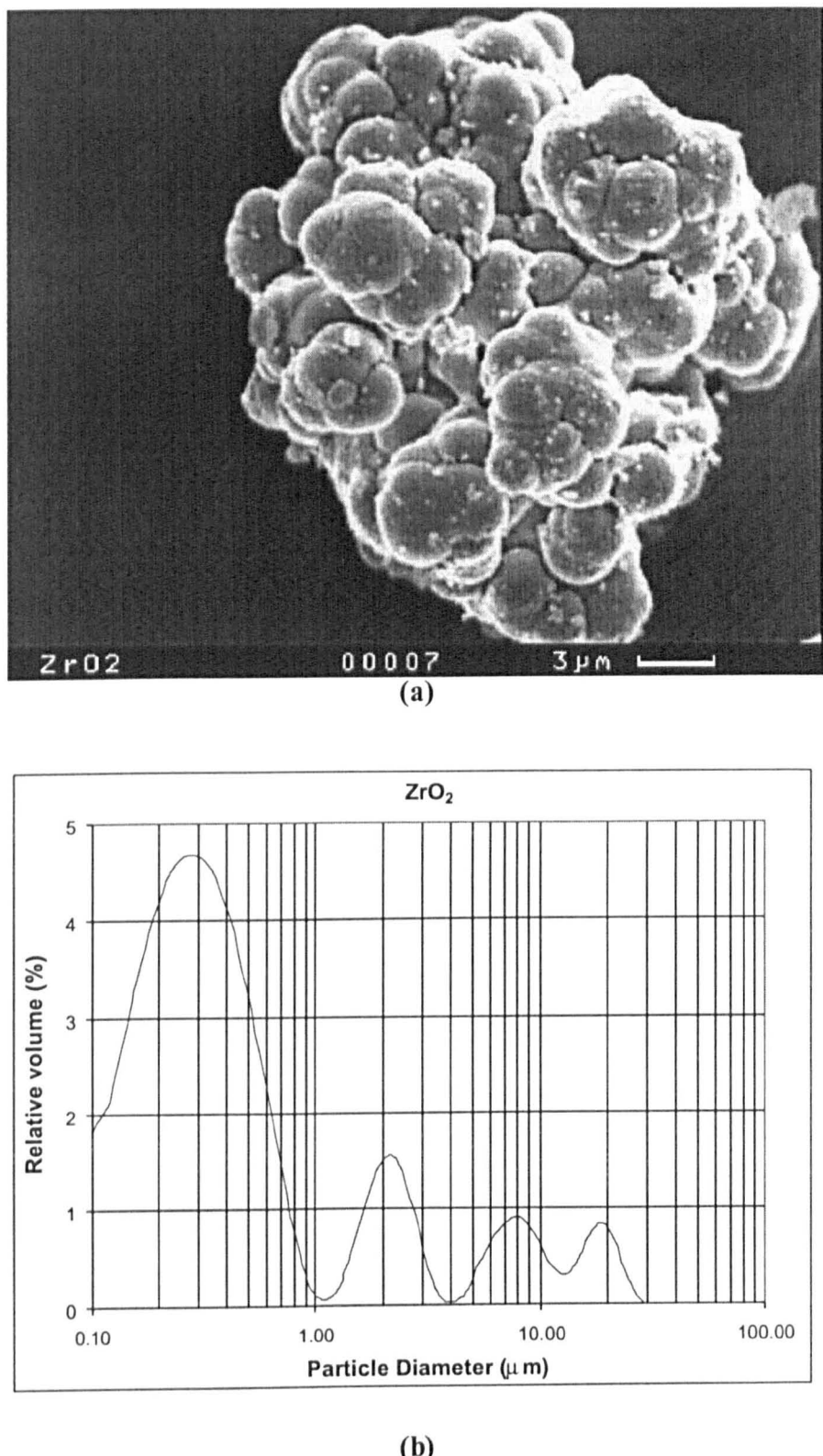


Figure 4.4 Particle morphology (a) and size distribution (b) of raw material ZrO_2

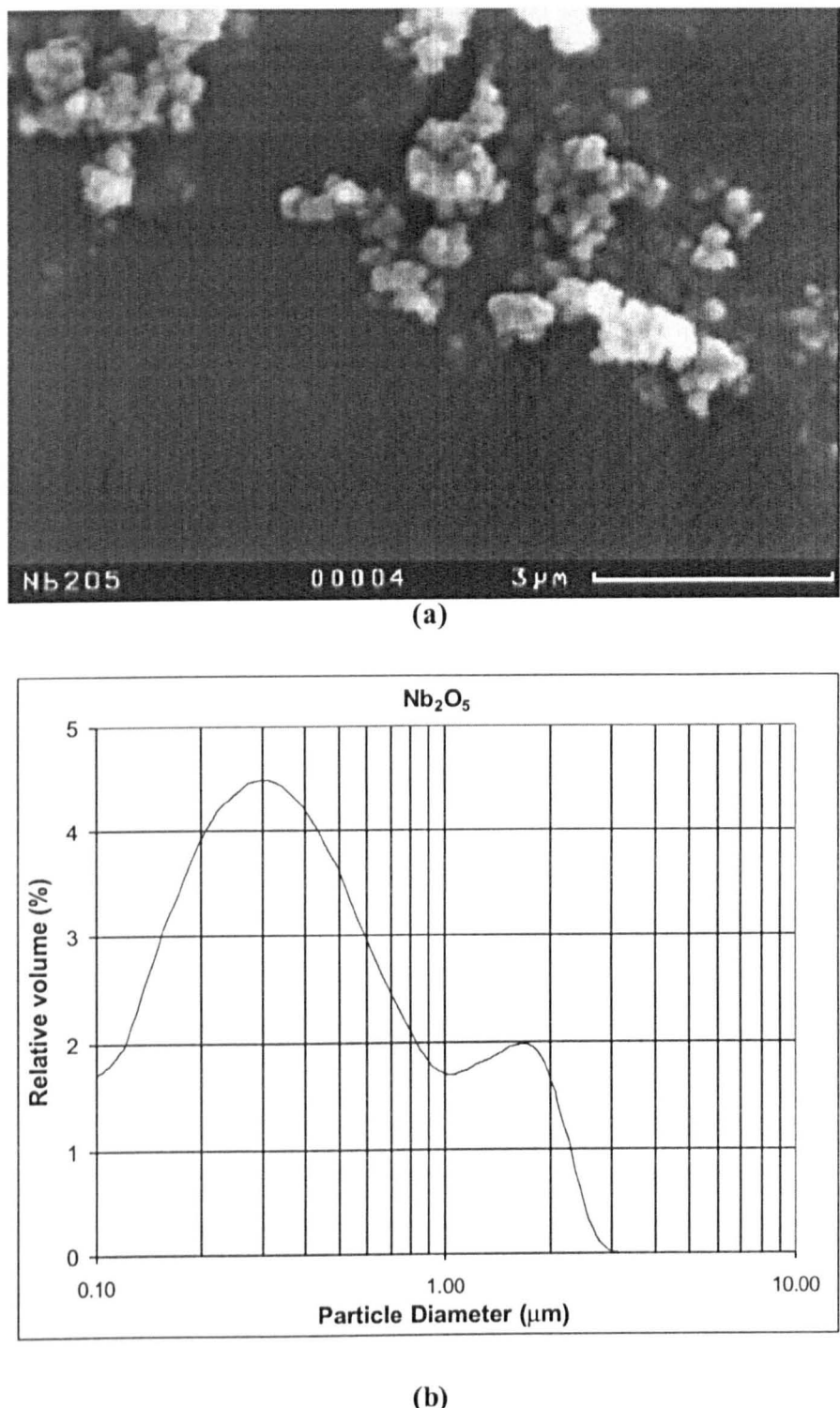
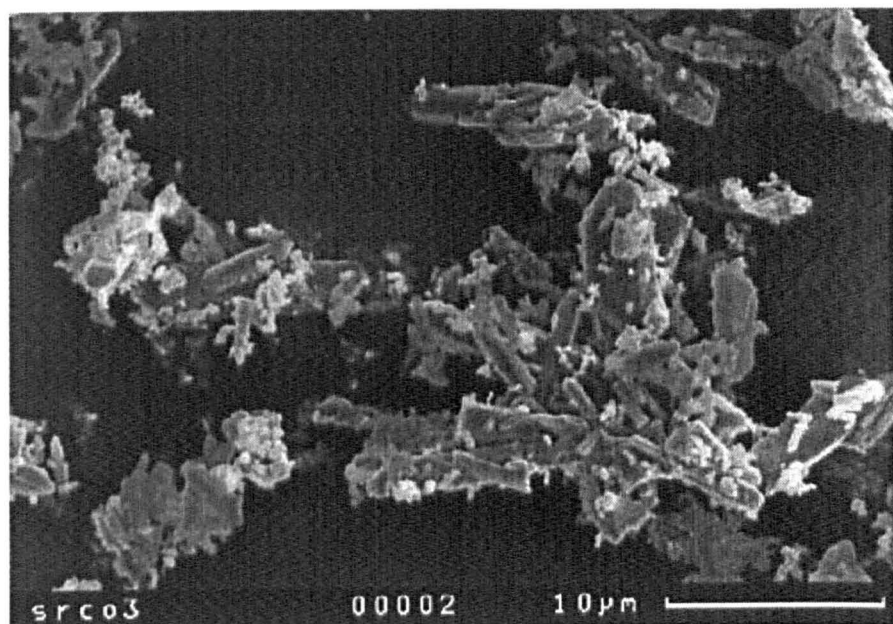
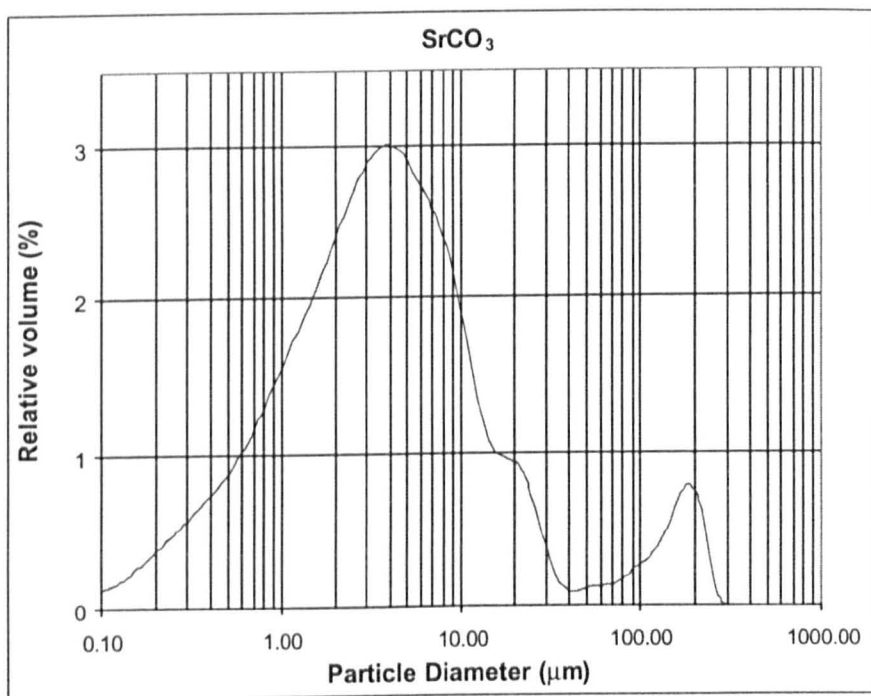


Figure 4.5 Particle morphology (a) and size distribution (b) of raw material Nb_2O_5

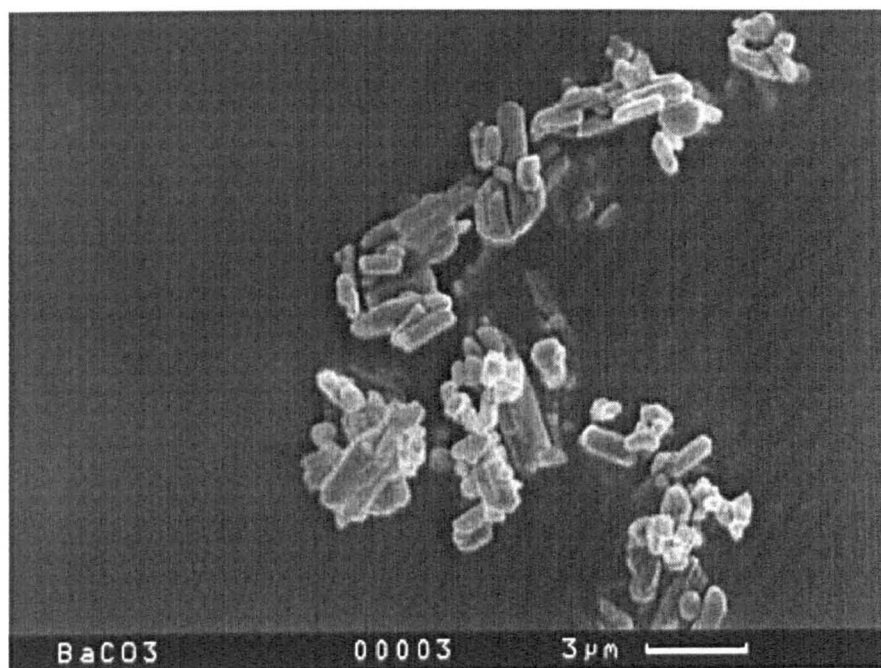


(a)

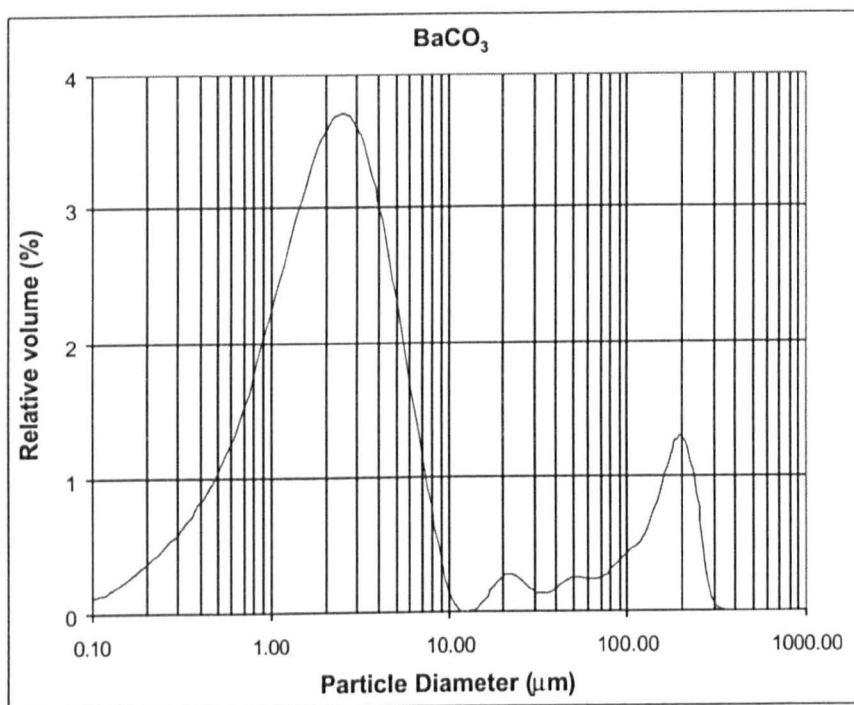


(b)

Figure 4.6 Particle morphology (a) and size distribution (b) of raw material SrCO₃

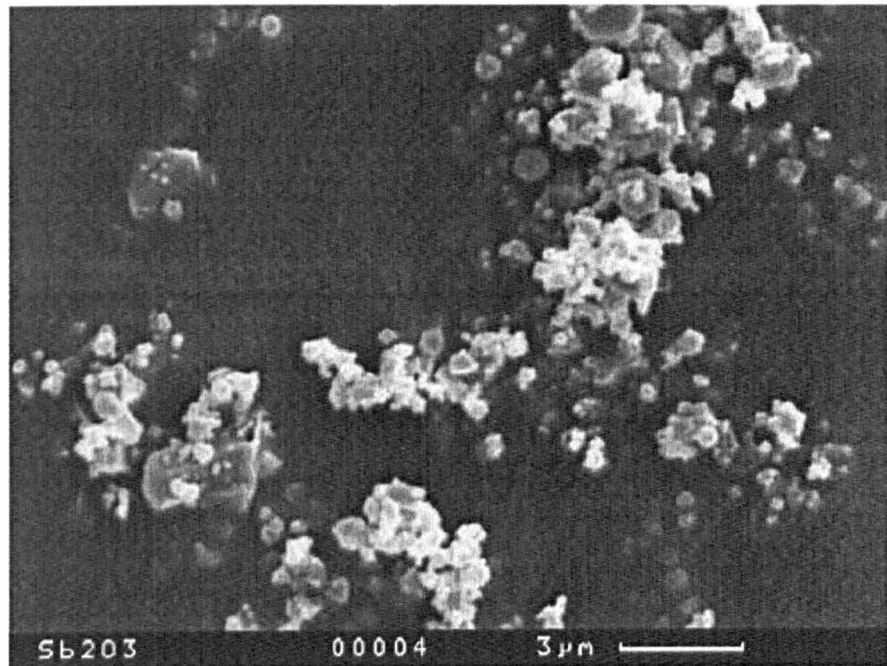


(a)

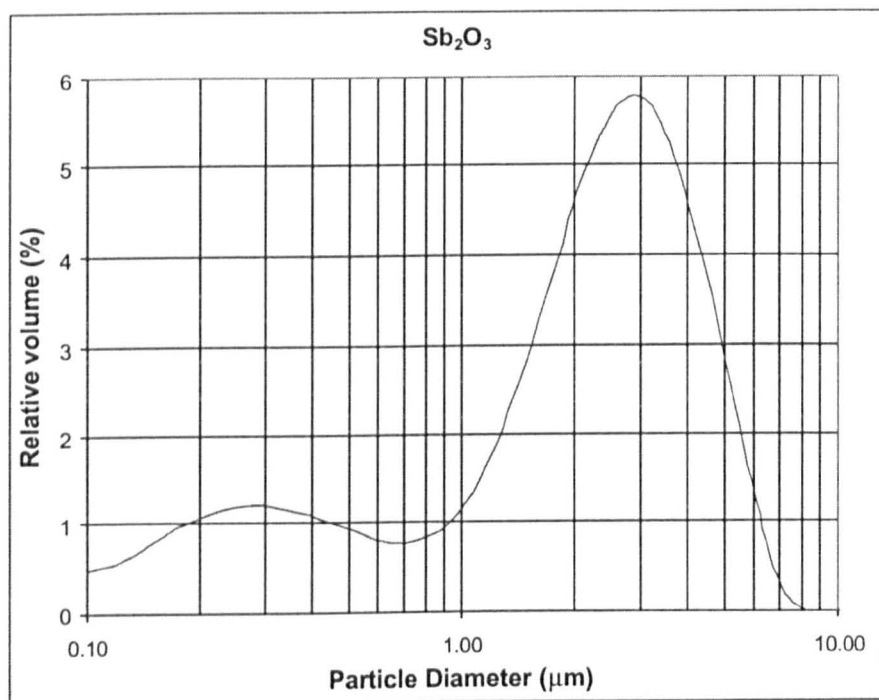


(b)

Figure 4.7 Particle morphology (a) and size distribution (b) of raw material BaCO₃



(a)



(b)

Figure 4.8 Particle morphology (a) and size distribution (b) of raw material Sb₂O₃

4.1.3 XRD Analysis

XRD spectra of the starting raw materials are shown in Figures 4.9 (a-g) respectively.

Peak positions of PbO agree with the ICDD card 38-1477 orthorhombic PbO (Massicot), but relative intensities of each peak deviate from those of ICDD card values implying a strong preferred orientation along $<001>$. The traces of TiO₂ match with ICDD card 21-1272 tetragonal TiO₂ (Anatase). The profile of ZrO₂ agrees with ICDD card 37-1484 monoclinic ZrO₂. The trace of Nb₂O₅ fits to ICDD card 27-1313 orthorhombic Nb₂O₅. The trace of SrCO₃ matches with ICDD card 5-418 orthorhombic SrCO₃. BaCO₃ profile agrees with ICDD card 5-378 orthorhombic BaCO₃. The trace of Sb₂O₃ fits to ICDD card 43-1071 cubic Sb₂O₃.

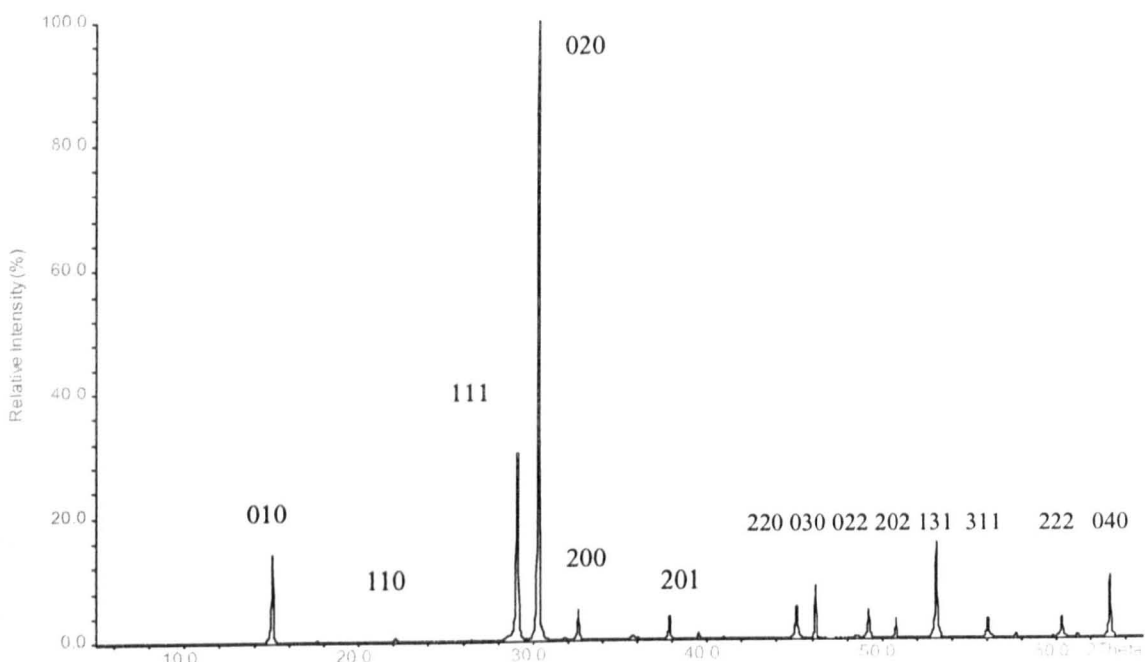


Figure 4.9(a) XRD trace of raw material PbO

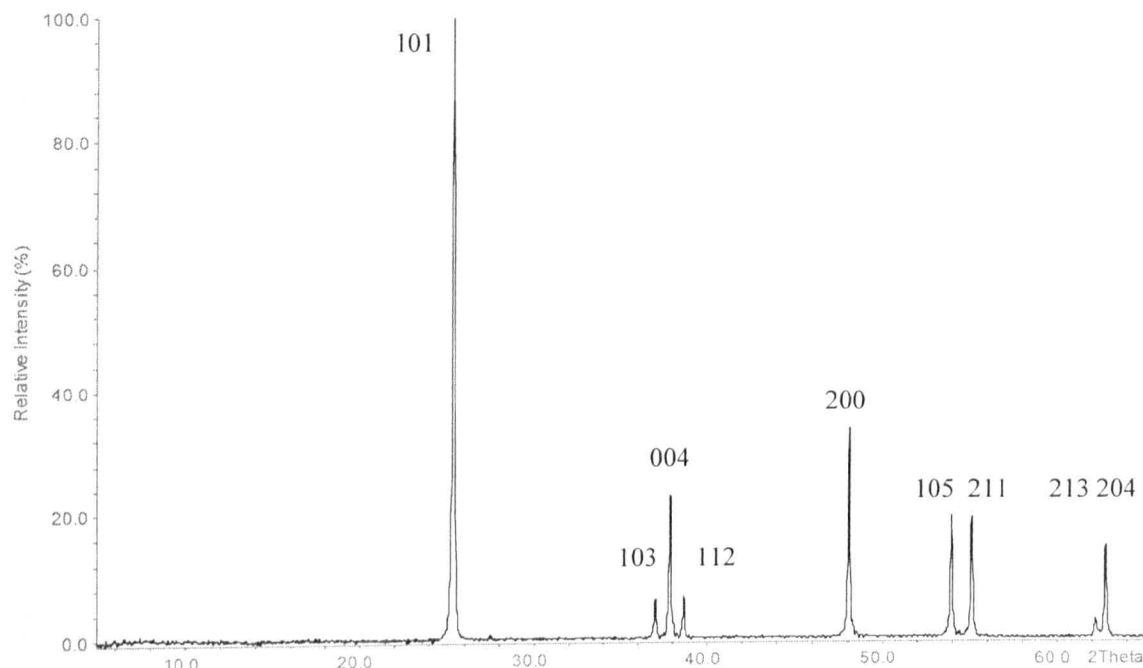


Figure 4.9(b) XRD trace of raw material TiO_2

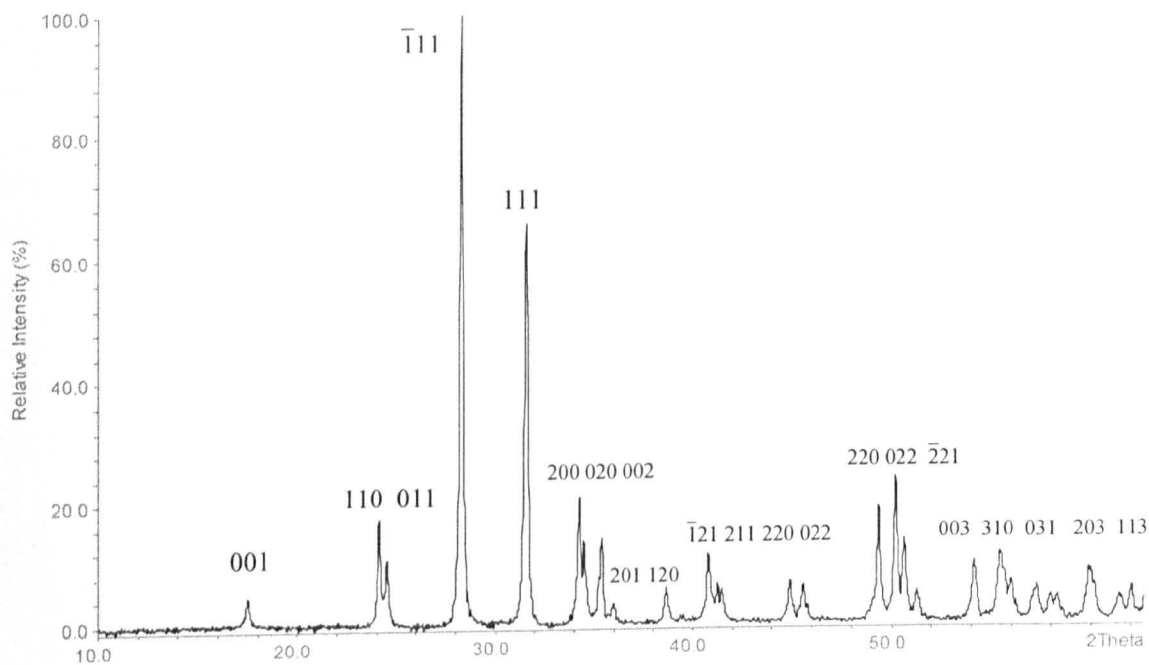


Figure 4.9(c) XRD trace of raw material ZrO_2

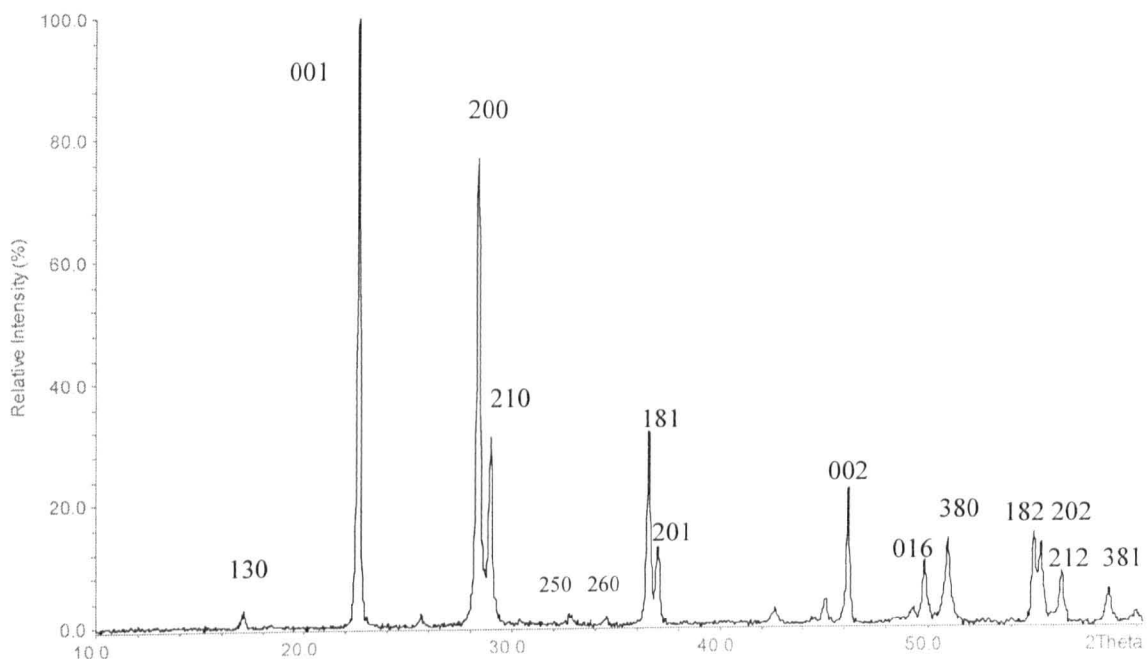


Figure 4.9(d) XRD trace of raw material Nb_2O_5

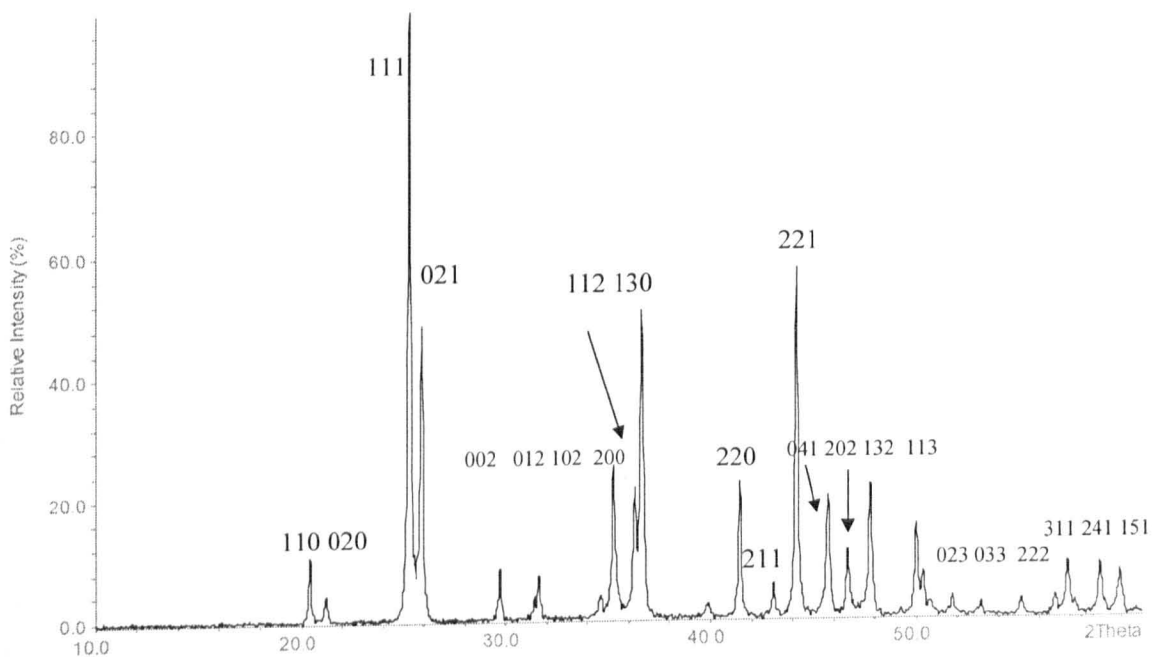


Figure 4.9(e) XRD trace of raw material SrCO_3

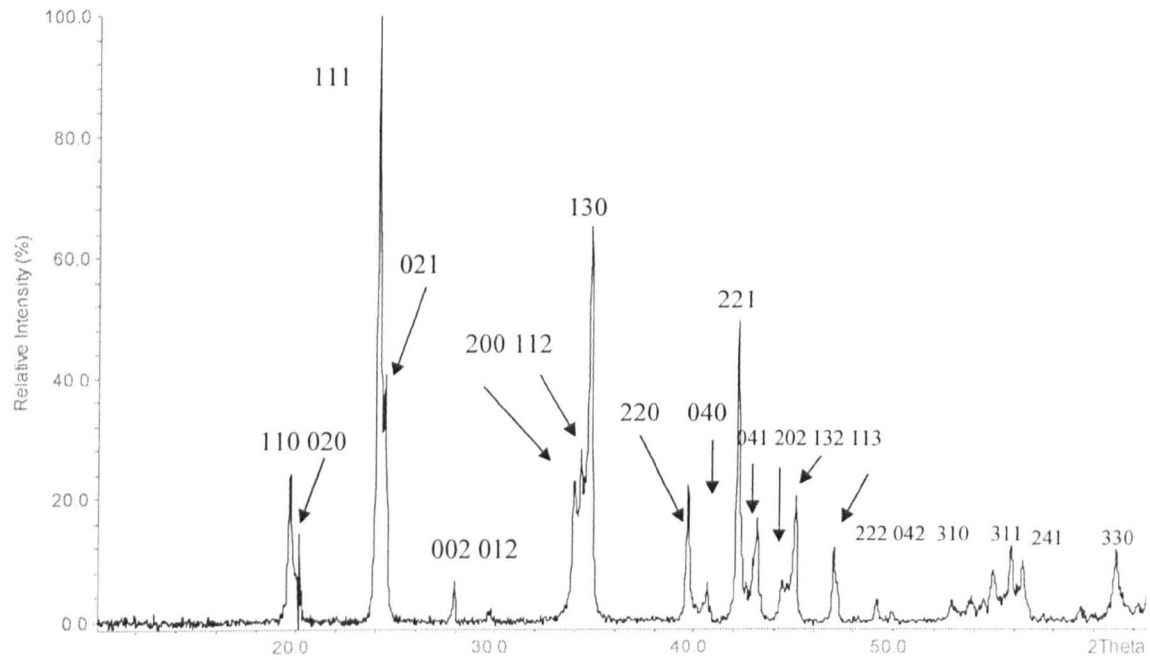


Figure 4.9(f) XRD trace of raw material BaCO_3

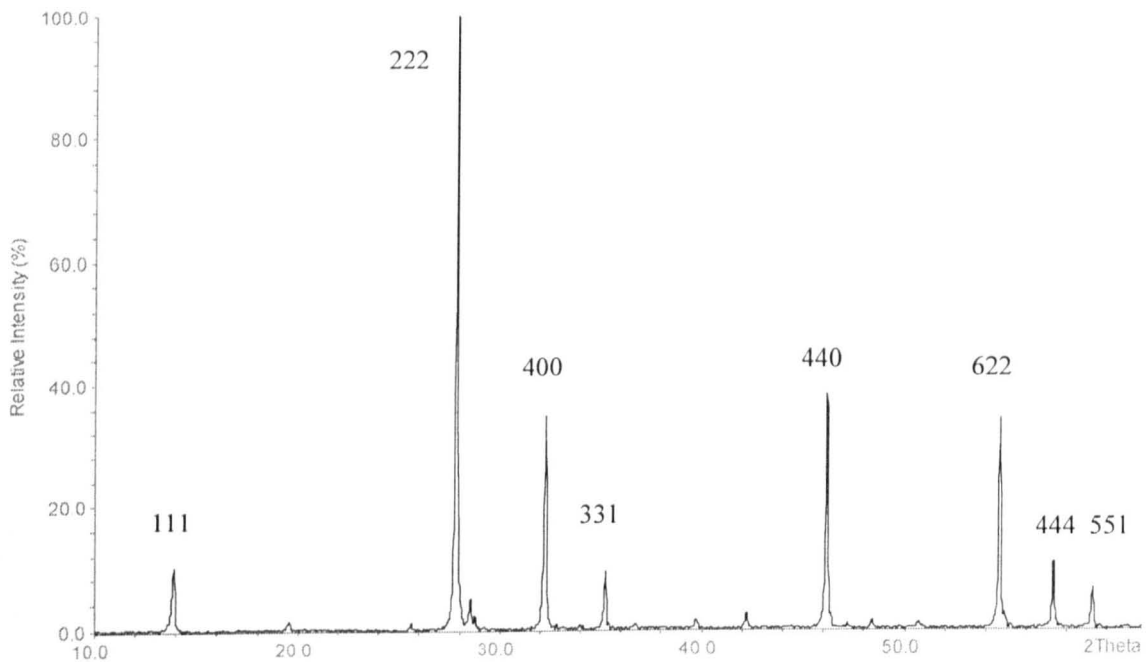


Figure 4.9(g) XRD trace of raw material Sb_2O_3

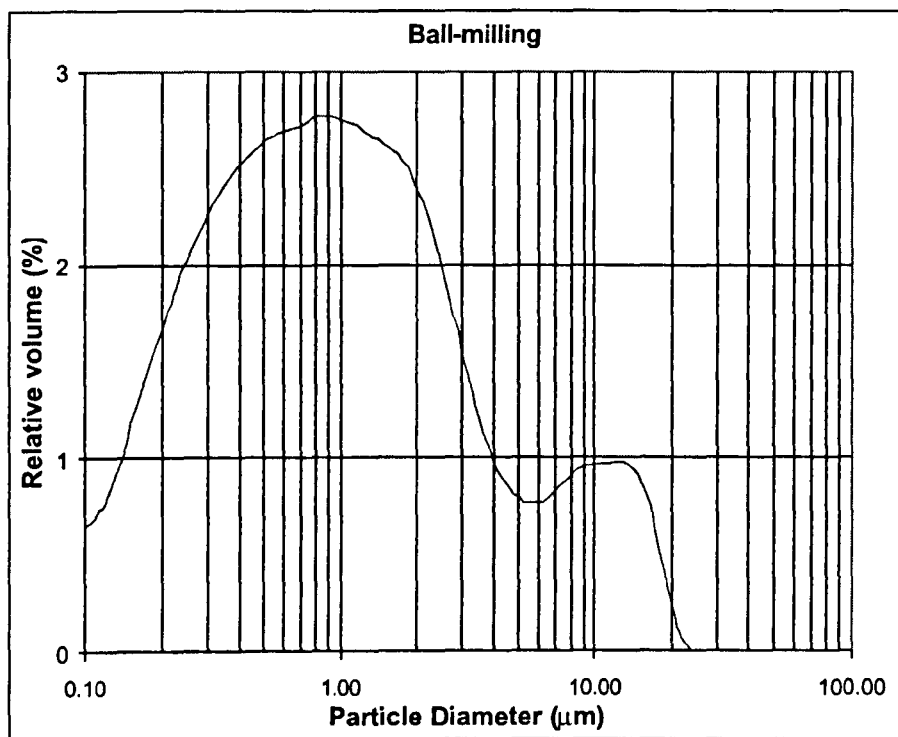
For all these raw materials, no significant second phase peaks were detected, which confirmed the purity of these raw materials within the accuracy of XRD.

4.2 Calcined Powders

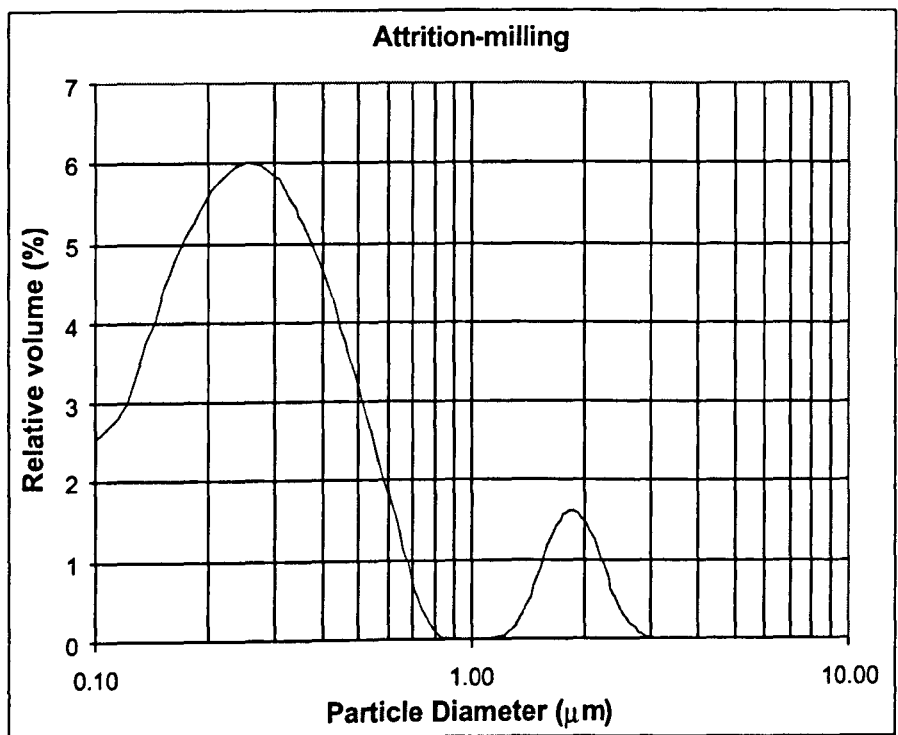
4.2.1 A Comparison between Ball-milling and Attrition-milling

Calcined powders from the same batch were treated by ball-milling for 10h and attrition-milling for 2h respectively and their particle size distributions are compared in Figure 4.10 where the abscissa is the particle size and the ordinate is the relative volume percentage of particles at this size.

Ball-milled powder has a broad particle size distribution with 90% of particles below $10 \mu m$ and the median particle size is about $1.1 \mu m$, Figure 4.10(a). In comparison, attrition-milled powder has a homogeneous particle size distribution with 90% of particles below $0.7 \mu m$. The median particle size is only about $0.3 \mu m$, Figure 4.10(b). Thus powders treated by attrition-milling are much more homogeneous and finer than those treated by ball-milling. This is further confirmed by SEM images (Figure 4.11), showing that the average size of ball-milled powder is $\sim 1.6 \pm 0.2 \mu m$ and the attrition-milled particles are typically $< 0.5 \mu m$.



(a) Ball-milled



(b) Attrition-milled

Figure 4.10 Particle size distribution of (a) ball-milled and (b) attrition-milled calcined powders

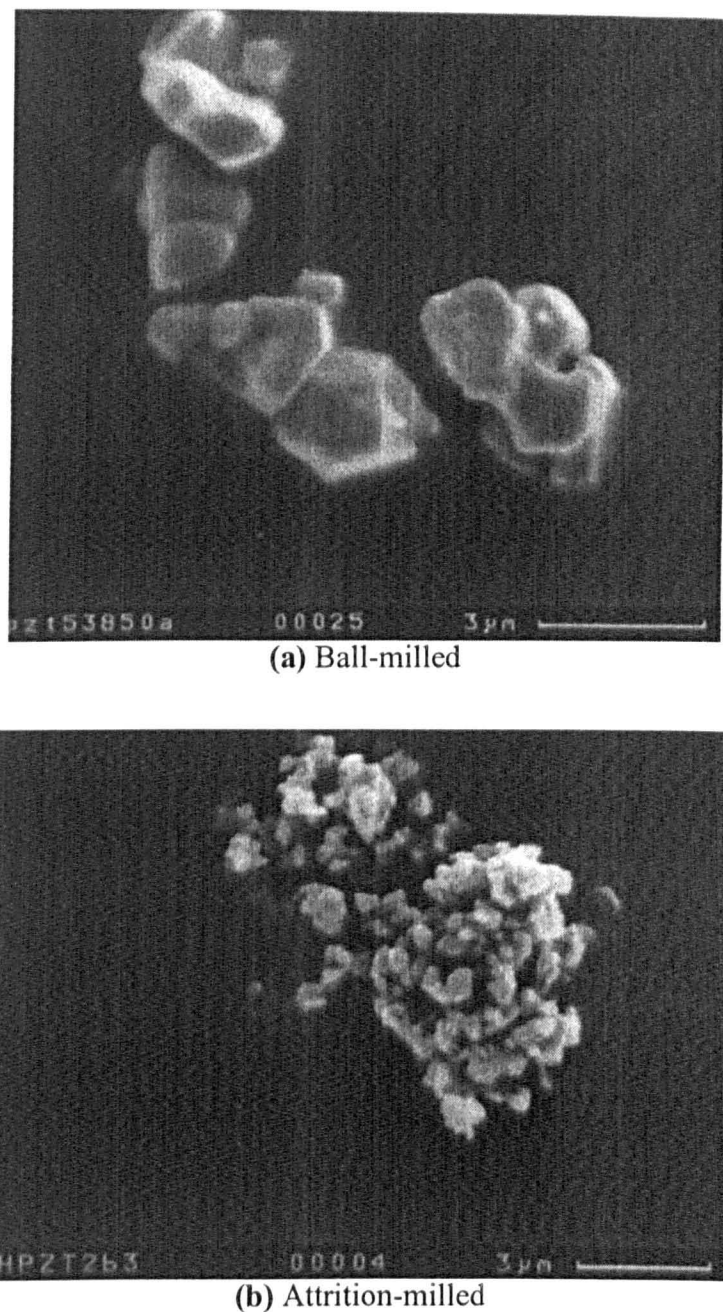


Figure 4.11 SEM photographs of (a) ball-milled and (b) attrition-milled calcined powders

The improved particle size distribution and reduced particle size of attrition-milled compared to ball-milled powders led to the use of the former milling technique throughout the course of this project. Contamination from attrition-milling may be more

severe than ball-milling, however since ZrO_2 balls are used in the attrition-milling process and ZrO_2 is a major component of the starting materials, the contamination from the milling media (ZrO_2 ball) may not influence the quality of final ceramics, although the Zr:Ti ratio in the final ceramics may be altered slightly.

4.2.2 Perovskite Phase Formation

The XRD pattern from a PNZT0/47 powder, calcined 4h at 925°C, Figure 4.12 reveals that only peaks associated with a perovskite-structured phase are present. This XRD profile agrees well with tetragonal $\text{Pb}(\text{Zr}_{0.52}\text{Ti}_{0.48})\text{O}_3$ (ICDD card 33-0784). Similar results were obtained from PSZT and PSBZT powders, which suggest that the calcination temperature of 925°C is appropriate for the majority of PZT compositions prepared in this study.

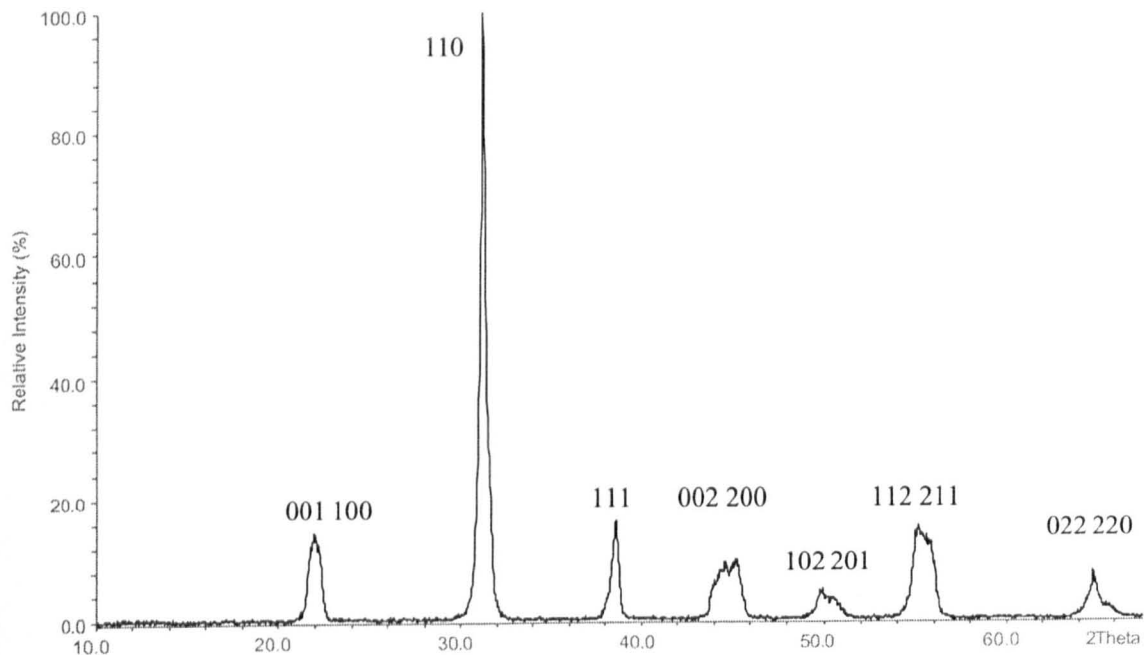


Figure 4.12 XRD pattern from a PNZT powder calcined 4h at 925°C

4.3 Dense Ceramics

Densities > 95% of theoretical are required for dielectric property measurements since porosity will influence the value of d_{33} and ϵ_r .

The major problem concerning PbO-containing samples for a desired density is their volatility on sintering. To overcome this problem, pellets were buried in 90 wt.% $\text{PbZrO}_3 + 10 \text{ wt.\% ZrO}_2$ powder and fired in closed alumina crucibles. Despite these precautions, loss of the initial PbO content was detected by comparing the weight of pellets before and after sintering, which is compensated by an addition of 2 wt.% excess PbO to the starting materials. The addition of excess PbO also enhances liquid phase sintering and promotes the densification of PZT ceramics. A further way of improving the density is to ensure that the reacting particles are submicron by employing attrition-milling as described earlier.

4.3.1 Effect of Sintering Temperature on Phase Formation

The XRD patterns of $\text{Pb}(\text{Zr}_{0.53}\text{Ti}_{0.47})\text{O}_3$ ceramics sintered 4h at different temperatures are shown in Figure 4.13. In general, perovskite tetragonal phase is formed over the whole sintering temperature range from 1000°C to 1240°C. These profiles match with $\text{Pb}(\text{Zr}_{0.52}\text{Ti}_{0.48})\text{O}_3$ (ICDD card 33-0784). No traces of TiO_2 or ZrO_2 , or second phase can be detected.

In comparison with Figures 2.6 & 2.10, which indicate that $\text{Pb}(\text{Zr}_{0.53}\text{Ti}_{0.47})\text{O}_3$ composition lies at the MPB rather than tetragonal. This discrepancy may be due to different sources of raw materials (minor impurities) used in our study. Any deviations

in ceramic processing such as sintering temperature and milling method will also alter the absolute values of Zr:Ti ratio. Therefore the same sources of raw materials were used and the ceramic processing were always kept identical throughout this thesis.

With decreasing temperature, the tetragonal phase, identified by the {002} peak splitting, diminishes and the rhombohedral phase emerges, indicated by three subpeaks on the {002} position and a shoulder on the {111} peak. There is also a strong preferred orientation along the *c* axis, represented by $I_{002}/I_{200} (>0.5)$ (the ratio of relative intensity of (002) and (200) X-ray diffraction peaks) in all samples, which is in good agreement with observations of other researchers^[86]. Small quantities of PbO are evident in ceramics fired at 1000°C.

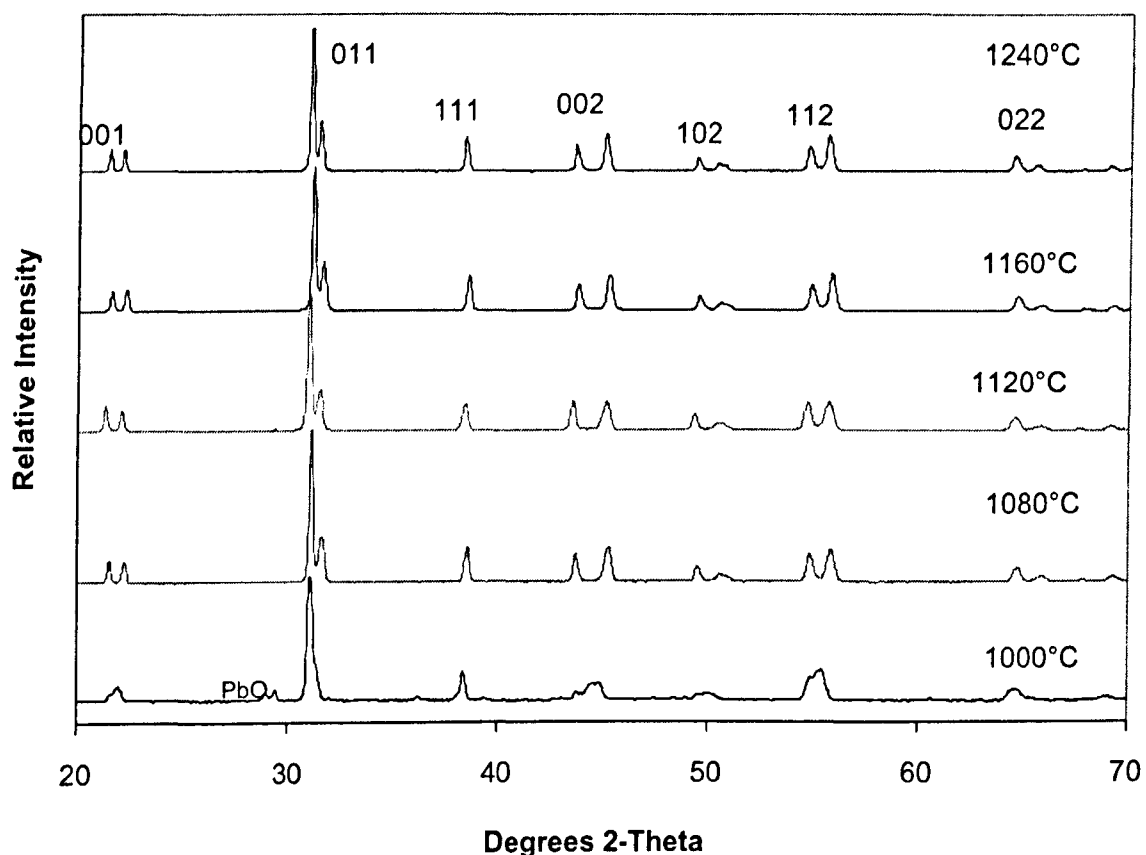


Figure 4.13 XRD traces of PNZT0/47 ceramics sintered 4h at different temperatures

Unit cell constants of the perovskite phase were calculated using the d-spacings of (200) and (002) peaks as described in Section 3.5.5. Table 4.1 lists lattice constants a , b and c of samples sintered at different temperatures. It can be seen that a , c values are slightly smaller than those published (a : 4.036, c : 4.146)^[87], however c/a is greater than that published (c/a : 1.0273)^[88]. It is also worth noting that c/a value diminishes slightly with increasing sintering temperature.

Table 4.1 a , c and c/a of PNZT0/47 sintered at different temperatures

Sintering temperature(°C)	a (Å)	c (Å)	c/a
1080	4.004	4.140	1.034
1120	4.006	4.140	1.033
1160	4.006	4.136	1.033
1230	4.012	4.134	1.030
1250	4.022	4.136	1.028

In this thesis, XRD patterns of compositions in the vicinity of MPB were unambiguously indicated a tetragonal/rhombohedral mixed phase rather than monoclinic phase mentioned in Section 2.4.2.

4.3.2 Effect of Grinding and Polishing

The XRD trace shown in Figure 4.14 was obtained from a PNZT0/47 ceramic before and after grinding and polishing. Initially the {200} reflections are split but the {111} reflections appear as a single peak, suggesting a completely tetragonal structure after firing. After grinding and polishing, the {002} reflections are still split but the {111} peaks also exhibit separation. The phase assemblage has now altered to a mixed rhombohedral and tetragonal phase, indicating that grinding and polishing is able to

ferroelastically pole the surface of PZT. Other published work^[88-89] has also reported phase transformations of this nature caused by grinding and polishing.

There are 8 equivalent $<111>$ directions and only 6 $<001>$ for PZT in a pseudocubic setting. Therefore, statistically a greater number of grains and domains are oriented such that a component of a $<111>$ rather than $<001>$ direction lies in the plane of the surface, parallel with the grinding direction. Ferroelastically poling therefore statistically favours a rhombohedral rather than tetragonal structure. Interestingly, a similar argument may be made for conventional ferroelectric poling. The results imply that a composition which is close to the MPB but tetragonal after sintering will be mixed phase after electric poling, provided the free-energy difference between the two phases is negligible.

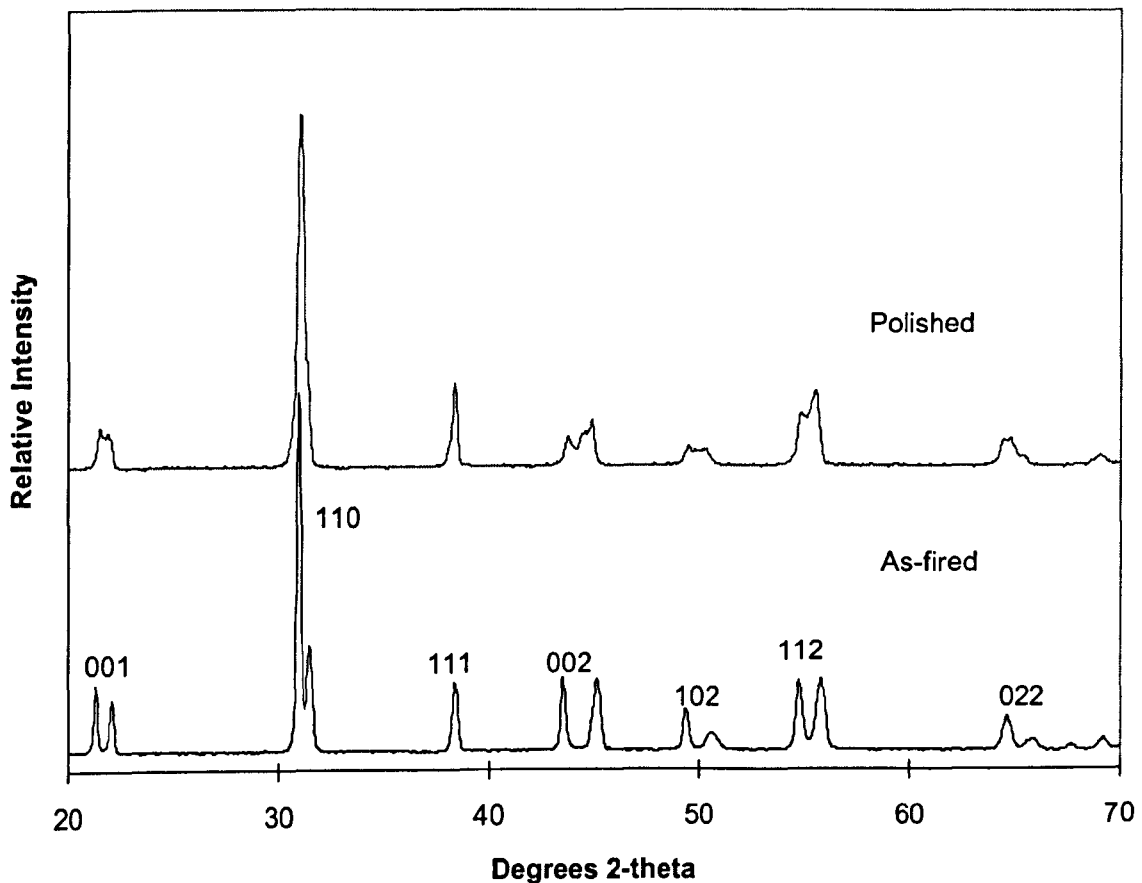


Figure 4.14 XRD profiles of PNZT0/47 ceramics sintered 4h at 1120°C

4.4 Conclusions

- The reactivity of the starting powder can be improved by attrition-milling.
- Dense PZT ceramics can be produced by adding 2 wt.% excess PbO and embedding pellets in PZ/ZrO₂ powders.
- Increasing sintering temperature promotes the tetragonal over the rhombohedral phase in PZT materials.
- Tetragonal-rhombohedral phase transformation can be induced by an applied mechanical stress.

5. EFFECTS OF B-SITE Nb⁵⁺ DOPING ON PZT

5.1 Effect of Nb⁵⁺ Content

PNZT compositions with a fixed Zr/Ti ratio (53/47) were modified with different Nb⁵⁺ contents from 0 to 7.2 mol% on the A-site, which were formulated as in Table 3.3. The values of Nb⁵⁺ content were chosen to be integer multiplications of 2.4 mol% since this concentration is used in the commercial Morgan Electroceramic composition PC5.

Ceramics were fabricated as described in Section 3.2 and all the fired samples had relative densities above 95% of theoretical. Their structures and microstructures were then investigated using XRD, SEM and TEM.

5.1.1 XRD

Figure 5.1 shows XRD traces from a series of PZT compositions in which the Zr:Ti ratio is constant (1.13 or 53:47) but the Nb⁵⁺ concentration increases. With no dopant the PZT peaks are doublets indicating a purely tetragonal phase structure. At 2.4 mol% Nb⁵⁺ on the B-site, a tetragonal phase is also formed which implies that donor dopant ions are incorporated into the perovskite PZT structure, forming a solid solution.

As the Nb⁵⁺ content increases, the degree of tetragonality decreases indicated by a gradual decrease (from ~1.03 to 1.02) in the $c:a$ ratio taken from splitting of the {002} peaks, Figure 5.2. In addition, three subpeaks exist on the {002} peak and the {111} peak develops a shoulder when 7.2 mol% Nb⁵⁺ is present on the B-site. This suggests that the ceramic now contains both rhombohedral and tetragonal phases. Nb⁵⁺ doping on the B-site of PZT therefore stabilises the rhombohedral over the tetragonal phase.

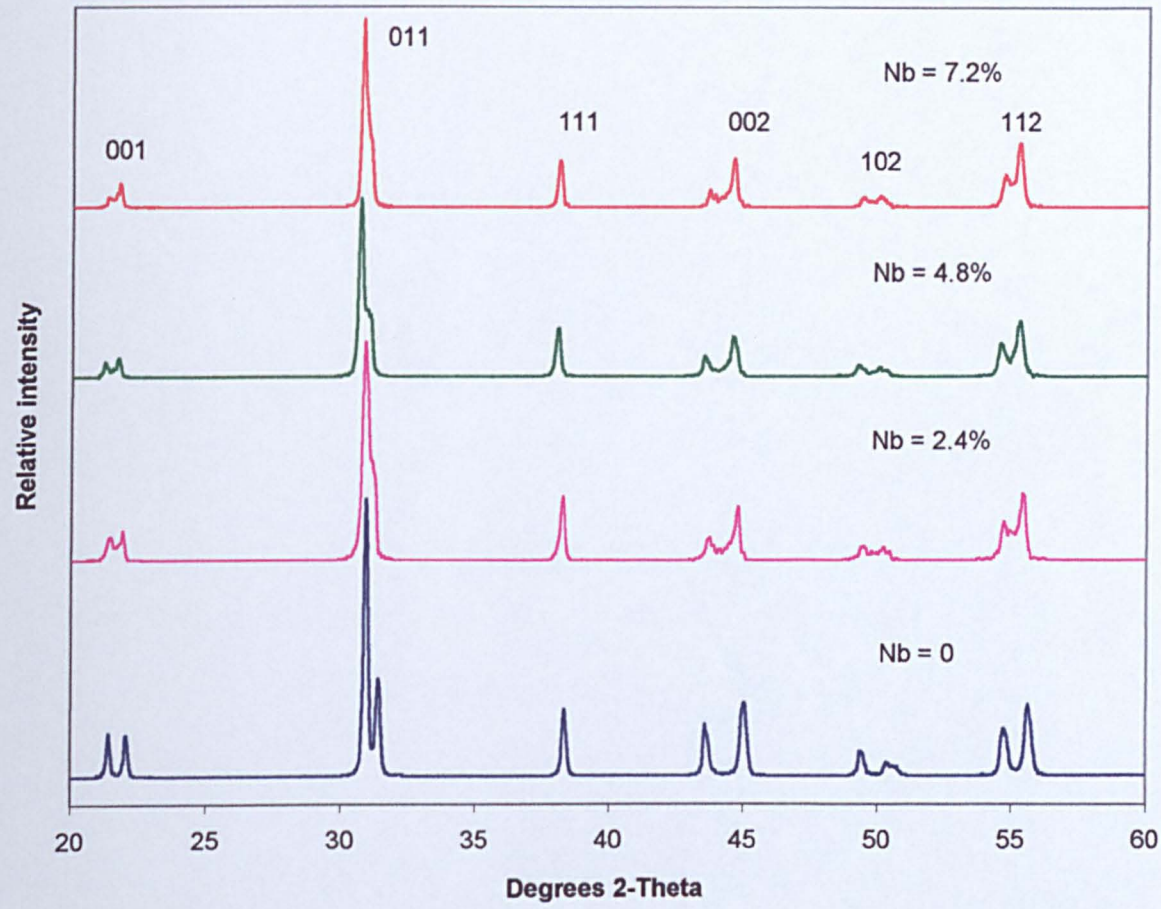


Figure 5.1 XRD traces of Nb-doped PZT ceramics (Zr:Ti ratio: 1.13), sintered 4 h at 1240°C

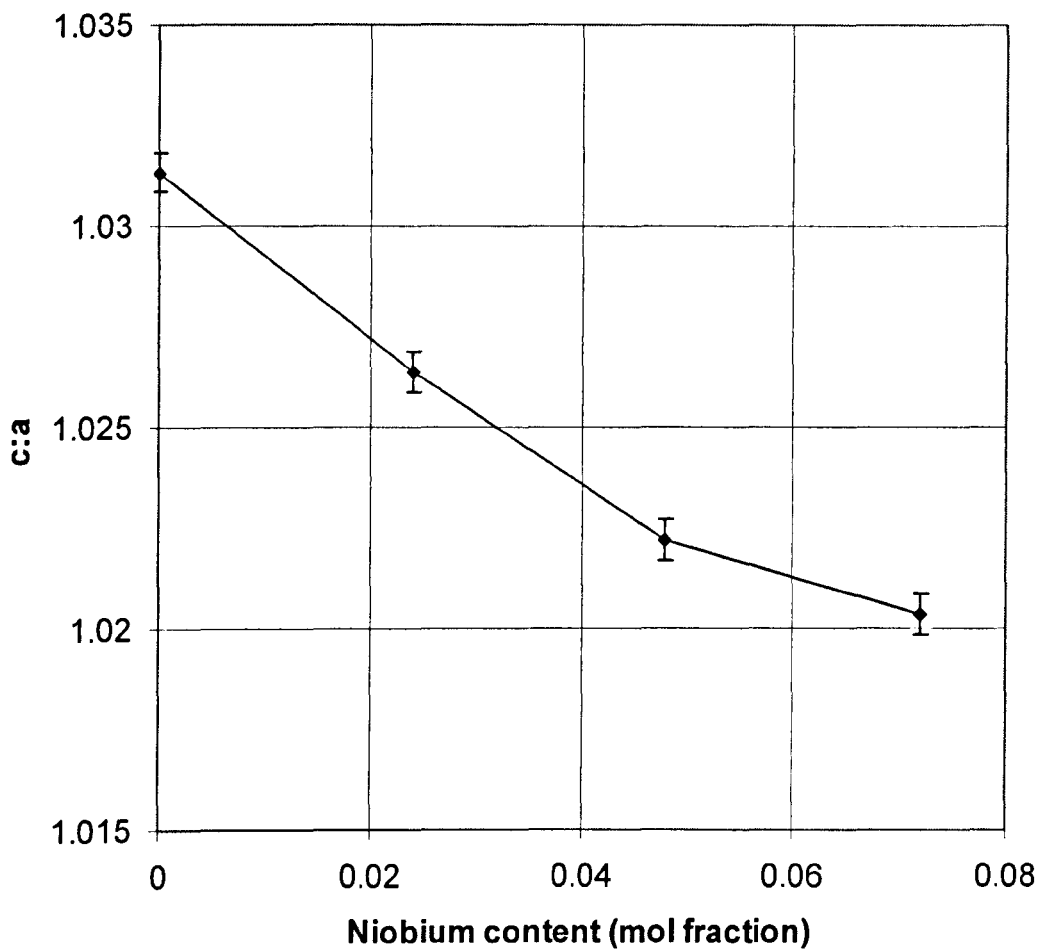


Figure 5.2 $c:a$ ratio, determined by level of splitting of the $\{002\}$ peaks, as a function of niobium content in PNZT ceramics

5.1.2 Grain Structure

Figures 5.3 (a)-(d) is a series of SEI photographs of PNZT ceramics with various Nb^{5+} contents. Their microstructures consist of randomly-orientated equiaxed grains. There is no evidence of second phase particles or grain boundary phases except in PNZT7.2/47 where small ($< 50 \text{ nm}$) precipitates are present inside some grains (arrowed in Figure 5.3(d)). Since these precipitates appear at high Nb^{5+} concentrations,

it is reasonable to suggest that they are Nb-rich, which may imply that the Nb^{5+} solubility in PZT is below 7.2 mol%.

Pereira *et al.*^[90] studied the effect of Nb^{5+} doping in PZT and demonstrated that the solubility of Nb^{5+} in PZT is around 7 mol%, which is in good agreement with our observation. However these small precipitates were not observed by TEM of identical composition ceramic samples. This may be due to the fact that these small precipitates were preferentially ion-milled during TEM sample preparation.

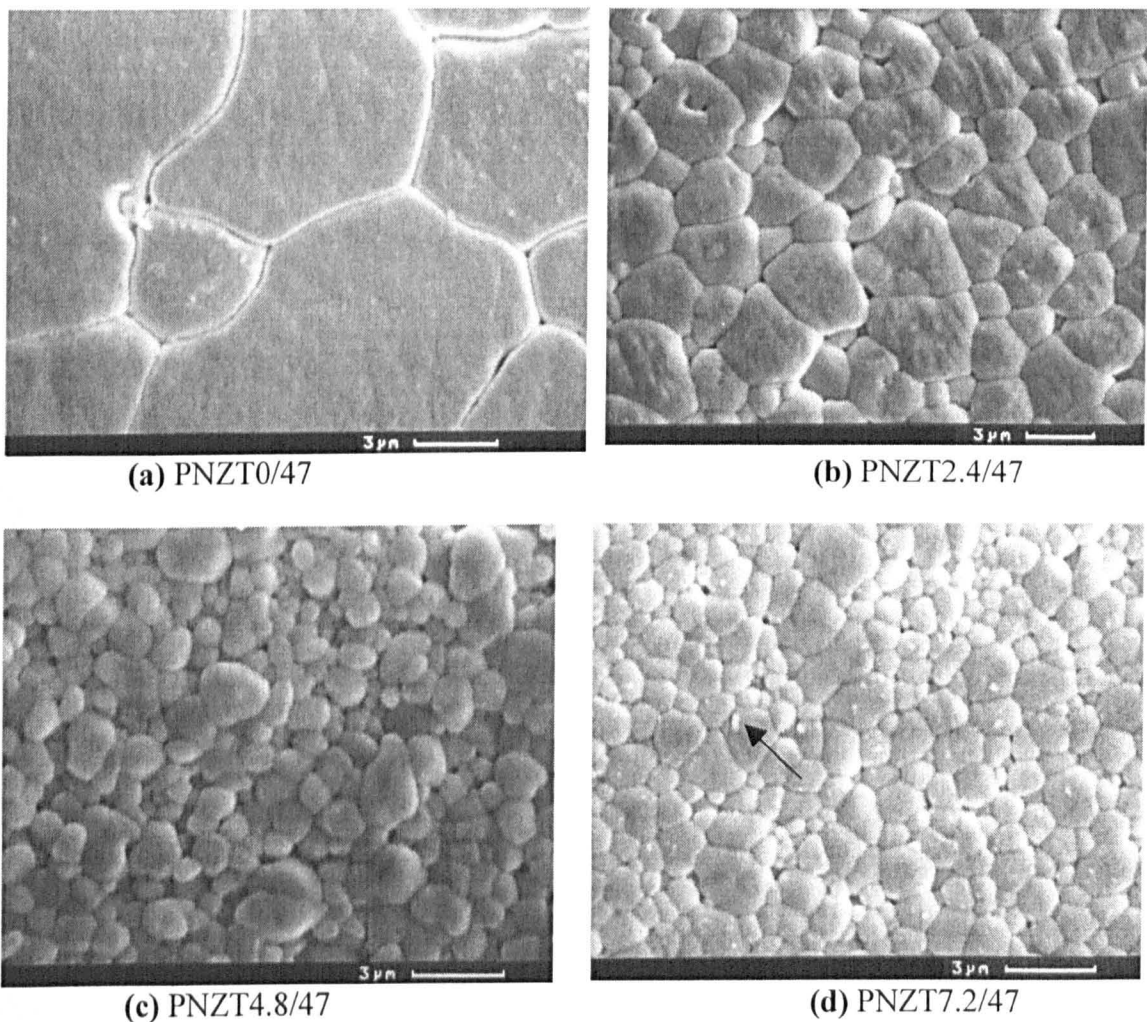


Figure 5.3 SEI's of PNZT ceramics doped with Nb^{5+} from 0 to 7.2mol%

For undoped PZT ceramic, Figure 5.3(a) the average grain size is $11 \pm 2 \mu\text{m}$, which is larger than seen in other studies^[91]. Grain size however, decreases drastically

to $2.5 \pm 0.2 \mu\text{m}$ by doping with 2.4 mol% Nb⁵⁺, Figure 5.3(b). Increasing Nb⁵⁺ concentration further decreases grain size to $1.0 \pm 0.1 \mu\text{m}$ (PNZT4.8/47, Figure 5.3(c)), but there is no significant change from this value in PNZT7.2/47, Figure 5.3(d). The decrease in grain size by Nb⁵⁺ doping has been detected previously and is possibly due to grain boundary pinning by Nb⁵⁺ on the B-site^[92]. It has been reported that the diffusion rate of Nb⁵⁺ in PZT is relatively low^[93], which results in it concentrating at grain boundaries. This may pin grain boundaries and inhibit grain growth on sintering.

5.1.3 Domain Structure

The evolution of domain structures was studied as a function of niobium content using TEM: Most images were taken at specific zone axes, which are given as insets to the images and the rest were taken in general two-beam conditions, not at specific zone axes.



Figure 5.4(a) BF-TEM image showing domain structures in PNZT0/47 ceramics

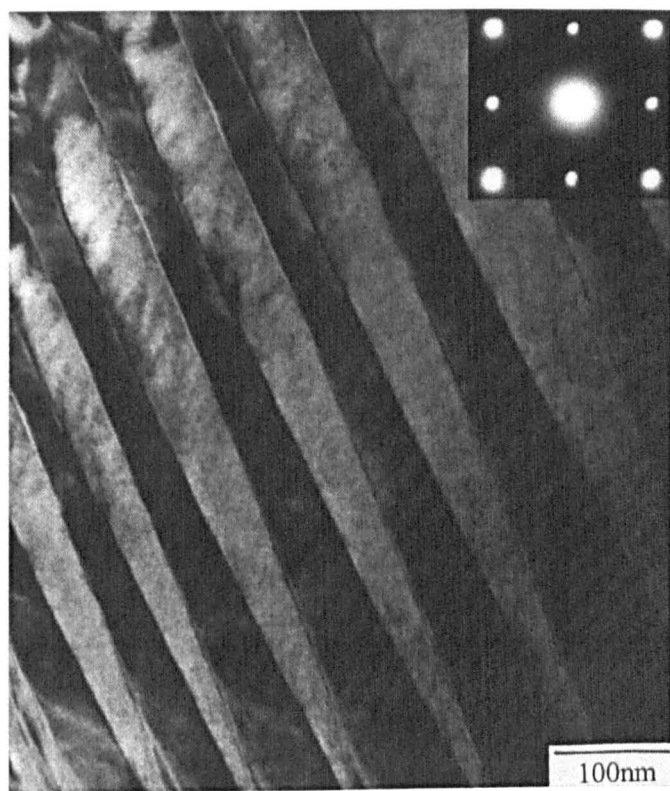


Figure 5.4(b) BF-TEM image showing 90° domains in PNZT0/47 ceramics.

Inset is the associated [100] zone axis diffraction pattern

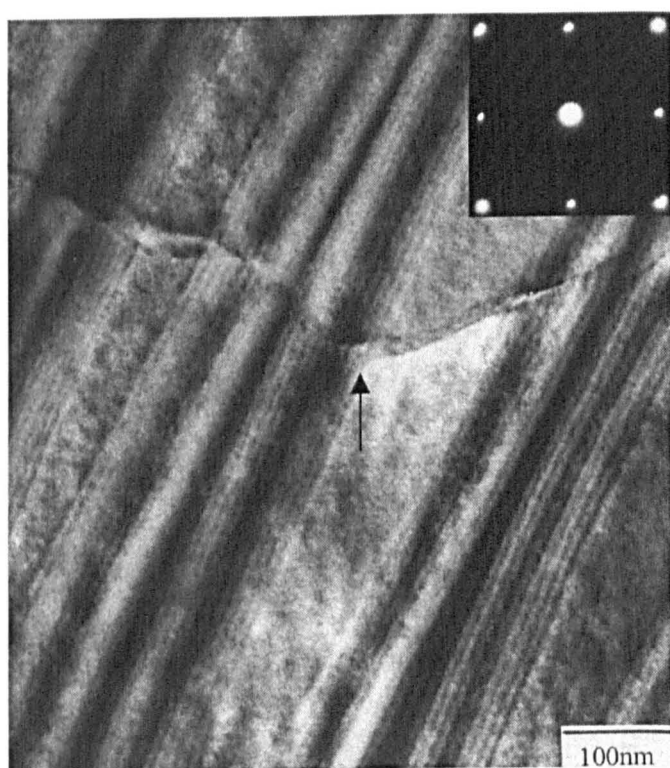


Figure 5.4(c) BF-TEM image showing an inversion domain boundary (arrowed) in PNZT0/47 ceramics. Inset is the associated [100] zone axis diffraction pattern

Figures 5.4(a-c) show several types of domain structures found in undoped PZT. The domain morphologies in some grains are complex (Figure 5.4(a)), but others have parallel, wedge-shaped configurations 50~80 nm wide, Figure 5.4(b), typical of ferroelectric-ferroelastic (non-180°) domains^[94]. Figure 5.4(c) shows a planar defect exhibiting ribbon-like contrast that runs through a series of fringes associated with wedge shaped non-180° domains. The ribbon-like morphology suggests an inversion domain boundary since such boundaries are not constrained to reside on any one set of crystallographic planes^[94]. On the other hand, non-180° domain walls are constrained by strain criteria to lie on specific sets of planes, {110} is permitted in tetragonal and {100} and {110} in rhombohedral PZT's^[95].

The nature of the domain walls varies with the crystal structure. Domain walls can only arise along planes where the conditions of mechanical compatibility are satisfied, i.e., the spontaneous deformation of two neighbouring domains fits each other^[95]. The orientations of the permissible domain walls can therefore be predicted for the various pseudo-cubic ferroelectric phases of the perovskite structure. For the tetragonal phase, an electric dipole is generated on one of the <100> directions, associated with the displacement of cations along that direction to give a tetragonal unit cell. The rotation of the polarisation vector from one domain to the next can only be 90° or 180°. The permissible uncharged walls, i.e., with a head-to-tail arrangement of the dipoles, correspond to {110} planes for the 90° domains, and any plane parallel to the polarisation vector for the 180° type. The polarisation vector for the rhombohedral phase is <111>. The rotation between neighbouring domains depends on the cell angle. For PZT, the rhombohedral angle equals 91°, and the possible types of domain can be calculated as 109°, 71° and 180°. The orientation of the permissible uncharged walls is {110} for 109°, {001} for 71° and any plane parallel to the polarisation vector for 180° domains^[95].

Grains where complex non-wedge shaped domain structures occur are less easy to explain. However, the compositions are at the MPB and frustration arising from competition between tetragonal and rhombohedral phases may be present even within a

grain. Regions of competing distortions are likely to give rise to non-trivial domain configurations.

Figure 5.5 is a BF-TEM image of PNZT2.4/47 ceramic. There is no great change in either domain morphology or size compared to PNZT0/47. Finer-scale domains ($10\text{-}20\text{ nm}$) however, can be seen in PNZT7.2/47, Figure 5.6(a). In addition, more dislocations were qualitatively observed, Figure 5.6(b). Such defects may have great influence on the elastic-dielectric and switching properties of ferroelectrics^[96] and are possibly symptomatic of increasing lattice perturbation with increasing Nb^{5+} concentration if it is assumed that the number of cation vacancies increases commensurately. Furthermore, the fine scale domains observed in PNZT7.2/47 are direct evidence that the scale length of dipole-dipole interaction is diminishing^[97].

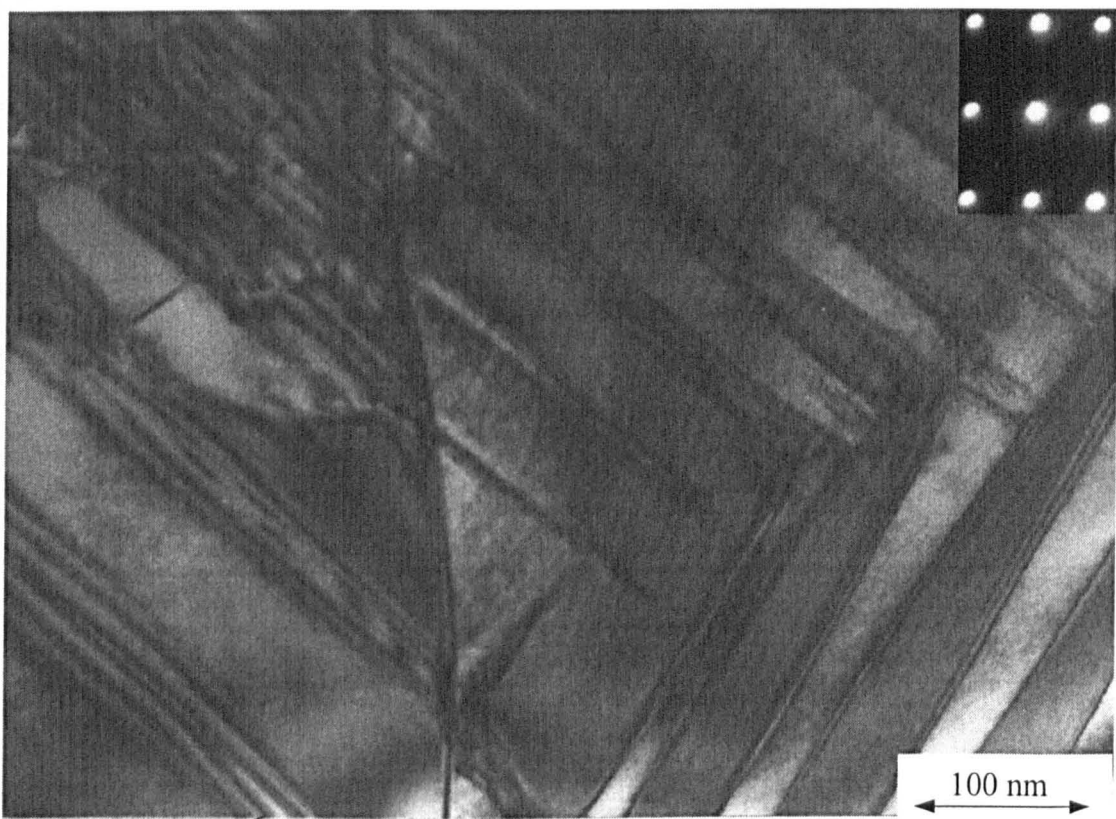


Figure 5.5 BF-TEM image showing 90° domains in PNZT2.4/47 ceramics. Inset is the associated [110] zone axis diffraction pattern

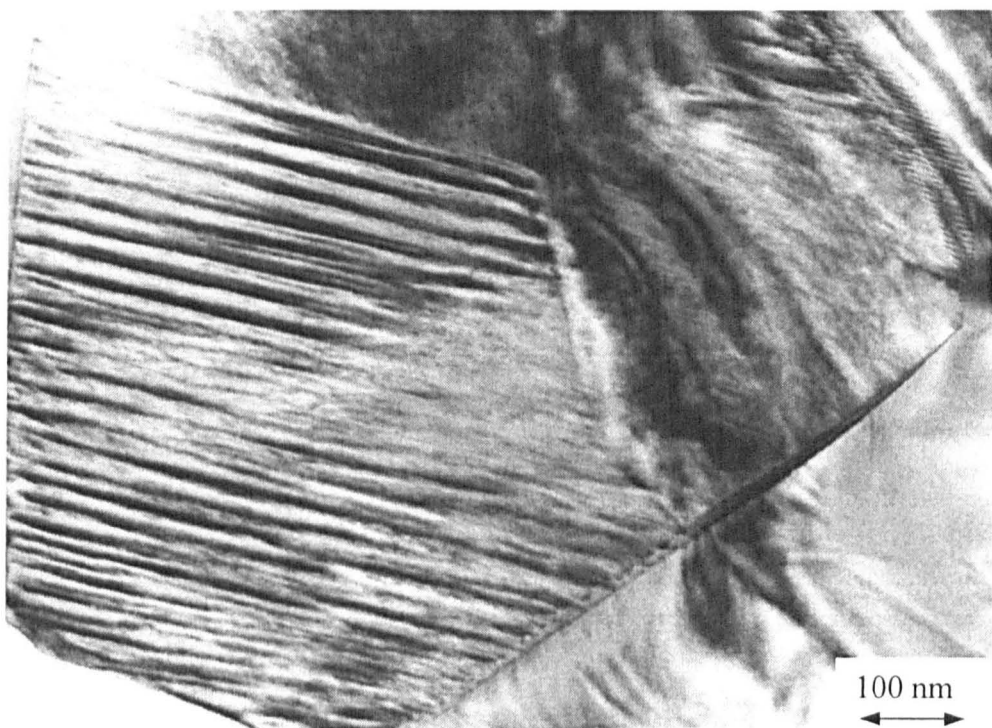


Figure 5.6(a) BF-TEM image showing fine-scale domains in PNZT7.2/47 ceramics



Figure 5.6(b) BF-TEM image showing dislocations in PNZT7.2/47 ceramics

Similar evolution from a normal micron-size domain state to a polar nanodomain state has been observed with increasing La³⁺ content in La-doped PZT. Dai *et al.*^[97] studied the solid solutions of Pb_{1-x}La_x(Zr_{1-y}Ti_y)_{1-x/4}O₃ (PLZT 100x/100(1-y)/100y) and concluded that normal micron-sized ferroelectric domain structure with strip-like patterns were dominant in undoped PZT65/35, and still apparent at a La³⁺ content of 6 *at.%*. However, a domain structure with a striation-like morphology was observed in the background. These indicated that normal and disordered ferroelectric states coexisted at room temperature for PLZT6/65/35. For PLZT7/65/35, no normal micron-sized domains were found; rather local random contrast representing a polar nanodomain (relaxor) state was observed. With further increment of the La³⁺ content to 9 *at%*, polar nanodomains became smaller^[97]. Dai *et al.*'s^[97] studies clearly indicate that the degree of long-range polar order is decreased by La³⁺ substitution, eventually preventing the formation of normal micron-sized domains and favouring the establishment of polar nanodomains (relaxor state) at high La³⁺ contents. Our observations show that long-range co-operative interaction is still present in Nb-doped PZT, though the material displays a macroscopic distortion. However, it is plausible to suggest that increasing the Nb⁵⁺ (a B-site donor dopant) concentration may result in a relaxor-ferroelectric response. This general trend may well be arrested however, by the solubility limit of Nb⁵⁺ in PZT, which appears to have been reached in the current composition, as indicated by the appearance of Nb rich precipitates in PNZT7.2/47 detected in the SEM, Figure 5.2(d).

5.1.4 Dielectric Properties

The dielectric responses of PNZT compositions as a function of temperature are shown in Figure 5.7. The paraelectric-ferroelectric (PE-FE) transformation temperature (T_C) determined from the dielectric maximum for PNZT0/47 is in good agreement with the PE-FE phase boundary in most PZT phase diagrams^[26]. The relative permittivity at T_{max} of undoped PZT ceramics is high (~29000) compared with the value (~6000) measured by Gupta *et al.*^[98].

The peak permittivity gradually decreases as Nb^{5+} concentration increases, whereas the room-temperature value of ε_r increases. More importantly, increasing Nb^{5+} content shifts the Curie point from 374°C (0 Nb^{5+}) to 308°C (7.2 mol% Nb^{5+}). This trend is linear and is illustrated in Figure 5.8. The aliovalent substitution of Nb^{5+} for Ti^{4+} or Zr^{4+} may break the coupling between ferroelectrically active BO_6 octahedra. Consequently, the micron-size domain structures typical of normal long-range ferroelectrics may be disrupted, as observed in TEM images (Figure 5.6(a-b)). This disruption may lead to changes in the switching characteristic on polarisation reversal and shifts the Curie point downward^[99]. The increase in the room temperature ε_r is commensurate with the reduction in T_C .

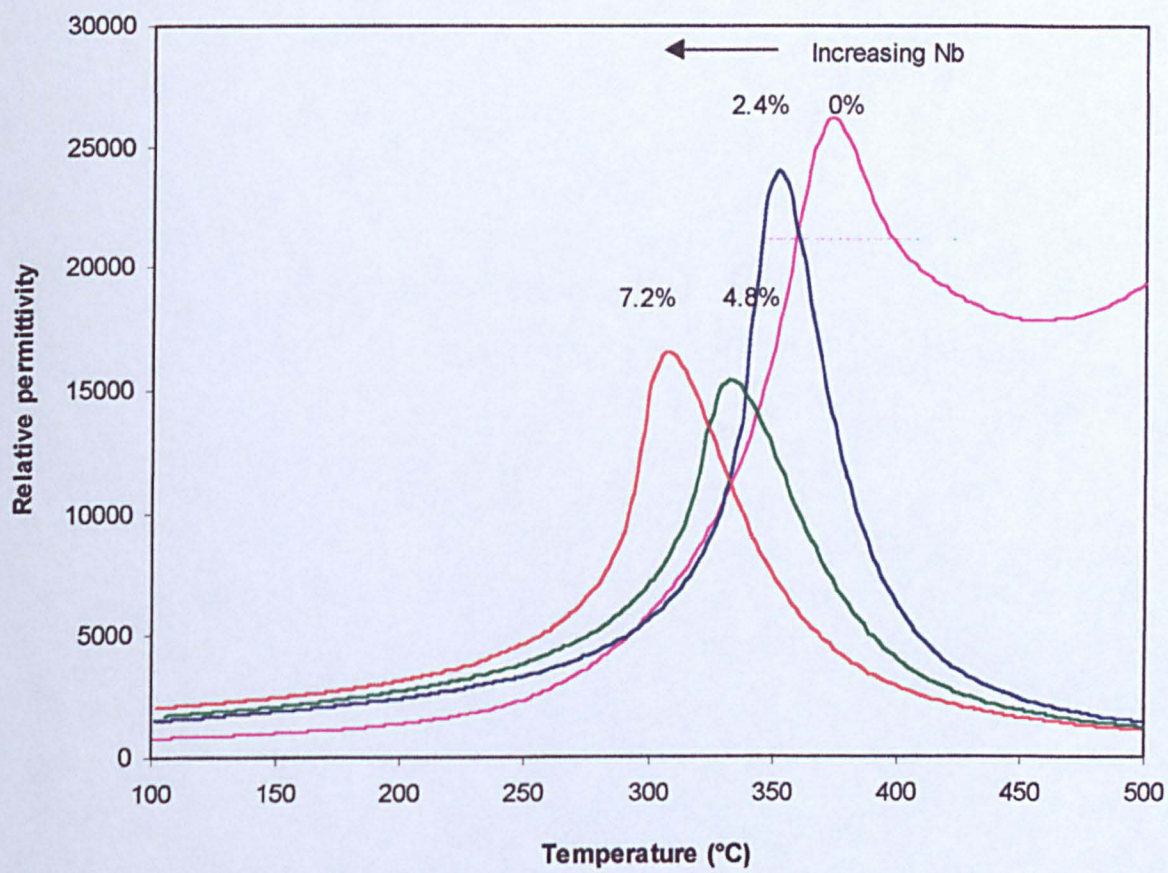


Figure 5.7 Relative permittivities of Nb-doped PZT (Zr:Ti ratio:1.13, sintered 4h at 1240°C)

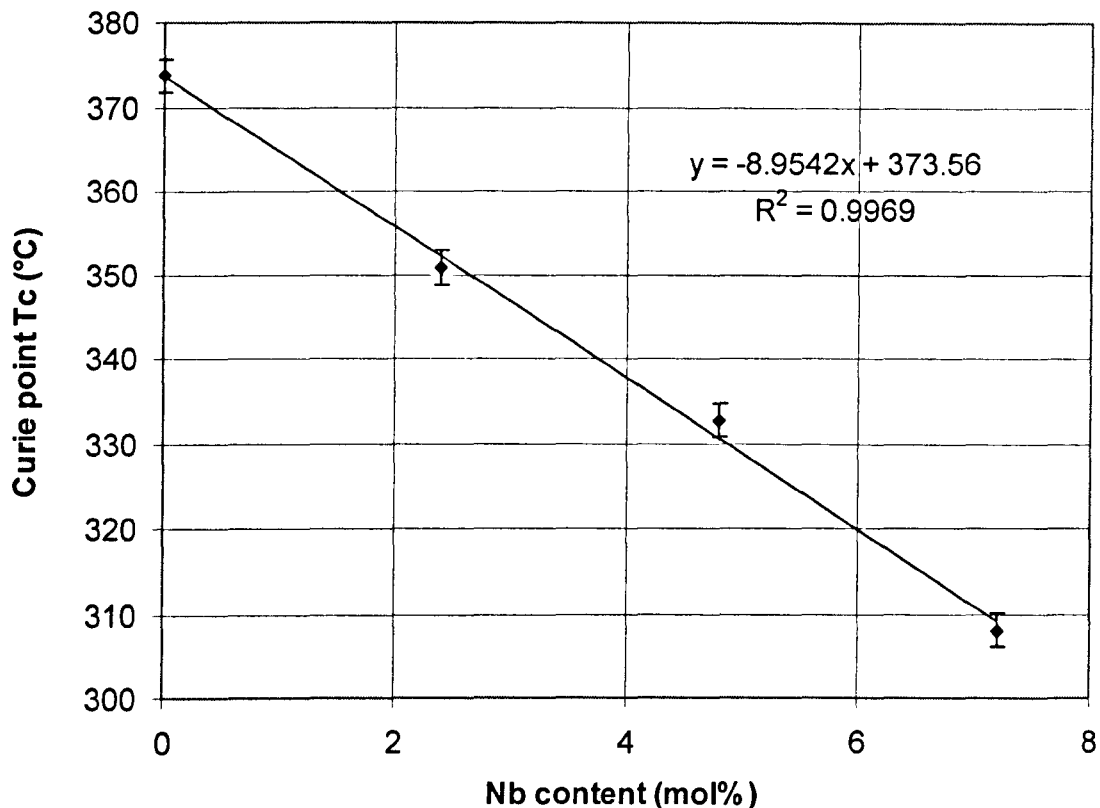


Figure 5.8 Curie point T_C as a function of Nb⁵⁺ content

5.1.5 d_{33} Piezoelectric Coefficients

Figure 5.9 is a plot of d_{33} versus Nb⁵⁺ dopant concentration in PNZT0/47. d_{33} values showed a significant increase (140 to 320 pC/N) when 2.4 mol% Nb⁵⁺ was added but subsequent increases with increasing Nb⁵⁺ content to 7.2 mol% were less dramatic.

The Nb⁵⁺ cation is a well-known higher-valency substitution on the B-site in PZT, which creates either A-site vacancies or reduces the oxygen vacancy concentration to preserve charge neutrality. It is generally believed that A-site vacancy defect complexes are relatively immobile, resulting in a random defect distribution within the domains. Consequently, defects cannot diffuse to domain boundaries, which causes breakage of the long-range polar order, leading to an enhanced ease of polarisation

switching^[1]. On the contrary, the defect dipoles associated with oxygen vacancies are relatively mobile, and orient in the field of the domain, slowly stabilising the existing variant over other possible domain states^[100]. Thus the reduction in the concentration of oxygen vacancies leads to a reduction in the concentration of domain-stabilising defect dipoles, resulting in an increased d_{33} .

In addition, when the Zr:Ti ratio is fixed, increasing Nb^{5+} doping on the B-site shifts the phase closer to the MPB as ascertained by Figure 5.1, which may result in an increased d_{33} as described in Section 2.4.3.

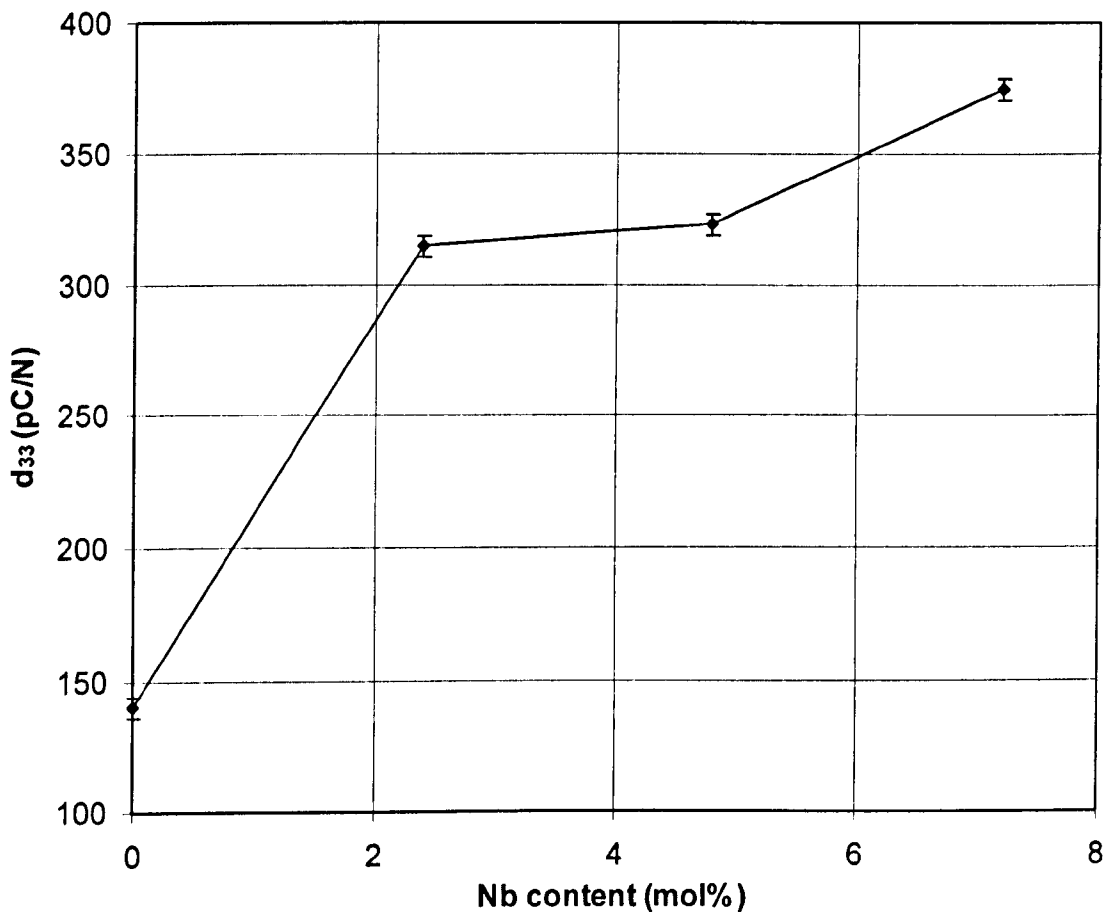


Figure 5.9 d_{33} as a function of Nb^{5+} doping in PZT (Zr:Ti ratio:1.13)

5.2 Effect of Zr:Ti ratio in 2.4 mol% Nb-doped PZT

From section 5.1, it is evident that the substitution of 2.4 mol% Nb⁵⁺ onto the B-site of PZT initially doubles d_{33} but, as the Nb⁵⁺ concentration rises, further increases are less dramatic. The Zr:Ti ratio in the previous section was fixed at 1.13, a nominal value equivalent to 53:47 and considered as the MPB for undoped ceramics. The addition of up to 7.2 mol% Nb⁵⁺ stabilises the rhombohedral phase, effectively moving the composition away from the MPB. This would suggest that, to optimise d_{33} , the Zr:Ti ratio must be adjusted to compensate for the rhombohedral shift caused by Nb⁵⁺ doping. However, the XRD studies (Figures 5.1 & 5.2) show that with 2.4 mol% Nb⁵⁺ on the B-site, the macroscopic symmetry remains tetragonal with a diminished $c:a$ ratio. Therefore, to investigate this conflicting data and to study the effect of the MPB on d_{33} , PNZT compositions with a fixed Nb⁵⁺ content (2.4 mol%) were prepared with varying Zr:Ti ratios as described in Table 3.4. All the fired samples had relative densities above 95% of theoretical, and their structures and microstructures were examined using XRD, SEM and TEM.

5.2.1 XRD

As the Zr:Ti ratio increases from 1.0 to 1.9, XRD patterns indicate a structural change from tetragonal to rhombohedral, Figure 5.10. Compositions with Zr:Ti ratio <1.2 (53:47), exhibit {002} peak splitting, indicating that they are tetragonal. Compositions where the Zr:Ti ratio is >1.2 show evidence of rhombohedral symmetry by {111} peak splitting. At a Zr:Ti ratio = 1.2, both peak splittings of {111} and {002} are apparent, indicating the coexistence of rhombohedral and tetragonal phases. A Zr:Ti

ratio of 1.2 is therefore considered to be the morphotropic phase boundary of 2.4 mol% Nb-doped PZT ceramics, for the as-sintered condition.

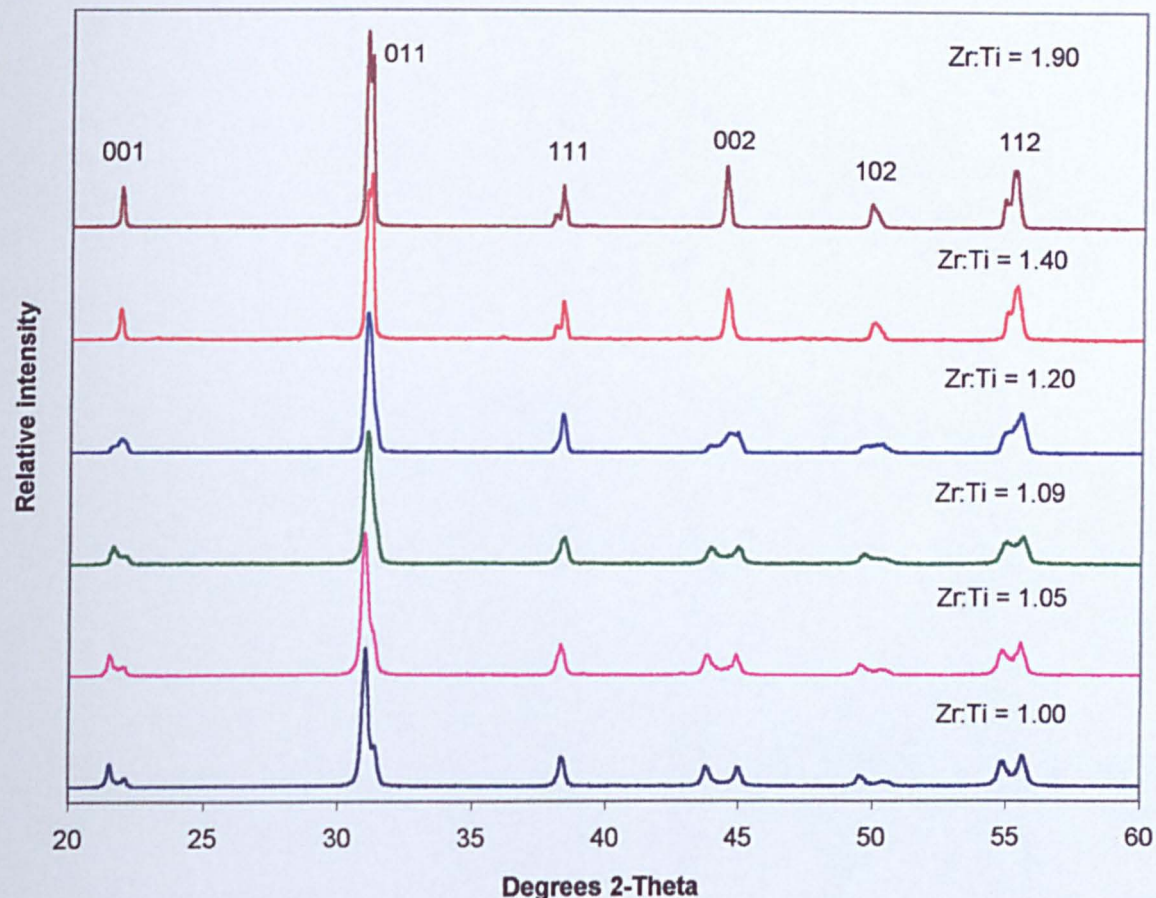


Figure 5.10 XRD traces of 2.4 mol% Nb-doped PZT with varying Zr:Ti ratio, sintered 4h at 1240°C

5.2.2 Grain Structure

Figures 5.11 (a)-(d) are SEI images from PNZT2.4 ceramics sintered 4h at 1140°C, in which the Zr:Ti ratio has been varied across the MPB. The abbreviation is PNZT $100y/100x$ according to the formula $\text{Pb}(\text{Zr}_{1-x}\text{Ti}_x)_{1-y}\text{Nb}_y\text{O}_3$ where y represents Nb^{5+} content and x represents Ti^{4+} amount on the B-site as stated in Table 3.4.

No second phase was observed and all grains were equiaxed. The mean grain size of PNZT2.4/47 ceramics (Zr:Ti ratio:1.09, tetragonal phase as ascertained by XRD, Figure 5.10) is $2.6 \pm 0.2 \mu\text{m}$ and that of PNZT2.4/44 ceramics (Zr:Ti ratio:1.2, MPB as ascertained by XRD, Figure 5.10) is $2.2 \pm 0.2 \mu\text{m}$. The mean grain size of PNZT2.4/41 ceramics (Zr:Ti ratio:1.4, rhombohedral phase as ascertained by XRD, Figure 5.10) is $2.6 \pm 0.2 \mu\text{m}$ and that of PNZT2.4/34 ceramics (Zr:Ti ratio:1.9, rhombohedral phase as ascertained by XRD, Figure 5.10) is $3.8 \pm 0.2 \mu\text{m}$. It seems the MPB composition has the smallest grain size, and the grain size increases when the phase is moved toward the rhombohedral side, but this effect is not dramatic. No reports of this behaviour have appeared in the literature.

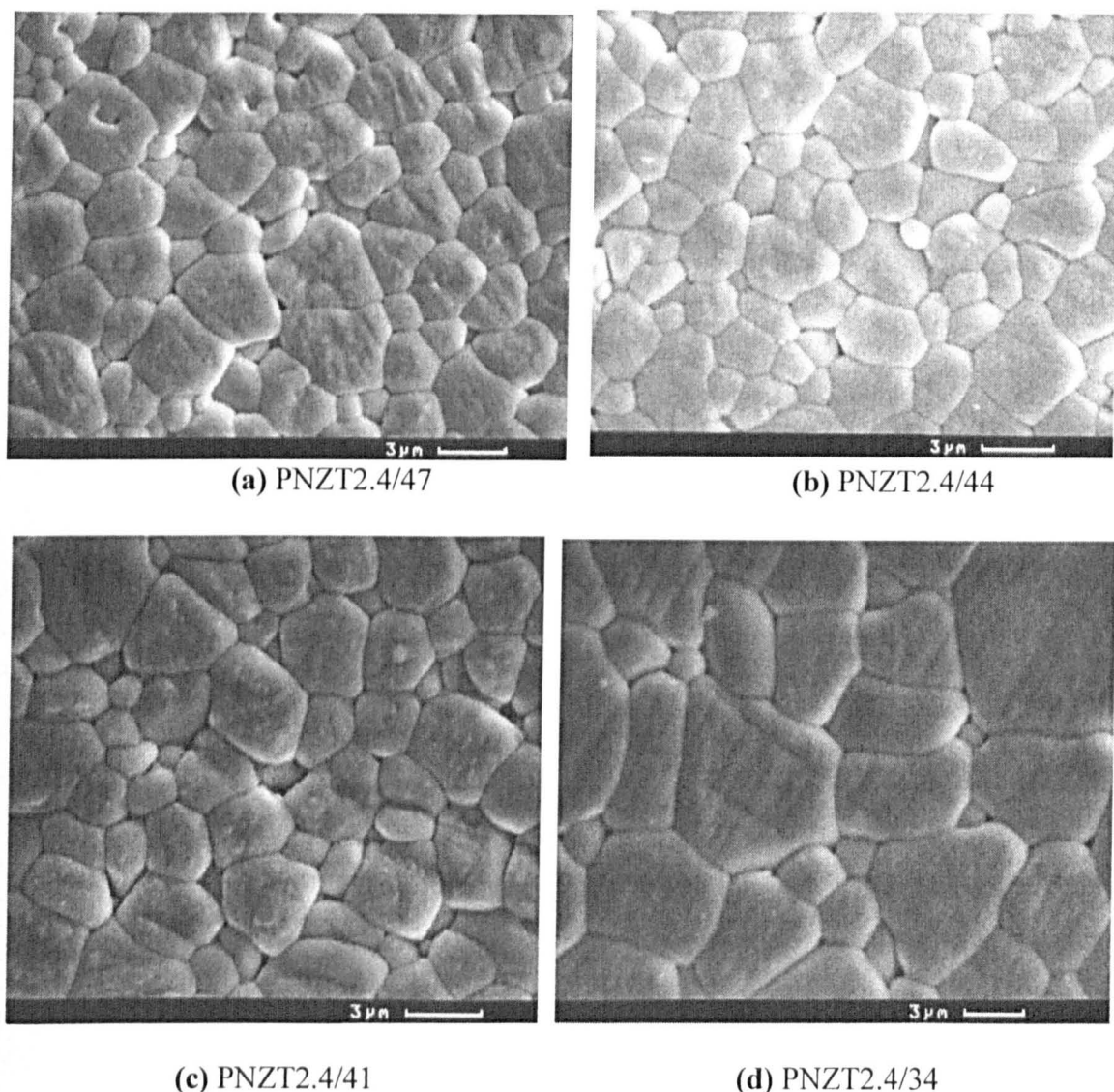


Figure 5.11 SEI SEM pictures of 2.4mol% Nb-doped PZT with various Zr:Ti ratios

5.2.3 Domain Structure

Domain size was not influenced by changes in the Zr:Ti ratio, but domain morphology varied with respect to Zr:Ti ratio.

Wedge-shaped domains were observed in tetragonal phase grains as shown in Figure 5.5. However, zig-zag domains, absent in tetragonal phase grains, were commonly observed in rhombohedral phase grains, Figure 5.12.

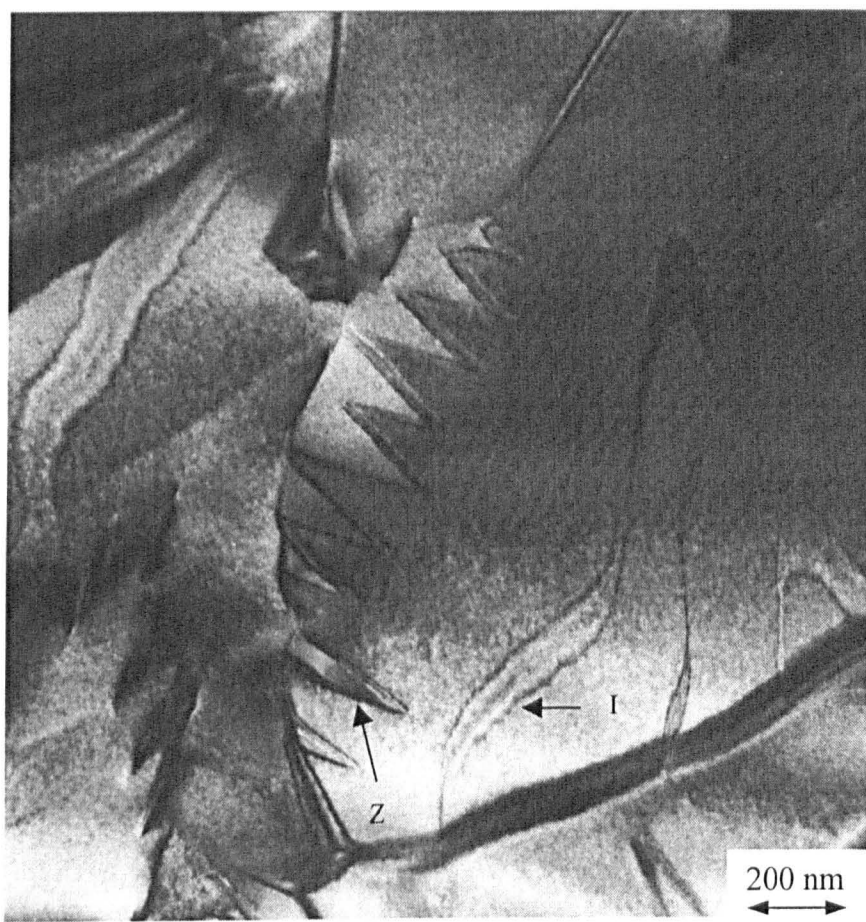


Figure 5.12 BF TEM image showing zig-zag (Z) domains and inversion domain boundaries (I) in rhombohedral PNZT2.4/34 ceramics

It has been suggested^[95] that local random oxygen octahedral rotations exist in the rhombohedral phase, which produce strains and disrupt the long-range polar order. As the domain walls are created to minimise the elastic and electric stresses, these variations in stress can affect the positions of the domain walls and probably cause the observed zig-zag domains, which deviate from the parallel-walled domains in the tetragonal phase. This effect is enhanced by the lower $c:a$ ratio associated with rhombohedral ($c:a=1$) rather than tetragonal ($c:a=1.03$) ferroelectrics. Since it is spontaneous strain that is accommodated at a domain wall, phases with larger distortions (i.e. tetragonal) will have higher domain energy. Any movement of the domain wall away from its natural crystallographic habit plane is therefore more difficult in the tetragonal grains.

5.2.4 Dielectric Properties

Figure 5.13 is a plot of relative permittivity versus temperature for PZNT2.4 compositions in which Zr:Ti ratio has been varied. The Curie temperature diminished from 360 to 320°C as the Zr:Ti ratio increased from 1 to 1.9. Similar to undoped PZT, increasing Zr⁴⁺ level on the B-site reduces the T_C as the phase transition temperature for PbTiO₃ is ~480°C and that of PbZrO₃ is only ~230°C.

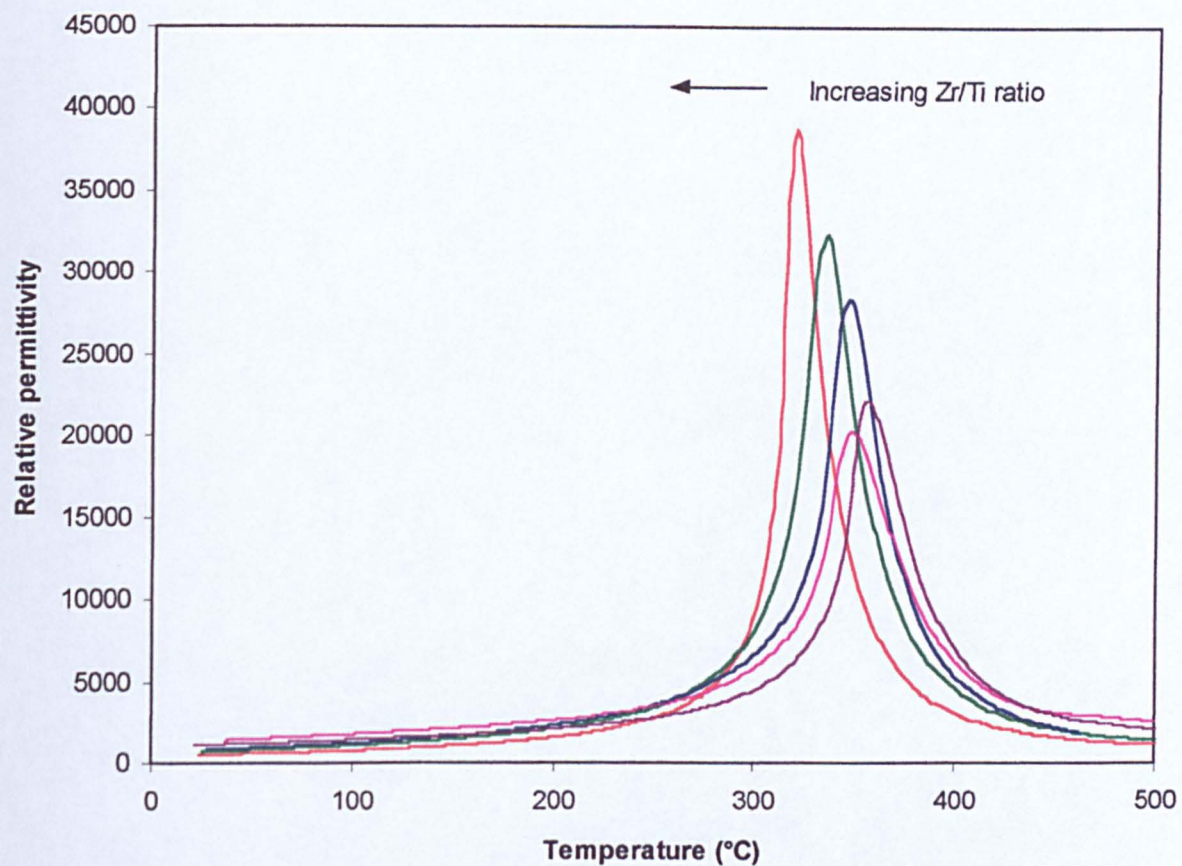


Figure 5.13 Relative permittivities of 2.4 mol% Nb-doped PZT as a function of Zr:Ti ratio (sintered 4h at 1240°C)

5.2.5 d_{33} Piezoelectric Coefficients

Figure 5.14 is plot of d_{33} vs Zr:Ti ratio for PNZT2.4 ceramics. The d_{33} value rises as Zr:Ti ratio increases from 1 to 1.09 after which it decreases dramatically. The maximum d_{33} value (420 pC/N) was obtained however, not at Zr:Ti ratio 1.2, the nominal MPB, but at 1.09, a composition which is macroscopically tetragonal, as ascertained by XRD, Figure 5.10.

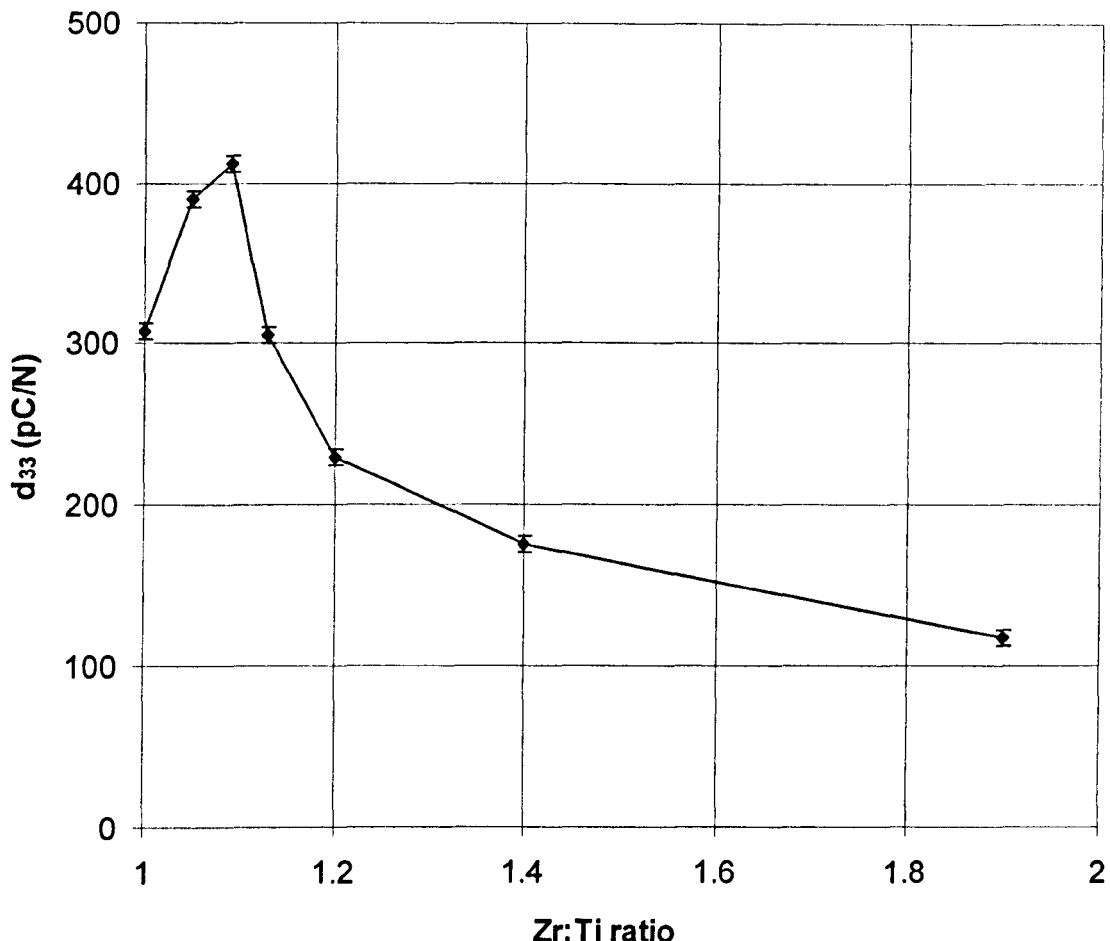


Figure 5.14 d_{33} as a function of Zr:Ti ratio in 2.4 mol% Nb-doped PZT

It has been widely accepted that the coexistence of tetragonal and rhombohedral phases in MPB composition gives a total of fourteen possible pseudocubic polarisation directions, which enable optimised crystallographic orientations to be established from grain to grain during poling. The material which is closest to the MPB therefore should have the highest d_{33} values. However, the present studies show that in PNZT ceramics, the d_{33} is not optimised at the precise MPB composition, but in the tetragonal phase close to the MPB.

5.2.6 Hysteresis Loops

Figure 5.15 shows hysteresis loops from four PNZT2.4 ceramics. The coercive field first decreases with decreasing Zr:Ti ratio when the phase changes from tetragonal (Zr:Ti ratio = 1.0) to the MPB (Zr:Ti ratio = 1.2, as determined by XRD.). The lowest coercive field (~ 1.0 kV/m) occurs for the nominal MPB composition (Zr:Ti ratio = 1.20).

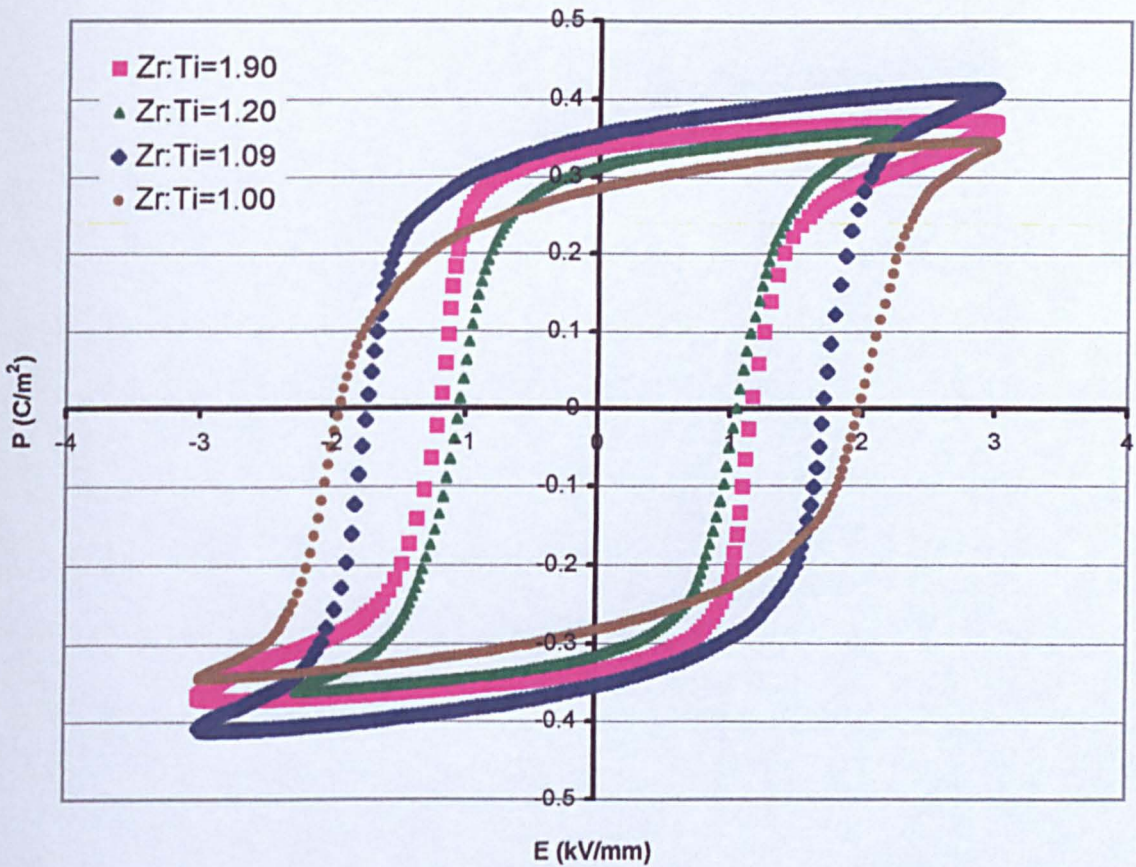


Figure 5.15 Hysteresis loop as a function of Zr:Ti ratio in 2.4 mol% Nb-doped PZT

With increasing Zr:Ti ratio, as the phase is moved toward the rhombohedral side, the coercive field increases. In principle, domains are more easily switched at the MPB since rhombohedral and tetragonal phases have the same free energy.

The largest remnant polarisation ($\sim 0.37 \text{ C/m}^2$) lies at a slightly tetragonal phase composition (Zr:Ti ratio = 1.09), which corresponds to the highest d_{33} value (420 pC/N). Compared to rhombohedral, the tetragonal phase possesses a higher $c:a$ ratio and therefore has a greater fraction of ferroelastic domain switching, which results in a higher remnant polarisation.

5.3 Conclusions

- Nb^{5+} additions to PZT promote the rhombohedral over the tetragonal phase, reduce grain size, lower T_C , and enhance d_{33} .
- Domain walls become finer ($100 - 20 \text{ nm}$) with increasing Nb^{5+} content, indicating a reduction in the correlation length of dipole-dipole interaction.
- Increasing Zr:Ti ratio changes the phase from tetragonal to rhombohedral. This strongly affects d_{33} , which is optimised ($\sim 420 \text{ pC/N}$) in the tetragonal phase close to the MPB.
- The lowest E_C ($\sim 1.05 \text{ kV/mm}$) was found for ceramics at the MPB with a Zr:Ti ratio of 1.20. But the highest remnant polarisation occurs for a slightly tetragonal phase with a Zr:Ti ratio of 1.09, which corresponds to the highest d_{33} values for this composition.

- Wedge-shaped non-180° and ribbon-like 180° inversion domains are commonly seen in tetragonal and rhombohedral phases. Zig-zag domains are completely absent in the tetragonal but often observed in the rhombohedral phase grains.

6. EFFECTS OF A-SITE Sr^{2+} SUBSTITUTION ON PZT

In the previous chapter, the effect of Nb^{5+} donor doping (B-site) on structure and piezoelectric properties was discussed and the d_{33} was optimised ($\sim 420 \text{ pC/N}$) in the tetragonal phase close to the MPB in 2.4 mol% Nb-doped PZT ceramics.

To further increase d_{33} , it is postulated that the phase transition temperature may be reduced by substituting, e.g., Sr^{2+} for Pb^{2+} on the A-site while retaining a MPB composition. Therefore, using an optimised PNZT2.4/47 composition (Nb^{5+} doping is fixed at 2.4 mol%, Zr:Ti ratio = 1.094) as a starting point, a series of PSZT ceramics were prepared with various Sr^{2+} doping concentrations on the A-site, which were formulated according to Table 3.5. All the fired samples have relative densities $> 95\%$ of theoretical. Their structures and microstructures were examined using XRD, SEM and TEM.

6.1 Effect of Sr^{2+} Content

6.1.1 Structure and Microstructure

XRD patterns, Figure 6.1 reveal that PSZT ceramics containing $\leq 16 \text{ mol\% Sr}^{2+}$ on the A-site are tetragonal whereas those containing 32 mol% Sr^{2+} are pseudocubic. As the Sr^{2+} concentration increases, the shoulder on the {111} peak disappears and tetragonal peaks become more intense, indicating that substitution of Sr^{2+} for Pb^{2+} on

the A-site promotes the tetragonal at the expense of the rhombohedral phase. Further data is required before an explanation may be offered for the pseudocubic pattern obtained for 32 mol% Sr.

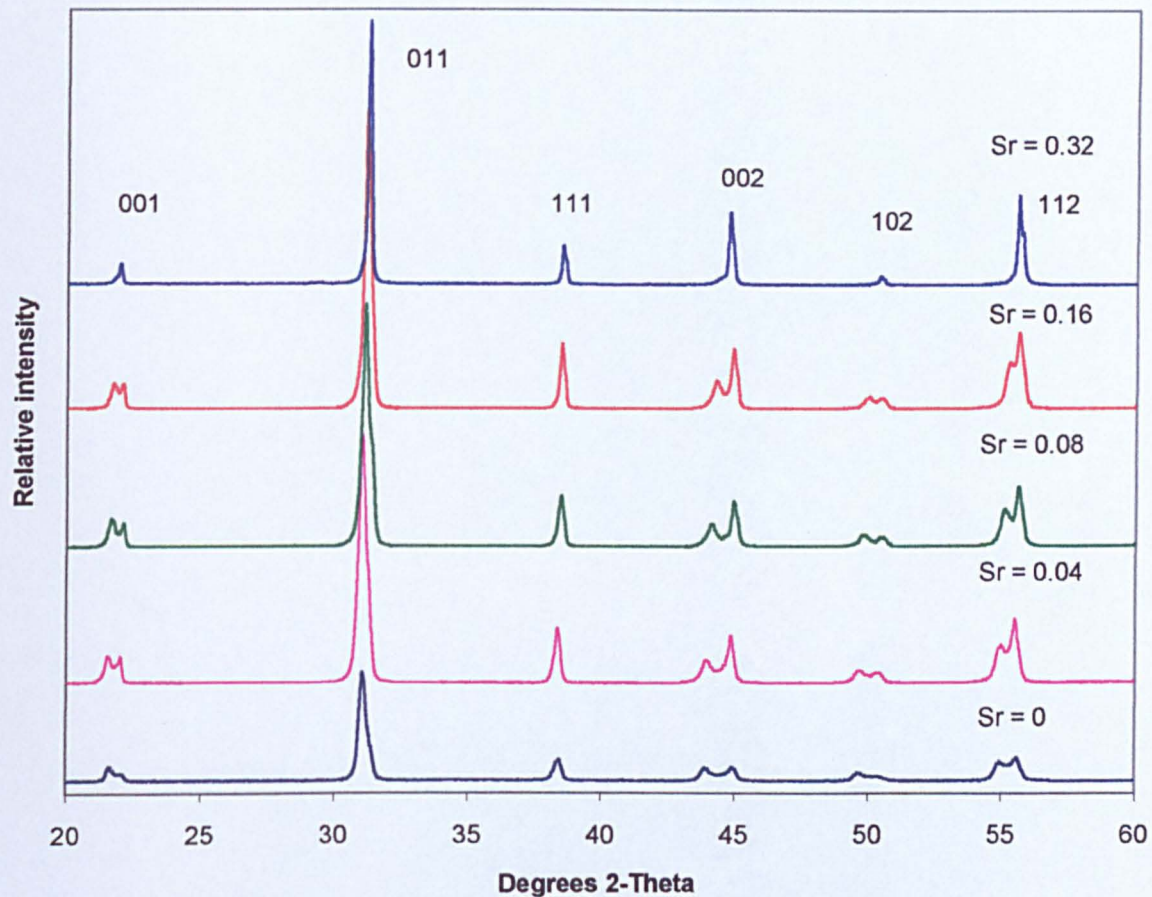
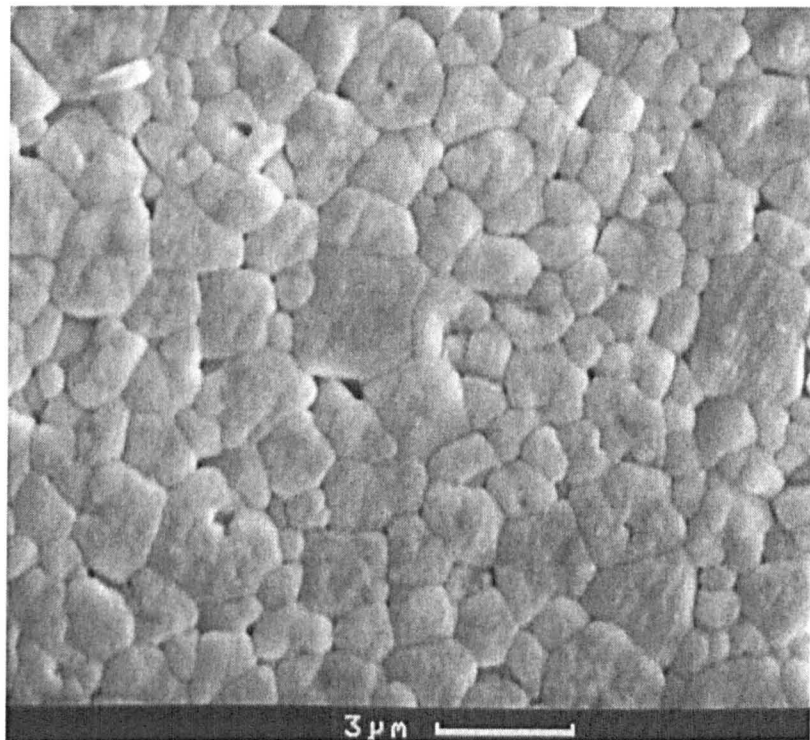


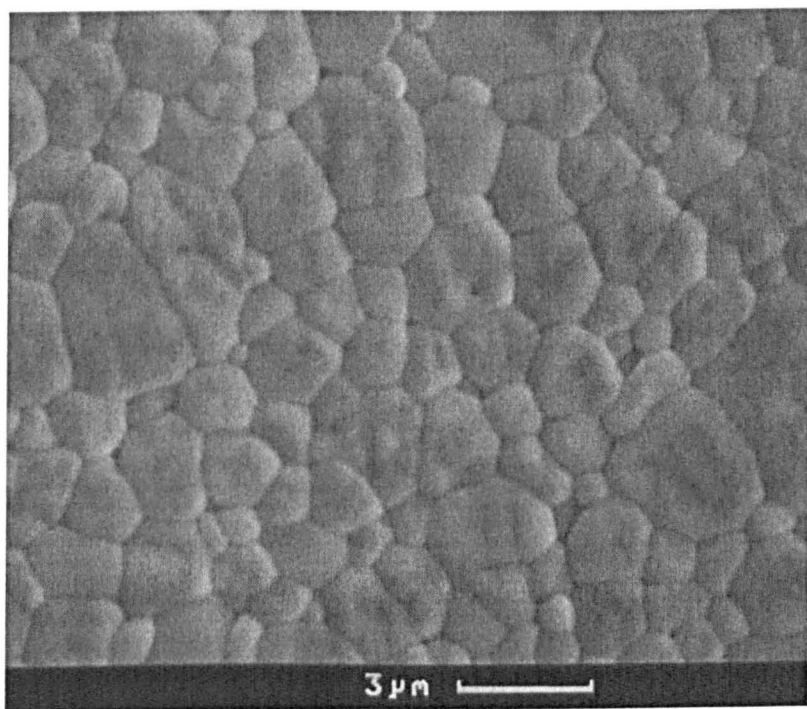
Figure 6.1 XRD from PSZT ceramics as a function of Sr²⁺ content

(Nb:Zr:Ti=2.4:51:46.6)

Figure 6.2 shows SEI SEM photographs of PSZT ceramics with 4 mol% (Fig. 6.2(a)) and 16 mol% (Fig. 6.2(b)) Sr^{2+} doping on the A-site (sintered 4h at 1140°C). Each sample exhibits an equiaxed grain structure ($1.5 \pm 0.2 \mu\text{m}$) and no second phase is detected. There is no significant variation either in grain size or morphology with varying Sr^{2+} content, which implies that strontium substitution on the A-site has little effect on the grain structure of PZT ceramics.



(a) PSZT4/47



(b) PSZT16/47

Figure 6.2 SEI SEM photographs of PSZT ceramics with (a) 4 mol% and (b) 16 mol% Sr^{2+} doping on the A-site, sintered 4h at 1140°C

The evolution of domain structures was studied as a function of Sr^{2+} content using TEM. These TEM images were taken in general two-beam conditions, not at specific zone axes.

Figure 6.3 is a BF-TEM image revealing domains ($\sim 80 \text{ nm}$ wide), typical of 0 mol% Sr-doped PZT. These domain walls lie on specific crystallographic planes and are characteristic of orientational or 90° domains.

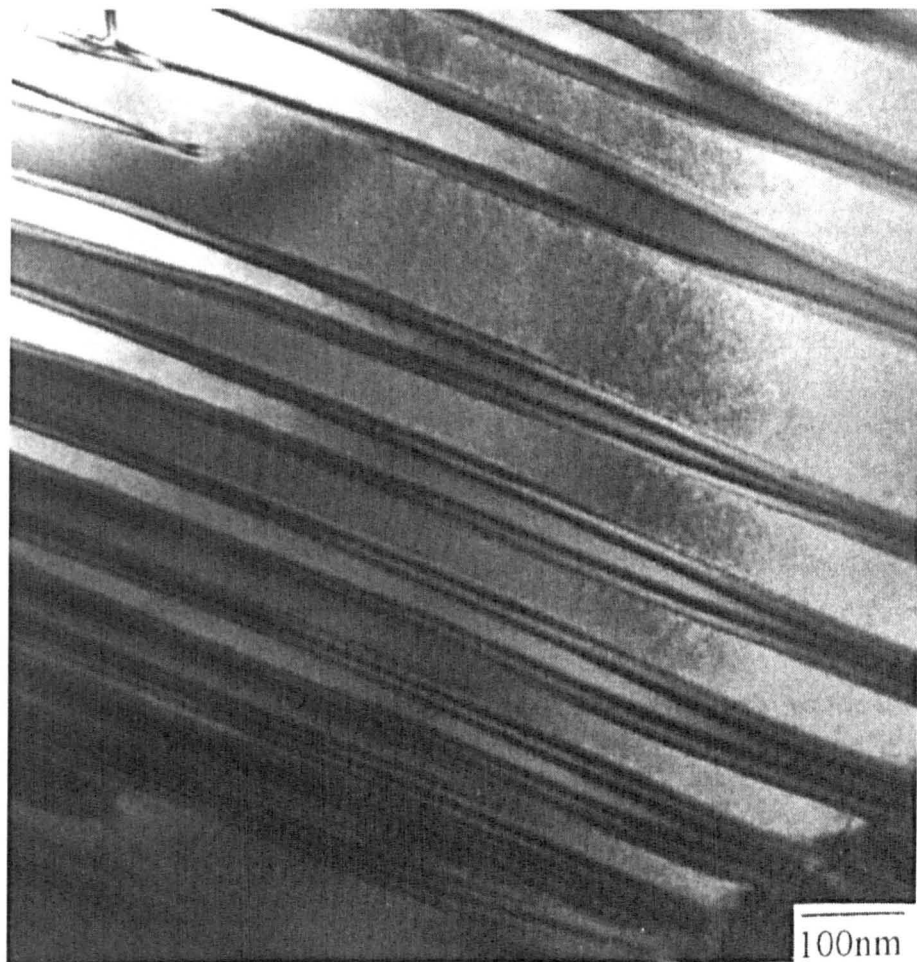


Figure 6.3 BF-TEM image showing 90° domains in 0 mol% Sr-doped PZT (Nb:Zr:Ti= 2.4:51:46.6)

Similar domain structures are observed in samples containing Sr^{2+} , but their width diminishes as the dopant level increases. In addition, intragranular heterogeneity

of the domain width is observed, an effect illustrated in Figure 6.4 for 16 mol% Sr^{2+} addition which shows $\sim 80\text{ nm}$ as well as finer $\sim 20\text{ nm}$ wide domains. The observation of regions with different domain structure implies a distribution of Sr^{2+} concentration (and/or Zr:Ti ratio) even within a grain. This could indicate a distribution of T_C within the ceramic, suggesting the possibility of broadening of the Curie maximum with increasing Sr^{2+} concentration.

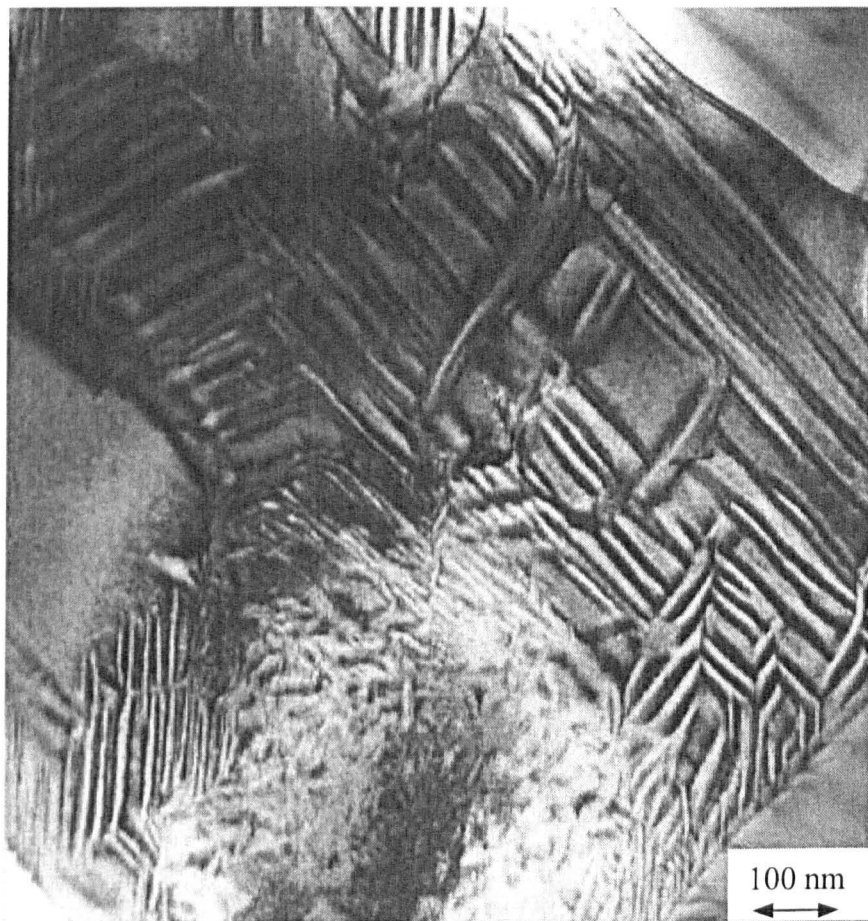


Figure 6.4 BF-TEM image showing fine scale domains in 16 mol% Sr-doped PZT
(Nb:Zr:Ti = 2.4:51:46.6)

Figure 6.5 also for 16 mol% Sr^{2+} addition reveals similar boundaries to those in Figure 6.4, but walls with ribbon-like contrast are also present, typical of inversion (180°) domains.

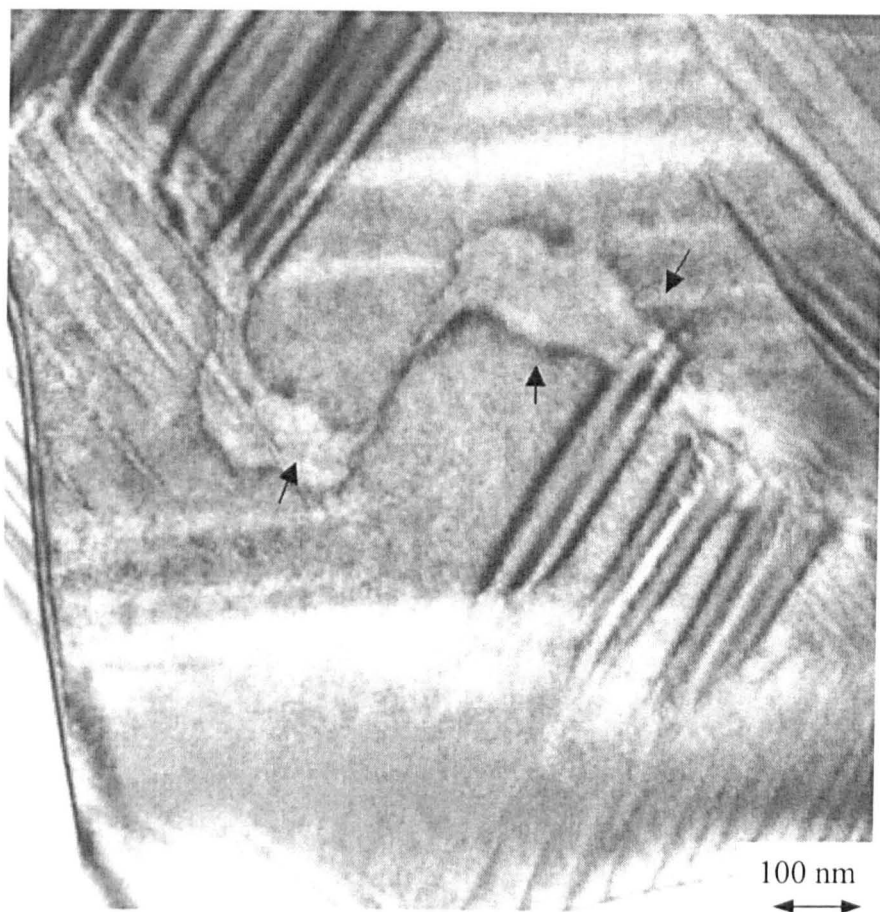


Figure 6.5 BF-TEM image showing an inversion domain boundary (arrowed) in 16 mol% Sr-doped PZT ($\text{Nb}:\text{Zr}:\text{Ti} = 2.4:51:46.6$)

6.1.2 Electrical Characterisation

Figure 6.6 shows plots of relative permittivity versus temperature for the PSZT compositions in Figure 6.1. The Curie temperature (T_C) is reduced from ~ 360 to $\sim 30^\circ\text{C}$ by doping with up to 32 mol% Sr^{2+} . In addition to decreasing the T_C , Sr^{2+} substitution broadens the phase transition maximum, implying that the distribution of Curie temperatures is increased within the ceramics. For 32 mol% Sr^{2+} samples, a broad Curie maximum is observed at 30°C , indicating that much of the ceramic has undergone a phase transition by room temperature. This is consistent with the pseudocubic pattern observed by XRD (Figure 6.1).

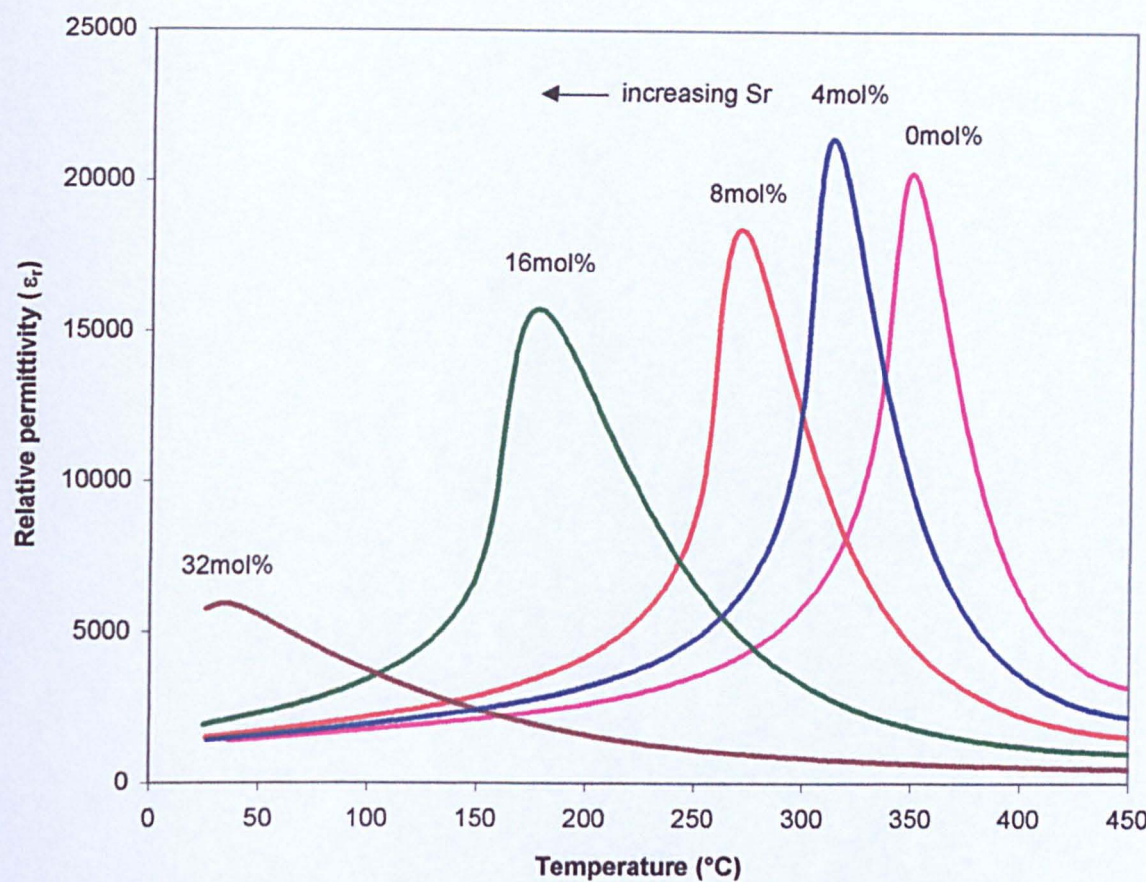


Figure 6.6 Relative permittivities of PSZT ceramics as a function of Sr^{2+} content (Nb:Zr:Ti = 2.4:51:46.6)

Similar effects on T_C have been found in La-doped PZT (PLZT)^[101] and Sr-doped BaTiO_3 (BST)^[102]. With partial substitution of Pb^{2+} by La^{3+} in PLZT or Ba^{2+} by Sr^{2+} in BST, the variation of the permittivity around the Curie temperature was found to smear out, inducing a diffuse phase transition (DPT). Smolenskii *et al.*^[103] and Cross^[40] have proposed that the origin of the DPT is due to compositional heterogeneity. Statistical compositional fluctuations lead to large fluctuations in the Curie temperature and thus over a wide temperature range there is an intimate mixture of ferroelectric (polar) and para-electric (non-polar) regions, with the balance becoming steadily more polar as the temperature is reduced. It is therefore assumed that a non-homogeneous distribution of Pb^{2+} and Sr^{2+} on the A-site in Sr-doped PZT would lead to a DPT, consistent with TEM observations of domain width heterogeneity, Figure 6.4.

Although a decrease in the Curie temperature is observed (one of the mechanisms by which domain wall motion is made easier), the value of d_{33} diminishes as the Sr^{2+} content increases, Figure 6.7. This is due to the fact that increasing Sr^{2+} on the A-site moves compositions away from the MPB, suggesting that controlling the Zr:Ti ratio is more important to domain wall motion than simply reducing the phase transition temperature alone. In accordance with d_{33} , k_p also decreases with increasing the Sr^{2+} content, Figure 6.7.

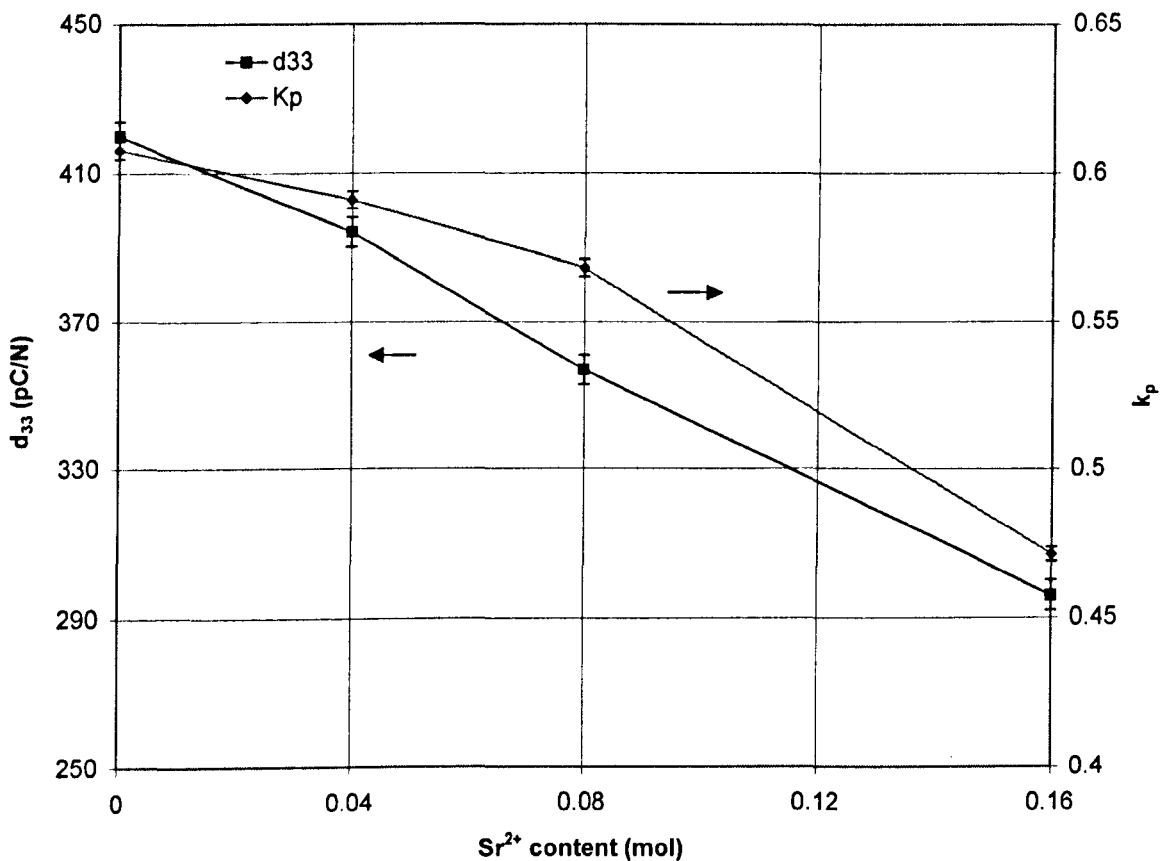


Figure 6.7 d_{33} and k_p as a function of Sr^{2+} content in PSZT ceramics
(Nb:Zr:Ti=2.4:51:46.6)

6.2 Effect of Zr:Ti ratio in 8 mol% Sr-doped PZT

Since Sr²⁺ substituting for Pb²⁺ on the A-site shifts the phase towards tetragonal, the Zr:Ti ratio in 8 mol% Sr-doped PZT compositions was adjusted to move the ceramic closer to the MPB in order to maximise d_{33} . The compositions prepared in this section are formulated according to Table 3.6. All the fired samples have relative densities above 95% of theoretical and their structures and microstructures were investigated using XRD, SEM and TEM.

6.2.1 Structure

Figure 6.8 shows XRD patterns from PSZT samples containing 8mol% Sr²⁺ on the A-site, in which the Zr:Ti ratio has been varied to compensate the increase in tetragonality observed in Figure 6.1. A structural change is observed from tetragonal to mixed phase as the Zr:Ti ratio increases, indicated by a change from {002} to mixed {111}/{002} peak splitting. Ceramics with Zr:Ti ratio = 1.203 are still tetragonal, indicated by peak splitting on the {002}. However, ceramics with Zr:Ti ratio ≥ 1.335 appear rhombohedral, indicated by peak splitting on the {111}.

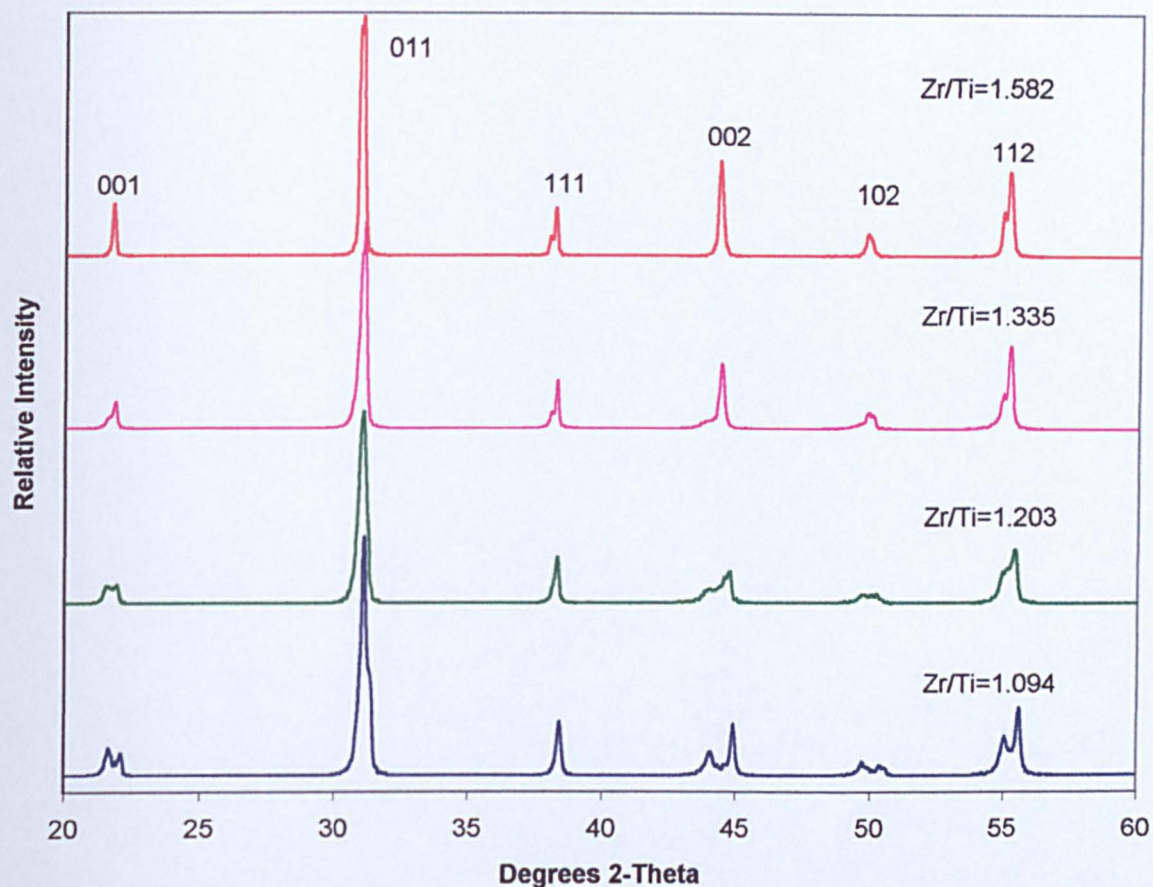


Figure 6.8 XRD from 8mol% Sr-doped PZT ceramics with varying Zr:Ti ratio

6.2.2 Electrical Characterisation

Figure 6.9 show plots of relative permittivity versus temperature for the samples in Figure 6.8. T_C decreases from $\sim 270^\circ\text{C}$ to $\sim 230^\circ\text{C}$ when the Zr:Ti ratio is increased from 1.094 to 1.582 similar to the effect of Zr:Ti ratio observed in PNZT ceramics in Chapter 5.

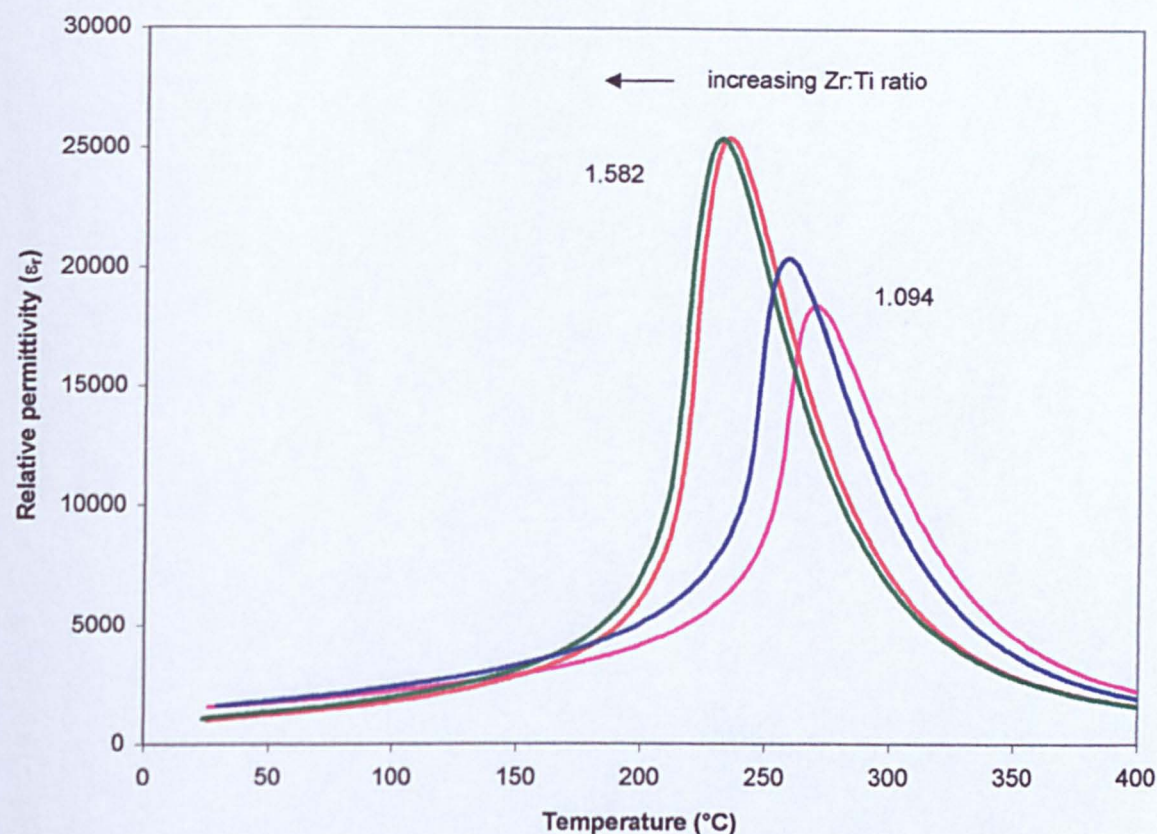


Figure 6.9 Relative permittivities of 8 mol% Sr-doped PZT as a function of Zr:Ti ratio

d_{33} , Figure 6.10 increases with increasing Zr:Ti ratio, approaching a maximum ($\sim 540 \text{ pC/N}$) at Zr:Ti = 1.203 (tetragonal phase, as ascertained by XRD, Figure 6.8). d_{33} then decreases as the composition moves away from the MPB into the rhombohedral phase. k_p values show a similar trend to d_{33} . d_{33} and k_p data presented here again demonstrate that the optimisation of these properties occurs in the tetragonal phase close to, rather than at, the precise MPB, in good agreement with the observation in Chapter 5. It is also worth noting here that the d_{33} is sensitive to Zr:Ti ratio, the optimised d_{33} values only occur in a narrow Zr:Ti ratio region and deviations from this region lead to a large decrease in d_{33} values.

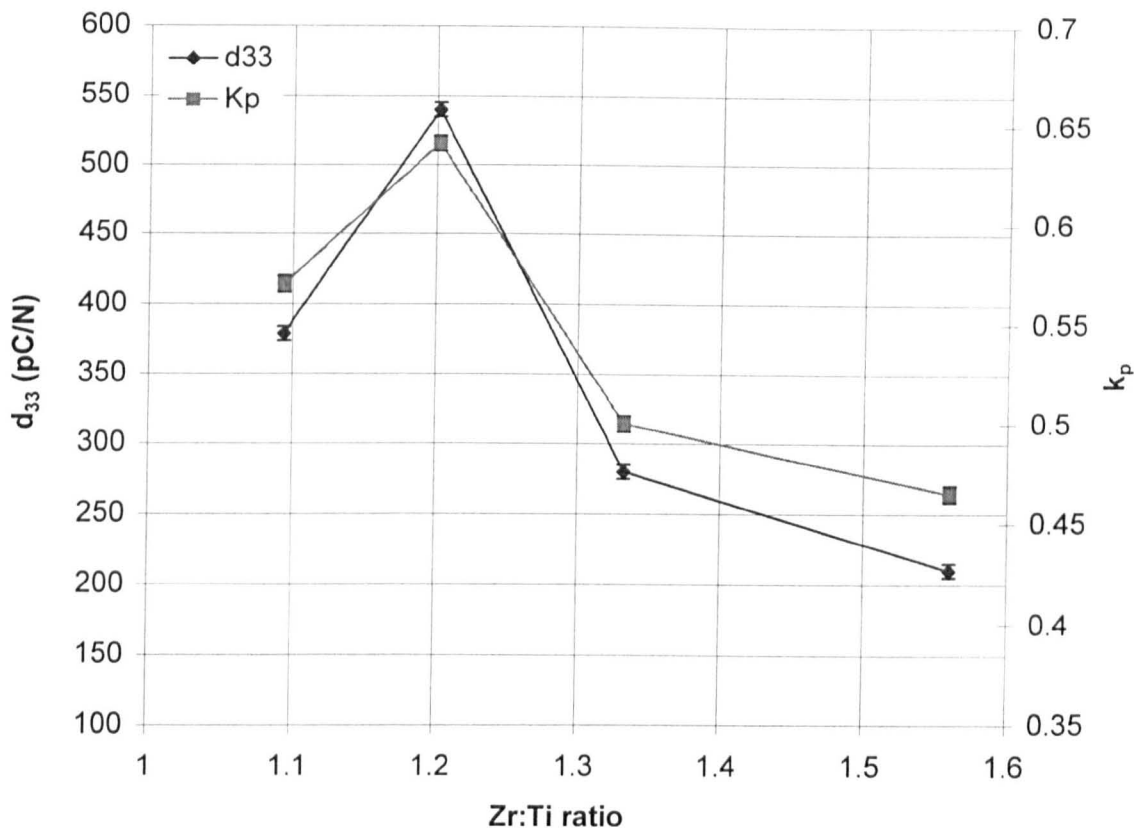


Figure 6.10 d_{33} and k_p as a function of Zr:Ti ratio in 8 mol% Sr-doped PZT

Hysteresis curves, Figure 6.11 indicate that increasing Zr:Ti ratio from 1.094 to 1.335 decreases the coercive field from ~ 1.66 to 1.00 kV/mm , as a result of the phase moving closer to the MPB. This is consistent with the observation in Nb-doped PZT in Chapter 5. Saturation polarisation (P_S) increases or decreases in a similar way to P_r . The difference, $P_S - P_r$ is almost constant for all samples. No E_C asymmetry ($|+E_C| - |-E_C|$) is observed regardless of Zr:Ti ratio, which means no internal bias is present in these samples, implying no second phase or phase segregation and also a homogenous distribution of dopants within the samples.

The composition with a Zr:Ti ratio of 1.335 (rhombohedral phase) had the lowest coercive field, but it did not have the highest remnant polarisation. The highest

remnant polarisation (0.36 C/m^2) was found at a Zr:Ti ratio of 1.203 (tetragonal phase). This result can be interpreted by considering the fact that the spontaneous strain associated with the tetragonal distortion is much larger than the spontaneous strain associated with the rhombohedral distortion. The rhombohedral strain, given by $[(90^\circ - \beta) / 90^\circ]$, where β is the angle of the rhombohedral unit cell, is less than 0.5% at the MPB and remains nearly constant with increasing Zr/Ti ratio^[104]. The tetragonal strain, given by $[(c - a) / a]$, where c and a are the axes of the tetragonal unit cell, is greater than 2% at the MPB and increases with increasing Ti⁴⁺ concentration up to more than 6% for pure PbTiO_3 . The 90° domain walls in tetragonal PZT ceramics are likely to be already partly clamped by local internal stresses, which originate from the high tetragonal distortion. On the other hand, the 109° and 71° rhombohedral domain walls are relatively free to move because internal stresses due to the structural distortion are significantly smaller in rhombohedral compositions^[105].

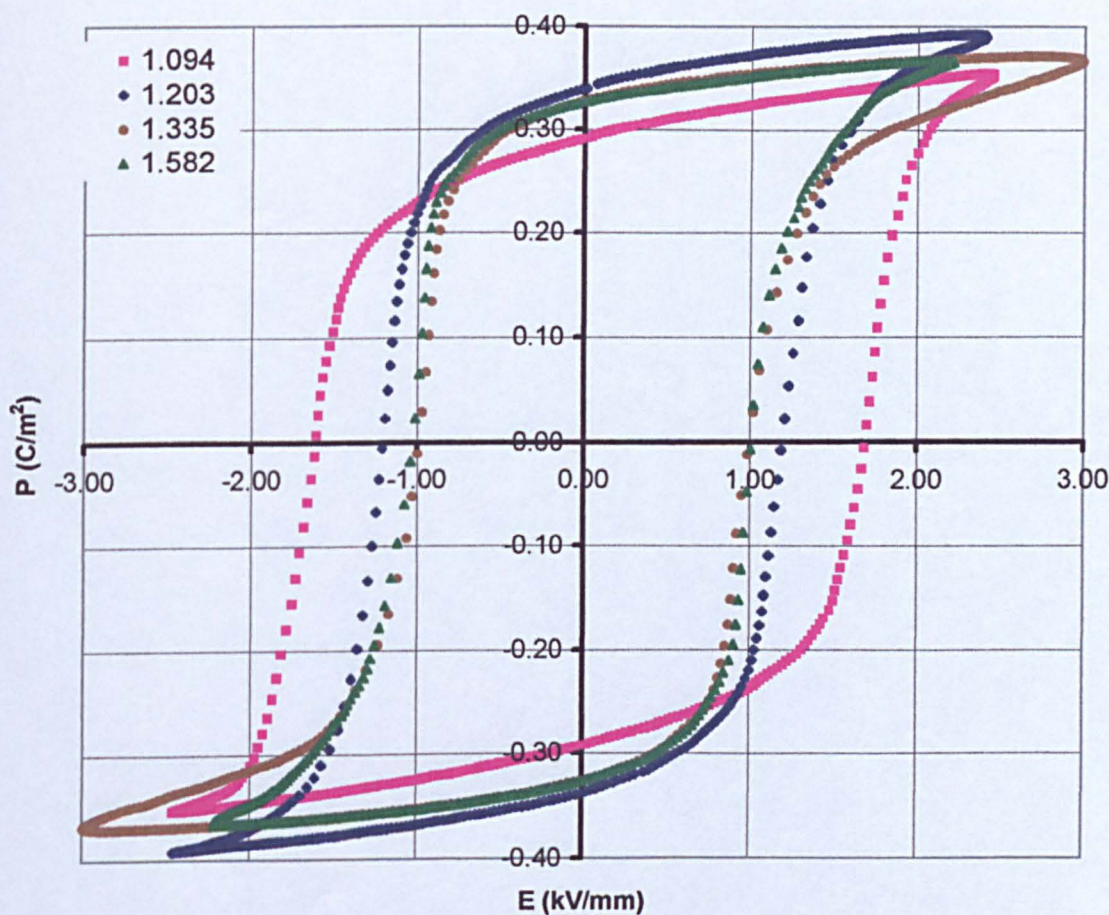


Figure 6.11 Hysteresis loop as a function of Zr:Ti ratio in 8 mol% Sr-doped PZT

Damjanovic and Demartin^[105] reveal, that the fraction of the piezoelectric response that is due to the irreversible displacement of domain walls is largest in the rhombohedral composition followed by the MPB and finally the tetragonal composition. Their results imply easier domain wall motion under the action of an electric field in rhombohedral phase, which agrees with our observations that the rhombohedral phase has the lowest coercive field.

As stated previously, the highest remnant polarisation was found in ceramics with a Zr:Ti ratio of 1.203. This composition also had the highest d_{33} value ($\sim 540 \text{ pC/N}$). This may suggest that an increase in d_{33} is associated with the increase in P_r , rather than the decrease in E_C .

6.3 Effect of Zr:Ti ratio in 16 mol% Sr-doped PZTs

The 8 mol% Sr-doped PZT series demonstrated that a combination of Sr^{2+} substitution on the A-site with the proper control of Zr:Ti ratio could improve the d_{33} up to $\sim 540 \text{ pC/N}$. In an attempt to enhance the soft behaviour of PZT by reducing the T_C further, 16 mol% Sr-doped PZT ceramics were prepared with varying Zr:Ti ratios. Ceramics were formulated according to Table 3.7. All the fired samples have relative densities above 95% of theoretical and their structures and microstructures were examined using XRD and TEM.

6.3.1 Structure

Figure 6.12 shows XRD patterns from PSZT samples containing 16 mol% Sr^{2+} on the A-site, in which, the Zr:Ti ratio has been varied in a similar manner to that

described in Section 6.2. As the Zr:Ti ratio increases, peak splitting of the {002} diminishes, indicating that the ceramics have moved from a tetragonal to rhombohedral structure. The MPB was considered to occur at Zr:Ti ratio of 1.335, implied by both a shoulder on the {111} and a diminished peak splitting on the {002}.

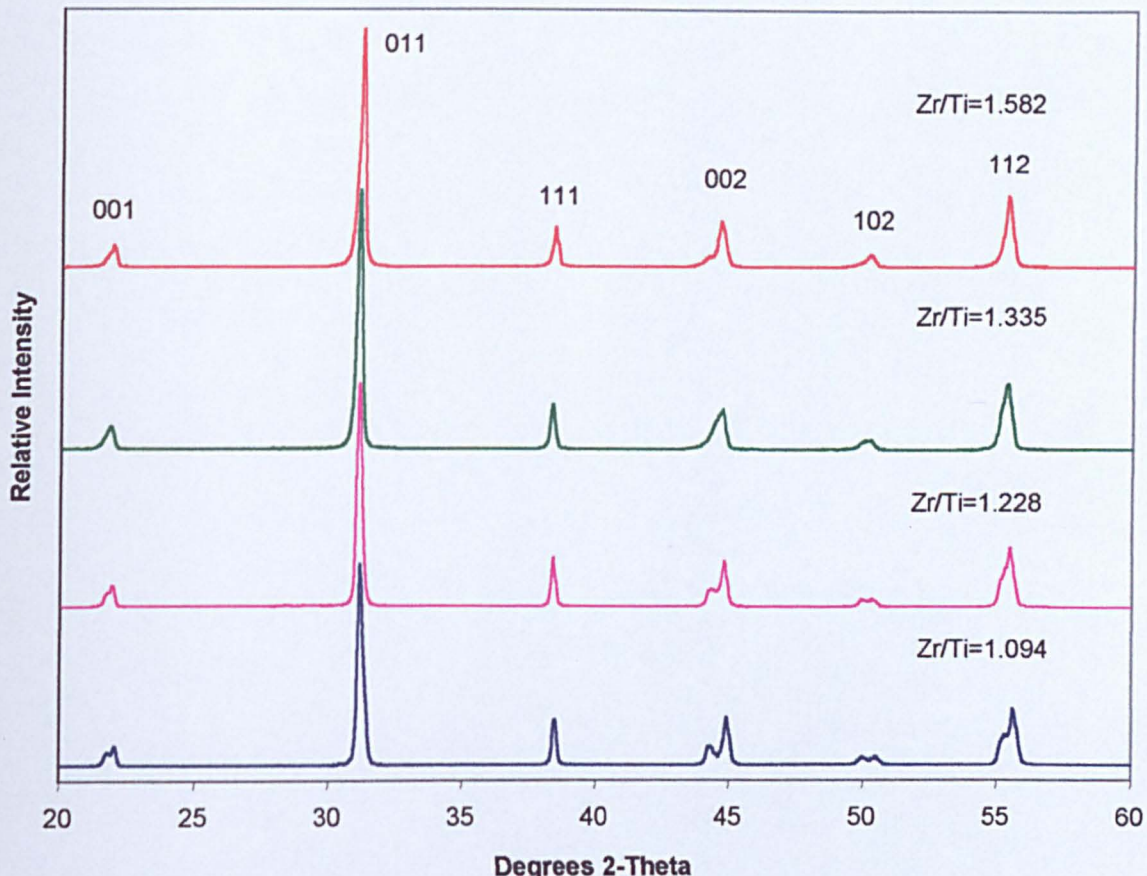


Figure 6.12 XRD of 16 mol% Sr-doped PZTs with varying Zr:Ti ratio

6.3.2 Electrical Characterisation

Figure 6.13 reveals relative permittivity as a function of temperature data associated with the change in Zr:Ti ratio in 16 mol% Sr-doped PZT ceramics. The same trend is observed as in Figure 6.9 (8 mol% Sr-doped PZT) except here the T_C decreases from $\sim 180^\circ\text{C}$ to $\sim 140^\circ\text{C}$ as the Zr:Ti ratio is increased from 1.094 to 1.582.

Figure 6.14 illustrates the effect of changing Zr:Ti ratio on d_{33} in 16 mol% Sr-doped PZT. Initially, d_{33} increases with Zr:Ti ratio reaching a maximum at 1.335 (375 pC/N). This can be explained by considering that phase composition is moved closer to the MPB. d_{33} then decreases with respect to the previous value. It is possible that this composition has moved to the rhombohedral side of the MPB and is no longer optimised for d_{33} . Another feature is that the optimise d_{33} values in 16 mol% Sr-doped PZT (375 pC/N) are lower than those in 8 mol% Sr-doped PZT (540 pC/N) even though T_C is lower.

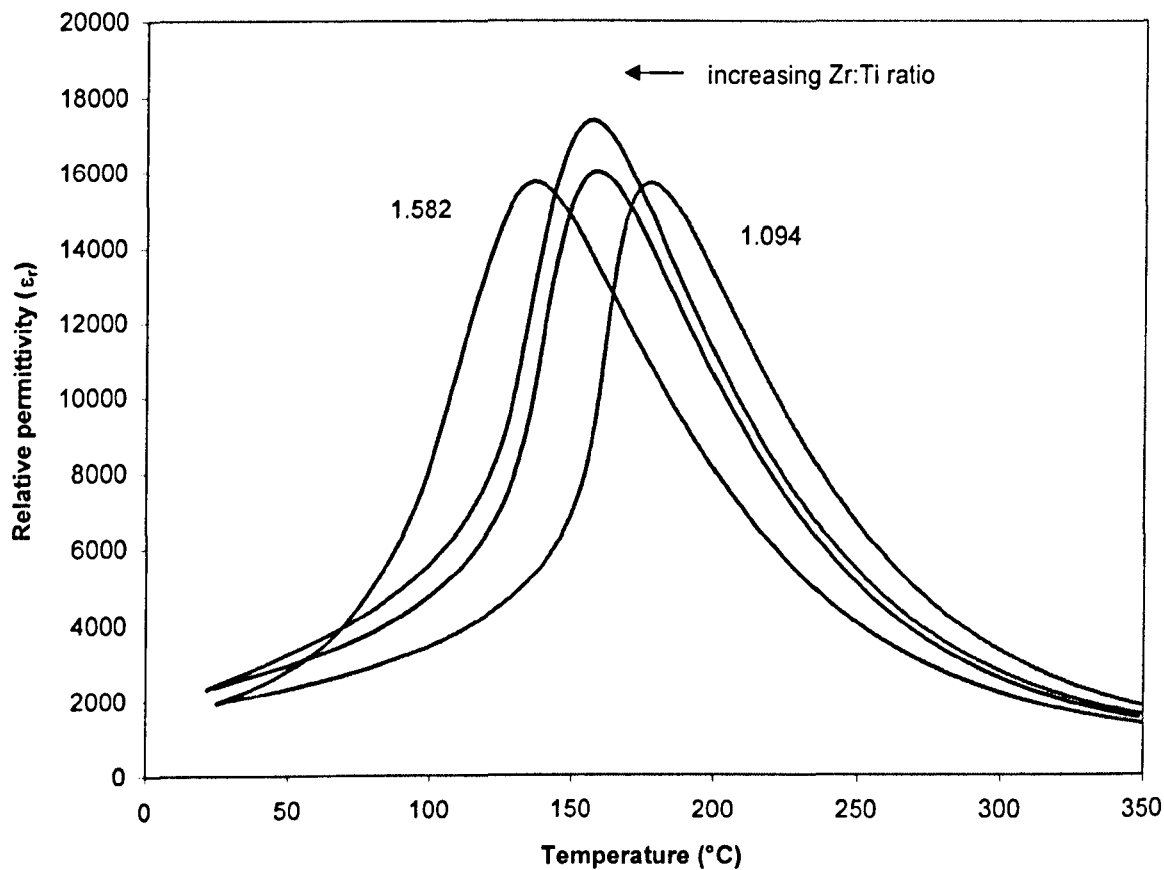


Figure 6.13 Relative permittivities of 16mol% Sr-doped PZT as a function of Zr:Ti ratio

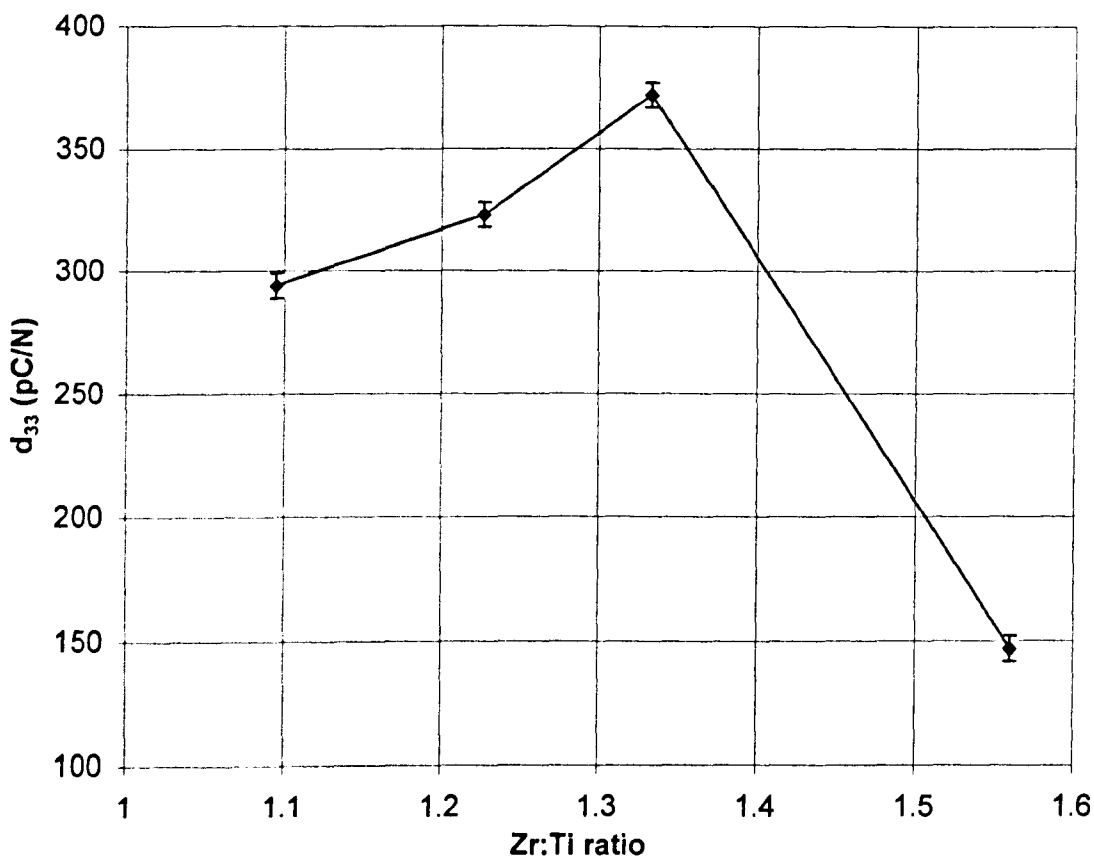


Figure 6.14 d_{33} as a function of Zr:Ti ratio in 16 mol% Sr-doped PZT

Hysteresis curves, Figure 6.15 indicate that increasing Zr:Ti ratio from 1.094 (tetragonal, ascertained by XRD, Figure 6.12) to 1.582 (rhombohedral, ascertained by XRD, Figure 6.12) decreases the coercive field from ~ 1.2 to 0.7 kV/mm . Further increasing Zr:Ti ratio to 1.882 increases E_C to $\sim 1.1 \text{ kV/mm}$, resulting from the phase being moved far away from the MPB. This result is consistent with the observations in Section 6.2 that coercive field is lowest in a slightly rhombohedral phase close to the MPB. But moving far away from the MPB will increase E_C again. Ceramics with a Zr:Ti ratio of 1.582 (rhombohedral phase) had the lowest coercive field, but not the highest remnant polarisation. The highest remnant polarisation (0.23 C/m^2) is found in compositions with a Zr:Ti ratio of 1.335, corresponding to the highest d_{33} ($\sim 375 \text{ pC/N}$). This is consistent with the observation in 8 mol% Sr-doped PZT in Section 6.2.

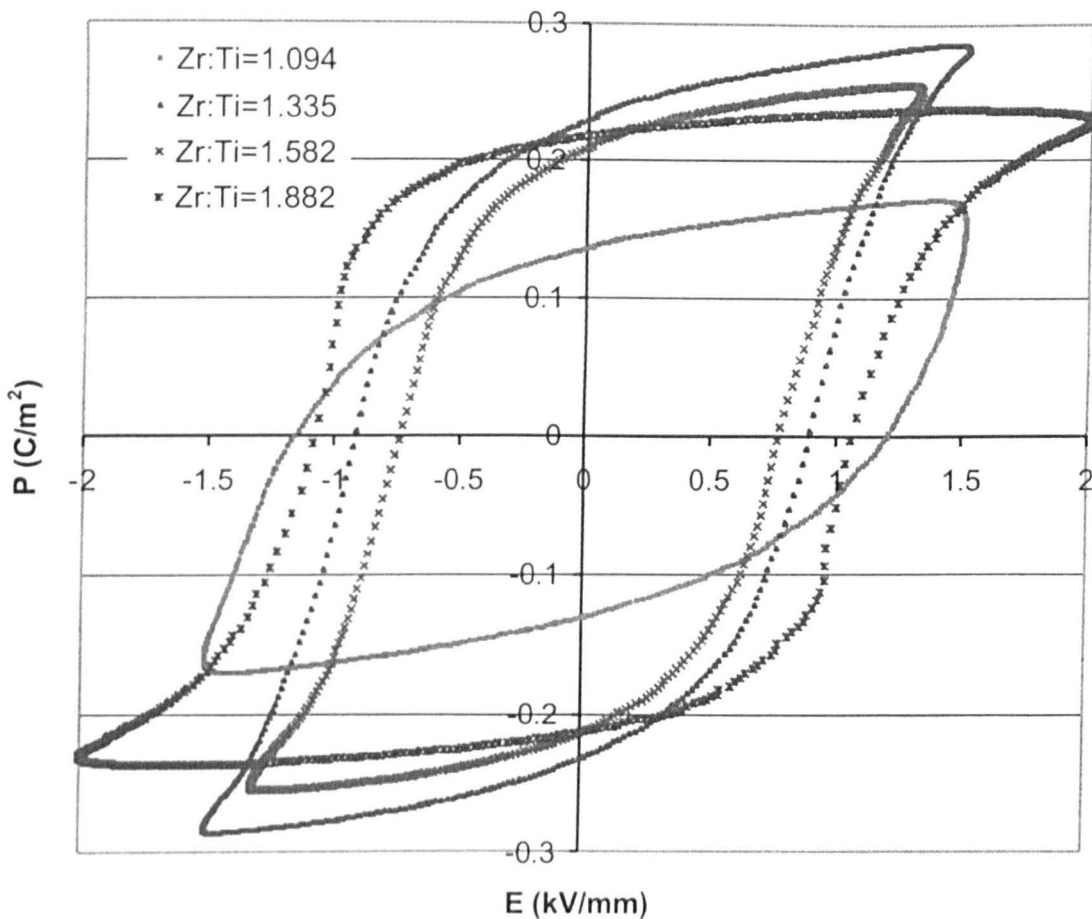


Figure 6.15 Hysteresis loop as a function of Zr:Ti ratio in 16 mol% Sr-doped PZT

It is also worth noting that compared to the 8 mol% Sr-doped PZT series (Figure 6.11), though E_C in 16 mol% Sr-doped PZT is decreased, P_S and P_r drop substantially in agreement with the lower d_{33} values.

The optimised values of d_{33} ($\sim 375 \text{ pC/N}$) in MPB 16 mol% Sr-doped PZT compositions are lower than those in 8 mol% Sr-doped PZT ($\sim 540 \text{ pC/N}$). This decrease is commensurate with a decrease in P_r , suggesting that there may be a reduction in the intrinsic piezoelectric activity. However, the intrinsic contribution to d_{33} in soft PZT based ceramics is considered negligible compared to extrinsic contributions. Therefore the drop in P_r only partially explain the reduction in d_{33} and the effect of Sr^{2+} doping on extrinsic contributions must also be considered.

To further explain the above results, detailed structural characterisation was carried out using TEM and the results will be presented in Chapter 7.

6.4 Conclusions

- Sr²⁺ substitution on the A-site in PZT promotes the tetragonal over the rhombohedral phase for a fixed Zr:Ti ratio.
- T_C is greatly reduced by Sr²⁺ doping but the d_{33} still decreases suggesting that control of Zr:Ti ratio is more important for d_{33} than simply reducing T_C .
- Domain width is finer in samples doped with Sr²⁺. In addition the distribution of domain widths is inhomogeneous even within a grain, varying from ~ 100 to $\sim 20nm$, which is consistent with the increased width of the relative permittivity maximum.
- By fixing Sr doping and varying Zr:Ti ratio, d_{33} of $\sim 540\text{ pC/N}$ with a $T_C \sim 250^\circ\text{C}$ is achieved in 8 mol% Sr-doped PZT (Zr:Ti ratio = 1.202). d_{33} of $\sim 375\text{ pC/N}$ with a lower $T_C (\sim 150^\circ\text{C})$ is obtained in 16 mol% Sr-doped PZT (Zr:Ti ratio = 1.335).

7. OXYGEN OCTAHEDRAL TILTING IN Sr-DOPED PZT

In Chapters 5 & 6, by combining Nb⁵⁺ donor doping on the B-site, Sr²⁺ substitution on the A-site with proper control of Zr:Ti ratio, d_{33} values were improved to ~540 pC/N in 8 mol% Sr-doped PZT although they decreased in 16 mol% Sr-doped PZT.

To complete a series of d_{33} -optimised PSZT compositions, PSZT12/44 (formula: $(\text{Pb}_{0.88}\text{Sr}_{0.12})(\text{Zr}_{0.538}\text{Ti}_{0.438}\text{Sb}_{0.024})\text{O}_3$) was prepared. This composition was chosen because it had the optimum d_{33} values in the 12 mol% Sr-doped PZT series^[106]. The d_{33} measurements show that this composition has values of ~640 pC/N ($T_C \sim 180^\circ\text{C}$), which is still far lower than the recently-developed soft material PZT-PNN ($d_{33} > 1000$ pC/N)^[107] (a similar $T_C \sim 180^\circ\text{C}$). The three softening mechanisms currently in favour, described in Section 2.4, therefore encounter difficulties in explaining these two different figures. The observation of the decreased d_{33} in 16 mol% Sr-doped PZT in Chapter 6 is also very difficult to explain based on existing knowledge of softening mechanisms.

It is well known that soft behaviour of PZT results from promotion of domain wall motion^[4-6], which is intimately related to the phase structures and microstructures of the ceramics. Changes in the dielectric and piezoelectric properties are directly associated with structural changes occurring in various doped soft PZT's. Recently, TEM has been widely used in structural studies revealing information, complementary to that obtained by using bulk scattering techniques such as X-ray, neutron scattering, and spectroscopy. This chapter therefore focuses on investigating electron diffraction patterns, which can reveal the crystallographic structure information, as a function of Sr²⁺ substitution for Pb²⁺ on the A-site.

To focus on the effect of Sr^{2+} substitution, four d_{33} -optimised compositions with Sr^{2+} doping at 0, 8 mol%, 12 mol% and 16 mol% respectively on the A-site were investigated in this chapter. Optimised d_{33} was achieved by adjusting Zr:Ti ratio at a fixed Sr^{2+} content as described in Sections 6.2 and 6.3.

7.1 Phase Structure

It has been found in Section 6.1 that doping a MPB composition ($\text{Sr}^{2+} = 0$) with Sr^{2+} results in an increase in tetragonality. Therefore, as the Sr^{2+} content is increased, the Zr:Ti ratio is raised accordingly to maintain compositions always close to the MPB.

Figure 7.1 shows XRD spectra from four d_{33} -optimised compositions with various Sr^{2+} (x mol) substitution for Pb^{2+} on the A-site where $x = 0, 0.08, 0.12, 0.16$ respectively. It is evident that these four compositions are all tetragonal with the presence of either peak splitting or a shoulder on the $\{002\}$ peak. No peak splitting or shoulder occurs on the $\{111\}$, confirming that the rhombohedral phase is absent. It is worth emphasising that these four optimised compositions possess very similar tetragonal phase assemblage regardless of Sr^{2+} content.

It has been commonly accepted that d_{33} is optimised at the MPB, but our studies consistently show that, both in Nb-doped (Chapter 5) and Sr, Nb co-doped PZT (Chapter 6), d_{33} is always optimised in the tetragonal phase *close to*, rather than *at*, the precise MPB. By using the observation that grinding and polishing induce the phase transformation from tetragonal to rhombohedral in MPB PZT compositions in Section 4.3.2, it can be postulated that these d_{33} -optimised compositions may appear tetragonal after firing, but switch to the mixed phase after electric poling and therefore exhibit the highest d_{33} values.

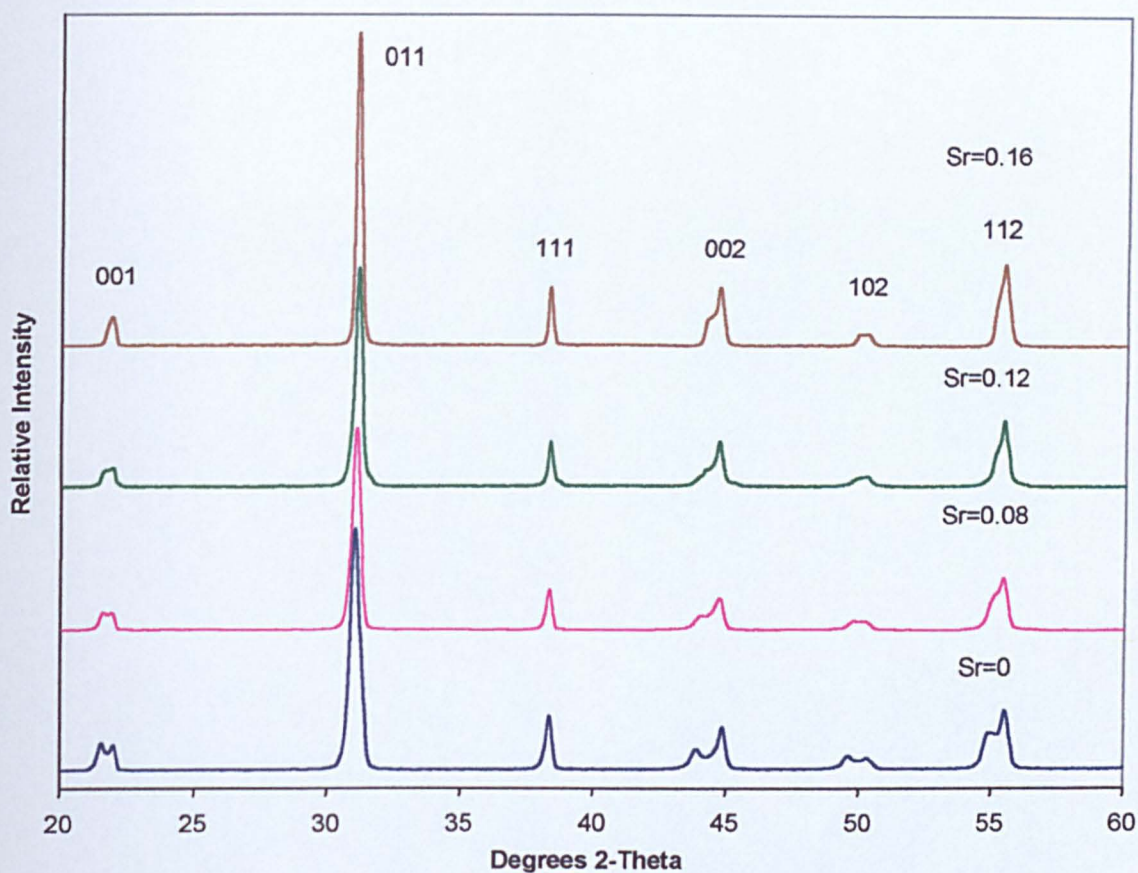


Figure 7.1 XRD patterns from various d_{33} -optimised Sr-doped PZT ceramics

7.2 Selected Area Electron Diffraction

Figure 7.2 shows selected area electron diffraction patterns along the pseudocubic $\langle 110 \rangle$ zone axes of these optimised compositions as a function of Sr^{2+} concentration ($x = 0, 0.08, 0.12, 0.16$). For simplicity and direct comparison they are indexed using the pseudocubic simple perovskite unit cell. The most intense reflections in these four patterns can be indexed according to the fundamental perovskite structure with $a = \sim 0.40 \text{ nm}$, consistent with the presence of tetragonal/rhombohedral phases in

the PZT. Figure 7.2 (a) ($x = 0$) only contains spots associated with the fundamental perovskite lattice and there is no evidence of superlattice reflections. However, Figures 7.2 (b) - (d) show superlattice reflections occurring at the $\{h+\frac{1}{2}, k+\frac{1}{2}, l+\frac{1}{2}\}$ positions and their intensities become qualitatively stronger with increasing Sr^{2+} concentration.

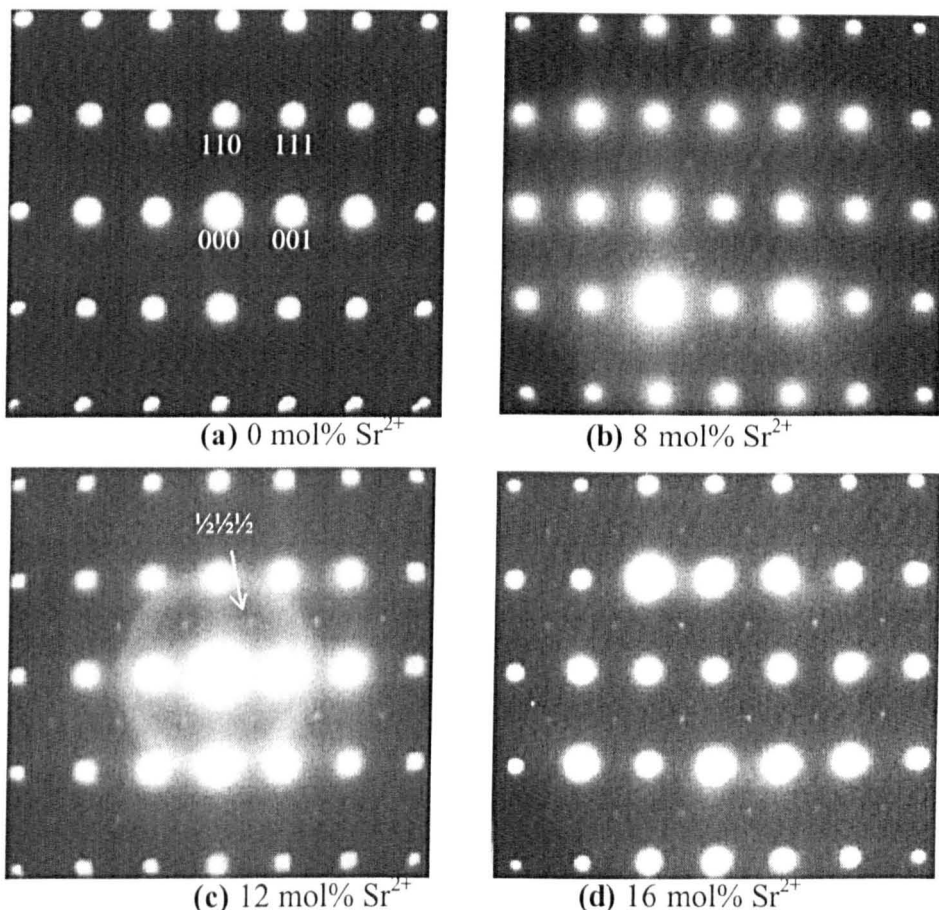


Figure 7.2 Electron diffraction patterns along the pseudocubic $<110>$ zone axes as a function of Sr^{2+} content in optimised Sr-doped PZT ceramics. The diffraction ring in (c) is an artefact probably arising from an amorphous contaminant film.

In general there are three possible sources of superlattice reflections in stoichiometric perovskites^[19-20]:

- i) Ordering of cations as occurs in complex perovskites such as barium zinc tantalate. Typically cation species of differing valence states order themselves on $\{111\}$ planes perpendicular to a $<111>$ direction of the pseudocubic

perovskite cell. For ordered $\frac{1}{2}:\frac{1}{2}$ complex perovskite such as Pb_2MgWO_6 , alternative {111} planes are occupied by each B-site cation species. The resulting superlattice is doubled along all three principal axes and a face centred cubic structure is formed. In diffraction, this is typified by the appearance of $\frac{1}{2}\{\text{hkl}\}$ reflections^[108].

- ii) Antiparallel cation displacement e.g. in antiferroelectric, AFE, compounds. An AFE compound such as PbZrO_3 is quadrupled along a <110> direction, with respect to a simple pseudocubic perovskite cell, giving rise to $\pm \frac{1}{4}\{\text{hk0}\}$ reflections in diffraction patterns^[28].
- iii) Rotations (tilting) of the oxygen octahedra e.g. CaTiO_3 . Octahedral tilt transitions occur by the rotation of the octahedra around given axes of the pseudocubic perovskite cell. Glazer^[19-20] described a notation based on rotations of octahedra about the 3 principal axes for all possible tilt configurations. Anti-phase rotations are denoted as '-' and give rise to reflections which lie at the $\frac{1}{2}\{\text{hkl}\}$ position when $l = k \neq h$ in magnitude, e.g. $\{3/2,1/2,1/2\}$. In-phase rotations are ascribed the notation '+' and give rise to reflections which lie at the $\frac{1}{2}\{\text{hk0}\}$ positions when $h \neq k$ in magnitude, e.g., $\{3/2,1/2,0\}$. However, because of double diffraction effects in electron diffraction patterns, normally $\frac{1}{2}\{\text{hkl}\}$ and $\frac{1}{2}\{\text{hk0}\}$ are observed for all values of h , k , l ^[109].

For the case of ordering, a 1:1 ratio of dissimilar cations on the A or B-site would give superlattice reflections of the type observed in Figure 7.2 but there are insufficient Sr^{2+} ions (≤ 16 mol%) to have a 1:1 cation ratio. Furthermore, ordering tends to occur when the charge and size differences between cations are large. The ionic size difference between Pb^{2+} and Sr^{2+} is small (0.05\AA) and they are isovalent. Therefore, ordering is extremely unlikely as the source of the superlattice reflections.

As compositions close to the MPB in the PZT phase diagram are all FE, and there is no evidence of AFE behaviour, anti-parallel cation displacement can also be dismissed as the source of the superlattice reflections. By elimination, it can be

concluded that the superlattice reflections in Figure 7.2 must arise from rotations of oxygen octahedra and based on the $1/2 \{hkl\}$ type of superlattice reflections observed, this octahedral tilting occurs in anti-phase.

This postulation is further testified by Figure 7.3, which shows electron diffraction patterns along the pseudocubic $<100>$ zone axes as a function of Sr^{2+} content. There is no evidence of superlattice reflections at either $\frac{1}{2} \{\text{hk}0\}$ or $\frac{1}{2} \{\text{h}00\}$ positions, revealing the absence of anti-parallel displacement of cations or in-phase oxygen octahedral tilting in Sr-doped PZT.

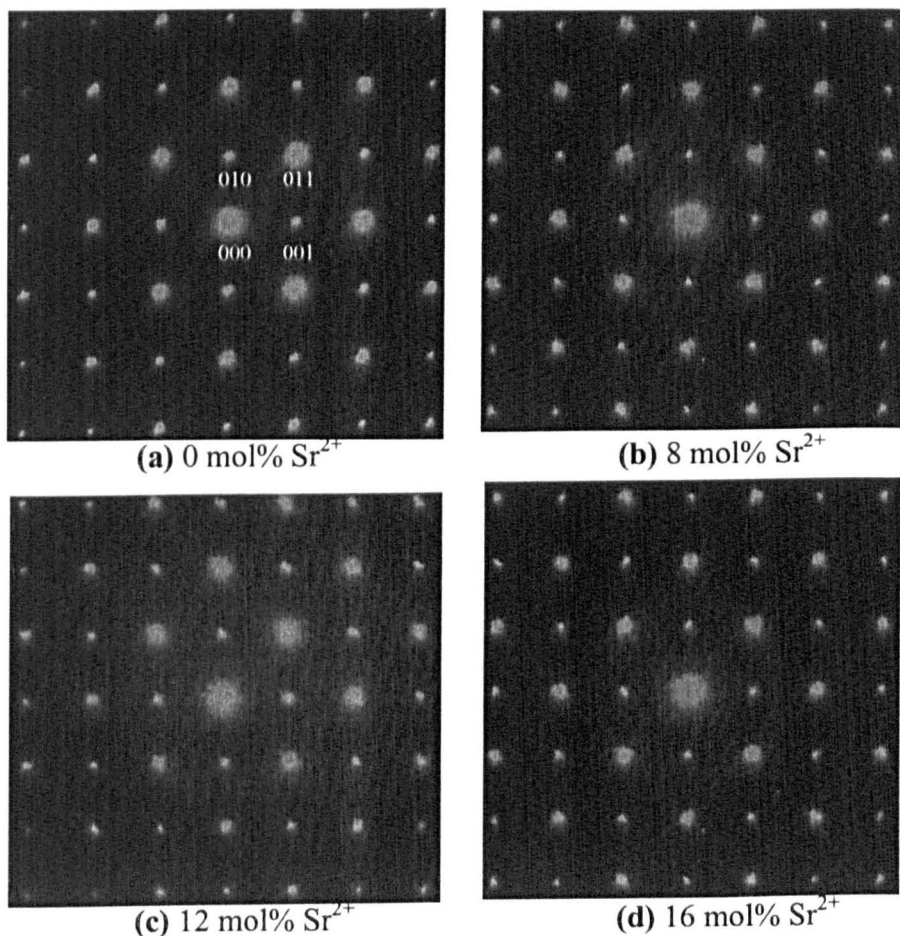


Figure 7.3 Electron diffraction patterns along the pseudocubic $<100>$ zone axes as a function of Sr^{2+} content in optimised Sr-doped PZT ceramics

7.3 Anti-phase Oxygen Octahedral Tilting

Megaw^[17-18] and Glazer^[19-20] studied phase transitions in perovskites driven by octahedral rotations (tilting) and concluded that reflections of the $\frac{1}{2}\{311\}$ type arose due to rotations in antiphase which can be resolved around the 3 principal, pseudocubic axes. In Figure 7.2 (b-d), these $\frac{1}{2}\{311\}$ type reflections are present as weak and/or diffuse intensities. However, Glazer's structure factor calculations suggest that the $\frac{1}{2}\{111\}$ type reflections, also present in Figure 2 (b-d), are forbidden and cannot arise by anti-phase rotations of the octahedra. More recent work by Reaney *et al.*^[110] has proposed that these reflections may appear in electron diffraction patterns by simple double diffraction,



Reaney *et al.*^[21] also suggested that antiphase rotations were likely to occur in compounds where the perovskite tolerance factor (equation 2.7) is less than ~ 0.985 . Table 7.1 lists the tolerance factor data at different x values calculated according to eq. 2.7 using data from Shannon and Prewitt^[111]. The radius of Sr^{2+} (1.44\AA) is slightly smaller than that of Pb^{2+} (1.49\AA). In addition, the Zr:Ti ratio increases in MPB compositions with increasing Sr^{2+} to compensate for the induced increase in degree of tetragonality. Zr^{4+} is larger (0.72\AA) than Ti^{4+} (0.605\AA) and consequently, t decreases from 0.988 ($x = 0$) to 0.983 ($x = 0.16$). The t values ($t < 0.985$) given by Reaney *et al.*^[21] for the presence of anti-phase rotations of the octahedra at room temperature were approximate and designed to relate to Ba and Sr based complex perovskites. Nevertheless, the values calculated for the PZT compositions in this study are in excellent agreement with those suggested by Reaney *et al.*^[21].

Table 7.1 Tolerance factor data as a function of x values

x	0	0.08	0.12	0.16
t	0.988	0.986	0.985	0.983

Superlattice reflections in Figure 7.2(b) and (c) ($x=0.08$ and 0.012 , respectively) are weak and diffuse, and in Figure 7.2(d) ($x=0.016$) they are weak but discrete. Although electron diffraction is not a quantitative scattering technique, in general weak intensities come from small scattering factor differences (small tilt angles) and diffuse reflections come from short-range ordered effects. Weak and diffuse implies that the amplitude of rotation is small and the correlation lengths over which they interact are also small, typically around $2\text{-}3\text{ nm}$. The weak, but discrete reflections in Figure 7.2(d) ($x = 0.16$) imply a small amplitude of tilt but long-range order. It may be concluded therefore, that the tilt transition temperatures in samples where $x = 0.08$ and 0.12 are effectively ambient in the microscope and thermal fluctuations result in diffuse reflections. For $x = 0.16$, the samples have undergone a phase transition above the ambient microscope temperature. Thermal fluctuations still exist but they never exceed the temperature of the phase transition and long-range order is maintained.

Anti-phase oxygen octahedral tilting is commonly observed in rhombohedral phase PZT, and has been widely reported^[112-113]. Such studies conclude that the oxygen octahedra tilt in the $\text{FE}_{\text{R(LT)}}$ phase of PZT is associated with the condensation of a zone-boundary Γ_{25} optical phonon mode at $\mathbf{q} = (111)(\pi/a)$ or the R-point of the Brillouin zone. The softening of the Γ_{25} mode results in opposite rotations of successive oxygen layers along the $\langle 001 \rangle$. The primitive unit-cell is thus doubled along the $\langle 001 \rangle$. In addition, the cog-wheel like rotations of the nearest-linked oxygen octahedron in the $\{001\}$ plane double the primitive unit-cell along the $\langle 100 \rangle$ and $\langle 010 \rangle$. Consequently, the condensation of the Γ_{25} mode results in the appearance of $\frac{1}{2}\langle 111 \rangle$ superlattice reflections (F-spots) in the electron diffraction patterns^[112]. Another type of oxygen rotation is due to an instability of the M_3 optical phonon mode at $\mathbf{q} = (110)(\pi/a)$ or the

M-point of the Brillouin zone. The softening of the M_3 mode results in rotations of octahedra along the same $<001>$ direction in all oxygen layers. The condensation of the M_3 mode does not double the primitive unit-cell along the $<001>$. However, the cog-wheel like rotations of the nearest-linked oxygen octahedron in the $\{001\}$ plane will double the primitive unit-cell along the $<100>$ and $<010>$. Consequently, $\frac{1}{2} <110>$ superlattice reflections can be expected to appear in the electron diffraction patterns^[113]. Viehland *et al.*^[112-113] believe that the polarisation can be constricted by the random octahedral strain due to local oxygen rotations. Constriction of the polarisation was only observed to occur due to R-type oxygen rotations (anti-phase tilt) and no constricted polarisation state was observed to occur due to M-type tilts (in-phase tilt). The constriction of the polarisation is caused by the coupling between the oxygen tilt structures and the spontaneous polarisation.

However, there have been no studies relating the occurrence of anti-phase oxygen octahedral tilting to the MPB or the tetragonal phase PZT compositions. Our studies suggest that anti-phase oxygen octahedral tilting can also occur in tetragonal PZT. Sr^{2+} substitution on the A-site therefore not only decreases T_C , but also introduces tilting of oxygen octahedra. The spontaneous polarisation can therefore be constricted by the random octahedral strain due to the antiphase octahedral tilting^[113]. In other words, the tilting of oxygen octahedra in Sr-doped PZT may obstruct the movement of the domain wall, making materials “harder”.

7.4 Electrical Characterisation

Figure 7.4 shows plots of relative permittivity versus temperature for these MPB compositions. The T_C reduces from ~ 350 to $\sim 150^\circ C$ on doping with up to 16 mol% Sr^{2+} . Broadening of the T_C maximum is also observed with increasing Sr^{2+} content, implying that compositional fluctuations become more evident at high Sr^{2+} content.

Similar results were observed by Pokharel *et al.*^[114] in Ba-doped PbZrO₃. It is assumed that the presence of microregions with local compositions (in the present context Pb²⁺/Sr²⁺ ratio) varying from the average composition is responsible for the broadening of the T_C maximum.

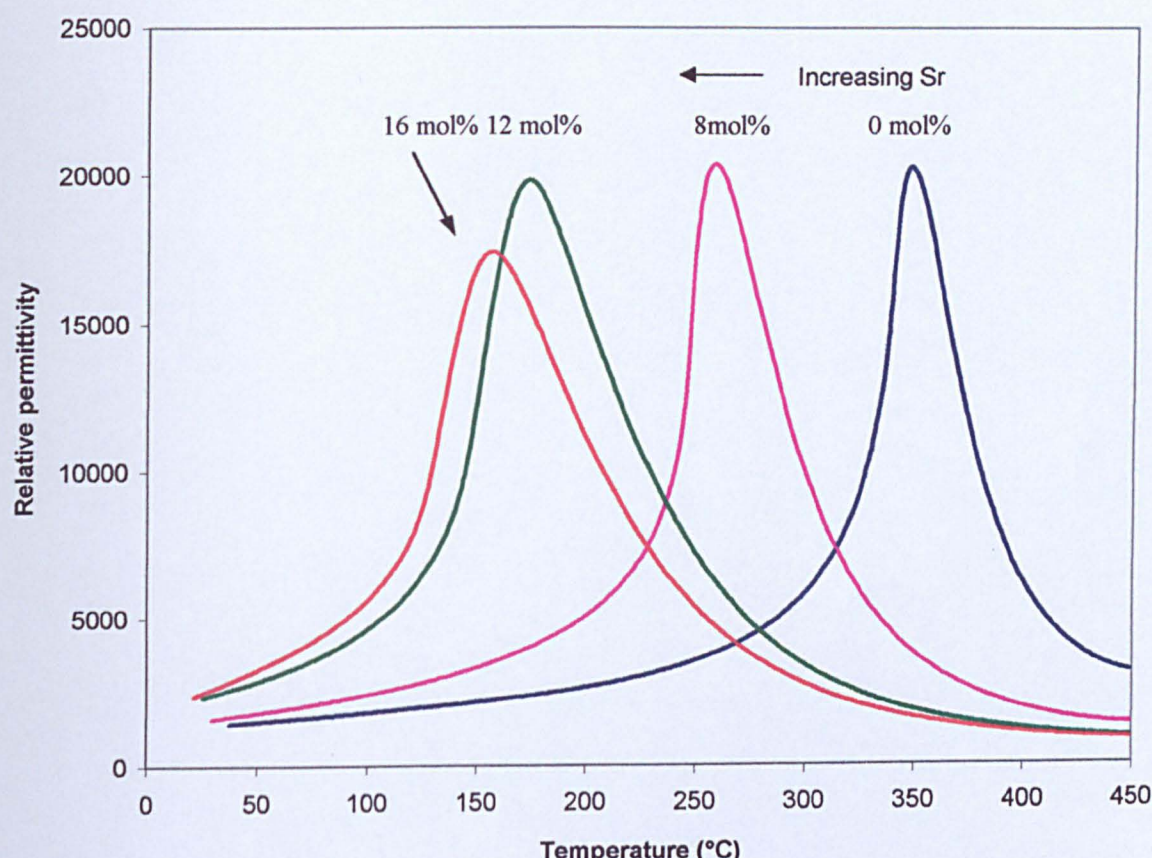


Figure 7.4 Relative permittivities as a function of Sr²⁺ content in optimised Sr-doped PZT ceramics

Consistent with the decrease in T_C , the value of d_{33} increases with increasing Sr²⁺ concentration, Figure 7.5. However, it reaches a maximum ($\sim 640 \text{ pC/N}$) at $\text{Sr}^{2+} = 0.12$, and then decreases for ceramics with $\text{Sr}^{2+} = 0.16$. The increase in d_{33} is commensurate with the decrease in T_C until $x = 0.12$ but the decrease for $x = 0.16$ does not fit this trend, Figure 7.6. This result disagrees with the premise that a lower T_C should reduce the activation energy for domain wall motion at room temperature, thereby softening the material.

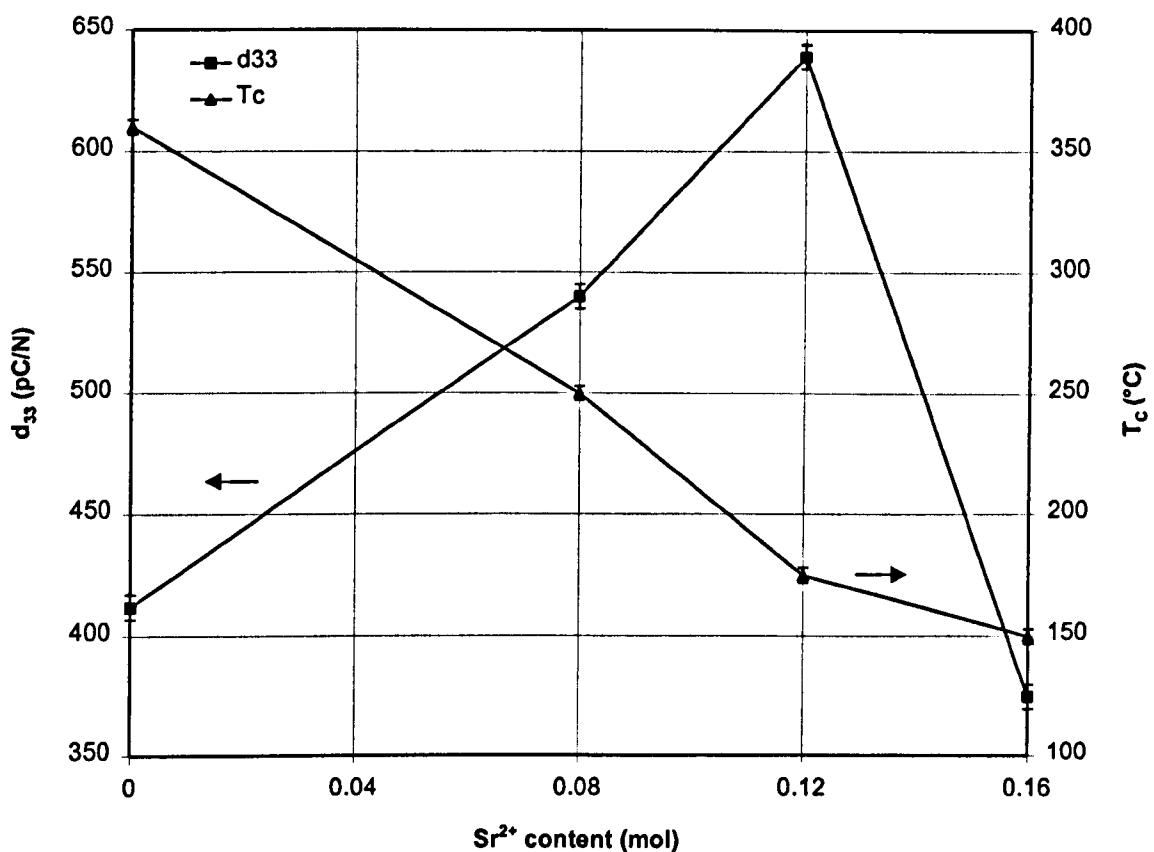


Figure 7.5 d_{33} and T_c as a function of Sr^{2+} content in optimised Sr-doped PZT ceramics

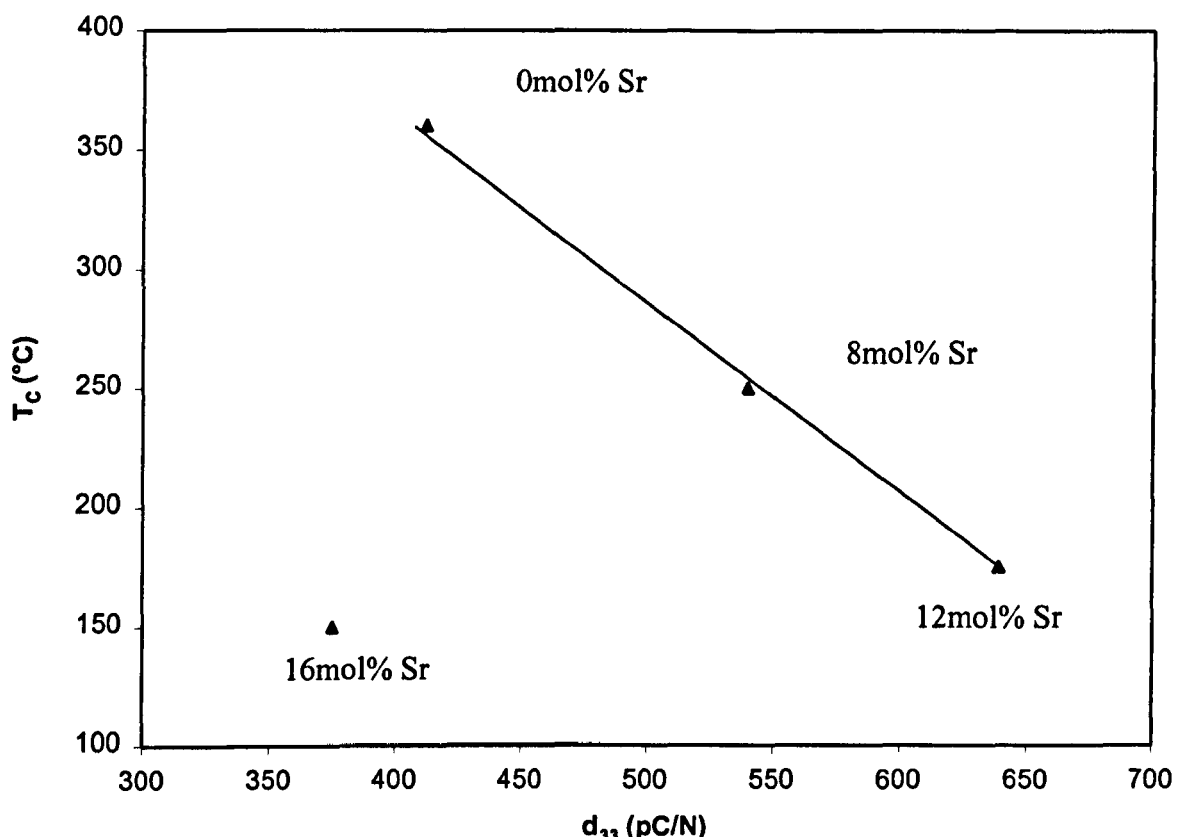


Figure 7.6 T_C versus d_{33} in optimised Sr-doped PZT ceramics

As described previously, in ceramics with $x = 0.08$ and 0.12 , the intensities associated with the superlattice reflections are diffuse and no long-range interaction of the amplitude of tilt occurs. The reflections observed in ceramics with $x = 0.16$ are discrete, implying long-range interaction. It is therefore proposed that for ceramics where $x = 0.16$, the octahedral tilt transition causes a long-range structural distortion which results in an increase in the strain energy of domain walls and therefore activation energy for domain wall motion. This would give rise to smaller extrinsic contributions to d_{33} . The short-range ordered tilting in ceramics where $x = 0.08$ and 0.12 will not cause further macroscopic distortion of the structure, neither increasing the strain energy of the domain walls nor their activation energies for motion.

Figure 7.7 shows hysteresis loops obtained at a frequency of 2 Hz at room temperature for ceramics with Sr^{2+} doping = 0, 0.08, 0.12, and 0.16 respectively. The ceramics all exhibit a square hysteresis loop, which is typical of that associated with a purely FE material. As Sr^{2+} content increases, the coercive field decreases from 1.7 kV/mm to ~ 1 kV/mm, but the remnant polarisation declines from 0.36 C/m^2 to 0.23 C/m^2 . Compared to the 8 and 12 mol% optimised Sr-doped PZT ceramics, the coercive field of the 16 mol% optimised Sr-doped PZT ceramic only slightly decreases, but there is a big drop in remnant polarisation. The lower remnant polarisation in 16 mol% Sr-doped PZT may imply the deterioration in piezoelectric properties, which, in fact, agrees well with the lower d_{33} values for 16 mol% Sr-doped PZT. This assumption is supported by the others's work^[112-113] on the rhombohedral phase PZT, who conclude that the remnant polarisation decreases when the oxygen octahedral tilting occurs.

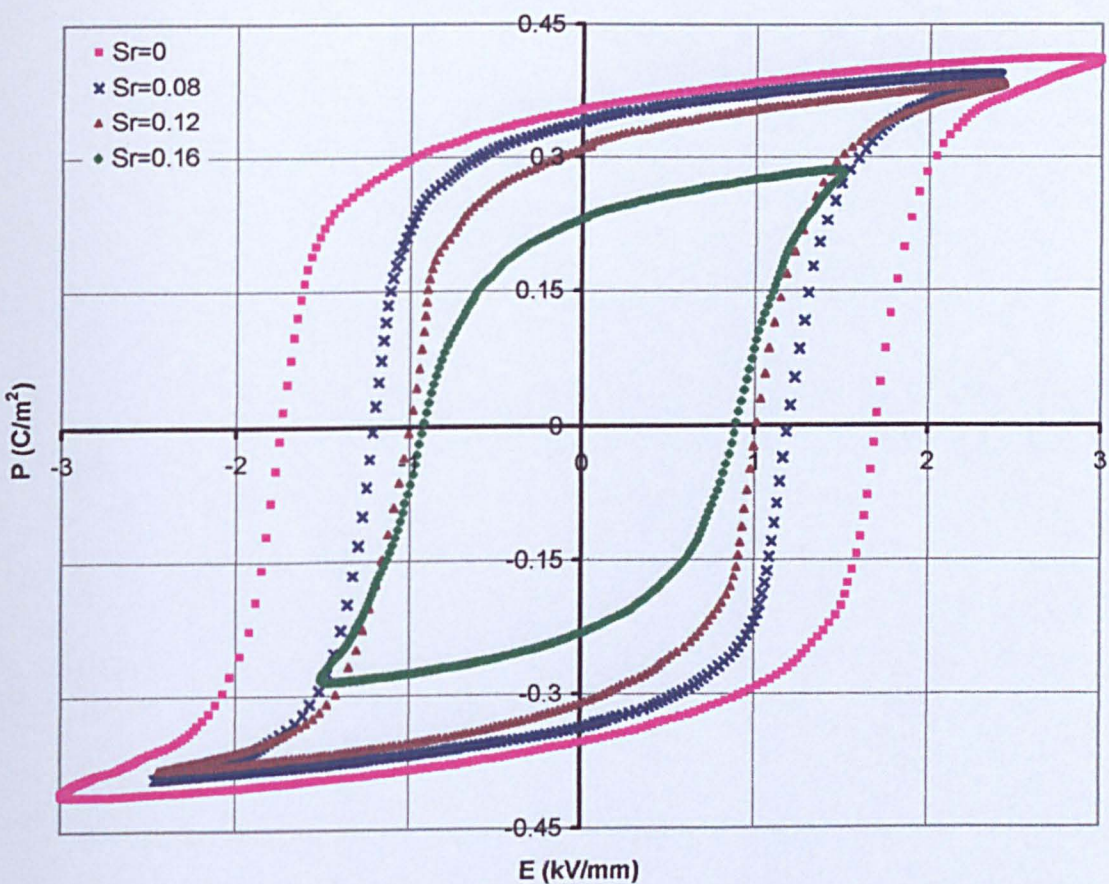


Figure 7.7 Hysteresis loop as a function of Sr^{2+} content in optimised Sr-doped PZT ceramics

7.5 Conclusions

- Sr^{2+} doping in PZT greatly reduces T_C , resulting in an increased d_{33} , which is optimised ($\sim 640 \text{ pC/N}$) in 12 mol% Sr-doped ceramics.
- Electron diffraction patterns suggest that Sr^{2+} doping in PZT promotes the onset of the oxygen octahedral tilting in MPB or tetragonal PZT. The oxygen octahedral tilting arises from the change in tolerance factor by Sr^{2+} substitution on the A-site.
- The presence of anti-phase oxygen octahedral tilting is thought to be responsible for reduction in piezoelectric properties in compositions containing $> 12 \text{ mol\% } \text{Sr}^{2+}$.

8. EFFECTS OF A-SITE Sr, Ba CO-DOPING ON PZT

As discussed previously, the onset temperature of oxygen octahedral tilting is controlled by tolerance factor t . In Chapter 6, Sr^{2+} was substituted onto the A-site in order to decrease T_C . Sr^{2+} has an effective ionic radius in 12-fold coordination with oxygen of 0.144 nm , smaller than Pb^{2+} (0.149 nm). Sr^{2+} substitution for Pb^{2+} on the A-site thus decreases the tolerance factor t and therefore results in the onset of oxygen octahedral tilting. Ba^{2+} , on the other hand, has a radius of $0.16\text{ nm}^{[111]}$, larger than Pb^{2+} . Substitution of Ba^{2+} onto the A-site will therefore tend to increase t but T_C will still reduce since Ba^{2+} has a lower polarisability than Pb^{2+} (T_C 's for PbTiO_3 and BaTiO_3 are 495°C and 130°C , respectively). For example, $(\text{Pb}_{1-x-y}\text{Sr}_x\text{Ba}_y)(\text{Zr}_{0.538}\text{Ti}_{0.438}\text{Sb}_{0.024})\text{O}_3$ ($x = y = 0.06$) has a t of 0.989 , similar to undoped $\text{Pb}(\text{Zr}_{0.538}\text{Ti}_{0.438}\text{Nb}_{0.024})\text{O}_3$ ($t = 0.988$). In this case, the temperature of the tilt transition would be expected to decrease to below room temperature and superlattice reflections should be absent.

A series of $(\text{Pb}_{1-x-y}\text{Sr}_x\text{Ba}_y)(\text{Zr}_{0.538}\text{Ti}_{0.438}\text{Sb}_{0.024})\text{O}_3$ compositions at different x, y values were made according to Table 3.8. All the fired samples have relative densities $> 95\%$ of theoretical. Their structures, microstructures were then characterised using XRD and TEM.

8.1 Sr, Ba co-doped PZT with a Fixed Zr:Ti ratio

8.1.1 Structure

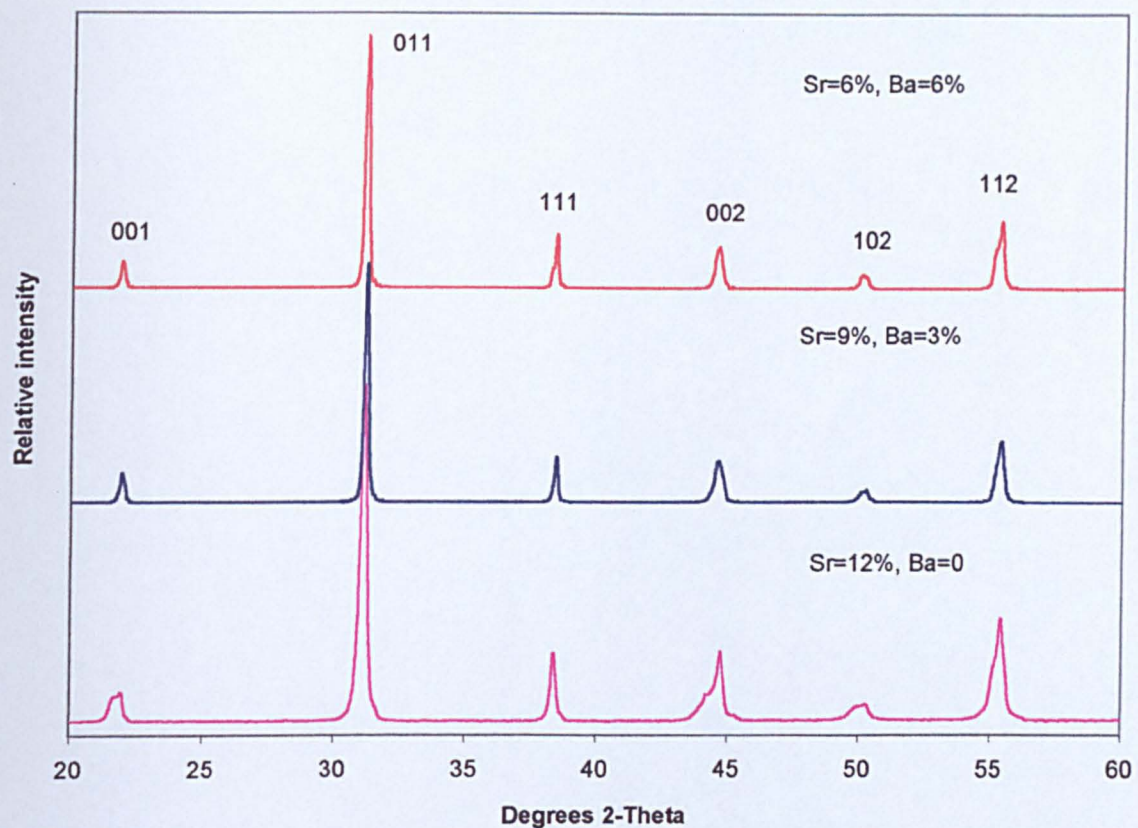


Figure 8.1 XRD traces from Sr, Ba co-doped PZT with a fixed Zr:Ti ratio of 1.227

Figure 8.1 reveals XRD patterns from $(\text{Pb}_{1-x-y}\text{Sr}_x\text{Ba}_y)(\text{Zr}_{0.538}\text{Ti}_{0.438}\text{Sb}_{0.024})\text{O}_3$ ceramics, sintered 4h at 1140°C where (a) $x = 0.12$, $y = 0$; (b) $x = 0.09$, $y = 0.03$; and (c) $x = 0.06$, $y = 0.06$. Ceramics with $x = 0.12$, $y = 0$ contain mixed rhombohedral/tetragonal phases. Increasing Ba^{2+} content stabilises the rhombohedral over the tetragonal phase. Ceramics with $x = 0.06$, $y = 0.06$ are purely rhombohedral,

indicated by peak splitting on the {111} and disappearance of peak splitting on the {002}. These results demonstrate that Ba^{2+} is less significant than Sr^{2+} in promoting tetragonality in PZT.

8.1.2 Electrical Characterisation

Figure 8.2 shows relative permittivity versus temperature for the compositions in Figure 8.1. It is evident that the effect of Ba^{2+} substitution on decreasing T_C is not as drastic as Sr^{2+} since the T_C for 6 mol% Sr and Ba co-doped PZT is about 20°C higher compared to that of 12 mol% Sr-doped PZT of the same Zr:Ti ratio.

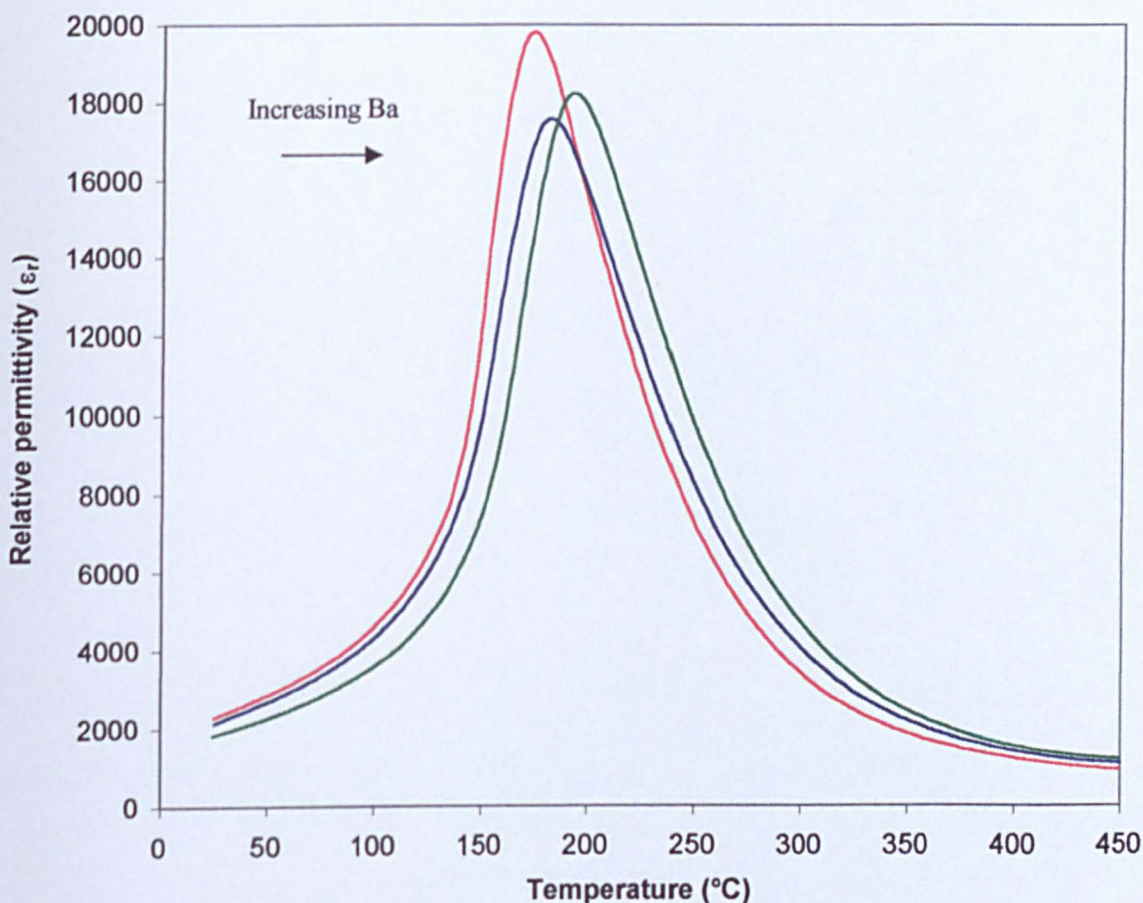


Figure 8.2 Relative permittivities of Sr, Ba co-doped PZT with a fixed Zr:Ti ratio of 1.227

Figure 8.3 shows the d_{33} data of samples in Figure 8.1. d_{33} decreases with increasing Ba^{2+} content mainly due to the fact that the phase has been moved away from the MPB when Ba^{2+} is incorporated on the A-site in PZT.

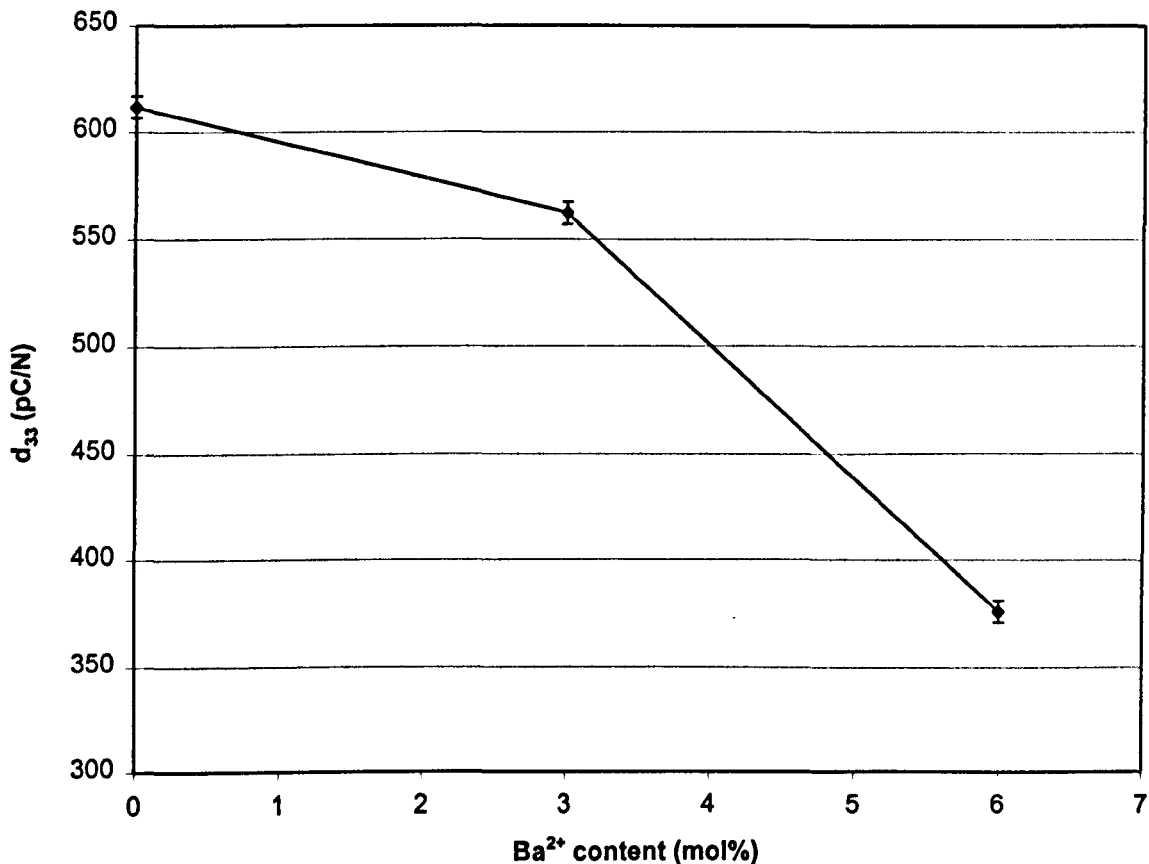


Figure 8.3 d_{33} data of Sr, Ba co-doped PZT with a fixed Zr:Ti ratio of 1.227

8.2 6 mol% Sr, Ba co-doped PZT with Varying Zr:Ti Ratio

To compensate the rhombohedral phase induced by Ba^{2+} doping for achieving the MPB composition and therefore the optimum d_{33} , 6 mol%Sr, and 6 mol%Ba co-doped PZT ceramics were prepared by varying Zr:Ti ratio.

8.2.1 Structure and Microstructure

XRD, Figure 8.4 reveals that decreasing Zr:Ti ratio changes the phase from rhombohedral across the MPB to tetragonal, indicated by emergence of {002} peak splitting and disappearance of {111} peak splitting. This observation is consistent with the results in Chapters 5 and 6 in Nb, and Sr-doped PZT.

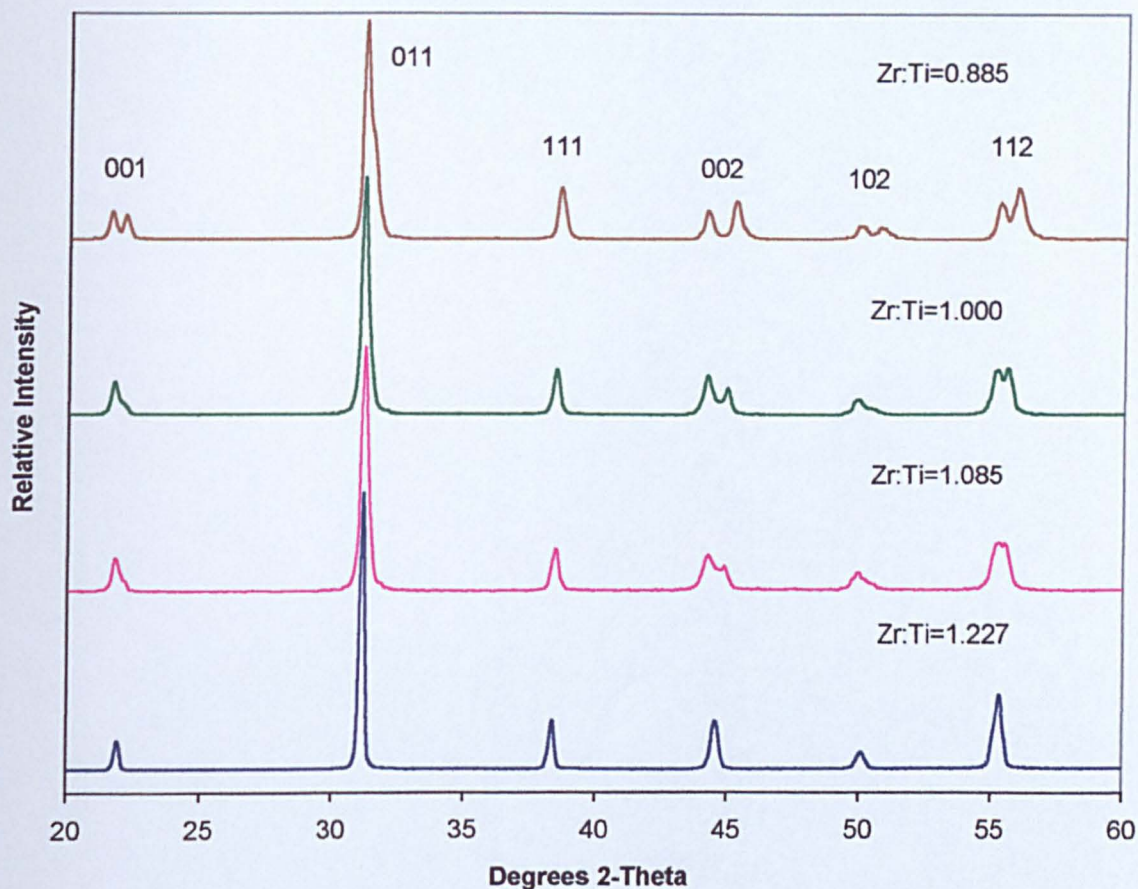


Figure 8.4 XRD traces from 6mol% Sr, Ba co-doped PZT as a function of Zr:Ti ratio

Figures 8.5 (a-b) show electron diffraction patterns along the pseudocubic $\langle 110 \rangle$ zone axes for 6 mol% Sr, Ba co-doped PZT where Zr:Ti ratio = 1.227 and 0.885 respectively. All the reflections can be indexed according to the fundamental perovskite structure, with $a = \sim 0.40\text{ nm}$. There is no evidence of superlattice reflections, which

verifies that Sr, Ba ($x = y = 0.06$) co-doping can eliminate the onset of the oxygen octahedral tilting transition to below room temperature.

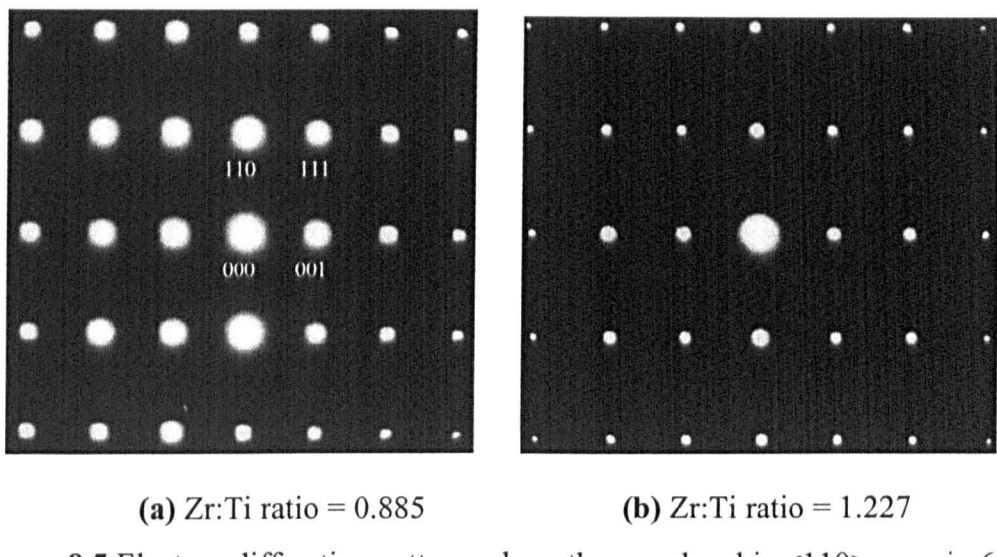


Figure 8.5 Electron diffraction patterns along the pseudocubic $<110>$ zone in 6 mol% Sr, Ba co-doped PZT ceramics

Figures 8.6 (a-b) are electron diffraction patterns along the pseudocubic $<100>$ zone axes for 6 mol% Sr, Ba co-doped PZT samples. No superlattice reflections occur either at $\frac{1}{2} \{hk0\}$ or $\frac{1}{2} \{h00\}$ positions, indicating neither antiparallel displacement of cations nor in-phase tilting occurs in Sr, Ba co-doped PZT.

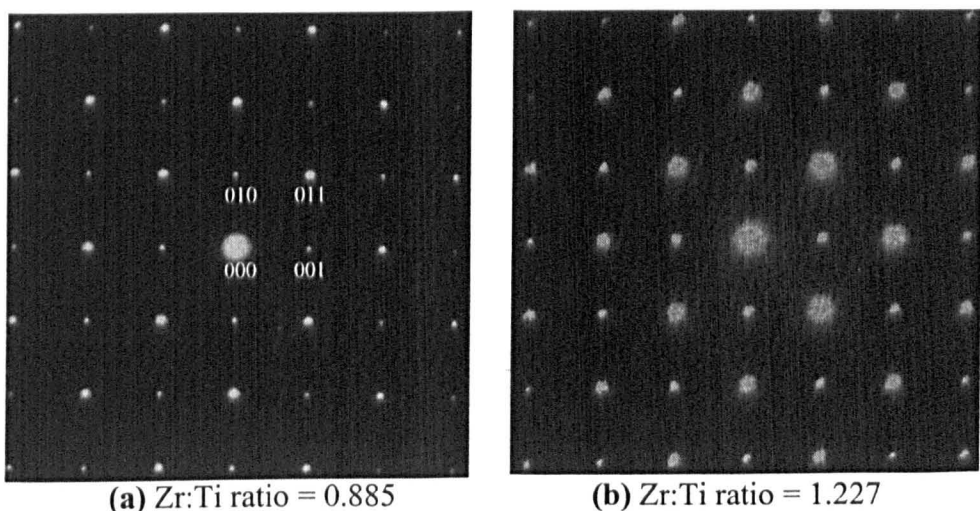


Figure 8.6 Electron diffraction patterns along the pseudocubic $<100>$ zone in 6 mol% Sr, and Ba co-doped PZT ceramics

Domain structures of Sr, Ba co-doped PZT ceramics were investigated using TEM. The following TEM images were taken at a general two-beam condition, not at a specific zone axis.

Figure 8.7 is a BF TEM image revealing 90° domains (~ 50 nm wide) in $x = y = 0.06$ co-doped tetragonal PZT (Zr:Ti ratio = 0.885) similar to those observed in Nb-doped tetragonal PZT in Chapter 5.

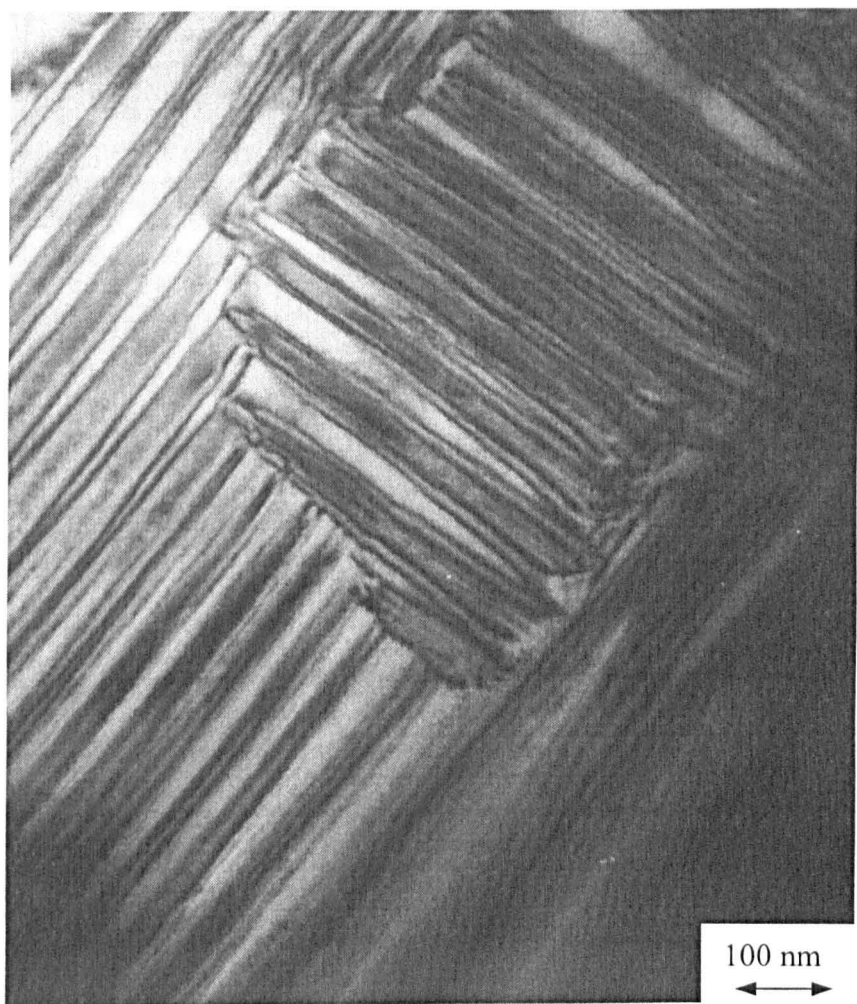


Figure 8.7 BF-TEM image showing 90° domains in 6 mol% Sr, and Ba co-doped tetragonal PZT

BF TEM images of ($x = y = 0.06$) rhombohedral PZT (Zr:Ti ratio = 1.227) revealed wavy domains (~ 10 nm wide) in almost all grains, rarely seen in Sr-doped PZT, Figure 8.8. This suggests that introducing Ba^{2+} in Sr-doped PZT not only eliminates the onset of oxygen octahedral tilting, but also may bring about changes in domain structure, particularly in the rhombohedral phase. Wavy domains are usually observed in relaxor materials, which imply that Ba^{2+} substitution in PZT may induce relaxor behaviour.



Figure 8.8 BF-TEM image showing wavy domains in 6mol% Sr, and Ba co-doped rhombohedral PZT

Substitution of Pb^{2+} by Ba^{2+} in an antiferroelectric material PbZrO_3 (PZ) was reported to induce relaxor behaviour^[114]. For $0.15 \leq x \leq 0.25$, $(\text{Pb}_{1-x}\text{Ba}_x)\text{ZrO}_3$ (PBZ) exhibited normal ferroelectric transition above room temperature. But for $x = 0.30$, PBZ exhibited relaxor behaviour. In PBZ with $0.15 \leq x \leq 0.25$, the room temperature phase is

ferroelectric and possesses a rhombohedral structure^[110, 114]. When ~30% Ba²⁺ is substituted onto the A-site, relaxor behaviour is induced in rhombohedral PBZ. Refined structural parameter studies^[114] show that the displacement of Pb²⁺/Ba²⁺ and Zr⁴⁺ along the [111] of the rhombohedral cell decreases with increasing Ba²⁺ content. Thermal parameters^[114] indicate disorder in the position of Pb²⁺/Ba²⁺ along the triad axis increases with Ba²⁺ content. This, along with the smaller shifts in A and B site cations, may be responsible for the relaxor behaviour for higher Ba²⁺ content PBZ. As Ba²⁺ content increases, the disruption of dipolar coupling also increases and its correlation length diminishes. This results in a decreasing domain size until short-range dipolar order (relaxor behaviour) is achieved with an effective domain size of ~ 5 – 10 nm^[41]. The reduction in domain width observed in PSBZT ceramics where x = y = 0.06 in this study represents a structure where the correlation length of dipolar coupling is reduced but not sufficiently to induce relaxor behaviour.

8.2.2 Electrical Characterisation

Figure 8.9 shows relative permittivity versus temperature for the compositions in Figure 8.4. As the Zr:Ti ratio is decreased from 1.227 to 0.885, the T_C rises from ~195°C to ~240°C. The effect of Ba²⁺ substitution on reducing T_C is not as dramatic as that of Sr²⁺ substitution since the T_C for $(\text{Pb}_{0.88}\text{Sr}_{0.06}\text{Ba}_{0.06})(\text{Zr}_{0.538}\text{Ti}_{0.438}\text{Sb}_{0.024})\text{O}_3$ is about 20°C higher than that of $(\text{Pb}_{0.88}\text{Sr}_{0.12})(\text{Zr}_{0.538}\text{Ti}_{0.438}\text{Sb}_{0.024})\text{O}_3$ which has the same isovalent dopant content.

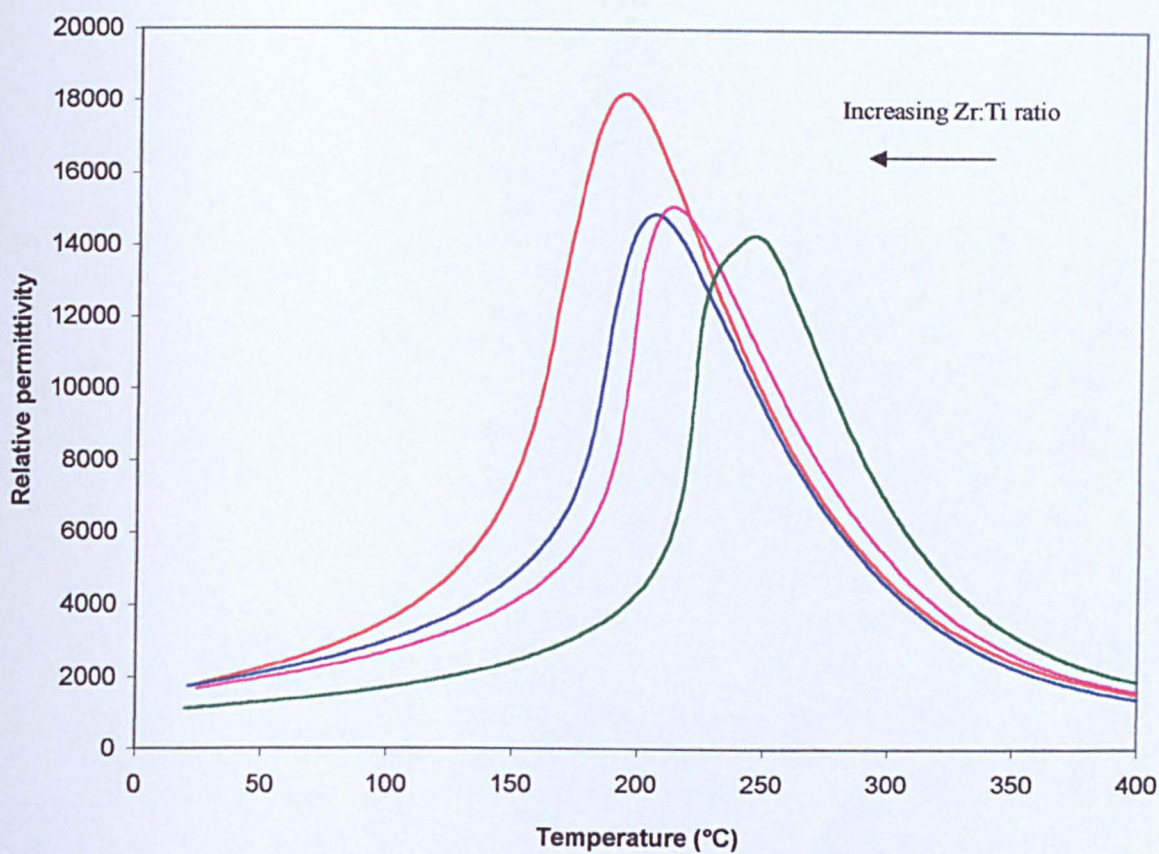


Figure 8.9 Relative permittivities of 6 mol% Sr, Ba co-doped PZT with varying Zr:Ti ratio

Figure 8.10 shows the d_{33} data of $(\text{Pb}_{1-x-y}\text{Sr}_x\text{Ba}_y)(\text{Zr}_{0.976-z}\text{Ti}_z\text{Sb}_{0.024})\text{O}_3$ ($x = y = 0.06$) at different Zr:Ti ratios. The optimised value of d_{33} is 520 pC/N at Zr:Ti = 1.085. This value is lower than the d_{33} for ceramics where $x = 0.12$, $y = 0$ but the T_C for the 6 mol% Ba and Sr co-doped PZT ceramics is 30°C higher ($d_{33} = 640 \text{ pC/N}$, $T_C = \sim 175^\circ\text{C}$ for $x = 0.12$, $y = 0$ and $d_{33} = 520 \text{ pC/N}$, $T_C = \sim 205^\circ\text{C}$ for $x = y = 0.06$). Ideally, to make a direct comparison, a Sr-doped PZT composition is required which has a T_C within a few degrees of the ceramics where $x = y = 0.06$. MPB ceramics where $x = 0.08$, $y = 0$, have a $T_C \sim 250^\circ\text{C}$, 45°C higher, but d_{33} ($\sim 540 \text{ pC/N}$) is still larger than Sr, Ba co-doped PZT ceramics ($d_{33} \sim 520 \text{ pC/N}$, $T_C \sim 205^\circ\text{C}$ for $x = y = 0.06$). This would suggest that Ba^{2+} and Sr^{2+} ($x = y = 0.06$) co-doping has little effect on ceramics in which short rather than long-range ordered tilting occurs. Using a co-doping technique to reduce T_C

to 150°C would give a direct comparison with ceramics where $x = 0.16$ in which long-range ordered octahedral tilting is present. However, the increased disruption in dipolar coupling associated with increasing Ba^{2+} content may lead to the formation of a relaxor phase which would have zero intrinsic piezoelectricity.

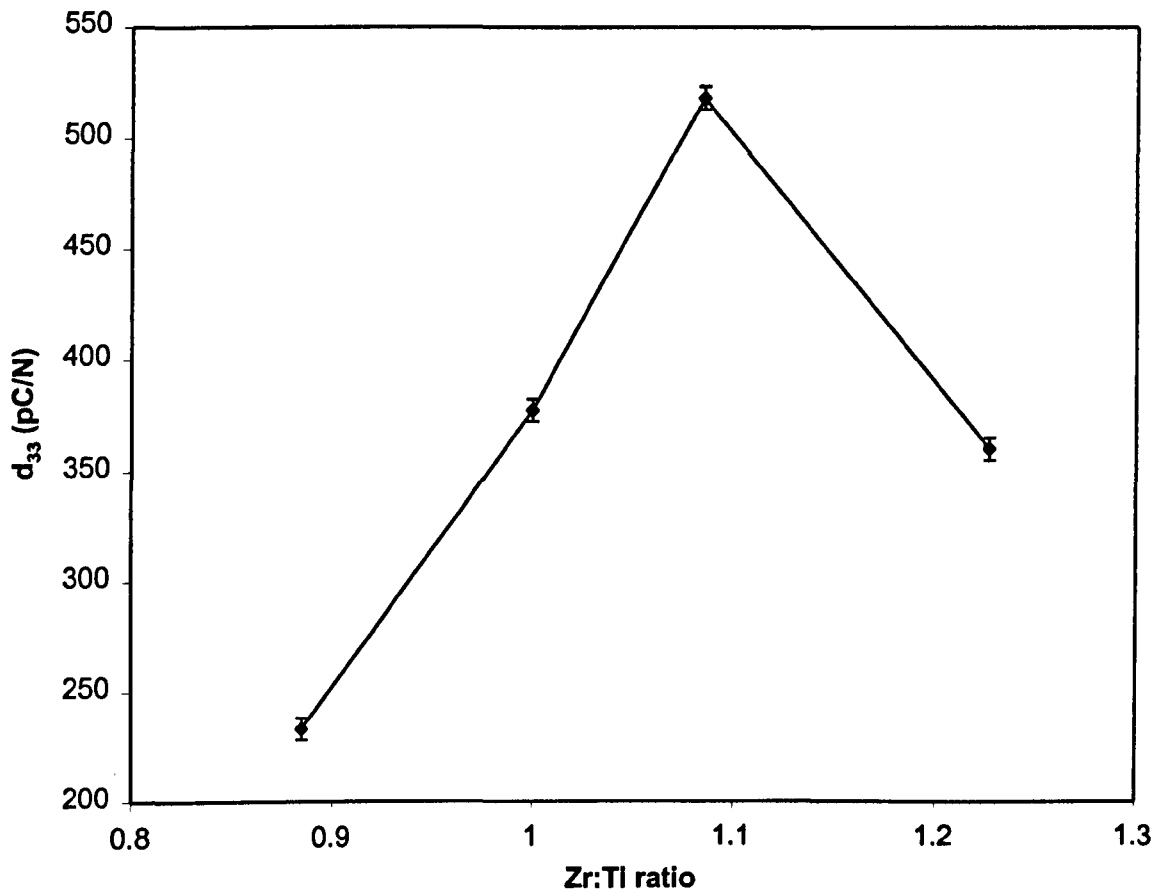


Figure 8.10 d_{33} data of 6 mol% Sr, Ba co-doped PZT with varying Zr:Ti ratio

8.3 Conclusions

- Sr, Ba co-doping can eliminate the onset of oxygen octahedral tilting, but it does not improve d_{33} .
- Ba²⁺ substitution on the A-site has a less dramatic effect than Sr²⁺ in promoting tetragonality in PZT.
- Wavy domains observed in Ba, Sr co-doped rhombohedral phase PZT imply that introducing Ba²⁺ on the A-site in PZT may induce relaxor behaviour, which is responsible for the deterioration in piezoelectric properties.

9. SURFACE DECOMPOSITION OF Sr-DOPED PZT

The volatility of the PbO component in PZT ceramics associated with the sintering has historically been a stumbling block to the reproducible production of high-quality PZT ferroelectric ceramics. PbO volatilisation, and the resultant variation in composition, affects both the density and the intrinsic electrical properties. In this chapter, the effect of sintering temperature on phase stability of $\text{Pb}_{0.88}\text{Sr}_{0.12}\text{Zr}_{0.538}\text{Ti}_{0.438}\text{Sb}_{0.024}\text{O}_3$ (PSZT12/44, d_{33} -optimised 12 mol% Sr-doped PZT) ceramics was examined. XRD, SEM and TEM were used to study the phase assemblage and microstructure, paying particular attention to the surface decomposition and its effect on relative permittivity ϵ_r .

9.1 Effect of sintering temperature on the stability of perovskite phase

XRD, Figure 9.1 from the surface of sintered PSZT12/44 ceramics reveals that, although the tetragonal perovskite phase is always present after sintering 4h from 1070–1280°C, the degree of tetragonality increases with sintering temperature. After 4h at 1070°C, asymmetry on the left side of the {002} peak occurs whereas clear splitting is evident after 4h at >1120°C. Simultaneously, the intensity of the second phase peak at 27° (20) increases with increasing sintering temperature and further non-perovskite reflections emerge at $T \geq 1170^\circ\text{C}$. After 4h at 1280°C, substantial second phase

reflections are present. All non-perovskite reflections fit with monoclinic ZrO_2 with $a = 0.5151\text{ nm}$, $b = 0.5212\text{ nm}$ and $c = 0.5317\text{ nm}$ ^[116].

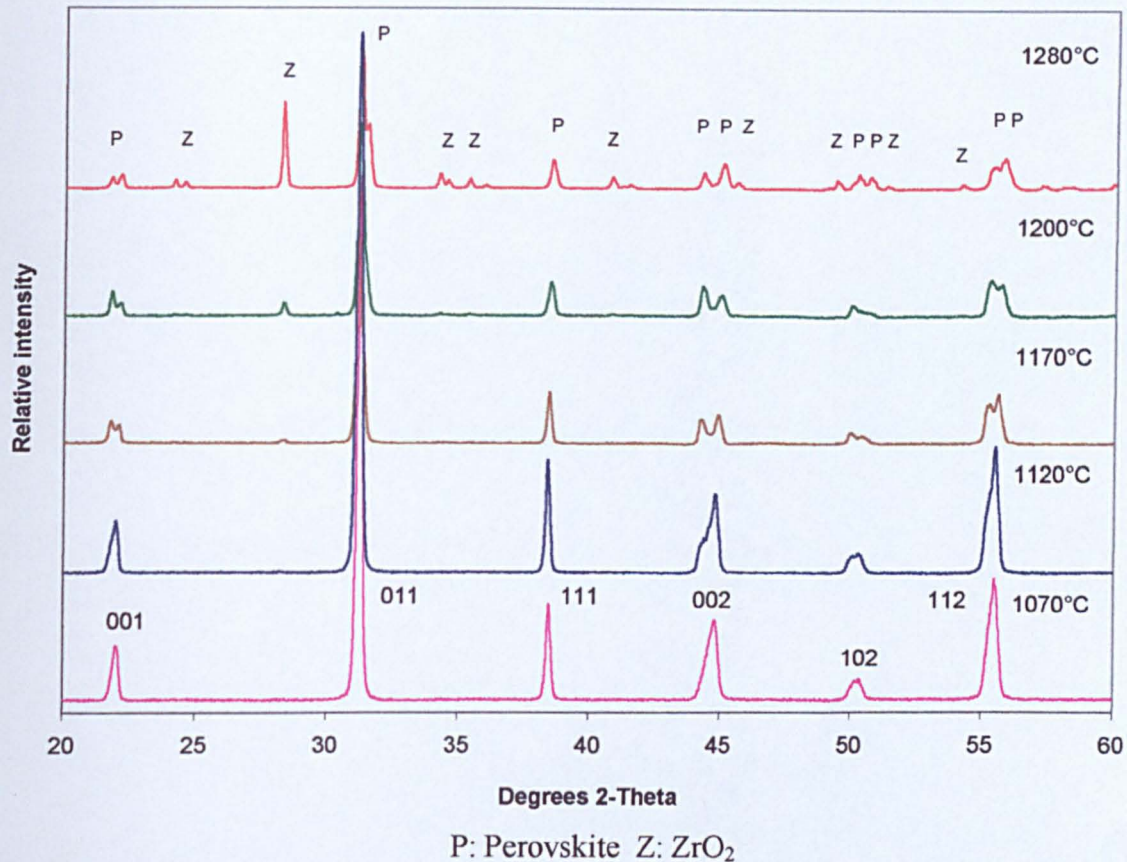


Figure 9.1 XRD traces of PSZT12/44 ceramics sintered 4h at different temperatures

The relative amounts of perovskite and second phase were quantified according to the following formula:

$$P_p \% = \frac{I_{P_p}}{I_{P_s} + I_{P_p}} \times 100 \quad P_s \% = \frac{I_{P_s}}{I_{P_s} + I_{P_p}} \times 100$$

where $P_p\%$ and $P_s\%$ are the volume percentage of perovskite and second phases formed respectively, I_{P_p} is the relative intensity of the major X-ray peak for the perovskite phase, which has a d spacing of 0.287 nm , and I_{P_s} is the relative intensity of the major X-ray peak for the second phase, which has a d-spacing of 0.316 nm .

Quantitative XRD indicated the sintered surface of PSZT12/44 ceramics contained 38 vol.% second phase. In addition, the $c:a$ ratio as a function of sintering temperature of the perovskite phase was calculated using the intensity of the split {002} peaks. After 4h at 1070°C the $c:a$ ratio is 1. However, after 4h at 1280°C, the $c:a$ ratio of the sintered surface of PSZT is 1.02.

To determine whether decomposition of PSZT12/44 was limited to sintered surfaces or was present throughout the bulk, XRD was performed on samples from which the surface was ground to a depth of ~0.5 mm. Samples still exhibited a tetragonal perovskite phase but the intensity of the main ZrO_2 peak was greatly reduced, giving a calculated value for the percentage second phase of only 4%, Figure 9.2.

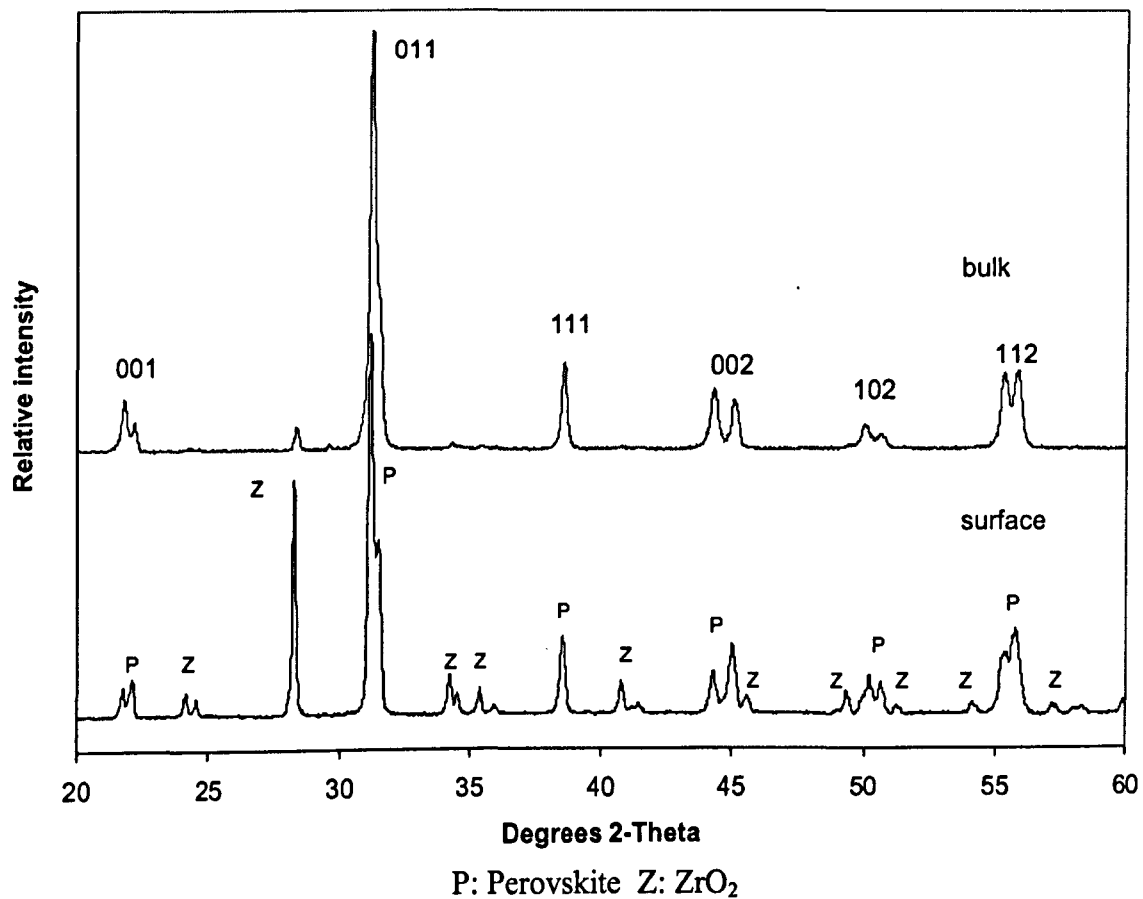


Figure 9.2 XRD traces of bulk and surface PSZT12/44 ceramics sintered 4h at 1280°C

A visual inspection of the pellets sintered 4h at 1280°C in cross section revealed a light contrast surface layer ($\sim 0.5\text{ mm}$). To further investigate this surface phenomenon, SEM, and TEM samples were prepared in cross-section.

9.2 Microstructure

Figure 9.3 shows a cross-sectional SEI SEM image of a thermally etched PSZT12/44 sample sintered 4h at 1280°C, revealing the change in morphology between surface and bulk.

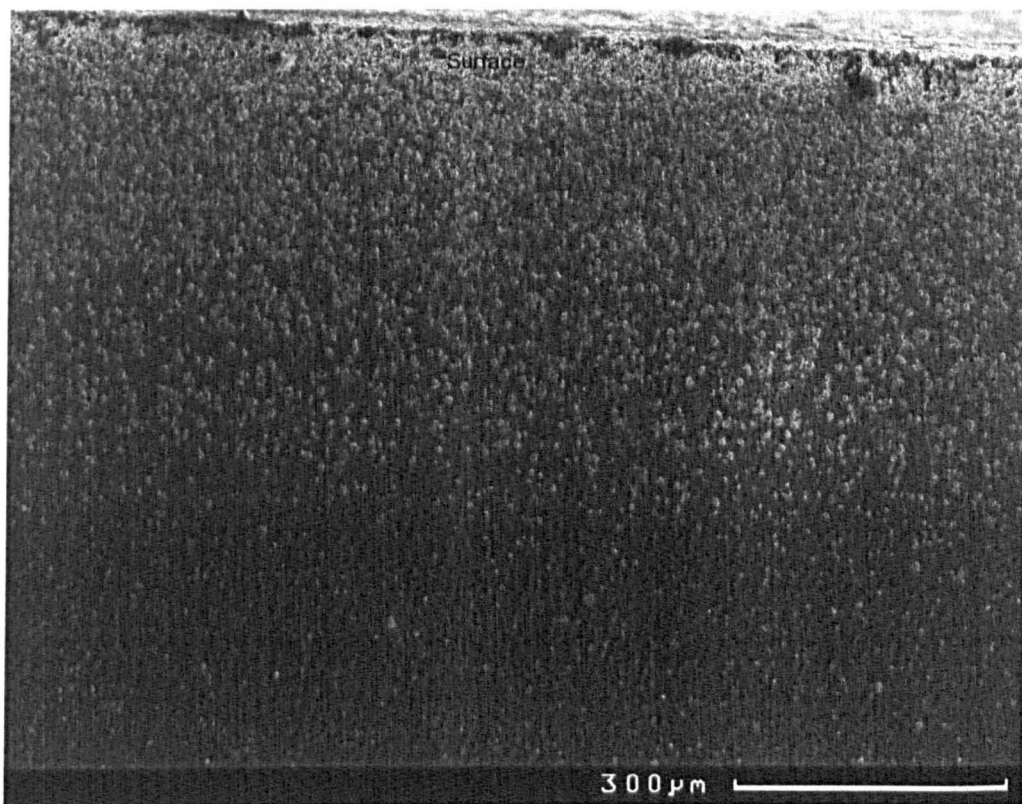


Figure 9.3 Cross-sectional SEI SEM image of a thermally-etched PSZT12/44 ceramic,
sintered 4h at 1280°C

In the region close to the surface, clusters of submicron ($\sim 0.8 \mu\text{m}$) fine particles are dispersed within large particles, shown in detail in Figure 9.4. SEM analysis also reveals high levels of porosity in this surface region consistent with PbO loss.

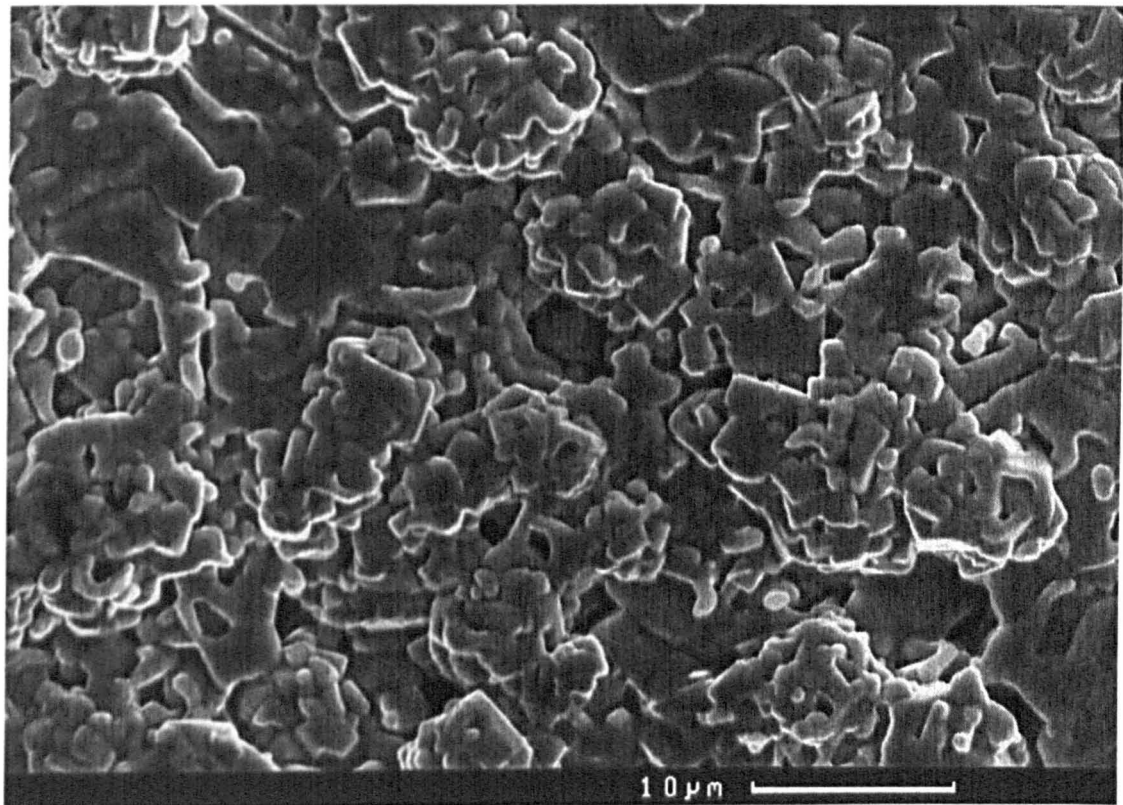


Figure 9.4 SEI showing a region close to the PSZT12/44 surface, sintered 4h at 1280°C

In the bulk of the sample, a conventional grain structure (3-4 μm in size), typical of PZT based ceramics^[117], is observed, Figure 9.5. Compared to the surface (Figure 9.4), levels of porosity are much lower in the bulk.

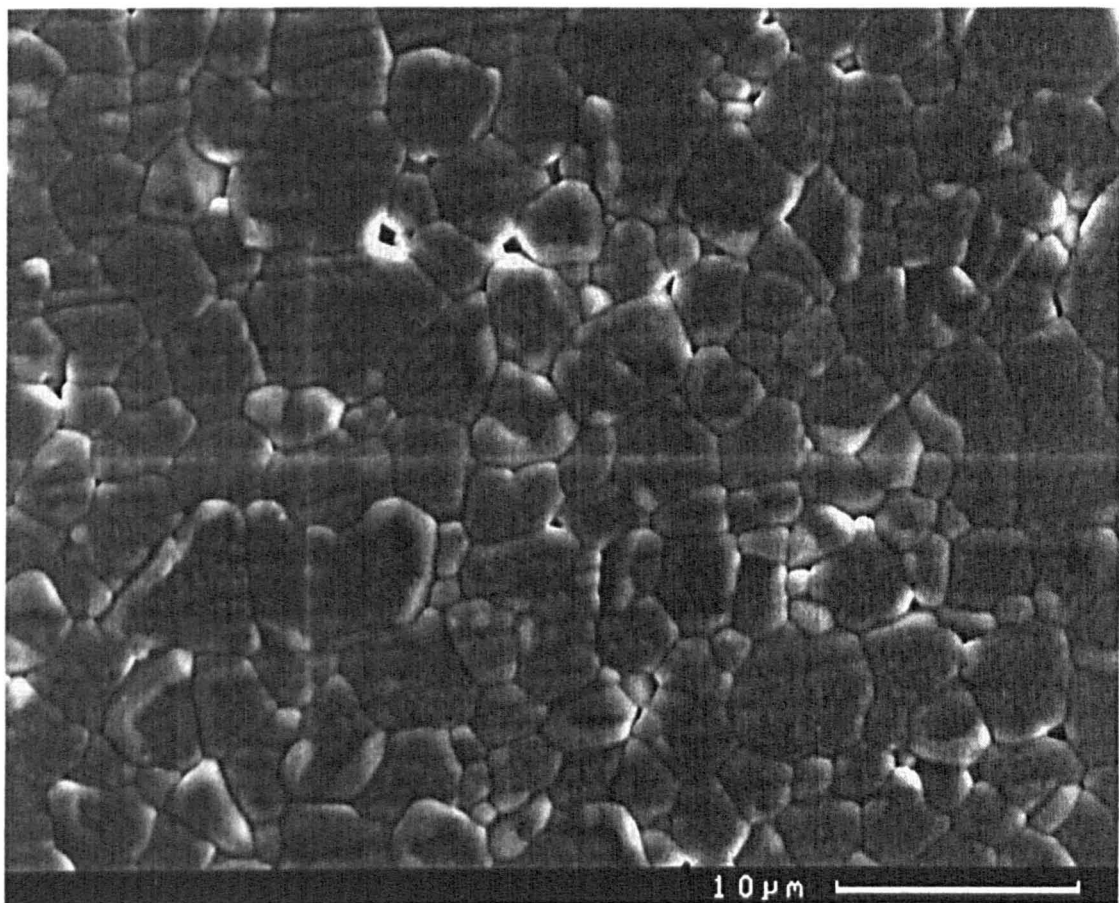


Figure 9.5 SEI showing perovskite grains in the bulk of PSZT12/44 (1280°C, 4h)

Figure 9.6(a) is a BF-TEM image from a cross-section of a PSZT12/44 sample sintered 4h at 1280°C. Regions of perovskite adjacent to second phase particles were commonly observed. Typically, each second phase particle was surrounded by several perovskite grains, which were identified by electron diffraction, Figure 9.6(b) and EDS, Figure 9.6(c).

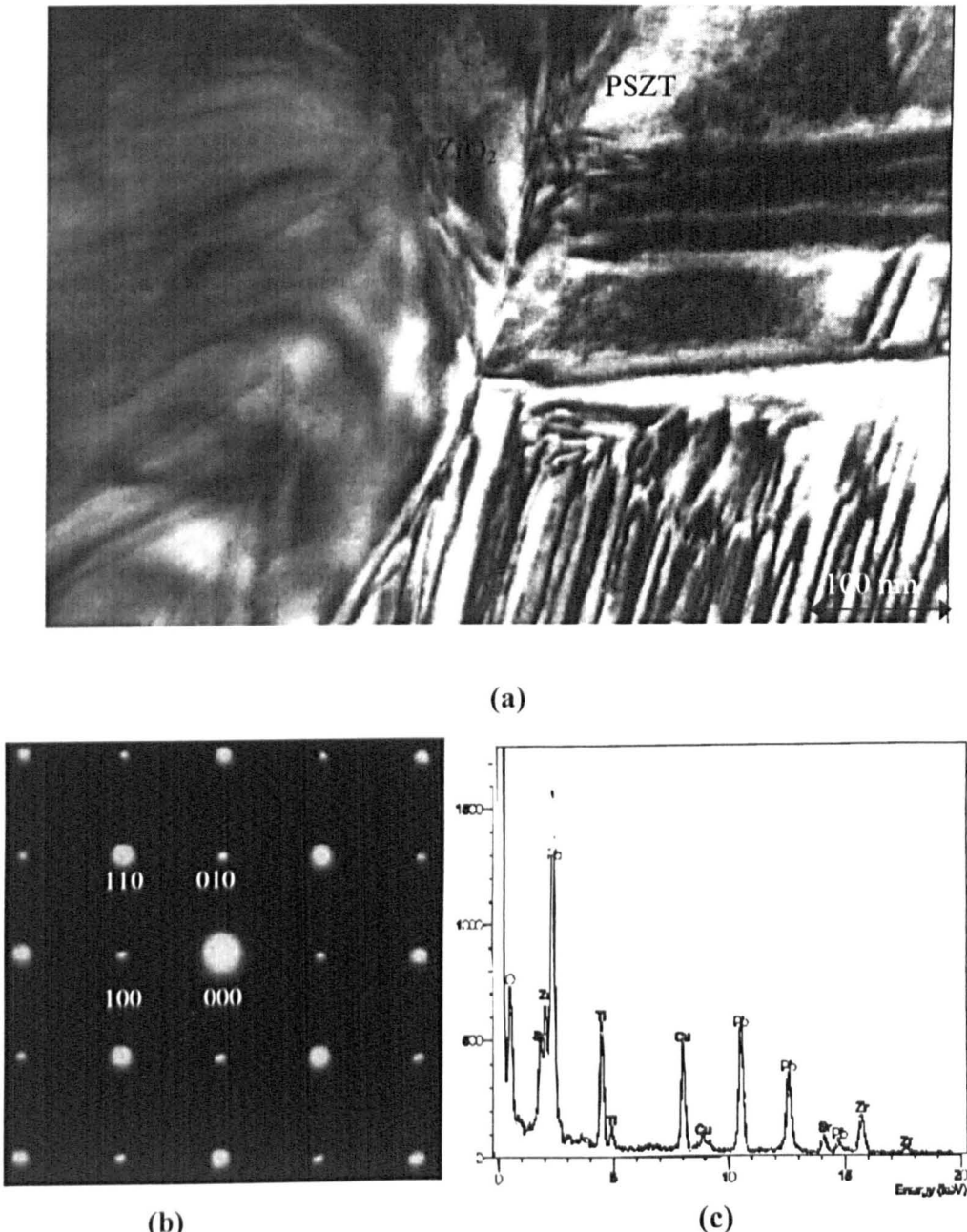
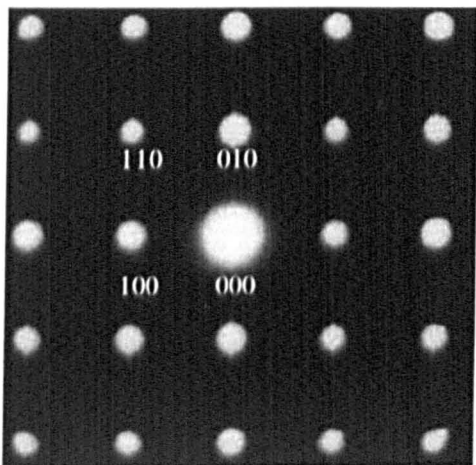


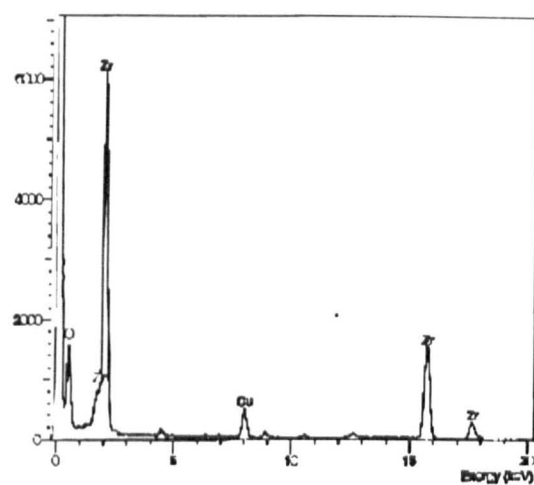
Figure 9.6 (a) BF-TEM image showing the interface between a second phase ZrO_2 and perovskite matrix phase (b) [001] zone axis electron diffraction pattern from a perovskite grain in PSZT12/44 (1280°C , 4h) (c) EDS spectrum from a perovskite grain in PSZT12/44 (1280°C , 4h). The Cu is from the sample supporting grid.



(a)



(b)



(c)

Figure 9.7 (a) BF-TEM image showing typical ferroelastic domains in monoclinic ZrO_2 (b) [001] zone axis electron diffraction pattern and (c) EDS spectrum from a ZrO_2 grain in PSZT12/44 (1280°C , 4h). The Cu is from the sample supporting grid.

The second phase was determined to be pure ZrO_2 by electron diffraction, Figure 9.7(b) and EDS, Figure 9.7(c), and contained a ferroelastic domain structure, 100 nm in width, typical of monoclinic ZrO_2 ^[118], Figure 9.7(a). In contrast, the regions of PZT contained ferroelectric/ferroelastic domains of about 30 nm in width. The lattice parameters of ZrO_2 and perovskite phase calculated from their electron diffraction patterns are $\sim 0.53\text{ nm}$ and $\sim 0.40\text{ nm}$ respectively in good agreement with XRD (Figures 9.1 & 9.2).

9.3 Mechanism of Decomposition

Two further facts help elucidate the decomposition reaction. First, PbO loss is known to occur from the surface of PZT at high temperatures^[119]. This effect becomes increasingly significant as temperature increases and results in decomposition by $\sim 1500^\circ\text{C}$. Second, substitution of Sr^{2+} onto the A-site stabilises the tetragonal rather than rhombohedral phase, and the $\text{Zr}:\text{Ti}$ ratio must be increased to produce an MPB composition, as described in Chapters 6 & 7. PbO , therefore is lost from the surface of PSZT not only due to its high volatility (PbO melts at 880°C)^[120] but also because Sr^{2+} favours a tetragonal perovskite structure, resulting in the precipitation of ZrO_2 particles from solid solution simultaneously with an increase in tetragonality of the PZT.

If the mechanism occurs as suggested, undoped PZT samples should be more stable and less prone to surface decomposition than Sr-doped PZT. Figure 9.8 is an XRD pattern from a MPB PZT composition sintered 4h at 1280°C , which has not been doped with Sr^{2+} on the A-site. There is no evidence of decomposition. However, since these two samples have $\text{Zr}:\text{Ti}$ ratios of 1.13 and 1.23, respectively, the influence of the

Zr:Ti ratio is not consistent. To further verify the decomposition mechanism, undoped PZT samples, which have Zr:Ti ratio of 1.23 were prepared. Figure 9.9 shows XRD from an undoped PZT with a Zr:Ti ratio of 1.23 sintered 4h at 1280°C. No evidence of decomposition is observed. The influence of the Zr:Ti ratio on the decomposition can therefore be regarded as not significant in this case.

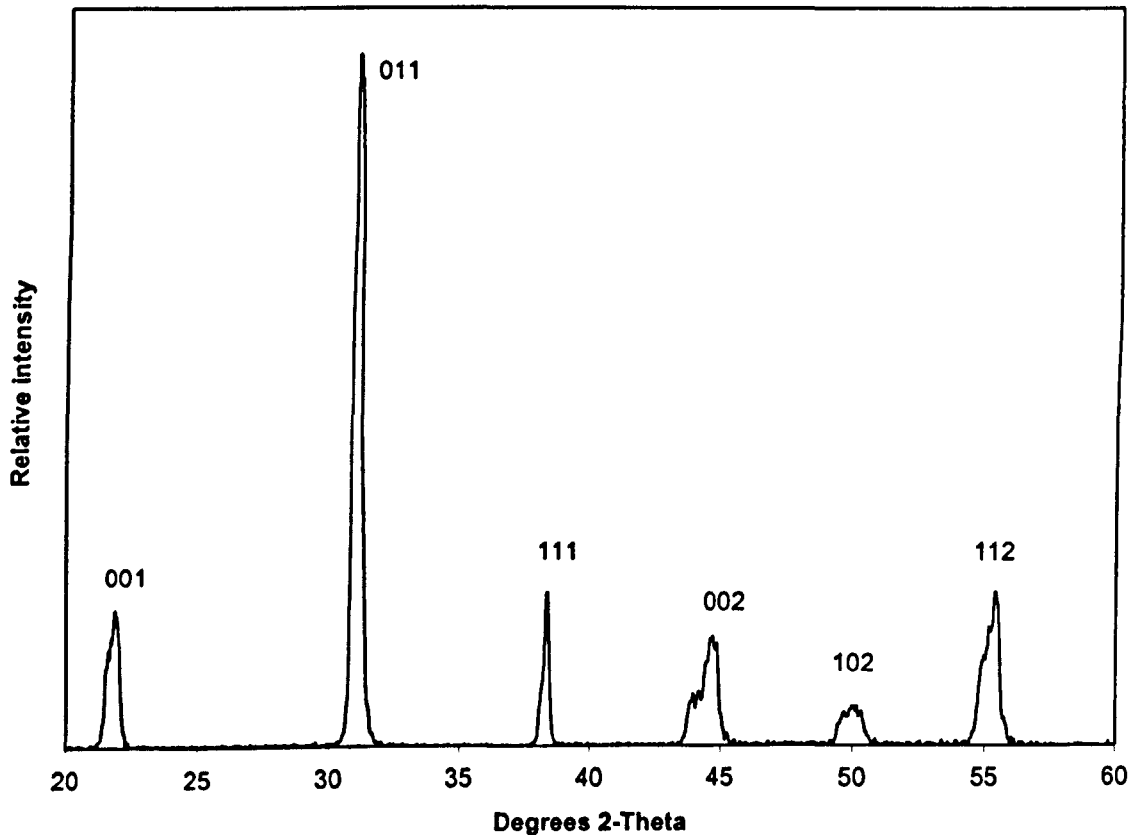


Figure 9.8 XRD from a MPB PZT composition without Sr-doping, sintered 4h at 1280°C

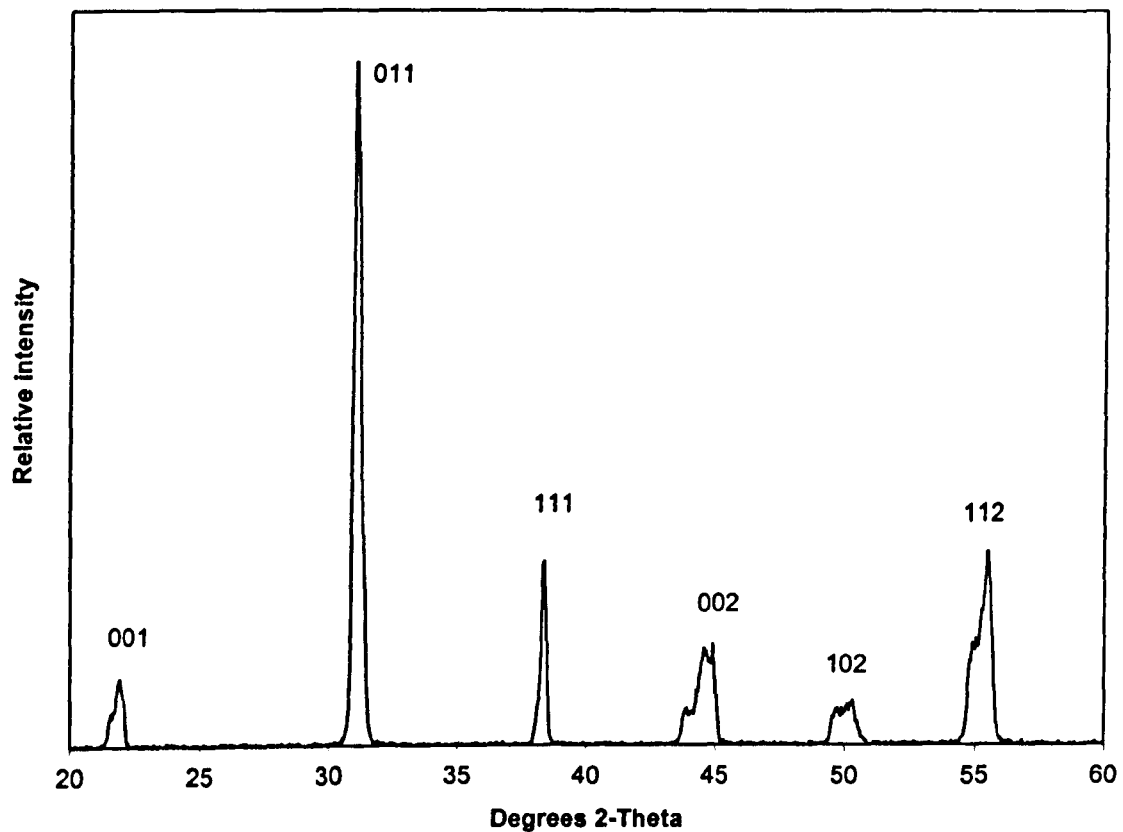


Figure 9.9 XRD from an undoped PZT sample with a Zr:Ti ratio of 1.23, sintered 4h at 1280°C

9.4 Dielectric Properties

Figure 9.10 shows the relative permittivity vs. temperature of PSZT12/44 ceramics sintered at different temperatures. T_C increases from 179°C to 187°C with sintering temperature between 1070° and 1280°C, respectively. This increase is due to an average decrease in the Zr:Ti ratio in the perovskite phase; in general, T_C increases

with Ti^{4+} concentration^[26]. Furthermore, the maximum permittivity drops drastically as the vol% of ZrO_2 increases due to a decrease in the average relative permittivity of the sample. The permittivity of ZrO_2 (12.5^[121]) is low relative to perovskite PZT (~ 2,000) at room temperature.

The effect of decomposition is also observed on the shape of the curve of permittivity vs. temperature, becoming more asymmetric as sintering temperature increases. This suggests that a higher T_C phase is developing heterogeneously (at the surface) in the sample. This latter observation confirms the formation of a surface Ti-rich, tetragonal PSZT phase.

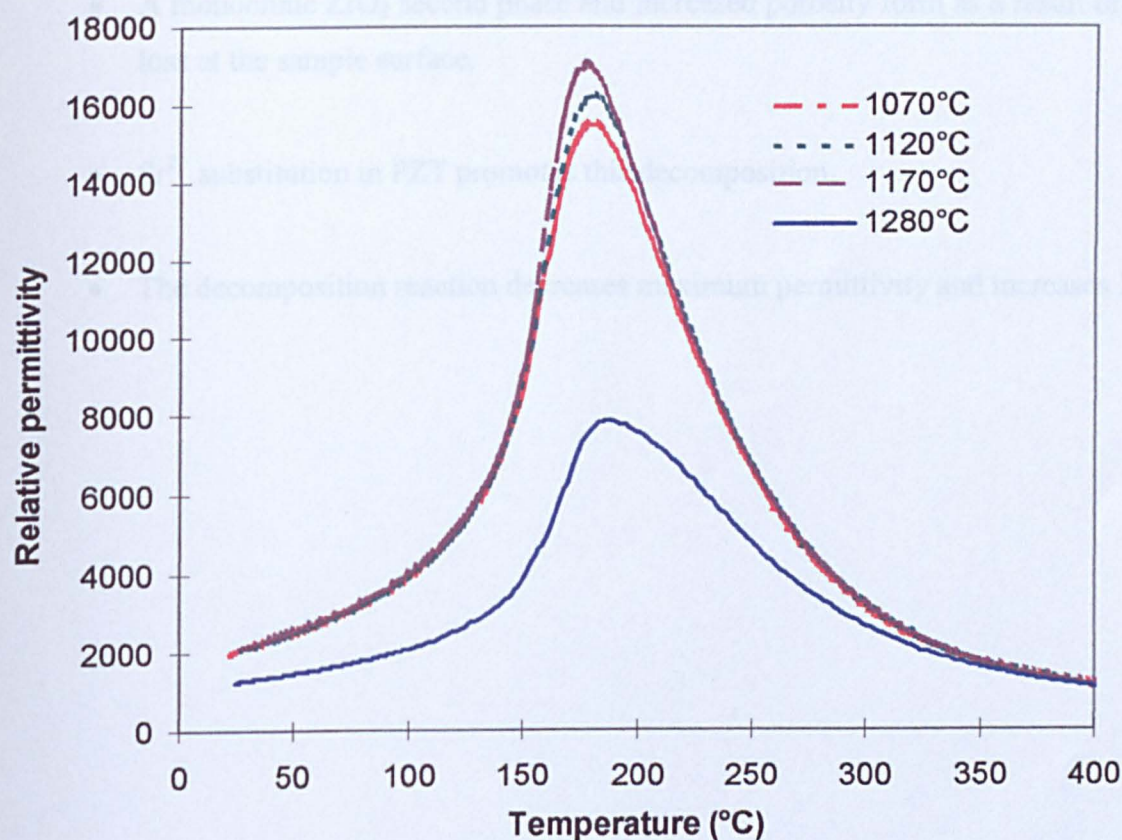


Figure 9.10 Relative permittivities vs. temperature as a function of sintering temperature for PSZT12/44

9.5 Conclusions

- Sintering temperature has a pronounced effect on the stability of perovskite phase in Sr-doped PZT. High temperatures ($>1120^{\circ}\text{C}$) favour the tetragonal over rhombohedral or MPB phases.
- A monoclinic ZrO_2 second phase and increased porosity form as a result of PbO loss at the sample surface.
- Sr^{2+} substitution in PZT promotes this decomposition.
- The decomposition reaction decreases maximum permittivity and increases T_C .

10. TWO-STEP CALCINATION PROCESSING ROUTE

PZT based compounds (Chapters 5-8) consistently reveal that d_{33} is sensitive to Zr:Ti ratio. High values of d_{33} only occur at a narrow Zr:Ti ratio in the tetragonal region close to the MPB of the binary phase diagram. Deviation from this region results in a rapid drop in piezoelectric activity. Ideally, the Zr:Ti ratio should be consistent from point to point within the structure to maximise piezoelectric properties. In practice, however a distribution of Zr:Ti ratios around the starting batch composition is inevitable due to the mixed oxide processing route used for preparing ceramic powders. Therefore locally the ceramic contains regions that are not of the optimised average batched ratio.

Furthermore, in Chapter 6, TEM studies reveal an inhomogeneous distribution of domain widths within grains in Sr-doped PZT, implying compositional fluctuations resulting in an inhomogeneous distribution of A or B site cations. Permittivity measurements as a function of temperature also indicate the existence of a diffuse phase transition (DPT) in Sr-doped PZT consistent with this premise. As proposed by Smolenskii *et al.*^[103] and Cross^[40], a non-homogeneous distribution of A-site or B-site cations would lead to a DPT response. Local inhomogeneities in chemistry and/or structure result in domains having a distribution of Curie temperatures, which account for the diffuse peak in the dielectric constant.

Any means by which the local Zr:Ti ratio may be confined to that of the average batch could potentially increase d_{33} by ensuring that a larger volume of material is of the optimised composition. One manner by which this may be achieved is to pre-react ZrO_2 and TiO_2 to form ZrTiO_4 , a compound in which the Zr:Ti ratio is well defined. This precursor compound may then be reacted with PbO and SrCO_3 to form two selected

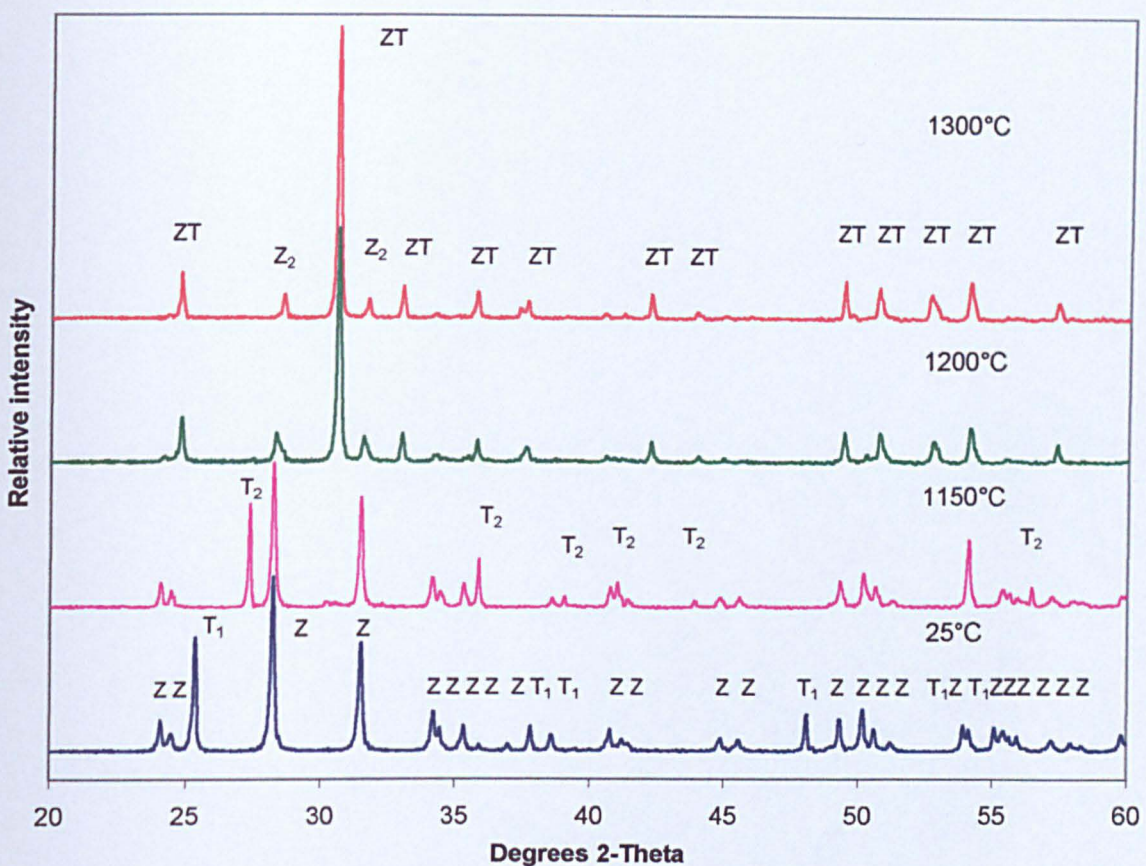
PSZT ceramics: PSZT8/44 ($\text{Pb}_{0.92}\text{Sr}_{0.08}(\text{Zr}_{0.553}\text{Ti}_{0.443}\text{Nb}_{0.024})\text{O}_3$) and PSZT12/44 ($\text{Pb}_{0.88}\text{Sr}_{0.12}(\text{Zr}_{0.538}\text{Ti}_{0.438}\text{Sb}_{0.024})\text{O}_3$). These two compositions are chosen because their d_{33} values are optimised for 8 mol% and 12 mol% Sr-doped PZT ceramics respectively. Such a process is termed master batching.

10.1 Two-Step Calcination Route

Synthesis of PSZT8/44 and PSZT12/44 powders was carried out by a two-step calcination method as described in Section 3.3. The powder obtained was then milled, mixed with binder and pressed into discs of 10 mm in diameter. The pellets were sintered 4h at temperatures between 1140 to 1240°C in closed alumina crucibles, identical to the sintering process described in Section 3.2.

10.2 Effect of Calcination Temperature on ZrTiO_4 Phase Formation

To determine the ZrTiO_4 phase formation temperature, XRD was performed on mixed ZrO_2 , TiO_2 powders calcined at different temperatures. XRD, Figure 10.1 shows that the attrition-milled ZrO_2 , TiO_2 raw powder is a mixture of ZrO_2 (monoclinic, ICDD card: 37-1484) and TiO_2 (tetragonal, ICDD card: 21-1272). The monoclinic ZrO_2 phase still exists at 1150°C, however TiO_2 has been transformed to a high-temperature form (tetragonal, ICDD card: 76-319). Single phase ZrTiO_4 (orthorhombic, ICDD card: 74-1504) is observed at 1200°C and this phase is retained up to 1300°C. Traces of ZrO_2 (monoclinic, ICDD card: 80-966) are also detected since the Zr:Ti ratio is greater than 1 in these two compositions (1.094 and 1.227 respectively).



ZT: ZrTiO₄, Z: ZrO₂(ICDD:37-1484), Z₂: ZrO₂ (ICDD:80-966)
 T₁: TiO₂(ICDD:21-1272), T₂: TiO₂(ICDD:76-319)

Figure 10.1 XRD of mixed ZrO₂, TiO₂ powders calcined 4h at different temperatures

A DTA trace, Figure 10.2, of the milled ZrO₂, TiO₂ raw powder shows an endothermic peak around ~1220°C, confirming the ZrTiO₄ phase forms above 1200°C, in good agreement with the XRD results. There is a small endothermic trough at 980°C, possibly due to transformation of tetragonal TiO₂ phase from low to high-temperature form.

From the XRD and DTA results, a calcination temperature of 1200°C/4h was therefore chosen for preparing the ZrTiO₄ precursor.

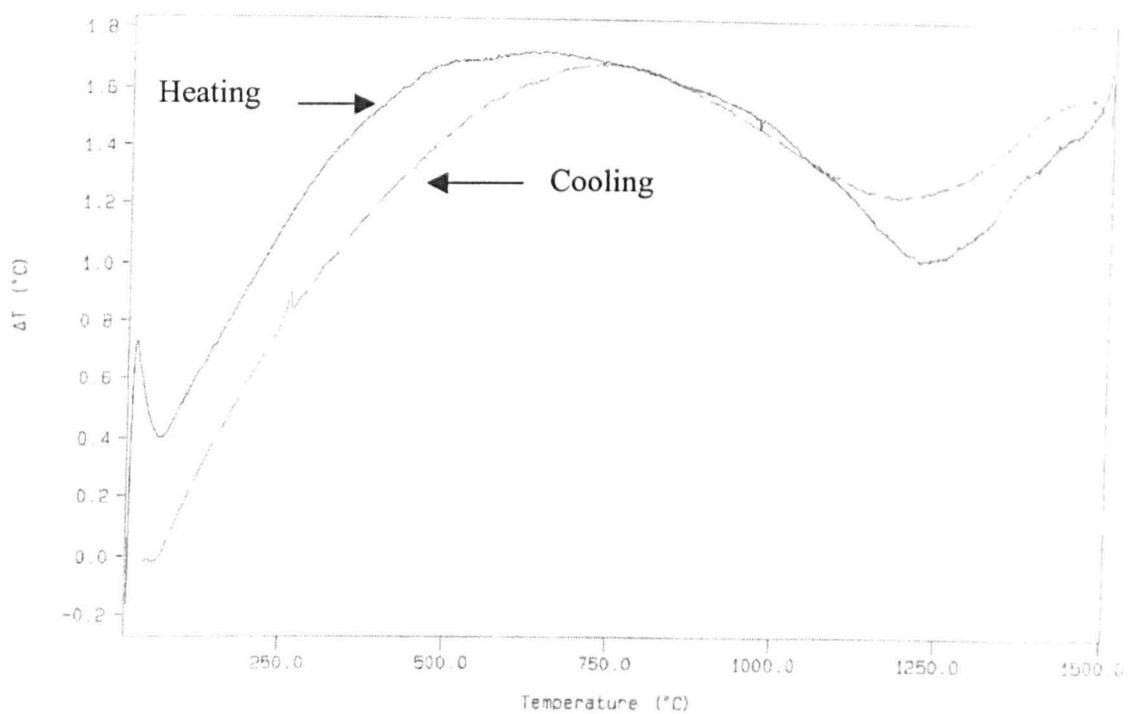


Figure 10.2 DTA trace of a mixed ZrO_2 , TiO_2 powder

10.3 Phase Structure of PSZT Prepared by Two-step Calcination Route

Figure 10.3 shows XRD traces of PSZT8/44 ceramics made from powders prepared by both two-step and one-step calcination methods respectively, which were sintered 4h at 1180°C. It is evident that both ceramics are tetragonal perovskite, indicated by the peak splitting on the {002}. Positions and relative intensities of each peak fit well for these two traces. However, compared to the identical composition prepared by the one-step calcination route, the degree of tetragonality is increased in

ceramics prepared by the two-step method, as indicated by the greater splitting of the {002} peak.

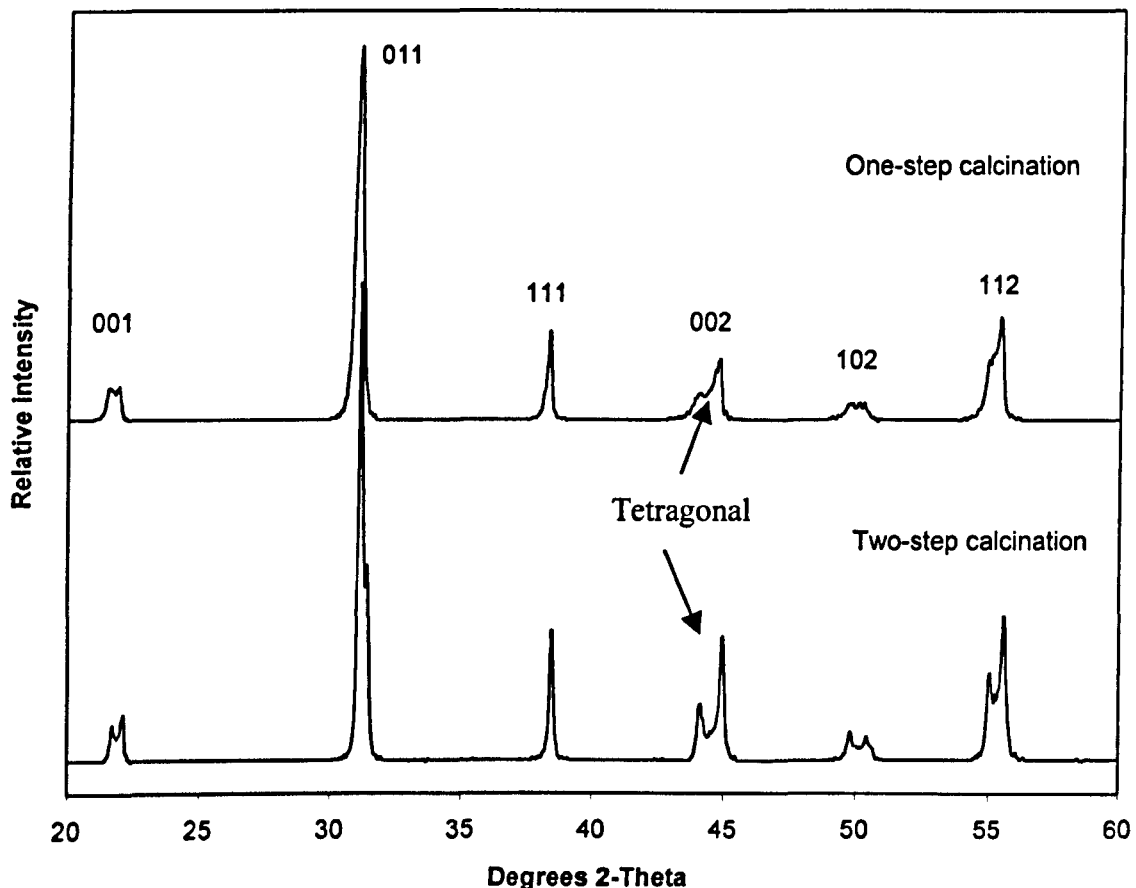


Figure 10.3 XRD of PSZT8/44 ceramics prepared by both one-step and two-step calcination routes, sintered 4h at 1180°C

Figure 10.4 shows XRD traces of PSZT12/44 ceramics made from powders prepared by two-step and one-step calcination methods respectively, both sintered 4h at 1180°C. Similar to PSZT8/44, Figure 10.3, greater tetragonality is observed in ceramics prepared by the two-step method. The cause of this increased tetragonality in ceramics prepared by the two-step calcination method is not clear. It is speculated that the extra calcination heat treatment involved in the two-step processing route may favour the formation of tetragonal over rhombohedral as high temperature heat treatment is observed to increase the degree of tetragonality in PZT, as discussed in Section 4.3.1.

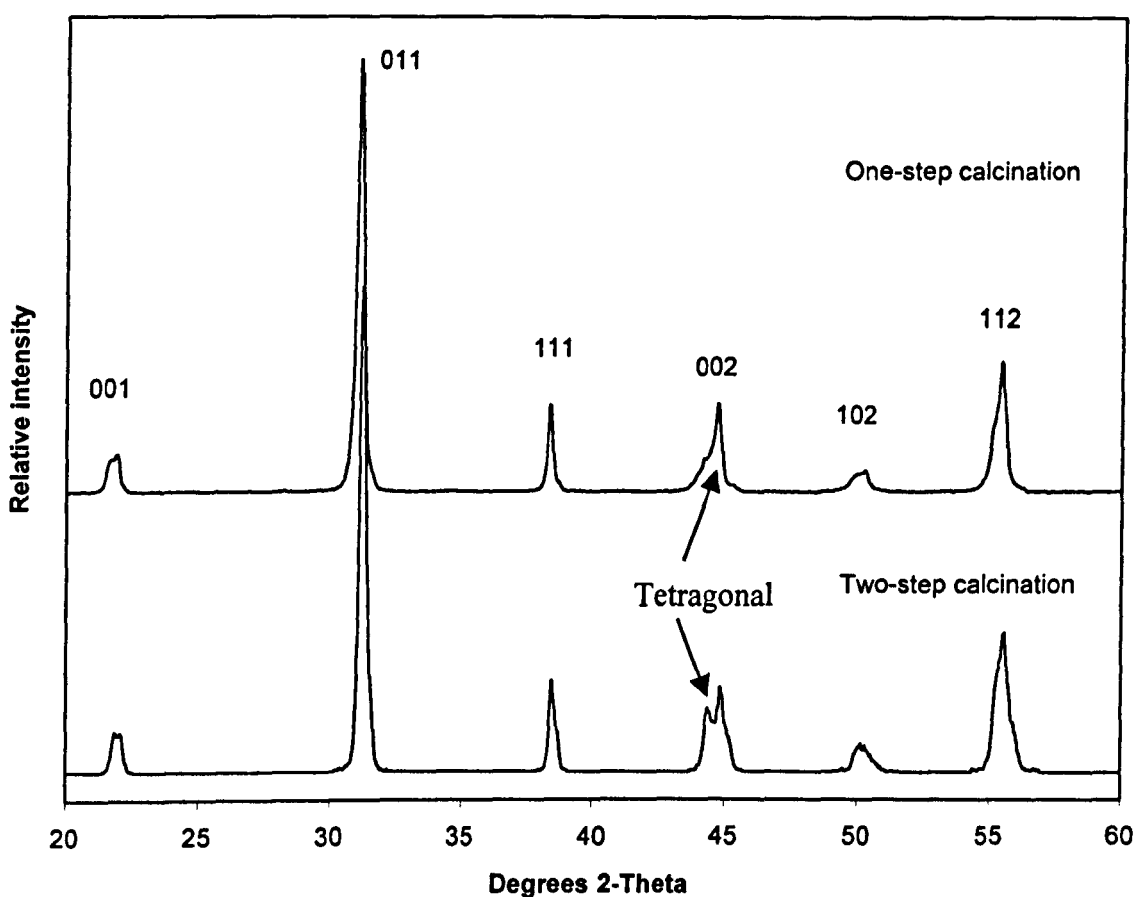


Figure 10.4 XRD of PSZT12/44 ceramics prepared by both one-step and two-step calcination routes, sintered 4h at 1180°C

10.4 Electrical Characterisation

Figure 10.5 shows relative permittivity vs. temperature of PSZT8/44 and PSZT12/44 ceramics, which were prepared by the two-step calcination route (sintered 4h at 1180°C). T_c 's of these two compositions are 255°C and 172°C respectively, ~2°C

lower than the equivalent compositions, prepared by the one-step calcination route. However by considering the accuracy of dielectric measurements, these values are still in reasonable agreement.

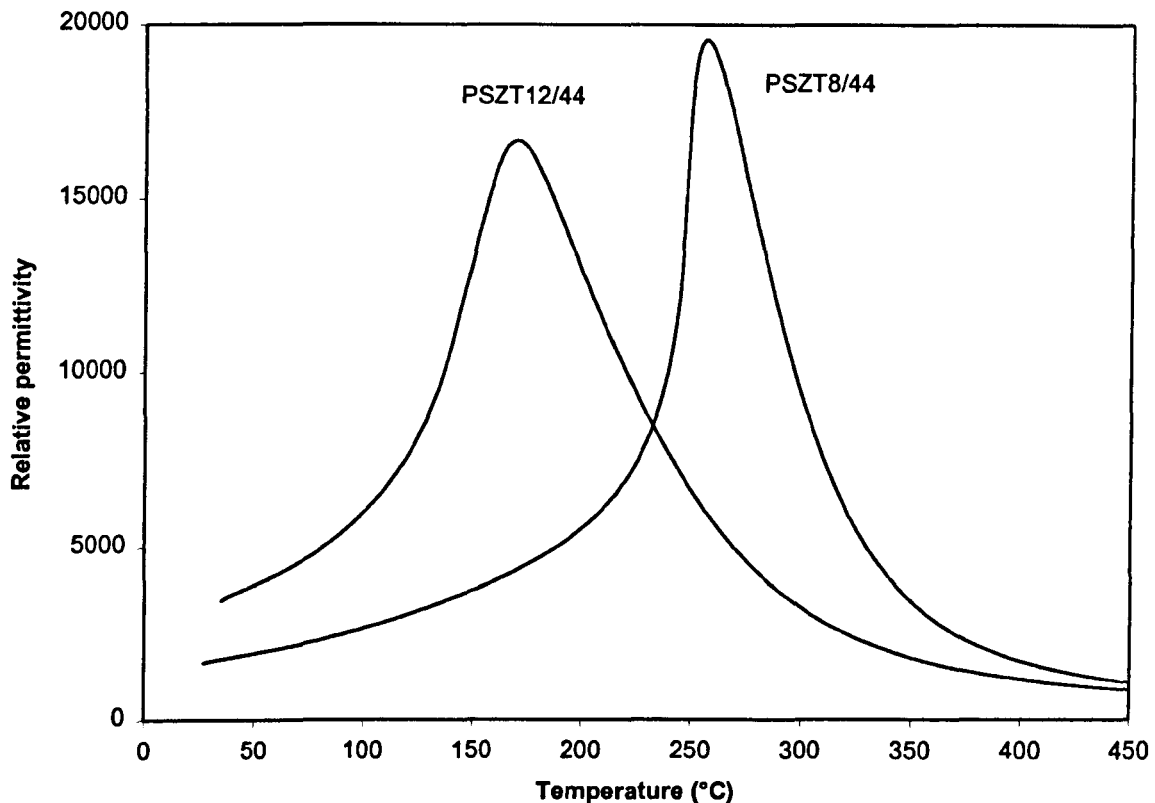


Figure 10.5 Relative permittivities of PSZT ceramics, prepared by the two-step calcination route

Table 10.1 shows the d_{33} values for the ceramics prepared by the two-step calcination route, which are marginally lower compared to the equivalent compositions prepared by the one-step calcination route, despite a nominally lower T_C .

Table 10.1 d_{33} values of PSZT8/44 and PSZT12/44 ceramics

Composition	PSZT8/44		PSZT12/44	
Preparation method	One-step calcination	Two-step calcination	One-step calcination	Two-step calcination
d_{33} (pC/N)	540	520	640	620

It is evident from the d_{33} result that introducing an extra calcination step does not improve the piezoelectric activity. It is unlikely therefore that the distribution of the Zr:Ti ratio within the ceramic has been improved (narrowed) by the two-step calcination route. However, direct proof from the microstructure is difficult due to the lack of sensitivity of EDS analysis in the TEM, which cannot detect the minor variation of Zr:Ti ratio from grain to grain. The d_{33} data presented in Table 10.1 implies that the use of attrition-milling may already be sufficient to homogenise the Zr:Ti distribution thereby optimising piezoelectric activity. Due to this reason, further investigations into the two-step calcination method were not carried out. This section, although short, is included as it demonstrates that the ceramics made in this study are well processed and therefore the electrical characterisation of these ceramics is representative and reliable.

10.5 Conclusions

- Two optimum compositions were prepared through a two-step calcination route.
- d_{33} however was marginally lower compared to the equivalent one-step calcined compounds.
- It is assumed that the use of attrition-milling has already effectively homogenised the A or B-site cation distribution and therefore the piezoelectric activity is optimised.

11. GENERAL DISCUSSION

The piezoelectric properties of PZT ceramics are composed of both intrinsic and extrinsic contributions. For soft PZT, intrinsic contributions are comparatively small and relate to the lattice whereas extrinsic contributions are associated with the vibration and motion of domain walls. The extrinsic contribution could account for approximately 60% of the piezoelectric activity of PZT, even at relatively low electric field levels ($E < 10 \text{ Vmm}^{-1}$)^[5]. The extrinsic contribution increases at higher field strengths, as larger scale domain wall translation plays an increasing role^[122].

In general, three softening methods have been investigated in this thesis for optimising extrinsic contributions to piezoelectric activity:

1. Proximity to the MPB

By modifying Zr:Ti ratio, the PZT composition can be made to lie in the proximity of the MPB, decreasing the free energy between rhombohedral and tetragonal phases such that structural re-arrangement during domain wall motion is easier. More recent work by Noheda *et al.*^[123] suggests the presence of a monoclinic phase in the vicinity of the MPB, which they postulate is responsible for optimum piezoelectric properties. Proximity to the MPB is important since this allows easy structural rearrangements. The existence of a monoclinic intermediate phase would decrease yet further the barrier to domain wall motion by creating an extra direction of polarisation.

The studies in this thesis show that piezoelectric properties (d_{33}) are optimised in PZT-based compounds in the tetragonal phase *close to* the MPB, which disagrees with the commonly-accepted concept that piezoelectric properties are optimised *at* the MPB. One plausible explanation may be that the ceramic, which appears tetragonal after firing may become mixed phase after electric poling, therefore exhibiting the highest d_{33} . Although there is no direct proof, a phase transformation from tetragonal to rhombohedral is observed when ceramics are subject to mechanical stress (grinding and polishing), analogous to electric poling.

The remnant polarisation is also maximised in the *tetragonal* phase close to the MPB, similar to the d_{33} . This can be explained by considering the fact that the spontaneous strain associated with the tetragonal distortion is much larger than the spontaneous strain associated with the rhombohedral distortion. The rhombohedral strain is less than 0.5% at the MPB and remains nearly constant with increasing Zr⁴⁺ content^[104]. The tetragonal strain is greater than 2% at the MPB and increases with increasing Ti⁴⁺ concentration up to more than 6% for PbTiO₃^[105].

On the other hand, the coercive field is lowest in the *rhombohedral*, rather than tetragonal, phase close to the MPB, which disagrees with the d_{33} and remnant polarisation values. In ferroelectrics, domain walls can be grouped into two categories: 180° walls, which separate domain with opposite polarisation vectors, and non-180° walls, which separate the remaining domains^[124]. The 180° domain wall movement produces only the dielectric response while non-180° domain movement produces the dielectric, piezoelectric and elastic responses^[32].

In ferroelectrics with tetragonal symmetry, the non-180° domain walls are 90° walls and with rhombohedral symmetry, the non-180° domain walls are 109° or 71° walls^[124]. It is postulated that the 90° domain walls in tetragonal PZT ceramics are likely to be already partly clamped by local internal stresses, which originate from high tetragonal distortion. The 109° and 71° rhombohedral domain walls are relatively free to move because internal stresses, due to the structural distortion, are significantly smaller in rhombohedral compositions^[105]. As a consequence, the external electric field has a

weak effect in the domain-wall contribution to the piezoelectric response in tetragonal compositions and a strong effect in rhombohedral compositions, resulting in the lowest coercive field in the *rhombohedral* phase close to the MPB. Although d_{33} , remnant polarisation and coercive field are optimised in different phases either tetragonal or rhombohedral, optimum piezoelectric properties always occur in the vicinity of the MPB. Moving compositions far away from the MPB will lead to a rapid drop in piezoelectric activity.

Zhang *et al.*^[124] suggested that, depending on the amplitude of the driving ac-field, at least two different types of domain wall contributions exist in soft PZT. First, domain walls are shown to contribute both to the ε_r and d_{33} already at low ac fields $20 \text{ mV/cm} < E < 40 \text{ V/cm}$, but no ac-field dependence can be detected within the measuring accuracy in this ac-field range^[125]. It is assumed that weak ac-fields excite oscillations of domain walls, which are pinned at the grain boundary and at randomly-distributed defects within the grain. The amplitude of these oscillations is thereby much smaller than the lattice constant. This type of domain contribution is referred to as reversible domain wall motion because no field hysteresis of the polarisation can be observed at weak fields^[124]. On the other hand, a threshold for the onset of nonlinearity exists in soft PZT at $E_C \approx 100 \text{ V/cm}$ ^[126]. Since the intrinsic nonlinearity in PZT is believed to be negligible at these fields, it is suggested that an additional type of domain wall movement sets in at E_C . Above the threshold, the $P(E)$ dependence is hysteretic and can be described by the Rayleigh law originally discovered in ferromagnetic systems^[105]. This type of domain contribution is referred to as irreversible domain wall motion. Both reversible and irreversible domain wall motions are greatly affected by crystal structure (rhombohedral or tetragonal or the MPB)^[105].

In this thesis, some information has been obtained on coercive field and remnant polarisation, which are strongly dependent on crystal structure, however it is insufficient to compare the difference in extrinsic domain wall contributions to the d_{33} resulting from different crystal structures i.e., tetragonal, rhombohedral or the MPB. It is also unable to distinguish reversible domain wall motion from irreversible domain wall motion contributions to the d_{33} . Weak ac-field or ac-pressure dependence^[105, 123-125] of

dielectric and piezoelectric properties of soft PZT ceramics ranging from the tetragonal, through the MPB to the rhombohedral, will give insight into the dependence of the extrinsic contributions to d_{33} on crystal structure in PZT.

In this thesis, it is found that substitution of Nb^{5+} on the B-site stabilises the rhombohedral phase. By contrast, substitution of cations such as Sr^{2+} or Ba^{2+} on the A-site stabilises the tetragonal phase. Both effectively move the composition away from that optimised for d_{33} . The Zr:Ti ratio has therefore to be adjusted in order to compensate and regain optimum piezoelectric coefficients.

The work reported in this thesis reveals that d_{33} is sensitive to Zr:Ti ratio. High values of d_{33} only occur in a narrow phase field region. Deviation from this narrow region results in a rapid drop in d_{33} . In practice, a distribution of Zr:Ti ratios within the ceramic around the starting batch composition is inevitable due to the mixed oxide processing route involved in the preparation of ceramic powders and therefore locally the ceramic will contain regions that are not of the optimised average composition. In an optimised composition, it is the distribution of Zr:Ti ratio regions, which controls the d_{33} . Narrow distributions where the vast majority of the ceramic has a Zr:Ti ratio equivalent to the batched composition will give high d_{33} values and broad distributions will result in lower d_{33} . Precursor processing to homogenise the Zr:Ti distribution, involving the formation of ZrTiO_4 , did not increase d_{33} and, in general, the results suggest that attrition milling the raw materials to submicron size prior to calcination is sufficient to minimise the distribution of the Zr:Ti ratio in the ceramic, maximising piezoelectric activity.

2. Donor doping with Nb^{5+} on the B-site.

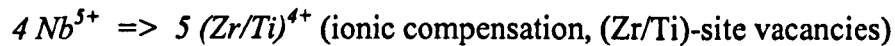
It is believed that donor doping in PZT gives rise to cation vacancies, which decrease oxygen vacancy concentration, therefore reducing pinning of domains by defect dipoles. The enhanced domain wall mobility results in an increase in permittivity and piezoelectric and coupling coefficients along with a commensurate reduction in

coercive electric field. For acceptor-doped PZT's, oxygen vacancies are created to form mobile defect dipoles. Zhang *et al.*^[32] believe that it is the difference in the mobility of the defects in the host lattice that makes the responses in soft and hard materials different. In this scenario, in PZT's with mobile defect dipoles (hard PZT), the dipoles will gradually align with the polarisation in the surrounding host lattice and, therefore, act as a local field stabilising the polarisation. As a result, the domain structure becomes stable, resulting in weak dielectric, piezoelectric and elastic responses. It is also this slow alignment of mobile dipoles with the polarisations in the surrounding lattices that causes a long aging time in hard PZT materials. On the other hand, the immobile defect dipoles (i.e., cation vacancies in the PZT lattice) will act as frozen in random fields which introduce frustration to the domain structures since some of the defect dipoles will not align with the preferred polarisation direction in a poled material. As a consequence, the domain structure is not stable against external applied fields and the material exhibits soft behaviour^[32].

The properties of piezoelectric ceramics are therefore derived from both the intrinsic contribution, which is the response from a single domain, and extrinsic contributions, which are from domain boundary motions. However, in the present work as stated previously, it is impossible to distinguish between these contributions. Weak-field property analysis would be helpful to distinguish intrinsic from extrinsic contributions to d_{33} . When a PZT piezoceramic is subjected to an external field, its domain structure will change. Therefore by comparing the dielectric, piezoelectric responses (ϵ_0 , d_{33}) of soft and hard ceramics subject to an external field, it is able to distinguish the functions of the dopants in PZT and the link between the defects formed due to the doping and the properties of the ceramics.

There are several possible mechanisms, which describe the substitution of donor dopants such as Nb^{5+} and La^{3+} in PZT, depending on whether charge compensation is electronic or ionic. In the case of ionic compensation, a cation vacancy may reside on either A or B-site. For La^{3+} , an ionic mechanism is generally assumed whereby one Pb^{2+} vacancy is created for every 2 La^{3+} . It is less clear what the compensation mechanisms are for B-site dopants such as Nb^{5+} . The following are some proposed charge

compensation equations that could describe the behaviour of Nb^{5+} substituted onto the Ti^{4+} site:



In the present work, it is impossible to evaluate the possible compensation mechanisms but impedance spectroscopy (IS) may give some information concerning defect compensation mechanisms.

IS is an effective characterisation method for analysing the properties of the intragranular and interfacial regions, their interrelations, their temperature and frequency dependences and the dc and ac phenomena in order to separate the individual contributions such as grain and grain boundary from the total cell impedance^[126]. The impedance spectrum in conjunction with a careful microstructural characterisation can be used to obtain information that is otherwise inaccessible, for example, regarding the conductivities of individual phases^[127]. The temperature dependence of the ferroelectric bulk capacitance can determine whether the ceramic obeys a Curie-Weiss law above the Curie temperature and whether the addition of the dopants has affected the first order transition in the ferroelectric bulk^[127]. The activation energies of ferroelectric bulk and grain boundary can also be derived, and can reveal whether the grain boundary conductivity arises from the same mechanism as the bulk. The temperature dependence of the ferroelectric bulk conductivity can provide some information on the defect-compensation mechanism associated with different dopings. To date, little IS work on soft PZT has been reported, except on La-doped PZT by Tanton^[128] and Barranco *et al.*^[127, 129]

3. Reducing phase transition temperature by substituting a less polarisable species (Sr^{2+}) onto the A- site.

By reducing the phase transition temperature (T_C), the total strain energy of the domain walls is diminished, thereby reducing their activation energy for domain wall motion. In this thesis, the reduction in T_C is achieved using Sr^{2+} substitution onto the A-site of MPB PZT compositions doped with a few mol% Sb/Nb⁵⁺ on the B-site. T_C is reduced greatly by Sr^{2+} substitution on the A-site, which decreases from $\sim 360^\circ\text{C}$ in d_{33} -optimised 0 mol% Sr-doped PZT to $\sim 150^\circ\text{C}$ in d_{33} -optimised 16 mol% Sr-doped PZT. Below 12 mol%, the optimised d_{33} values increase with increasing Sr^{2+} concentration, commensurate with the decrease in T_C . However, optimised d_{33} reaches a maximum ($d_{33} \sim 640 \text{ pC/N}$) in 12 mol% Sr-doped PZT ($T_C \sim 180^\circ\text{C}$). Further increasing Sr^{2+} substitution to 16 mol% reduces T_C to $\sim 150^\circ\text{C}$, however optimised d_{33} decreases to $\sim 375 \text{ pC/N}$.

Electron diffraction studies in this thesis suggest that increasing Sr^{2+} concentration from 0 – 16 mol% results in the onset of a structural phase transition, involving rotations of the oxygen octahedra in anti-phase. It is postulated that the macroscopic structural distortion induced by anti-phase octahedral tilting only occurs when Sr^{2+} concentration on the A-site is above 12 mol%. This increases domain wall energy, decreasing the extrinsic contribution to piezoelectric properties, resulting in deterioration of piezoelectric properties in 16 mol% Sr-doped PZT. The occurrence of this oxygen octahedral tilting is thought to result from the decreased tolerance factor t obtained by Sr^{2+} substitution on the A-site. Sr^{2+} is smaller than Pb^{2+} ; in addition the Zr:Ti ratio must be raised to obtain a d_{33} -optimised composition, which compensates for the increased degree of tetragonality induced by Sr^{2+} substitution. Zr^{4+} is larger than Ti^{4+} , consequently t decreases from 0.988 ($\text{Sr}^{2+} = 0 \text{ mol\%}$) to 0.983 ($\text{Sr}^{2+} = 16 \text{ mol\%}$). At $t < 0.985$, a structural phase transition involving rotations of the oxygen octahedra is likely to occur on cooling to room temperature^[130].

Most commercial compositions utilise these three softening methods to give a range of d_{33} values for PZT ceramics, in which T_C varies between $\sim 170^\circ\text{C} – 350^\circ\text{C}$. The work reported in this thesis shows that the maximum d_{33} value that may be achieved using such simple methods is $\sim 640 \text{ pC/N}$ ($T_C = \sim 180^\circ\text{C}$). However, solid solutions of PZT with some relaxor materials, such as PNN are reported as having $d_{33} > 800 \text{ pC/N}$.

for the same T_C ($\sim 175^\circ\text{C}$)^[52]. PZT-PNN compositions lie at an MPB between rhombohedral and tetragonal phases but they are macroscopically stoichiometric and not donor doped. The increase in d_{33} of almost 33% between Sr-doped PZT and PZT-PNN for similar T_C suggests that there might be a 4th method by which extrinsic contributions may be maximised. Empirical evidence^[52] suggests that this can be related to the presence of a relaxor phase as an end member of a pseudobinary solid solution with PZT or in some cases PbTiO_3 (PT).

Many ferroelectric (PZT, PT) - relaxor compositions have been reported with high d_{33} , including a new generation of single crystals ($d_{33} = 2,500$, $k_{33} = 0.9$)^[131]. However, aliovalent doping, e.g. with Ni^{2+} and Nb^{5+} , is not the only way of forming a relaxor-ferroelectric solid solution. It has been reported that isovalent substitution of Ba^{2+} onto the A-site of PZT forms a relaxor phase at around 20 mol%^[114]. In the present work, two donor-doped MPB compositions have been fabricated: the first with 8 mol% Sr^{2+} substituted onto the A-site and the second with 6 mol% Sr^{2+} and 6 mol% Ba^{2+} on the A-site. Despite having a nominal ‘relaxor content’ as indicated by a reduction in domain width in Ba, Sr co-doped compositions, the d_{33} values of Ba^{2+} containing ceramics were marginally inferior even though T_C is 20°C lower. This suggests that it is not simply a relaxor-ferroelectric solid solution that is required to maximise extrinsic contributions but one which specifically contains aliovalent species, such as those within Pb-based complex perovskites (e.g. PNN). To date, there is no detailed explanation for the unusually high piezoelectric activity of compounds such as PZT-PNN. However, it is speculated that the ‘4th method’ of optimising extrinsic contributions to d_{33} may relate to the greater width of the MPB in PZT relaxor compositions. In most PZT-relaxor solid solutions, there are 3/4 cations randomly distributed on the B-site and it has been suggested that this statistically increases the chance that the composition of any given volume will lie at or close to the MPB. Therefore, a greater volume fraction of the ceramic is ‘soft’. This mechanism is reasonable only for compositions where the relaxor content of the solid solution is high, e.g. 0.65PZT-0.35PNN, otherwise local proximity to the MPB will still be dominated by the Zr:Ti ratio.

The work reported in this thesis demonstrates several new features of highly commercial, conventional PZT's manufactured all over the world. Decomposition of Sr-doped compounds has been shown to occur at temperatures as low as 1170°C-1200°C, a typical processing window for commercial compositions. A new structural phase transition, involving oxygen octahedral tilting in anti-phase, has been observed which markedly decreases the extrinsic contribution to d_{33} . Most surprising, however, is the persistent observation that d_{33} is optimised in the *tetragonal* phase field, close to, but not at the MPB. Furthermore, it is evident that Sr²⁺ substituted, donor doped compositions have a maximum d_{33} of 640 pC/N. Stoichiometric relaxor ferroelectric compounds such as PZT-PNN have reported d_{33} values ~33% higher for the same T_C . Therefore, there is the intriguing possibility that a 4th method of optimising extrinsic contributions is operating in these compounds.

12. CONCLUSIONS

The main objective of this project was to assess the relative importance of known softening mechanisms in PZT:

- i) donor doping,
- ii) proximity to a morphotropic phase boundary and
- iii) lowering the paraelectric-ferroelectric phase transition temperature (T_c)

Based on these three softening methods, a systematic study on a range of soft PZT materials was performed and their electrical properties were characterised as a function of composition and related to their phase assemblage and microstructure. The main conclusions were as follows.

12.1 Nb-doped PZT Ceramics

PZT ceramics close to the MPB were investigated as a function of Nb^{5+} doping on the B-site for a fixed Zr/Ti ratio and as a function of Zr/Ti ratio for a fixed Nb^{5+} content. XRD analysis shows that both increasing Nb^{5+} content and Zr/Ti ratio promotes formation of rhombohedral at the expense of tetragonal phase. SEM studies indicate that Nb^{5+} substitution in PZT dramatically reduces grain size from 12 to 1 - 2 μm . Relative permittivity as a function of temperature measurements reveal that Nb^{5+} additions to

PZT lower the Curie temperature (T_C) and small amounts of Nb⁵⁺ in PZT (2.4 to 7.2 mol%) enhance the room-temperature relative permittivity, despite reducing the peak relative permittivity. In general, the piezoelectric coefficients (d_{33}) increase with increasing Nb⁵⁺ content, which is at a maximum in the *tetragonal* phase *close to*, but not *at*, the precise MPB. TEM reveals characteristic macrodomain structures with 90° and 180° inversion domain boundaries both existing in Nb-doped PZT. Domain morphology varies with composition. Normal macrodomain structures are more dominant and readily seen in low Nb⁵⁺ content ceramics. Finer domains and higher dislocation densities are observed in high Nb⁵⁺ content (> 4.8 mol%) ceramics.

12.2 Sr, Nb-doped PZT Ceramics

(Pb_{1-x}Sr_x)(Zr_{0.976-y}Ti_yNb_{0.024})O₃ solid solutions were investigated to understand the relationship between structural changes caused by Sr²⁺ substitution on the A-site and dielectric, and piezoelectric properties. XRD shows that increasing Sr²⁺ content on the A-site promotes formation of tetragonal over rhombohedral phase. T_C is greatly reduced from ~ 360°C to ~ 150°C by doping 16mol% Sr²⁺ on the A-site. As Sr²⁺ was substituted for Pb²⁺ on the A-site, the Zr:Ti ratio was modified so that the ceramics could have an optimised d_{33} . It was observed that as the Sr²⁺ content increased, optimised d_{33} also increased from 420 pC/N (x = 0) to 640 pC/N (x = 0.12), commensurate with a decrease in T_C from 350°C to 175°C. However, for ceramics where x = 0.16, optimised d_{33} decreased even though T_C for this composition was lower (~ 150°C). TEM revealed that low Sr²⁺ contents (x = 0 - 0.08) contained 80 nm wide ferroelectric domains whereas intragranular inhomogeneity in the domain structure with widths varying from ~80 to ~20 nm was observed in high Sr²⁺ content (x = 0.16) ceramics.

In addition, <110> pseudocubic electron diffraction patterns revealed superlattice reflections occurring at 1/2{hkl} positions associated with rotations of the

octahedra in anti-phase in Sr-doped PZT. It is suggested that Sr^{2+} substitution on the A-site decreases the tolerance factor t , resulting in the onset of oxygen octahedral tilting. In ceramics with $x = 0.08$ and 0.12 , the intensities associated with the superlattice reflections are diffuse, which implies that only short-range interaction of the amplitude of tilt occurs. However the reflections observed in ceramics with $x = 0.16$ are discrete, implying a long-range interaction. It is therefore proposed that for ceramics where $x = 0.16$, the octahedral tilt transition causes a long-range structural distortion, which results in an increase in the strain energy of domain walls and therefore activation energy for domain wall motion. This would give rise to smaller extrinsic contributions to d_{33} . The short-range ordered tilting in ceramics where $x = 0.08$ and 0.12 is insufficient to cause further macroscopic distortion of the structure, increasing neither the strain energy of the domain walls nor their activation energies for motion.

12.3 Ba, Sr, Nb-doped PZT Ceramics

To prevent oxygen octahedral tilting from occurring but still retain a similar T_C , $(\text{Pb}_{0.88}\text{Sr}_x\text{Ba}_y)(\text{Zr}_{0.976-z}\text{Ti}_z\text{Nb}_{0.024})\text{O}_3$ ceramics were investigated. It was found that co-doping ceramics with Sr^{2+} ($x = 0.06$) and Ba^{2+} ($y = 0.06$) resulted in the disappearance of the $1/2\{\text{hkl}\}$ superlattice reflections, confirming the elimination of oxygen octahedral tilting by Ba^{2+} substitution on the A-site. However, the d_{33} values of the optimised 6mol% Ba and Sr co-doped PZT ceramics were $\sim 520 \text{ pC/N}$ ($T_C \sim 205^\circ\text{C}$), similar to ceramics where $x = 0.08$, $y = 0$, which even had a higher T_C of 250°C . TEM revealed some evidence of relaxor behaviour in Sr, Ba co-doped PZT ceramics, which was assumed to be responsible for the deterioration in piezoelectric properties.

12.4 Surface Decomposition in Soft PZT Ceramics

Sintering temperature has a pronounced effect on the stability of perovskite phase in Sr-doped PZT. High temperatures ($>1120^{\circ}\text{C}$) favour the tetragonal over rhombohedral or MPB phases. A monoclinic ZrO_2 second phase forms as a result of PbO loss at the sample surface. Sr^{2+} substitution in PZT promotes this decomposition. The decomposition reaction decreases maximum permittivity and increases T_c .

12.5 One-Step and Two-Step Calcination Routes

In this thesis, one-step calcination was used as the standard powder processing route. With the aim to homogenise the distribution of Zr:Ti ratio regions in ceramics, two d_{33} -optimum compositions of 8 mol% and 12 mol% Sr-doped PZT were prepared through a two-step calcination route. The d_{33} was not increased by the two-step method compared to equivalent one-step calcined ceramics. It is assumed that the use of attrition-milling has already effectively homogenised the A or B-site cation distribution and optimised the piezoelectric activity.

13. FUTURE WORK

As mentioned in Chapter 11, it is impossible to distinguish extrinsic from intrinsic contributions to the d_{33} in the present work. To do this, future work on weak-field analysis such as dielectric constant, piezoelectric coefficients as a function of ac field or ac pressure, hysteresis analysis below the coercive field is essential.

The work reported in this thesis reveals uncertainty about the charge compensation mechanism in donor-doped PZT. Measurement of dielectric properties and high temperature conductivity using impedance spectroscopy (IS) should allow discrimination of various compensation mechanisms, which will be beneficial to understand the defect chemistry in various doped PZT's. From IS studies, distribution of defects within the microstructure may also be obtained, i.e., whether vacancies are in the bulk or at grain boundaries.

The current study demonstrates that the maximum d_{33} achievable by the three known softening methods is $\sim 640 \text{ pC/N}$, which is far less than solid solutions of PZT with relaxor materials such as PZT-PNN ($d_{33} > 1000 \text{ pC/N}$) for the same T_c ($\sim 175^\circ\text{C}$). It is thus speculated that there is a 4th method by which extrinsic contributions may be maximised. Empirical evidence suggests that this can be related to the presence of a relaxor phase of a solid solution with PZT. However, our experimental results using Ba, Sr co-doping on the A-site suggest that it is not simply a relaxor-ferroelectric solid solution that is required to maximise the extrinsic contributions but one which specifically contains aliovalent species. Therefore in the future, using aliovalent La³⁺ dopant on the A-site would be ideal for investigating the similarity between compositions such as PZT-PNN and La-doped PZT.

As stated previously, the d_{33} value is very sensitive to Zr:Ti ratio. High values of d_{33} only occur in a narrow region in conventional PZT's. On the other hand, in most PZT-relaxor solid solutions, 3/4 cations are randomly distributed on the B-site and it has been suggested that this statistically increases the chance that the composition of any given volume will lie at or close to the MPB. Therefore, future work using relaxor dopants to widen the MPB region would be of great interest.

Finally, TEM has been widely used in this study. In the future, *in-situ* heating and cooling may be performed using the appropriate specimen holder, which allows the microstructure to be studied as a function of temperature. The onset of structural phase transitions can therefore be monitored in more detail.

PUBLICATIONS

1. H. Zheng, I. M. Reaney, W. E. Lee, N. Jones and H. Thomas, "Effect of Sr substitution in Nb-doped PZT ceramics", *J. Euro. Ceram. Soc.*, 2001, 21[10-11], 1371-75
2. H. Zheng, I. M. Reaney, P. Wang and W. E. Lee, "Structure-property relations in soft PZT ceramics", *Ferroelectrics 2000 UK*, p. 51-58
3. H. Zheng, I. M. Reaney, W. E. Lee, N. Jones and H. Thomas, "Effects of octahedral tilting on the piezoelectric properties of Sr-doped lead zirconate titanate", to be published in *Ferroelectrics*
4. H. Zheng, I. M. Reaney, W. E. Lee, N. Jones, and H. Thomas, "Surface decomposition of Sr-doped soft PZT's", to be published in *J. Am. Ceram. Soc.*
5. H. Zheng, I. M. Reaney, W. E. Lee, N. Jones and H. Thomas, "Effects of octahedral tilting on the piezoelectric properties of Sr, Ba, Nb-doped soft PZT ceramics", submitted to *J. Am. Ceram. Soc.*, 2001

CONFERENCE PRESENTATIONS

1. H. Zheng, I. M. Reaney, W. E. Lee, N. Jones and H. Thomas, "Effects of octahedral tilting on the piezoelectric properties of Sr-doped lead zirconate titanate", oral presentation on the 10th International Meeting on Ferroelectricity, 3-7, September, 2001, Madrid, Spain.
2. H. Zheng, I. M. Reaney, W. E. Lee, N. Jones and H. Thomas, "Surface decomposition in Sr-doped PZT", poster presentation on Ferroelectrics UK 2001, 11-12, April, 2001, Sheffield, UK
3. H. Zheng, I. M. Reaney, H. Thomas and W. E. Lee, "Effect of Sr Substitution in Nb-doped PZT ceramics", poster presentation on the Electroceramics VII 2000 conference, 3-6, September, Portoroz, Slovenia.
4. H. Zheng, I. M. Reaney, H. Thomas and W. E. Lee, "Structure-property relations in Nb-doped PZT ceramics", poster presentation on the annual Materials Congress 2000, 11-14, April, 2000, Cirencester, UK.

REFERENCES

1. Q. Tan and D. Viehland, "Influence of thermal and electrical histories on domain structure and polarization switching in potassium-modified lead zirconate titanate ceramics", *J. Am. Ceram. Soc.*, 1998, **81**[2], 328-336
2. C. A. Randall, N. Kim, J. Kucera, W. Cao and T. R. Shrout, "Intrinsic and extrinsic size effects in fine-grained morphotropic-phase-boundary lead zirconate titanate ceramics", *J. Am. Ceram. Soc.*, 1998, **81**[3], 677-688
3. M. Kondo, M. Hida, M. Tsukada, K. Kurihara and N. Kamehara, "Piezoelectric properties of $\text{PbNi}_{1/3}\text{Nb}_{2/3}\text{O}_3\text{-PbTiO}_3\text{-PbZrO}_3$ ceramics", *Jpn. J. Appl. Phys.*, 1997, **36**, 6043-5
4. X. L. Zhang, Z. X. Chen, L. E. Cross and W. A. Schulze, "Dielectric and piezoelectric properties of modified lead titanate zirconate ceramics from 4.2K to 300K", *J. Mat. Sci.*, 1983, **18**, 968-72
5. Q. M. Zhang, H. Wang, N. Kim and L. E. Cross, "Direct evaluation of domain-wall and intrinsic contributions to the dielectric and piezoelectric response and their temperature-dependence on lead-zirconate-titanate ceramics", *J. Appl. Phys.*, 1994, **75**, 454-59
6. D. Damjanovic, M. Demartin, F. Chu and N. Setter, "Practical consequences of the extrinsic contributions to the properties of piezoelectric sensors and actuators", *Proc. 10th Int. Symp. Appl. Ferro.*, 1996, 251-57

7. J. Curie and P. Curie, "Development of charge on a crystal proportional to an applied mechanical stress", *Comp. Rend. Hebd. Acad. Sci.*, 1880, Paris, **91**, 294-95
8. W. G. Hankel, "Piezoelectricity", *Abhand Math. Phy Ksgw*, 1883, **12**, 457
9. W. C. Cady, "Piezoelectricity", McGraw-Hill, 1946, New York; Revised edition by Dover Publications, New York, 1964, 1-20
10. G. H. Haertling, "Ferroelectric ceramics: History and technology", *J. Am. Ceram. Soc.*, 1999, **82**[4], 797-818
11. J. Valasek, "Piezoelectric and allied phenomena in Rochelle salt", *Phys. Rev.*, 1921, **17**, 475-81
12. W. Kanzig, "Ferroelectrics and antiferroelectrics", *Solid State Physics*, 1957, New York, **4**, 1-199
13. W. Kanzig, "History of ferroelectricity. 2. History of ferroelectricity 1938-1955", *Ferroelectrics*, 1987, **74**[3-4], 285-91
14. H. D. Megaw, "Temperature changes in the crystal structure of barium titanium oxide", *Proc. Roy. Soc.*, London, 1947, **A189**, 261-83
15. G. C. Danielson, "Domain orientation in polycrystalline BaTiO₃", *Acta. Cryst.*, 1949, **2**, 90-94
16. J. K. Burfoot, "Ferroelectrics: An introduction to the physical principles", London: D. Van Nostrand Company Ltd., 1967, 195-208
17. H. D. Megaw, "Crystal structure of double oxides of the perovskite type", *Proc. Phys. Soc.*, 1946, **58**, 133-53

18. H. D. Megaw, "Crystals structures: A working approach", 1973, Philadelphia, PA: Saunders, London, 285-302
19. A. M. Glazer, "Classification of tilted octahedra in perovskites", *Acta Cryst. B*, 1972, **28**, 3384-92
20. A. M. Glazer, "Simple ways of determining perovskite structures", *Acta Cryst. A*, 1975, **31**, 756-62
21. I. M. Reaney, E. Colla and N. Setter, "Dielectric and structural characteristics of Ba- and Sr-based complex perovskites as a function of tolerance factor", *Jpn. J. Appl. Phys.*, 1994, **33**, 3984-90
22. F. S. Galasso, "Structure, properties and preparation of perovskite-type compounds", 1969, Pergamon, Oxford
23. A. J. Moulson and J. M. Herbert, "Electroceramics: materials, properties, applications", London: Chapman and Hall, 1990, 68-73, 280-287
24. G. Shirane, K. Suzuki and A. Takeda, "Phase transition in solid solutions of lead zirconate and lead titanate:II", *J. Phys. Soc. Japan*, 1952, **7[1]**, 12-8
25. B. Jaffe, R. S. Roth and S. Marzullo, "Piezoelectric properties of lead zirconate-lead titanate solid-solution ceramics", *J. Appl. Phys.*, 1954, **25**, 809-10
26. B. Jaffe, W. R. Cook and H. Jaffe, "Piezoelectric Ceramics", 1971, Academic Press, London, 136
27. M. E. Lines and A. M. Glass, "Principles and applications of ferroelectrics and related materials", Clarendon press, Oxford, first published in 1977, reprinted in 1996, 263

28. D. Viehland, J. F. Li, X.H. Dai and Z. Xu, "New perspective of high Zr-content lead zirconate titanate", *Ferroelectrics*, 1996, **183**, 311-319
29. R. B. Grey, "Transducer and method of making same", U.S. Pat. No. 2486560, 1949
30. J. H. Park, B. K. Kim, K. H. Song and S. J. Park, "Piezoelectric properties of Nb_2O_5 doped and MnO_2 - Nb_2O_5 co-doped $\text{Pb}(\text{Zr}_{0.53}\text{Ti}_{0.47})\text{O}_3$ ceramics", *J. Mater. Sci.*, 1995, **6**, 97-101
31. L. X. He and C. E. Li, "Effects of addition of MnO on piezoelectric properties of lead zirconate titanate", *J. Mater. Sci.*, 2000, **35**, 2477-80
32. Q. M. Zhang, J. Z. Zhao, K. Uchino and J. H. Zheng, "Change of the weak-field properties of $\text{Pb}(\text{ZrTi})\text{O}_3$ piezoceramics with compressive uniaxial stresses and its links to the effect of dopants on the stability of the polarizations in the materials", *J. Mater. Res.*, 1997, **12**(1), 226-34
33. L. L. Hench and J. K. West, "Principles of electronic ceramics", John & Sons, 1990, 273
34. B. Noheda, J. A. Gonzalo, L. E. Cross, R. Guo, S. E. Park, D. E. Cox and G. Shirane, "Tetragonal-to-monoclinic phase transition in a ferroelectric perovskite: the structure of $\text{PbZr}_{0.52}\text{Ti}_{0.48}\text{O}_3$ ", *Phys. Rev. B*, 2000, **61**[13], 8687-95
35. R. Guo, L. E. Cross, S. E. Park, B. Noheda, D. E. Cox and G. Shirane, "Origin of the high piezoelectric response in $\text{PbZr}_{1-x}\text{Ti}_x\text{O}_3$ ", *Phys. Rev. Lett.*, 2000, **84**[23], 5423-6
36. B. Noheda, D. E. Cox, and G. Shirane, J. A. Gonzalo, L. E. Cross and S. E. Park, "A monoclinic ferroelectric phase in the $\text{Pb}(\text{Zr}_{1-x}\text{Ti}_x)\text{O}_3$ solid solution", *Appl. Phys. Lett.*, 1999, **74**[14], 2059-61

37. S. M. Gupta and D. Viehland, "Tetragonal to rhombohedral transformation in the lead zirconium titanate lead magnesium niobate lead titanate crystalline solution", *J. Appl. Phys.*, 1998, **83**[1], 407-414
38. R. Gerson, "Variation in ferroelectric characteristics of lead zirconate titanate ceramics due to minor chemical modifications", *J. Appl. Phys.*, 1960, **31**[1], 188-94
39. S. J. Yoon, A. Joshi and K. Uchino, "Effect of additives on the electromechanical properties of $\text{Pb}(\text{Zr},\text{Ti})\text{O}_3$ - $\text{Pb}(\text{Y}_{2/3}\text{W}_{1/3})\text{O}_3$ ceramics", *J. Am. Ceram.*, 1997, **80**[4], 1035-9
40. L. E. Cross, "Relaxor ferroelectrics", *Ferroelectrics*, 1987, **76**, 241-67
41. O. Bidault, E. Husson and A. Morell, "Effects of lead vacancies on the spontaneous relaxor to ferroelectric phase transition in $\text{Pb}[(\text{Mg}_{1/3}\text{Nb}_{2/3})_{(0.9)}\text{Ti}_{0.1}]\text{O}_3$ ", *J. Appl. Phys.*, 1997, **82**[11], 5674-9
42. X. H. Dai, Z. Xu and D. Viehland, "Correlation of freezing dynamic and domain-like states in relaxor ferroelectrics", *Ferroelectrics*, 1996, **176**, 91-97
43. L. E. Cross, S. J. Jang, R. E. Newnham, S. Nomura and K. Uchino, "Large electrostrictive effects in relaxor ferroelectrics", *Ferroelectrics*, 1980, **23**, 187-92
44. D. Viehland, J. F. Li, S. J. Jang, L. E. Cross and M. Wuttig, "Glassy polarization behavior of relaxor ferroelectrics", *Phys. Rev.*, 1992, **46**[13], 8013-17
45. D. Viehland, S. J. Jang and L. E. Cross, "Deviation from Curie-Weiss behavior in relaxor ferroelectrics", *Phys. Rev. B*, 1992, **46**, 8003-6
46. D. Viehland, S. J. Jang, L. E. Cross and M. Wuttig, "An elastic relaxation and internal strain in lead magnesium niobate relaxors", *Phil. Mag. A*, 1991, **64**[4], 835-49

47. I. M. Reaney, J. Petzelt, V.V. Voitsekhovskii, F. Chu and N. Setter, "B-site order and infrared reflectivity in a (B'B'')O₃ complex perovskite ceramics", *J. Appl. Phys.*, 1994, **76**[4], 2086-92
48. C. A. Randall, D. J. Barber, R. W. Whatmore, and P. Groves, "A TEM study of ordering in the perovskite Pb(Sc_{1/2}Ta_{1/2})O₃", *J. Mat. Sci.*, 1986, **21**[12], 4456-62
49. E. Husson, M. Chubb and A. Morell, "Superstructure in PbMg_{1/3}Nb_{2/3}O₃ ceramics revealed by high-resolution electron-microscopy", *Mat. Res. Bull.*, 1988, **23**, 357-61
50. J. Chen, H. M. Chan and M. P. Harmer, "Ordering structure and dielectric-properties of undoped and La/Na-doped Pb(Mg_{1/3}Nb_{2/3})O₃", *J. Am. Ceram. Soc.*, 1989, **72**, 593-8
51. M. Kondo, M. Tsukada and K. Kurihara, "Temperature dependence of piezoelectric constant of 0.5PbNi_{1/3}Nb_{2/3}O₃-0.5Pb(Zr,Ti)O₃ ceramics in the vicinity of morphotropic phase boundary", *Jpn. J. Appl. Phys.*, 1999, **38**, 5539-43
52. D. Luff, R. Lane, K. R. Brown and H. J. Marshallsay, "Ferroelectric ceramics with high pyroelectric properties", *Trans. J. Br. Ceram. Soc.*, 1974, **73**, 251
53. X. H. Zhu, J. Xu and Z. Y. Meng, "Dielectric and piezoelectric properties of Pb(Ni_{1/3}Nb_{2/3})O₃ - PbTiO₃ - PbZrO₃ ceramics modified with bismuth and zinc substitutions", *J. Mater. Sci.*, 1997, **32**, 4275-82
54. J. Kuwata, K. Uchino and S. Nomura, "Dielectric and piezoelectric properties of 0.91Pb(Zn_{1/3}Nb_{2/3})O₃-0.09PbTiO₃ single-crystals", *Jpn. J. Appl. Phys.*, 1982, **21**, 1298-1302
55. H. X. Yu and C. A. Randall, "Dendritic domain configurations in Pb(Zn_{1/3}Nb_{2/3})O₃-PbTiO₃ single crystals", *J. Appl. Phys.*, 1999, **86**[10], 5733-38

56. D. S. Park, S. E. Park and T. R. Shrout, "Dielectric and piezoelectric properties of perovskite materials at cryogenic temperatures", *J. Mat. Sci.*, 1999, **34**, 469-73
57. M. L. Mulvihill, L. E. Cross, W. Cao and K. Uchino, "Domain-related phase transitionlike behavior in lead zinc niobate relaxor ferroelectric single crystals", *J. Am. Ceram. Soc.*, 1997, **80**[6], 1462-68
58. N. Yasuda, H. Ohwa, D. hasegawa, K. Hayashi, Y. Hosono, Y. Yamashita, M. Iwata and Y. Ishibashi, "Temperature dependence of piezoelectric properties of a high Curie temperature in $\text{Pb}(\text{In}_{1/2}\text{Nb}_{1/2})\text{O}_3$ - PbTiO_3 binary system single crystal near a morphotropic phase boundary", *Jpn. J. Appl. Phys.*, 2000, **39**, Part 1, No. 9B, 5586-88
59. R. E. Newnham, D. P. Skinner and L. E. Cross, "Connectivity and piezo-electric-pyroelectric composites", *Mater. Res. Bull.*, 1978, **13**, 525-36
60. S. M. Pilgrim, R. E. Newnham and L. L. Rohlfing, "An extension of the composite nomenclature scheme", *Mater. Res. Bull.*, 1987, **13**, 525-36
61. T. R. Gururaja, A. Safari, R. E. Newnham and L. E. Cross, "Piezoelectric ceramic-polymer composites for transducer applications", Ch. 2.3 in *Electronic Ceramics* edited by L. M. Levinson, Marcel Dekker, New York, 1987
62. A. Safari, "Development of piezoelectric composites for transducers", *J. Phys. III Appl. Phys. Mater. Sci., Fluids, Plasma, Instrum.*, 1994, **4**[7], 1129-49
63. Y. Matsuo and H. Sasaki, "Formation of lead zirconate-lead titanate solid solutions", *J. Am. Ceram. Soc.*, 1965, **48**[6], 289-91
64. G. H. Haertling and C. E. Land, "Recent improvements in the optical and electrooptic properties of PLZT ceramics", *Ferroelectrics*, 1972, **3**, 269-80

65. K. S. Mazdiyasni, "Fine particle perovskite processing", *Am. Ceram. Soc. Bull.*, 1984, **63**[4], 591-4
66. W. J. Dawson, "Hydrothermal synthesis of advanced ceramic powders", *Am. Ceram. Soc. Bull.*, 1988, **67**[10], 1673-8
67. A. Y. Wu, I. M. Salvado, P. M. Vilarinho and J. L. Baptista, "Lead zirconate titanate prepared from different zirconium and titanium precursors by sol-gel", *J. Am. Ceram. Soc.*, 1998, **81**[10], 2640-44
68. A. I. Kingon and J. B. Clark, "Sintering of PZT ceramics: II. Effect of PbO content on densification kinetics", *J. Am. Ceram. Soc.*, 1983, **66**[4], 256-60
69. G. S. Snow, "Elimination of porosity in $\text{Pb}(\text{Zr},\text{Ti})\text{O}_3$ ceramics by liquid-phase sintering," *J. Am. Ceram. Soc.*, 1973, **56**[2], 91-96
70. M. A. Akbas, M. A. McCoy and W. E. Lee, "Microstructural evolution during pressureless sintering of lead lanthanum zirconate titanate ceramics with excess lead (II) oxide", *J. Am. Ceram. Soc.*, 1995, **78**[9], 2417-24
71. F. Xia and X. Yao, "The role of PbO content on the dielectric and piezoelectric properties of PZN-based ceramics", *J. Mater. Sci.*, 2001, **36**, 247-53
72. R. B. Atkin, and R. M. Fulrath, "Point defects and sintering of lead zirconate - titanate," *J. Am. Ceram. Soc.*, 1971, **54**[5], 265-70
73. A. I. Kingon and J. B. Clark, "Sintering of PZT ceramics: I. Atmosphere control", *J. Am. Ceram. Soc.*, 1983, **66**[4], 253-56
74. K. H. Hardtl and H. Rau, "PbO vapour pressure in the $\text{Pb}(\text{Zr}_x\text{Ti}_{1-x})\text{O}_3$ system", *Solid State Commun.*, 1969, **7**[1], 41-45

75. L. F. Bazarova and F. K. Volynets, "Compaction kinetics of lead-lanthanum zirconate-titanate in hot pressing," *Izv. Akad. Nauk SSSR, Neorg. Mater.*, 1979, **5**[10], 1821-26
76. G. H. Haertling and C. E. Land, "Hot-pressed (Pb, La)(Zr,Ti)O₃ ferroelectric ceramics for electrooptic applications", *J. Am. Ceram. Soc.*, 1971, **54**[1], 1-11
77. K. G. Ewsuk and G. L. Messing, "Densification of sintered lead zirconate titanate by hot isostatic pressing", *J. Mater. Sci.*, 1984, **19**, 1530-34
78. T. Hayashi, T. Inoue and Y. Akiyama, "Low-temperature sintering and properties of (Pb,Ba,Sr)(Zr,Ti,Sb)O₃ piezoelectric ceramics using sintering aids", *Jpn. J. Appl. Phys.*, 1999, **38**, 5549-52
79. T. Hayashi, T. Inoue and Y. Akiyama, "Low temperature sintering of PZT powders coated with Pb₅Ge₃O₁₁ by sol-gel method", *J. Euro. Ceram. Soc.*, 1999, **19**, 999-1002
80. M. Deri, "Ferroelectric Ceramics", Maclaren and Sons Ltd., London, 1966, 80
81. Y. Sugawara, K. Onitsuka, S. Yoshikawa, Q. C. Xu, R. E. Newnham and K. Uchino, "Metal-ceramic composite actuators", *J. Am. Ceram. Soc.*, 1992, **75**[4], 996-8
82. K. Onitsuka, A. Dogan, J. F. Tressler, Q. C. Xu, S. Yoshikawa and R. E. Newnham, "Metal-ceramic composite transducer, the Moonie", *J. Intel. Mat. Syst. Str.*, 1995, **6**[4], 447-55
83. J. F. Fernandez, A. Dogan, J. T. Fielding, K. Uchino and R. E. Newnham, "Tailoring the performance of ceramic-metal piezocomposite actuators, 'cymbals'", *Sensor Actuat. A - Phys.*, 1998, **65**[2-3], 228-37

84. IEEE transactions on sonics and ultrasonics: IEEE standard on piezoelectricity, 1984, volume SU-31, No. 2
85. S. G. Robinovich, "Measurement errors and uncertainties: theory and practice", New York, 1999
86. T. Tsurumi, Y. Kumano, N. Ohashi, T. Takenaka and O. Fukunaga, "90° reorientation and electric-field-induced strain of tetragonal lead zirconate titanate ceramics", *Jpn. J. Appl. Phys.*, 1997, **36**, 5970-75
87. K. Kakegawa, J. Mohri, T. Takahashi, H. Yamamura and S. Shirasaki, "Compositional fluctuation and properties of Pb(Zr,Ti)O₃", *Solid State Commun.*, 1977, **24**[11], 769-72
88. A. Yamada, T. Ogawa and Y. Chung, "Crystal orientation of tetragonal lead zirconate titanate ceramics surface and its aging behavior", *Jpn. J. Appl. Phys.*, 1997, **36**, 5958-62
89. Y. Saito, "Hysteresis curve of X-ray diffraction peak intensity in lead zirconate titanate ceramics", *Jpn. J. Appl. Phys.*, 1997, **36**, 5963-69
90. M. Pereira, A. G. Peixoto and M. J. M. Gomes, "Effect of Nb doping on the microstructural and electrical properties of the PZT ceramics", *J. Euro. Ceram. Soc.*, 2001, **21**[10-11], 1353-56
91. M. Villegas, C. Moure, J. Jurado and P. Duran, "Improvement of sintering and piezoelectric properties of soft lead zirconate titanate ceramics", *J. Mater. Sci.*, 1994, **29**, 4975-83
92. J. H. Park, B. K. Kim, K. H. Song and S. J. Park, "Piezoelectric properties of Nb₂O₅ doped and MnO₂-Nb₂O₅ co-doped Pb(Zr_{0.53}Ti_{0.47})O₃ ceramics", *J. Mater. Sci.: Materials in Electronics*, 1995, **6**, 97-101

93. T. Kato, N. Yamada and A. Imai, "Effect of dopant Nb^{+5} on lead zirconate titanate", *Ferroelectrics*, 1992, **134**(1-4), 151-156
94. W. E. Lee, I. M. Reaney and M. A. McCoy, "Planar defects in electroceramics", *21st Century Ceramics, British Ceramic Proceedings*, 1996, No.55, edited by D. P. Thompson and H. Mandal, Published by Institute of Materials, 199-212.
95. J. Ricote, R. W. Whatmore and D. J. Barber, "Studies of the ferroelectric domain configuration and polarisation of rhombohedral PZT ceramics", *J. Phys.: Condens. Matter*, 2000, **12**, 323-37
96. M. A. Akbas, I. M. Reaney and W. E. Lee, "Domain structure-property relations in lead lanthanum zirconate titanate ceramics", *J. Mater. Res.*, 1996, **11**(9), 2293-301
97. X. H. Dai, Z. Fu, J. F. Li and D. Viehland, "Effects of lanthanum modification on rhombohedral $Pb(Zr_{1-x}Ti_x)O_3$ ceramics: part 1. Transformation from normal to relaxor ferroelectric behaviours", *J. Mater. Res.*, 1996, **11**[3], 618-25
98. S. M. Gupta, J. F. Li and D. Viehland, "Coexistence of relaxor and normal ferroelectric phases in morphotropic boundary compositions of lanthanum-modified lead zirconate titanate", *J. Am. Ceram. Soc.*, 1998, **81**(3), 557-64
99. H. J. Hwang, T. Nagai, T. Ohji, M. Sando, M. Toriyama and K. Niihara, "Curie temperature abnormality in lead zirconate titanate/silver composites", *J. Am. Ceram. Soc.*, 1998, **81**(3), 709-12
100. L. E. Cross, "Review: Ferroelectric materials for electromechanical transducer applications", *Mater. Chem. & Phys.*, 1996, **43**, 108-15

101. Q. Tan, J. F. Li and D. Viehland, "The influence of mobile vs. randomly quenched impurities on ferroelectric phase transformations", *Ferroelectrics*, 1998, **206-207**, 275-91
102. L. Q. Zhou, P. M. Vilarinho and J. L. Baptista, "Dependence of the structural and dielectric properties of $Ba_{1-x}Sr_xTiO_3$ ceramic solid solutions on raw material processing", *J. Euro. Ceram. Soc.*, 1999, **19**, 2015-20
103. G. A. Smolenskii, V. A. Isupov, A. I. Agranovskaya and S. N. Popov, "Ferroelectrics with diffuse phase transition", *Sov. Phys. Solid State*, 1961, **2**, 2584-94
104. M. J. Haun, Z. Q. Zhuang, E. Furman, S. J. Jang and L. E. Cross, "Electrostrictive properties of the lead zirconate titanate solid-solution system", *J. Am. Ceram. Soc.*, 1989, **72[7]**, 1140-44
105. D. Damjanovic and M. Demartin, "Contribution of the irreversible displacement of domain walls to the piezoelectric effect in barium titanate and lead zirconate titanate ceramics", *J. Phys.: Condens. Matter*, 1997, **9**, 4943-53
106. H. Thomas, Morgan Electroceramics, *Private communication*.
107. F. Levassort, P. Tran-Huu-Hue and E. Ringgaard, "High-frequency and high-temperature electromechanical performances of new PZT-PNN piezoceramics", *J. Eur. Ceram. Soc.*, 2001, **21[10-11]**, 1361-65
108. Z. Xu, D. Viehland, P. Yang and D. A. Payne, "Hot-stage transmission electron microscopy studies of phase transformations in tin-modified lead zirconate titanate", *J. Appl. Phys.*, 1993, **74[5]**, 3406-13
109. E. L. Colla, I. M. Reaney and N. Setter, "Effect of structural changes in complex perovskite on the temperature coefficient of the relative permittivity", *J. Appl. Phys.*, 1993, **74[5]**, 3414-25

110. I. M. Reaney, A. Glazounov, F. Chu, A. Bell and N. Setter, "TEM of antiferroelectric-ferroelectric phase boundary in $(\text{Pb}_{1-x}\text{Ba}_x)(\text{Zr}_{1-x}\text{Ti}_x)\text{O}_3$ solid solution", *Brit. Ceram. Trans.*, 1997, **96**[6], 217-224
111. R. D. Shannon and C. T. Prewitt, "Effective ionic radii in oxides and fluorides", *Acta Cryst.*, **B26**, 1970, 1046
112. X. Dai, Z. K. Xu, and D. Viehland, "Effect of oxygen octahedron rotations on the phase stability, transformational characteristics, and polarisation behavior in the lead zirconate titanate crystalline solution series", *J. Am. Ceram. Soc.*, 1995, **78**[10], 2815-27
113. D. Viehland, J. F. Li, X. H. Dai and Z. Xu, "Structual and property studies of high Zr-content lead zirconate titanate", *J. Phys. Chem. Solids*, 1996, **57**[10], 1545-54
114. B. P. Pokharel, R. Ranjan, D. Pandey, V. Siruguri and S. K. Paranjpe, "Rhombohedral superlattice structure and relaxor ferroelectric behavior of $(\text{Pb}_{0.70}\text{Ba}_{0.30})\text{ZrO}_3$ ceramics", *Appl. Phys. Lett.*, 1999, **74**[5], 756-58
115. H. Zheng, I. M. Reaney, P.Y. Wang and W. E. Lee, "Structure-property relations in soft PZT ceramics", *Proc. Ferroelectrics 2000 UK Workshop*, 2000, 51-58
116. R. H. French, S. J. Glass and F. S. Ohuchi, "Experimental and theoretical determination of the electronic structure and optical properties of three phases of ZrO_2 ", *Phys. Rev. B, Condensed Matter*, 1994, **49**[8], 5133-42
117. Q. Tan, Z. Xu, and D. Viehland, "Commonalties of the influence of lower valent A-site and B-site modifications on lead zirconate titanate ferroelectrics and antiferroelectrics", *J. Mater. Res.*, 1999, **14**[2], 465-74

118. J. Martínez-Fernández, M. Jiménez-Melendo and A. Domínguez-Rodríguez, “Ferroelasticity of the displacive tetragonal phase in Y_2O_3 partially stabilized ZrO_2 (Y-PSZ) single crystals”, *J. Mater. Res.*, 1996, **11**[8], 1972-78
119. F. Fernández, C. Moure, M. Villegas, P. Durán, M. Kosec and G. Drazic, “Compositional fluctuations and properties of fine-grained acceptor-doped PZT ceramics”, *J. Euro. Ceram. Soc.*, 1998, **18**(12), 1695-705
120. L. Sachelarie, E. Rezlescu and N. Rezlescu, “Influence of PbO on some properties of MgCuZn ferrites”, *Phys. Stat. Sol. A*, 2000, **179**[1]: R1-R3
121. M. A. Malik and X. Z. Jiang, “Destruction of VOCs by combination of corona discharge and catalysis techniques”, *J. Environ. Sci.*, 1998, **10**[3], 276
122. G. Robert, D. Damjanovic and N. Setter, “Preisach modelling of piezoelectric nonlinearity in ferroelectric ceramics”, *J. Appl. Phys.*, 2001, **89**[9], 5067-74
123. B. Noheda, D. E. Cox, G. Shirane, R. Guo, B. Jones and L. E. Cross, “Stability of the monoclinic phase in the ferroelectric perovskite $\text{PbZr}_{1-x}\text{Ti}_x\text{O}_3$ ”, *Phys. Rev.*, 2001, **63**[1], 4103-12
124. Q. M. Zhang, W. Y. Pan, S. J. Jang and L. E. Cross, “Domain wall excitations and their contributions to the weak-signal response of doped lead zirconate titanate ceramics”, *J. Appl. Phys.*, 1988, **64**, 6445-51
125. V. Mueller and Q. M. Zhang, “Threshold of irreversible domain wall motion in soft PZT-piezoceramic”, *Ferroelectrics*, 1998, **206-207**, 113-22
126. S. Li, W. Cao and L. E. Cross, “The extrinsic nature of nonlinear behavior observed in lead zirconate titanate ferroelectric ceramic”, *J. Appl. Phys.*, 1991, **69**, 7219-224

127. A. P. Barranco, F. C. Pinar, O. P. Martinez, J. S. Guerra and I. G. Carmenate, "AC behaviour and conductive mechanisms of 2.5 mol% La_2O_3 doped $\text{PbZr}_{0.53}\text{Ti}_{0.47}\text{O}_3$ ferroelectric ceramics", *J. Euro. Ceram. Soc.*, 1999, **19**, 2677-83
128. R. P. Tandon, "Impedance spectroscopy of lanthanum modified $\text{Pb}(\text{Zr,Ti})\text{O}_3$ ceramics", *J. Korean Phys. Soc.*, 1998, **32**, S327-29
129. A. P. Barranco, F. C. Pinar, O. P. Martinez and A. H. Tera, "The grain size, dielectric properties and impedance spectroscopy in a modified ternary system of $\text{Pb}(\text{Zr,Ti})\text{O}_3$ ", *J. Mater. Sci. Lett.*, 1997, **16**, 534-36
130. I. M. Reaney "Effect of octahedral tilt transitions on the properties of perovskites and related materials", *Ferroelectrics*, 1999, **222**, 143-52
131. M. Ozgul, K. Takemura, S. Tholier-Mckinstry and C. A. Randall, "Polarisation fatigue in $\text{Pb}(\text{Zn}_{1/3}\text{Nb}_{2/3})\text{O}_3$ - PbTiO_3 ferroelectric single crystals", *J. Appl. Phys.*, 2001, **89**(9), 5100-06